Reliable Design of Micro-Satellite Systems Using Combined Physics of Failure Reliability Estimation Models

by

Cass Adam Hussmann
B.Eng., University of Victoria, 2014

A Thesis Submitted for Partial Fulfillment of the Requirements for the Degree of

Master of Applied Science

in Mechanical Engineering

Reliable Design of Micro-Satellite Systems Using Combined Physics of Failure Reliability Estimation Models

by

Cass Adam Hussmann
B.Eng., University of Victoria, 2014

Supervisory Committee

Prof. Afzal Suleman, Supervisor
(Department of Mechanical Engineering)

Dr. Nikitas Dimopoulos, Outside Member
(Department of Electrical and Computer Engineering)

Supervisory Committee

Prof. Afzal Suleman, Supervisor
(Department of Mechanical Engineering)

Dr. Nikitas Dimopoulos, Outside Member
(Department of Electrical and Computer Engineering)

ABSTRACT

Up until 2015 the rate at which cube satellite missions achieved full mission success was only 44.1% for any organizations first mission (academic or corporate), the success rate increases to only 62% for cube satellites launched as a second mission. This thesis suggests that there are two main sources for the high failure rate: improper verification, and the common use of COTS components and their reliability in a space environment. The thesis provides a means of increasing mission assurance through the use of physics of failure reliability estimation models that incorporate the intrinsic and extrinsic failures of thermal mechanical effects as well as radiation effects on EEE components, a design methodology is also presented that incorporates reliability modeling as well as thorough software and hardware in loop testing to prevent failure due to improper verification. The environment and reliability models are calculated for the on board command and data handling system of the ECOSat-II cube satellite being developed by the University of Victoria ECOSat team using NX Siemens for thermal FEA modelling, SPENVIS for radiation environment, and MATLAB for reliability calculation.

Contents

List of Tables

List of Figures

ACKNOWLEDGEMENTS

I would like to thank:

Larry Reeves, for his hard work and dedication in organizing the Canadian Satellite Design Challenge, providing an opportunity for Canadian University students to get involved with space systems development which is otherwise completely unavailable.

Prof Afzal Suleman, for an amazing amount of mentoring, support, encouragement, and patience.

The ECOSat team, especially Justin Curran, and Nigel Syrotuck for their expertise and dedication to the project and their involvement in providing me an opportunity to join the project.

and

My family, for supporting me through many years of school.

Nomenclature

ACS	Attitude Control System
ADC	Analog to Digital Converter
ADCS	Attitude Determination and Control System
ADS	Attitude Determination System
BGA	Ball Grid Array
CAD	Computer Aided Design
CCVM	Collected Volatile Condensible Materials
COTS	Commercial Off The Shelf
CPU	Central Processing Unit
CSA	Canadian Space Agency
CSDC	Canadian Satellite Design Challenge
CTE	Coefficient of Thermal Expansion
DAC	Digital to Analog Converter
DD	Displacement Damage
EEE	Electronic, Electrical, and Electromechanical
EOL	End of Life
EOS	Electrical Over Stress

ESA	European Space Agency
ESD	Electro Static Discharge
FEA	Finite Element Analysis
FFT	Fast Fourier Transform
FPGA	Field Programmable Gate Array
GCR	Galactic Cosmic Ray
IQ	In phase, Quadrature
LDO	Low Dropout Regulator
LEO	Low Earth Orbit
LET	Linear energy transfer
LGA	Land Grid Array
MEMS	Micro-Electro-Mechanical Systems
MMC	Multi Media Card
NASA	National Aeronautics and Space Agency
NASTRAN	NASA STRucture ANalysis
NDA	Non Disclosure Agreement
OBC	On Board Computer
OSCAR	Orbiting Satellite Carrying Amateur Radio
QFN	Quad Flatpack No lead
Rx	Receive
SAA	South Atlantic Anomaly
SEB	Single Event Burnout
SECDED	Single Error Correction, Double Error Detection

SEE	Single Event Effect
SEFI	Single Event Functional Interrupt
SEGR	Single Event Gate Rupture
SET	Single Event Transient
SEU	Single Event Upset
TID	Total Ionizing Dose
TML	Total Mass Loss
Tx	Transmit

Chapter 1

Introduction

1.1 Background

1.1.1 CSDC

First starting in 2011, the Canadian Satellite Design Challenge (CSDC) provides an opportunity to post secondary students across Canada to get involved and gain experience in satellite and space systems design [1]. The CSDC competition challenges universities across Canada to design a three unit cube satellite mission involving the analysis, design, and management of a physical satellite to be manufactured and tested through preliminary and critical design reviews as well as environmental testing for vibrational tolerance and/or thermal vacuum results. The three unit cube satellite format required by the competition is a standardization on micro satellites created by California Polytechnic State University based on single units of 10cm x 10cm x 11.35cm and a mass limit of 1.33Kg. Its purpose was to help standardize launch interfaces to reduce the cost and therefore the barrier of entry to space for academic institutions and small companies. By creating a three-unit structure, universities participating in the CSDC are restricted to a 10cm x 10cm x 34cm structure and a maximum mass of 4Kg. Each round of the competition spans a timeline of 2 years with the ultimate goal of launching the winning satellite after full launch and space

environment qualification. Currently, the competition is continuing into its third round which will be ending in June of 2016.

Science and engineering is not the only focus of the CSDC competition. In addition to the goal of constructing a cube satellite, the CSDC has primary objectives focused on:

1. Enhancing public and educational outreach of science, technology, education, and math within Canada;
2. Enhancing the technical expertise and knowledge of space-related technology and development at Canadian Universities; and,
3. To provide an opportunity to Canadian post secondary students to gain experience in space-technology development and management.

1.1.2 ECOSat

The ECOSat project started at the University of Victoria (UVic) in 2011 as UVic's participation into the first round of the Canadian Satellite Design Challenge. The project is comprised of undergraduate and graduate students primarily from the Faculty of Engineering as well as students from the science, physics, math, and business departments. UVic ECOSat has a great track record within the competition placing 3^{rd} in the first round of the competition in 2012 and 1^{st} place in the second round in 2014. The team is currently involved in verifying ECOSat-2 and developing ECOSat-3 as participation in the third round of the competition. While the target orbit of both satellites is a sun-syncronous orbit at an altitude of 600km, they have very different missions.

The ECOSat-2 cube satellite focuses on both a science payload researching into the use of a thermally controllable diamagnetic material called pyrolytic graphite as a means of attitude control, as well as operation as an AMSAT in which it will provided amateur radio enthusiasts around the world with repeater and telemetry functionality. The AMSAT functionality helps contribute to the outreach and provides a very

practical example and demonstration of space applications to both education and the public.

The ECOSat-3 cube satellite focuses on continuing the space technology and systems development experience at the University of Victoria through a low resolution hyperspectral imaging payload that will image all of Canada once every 8 days, depending on weather and season. ECOSat-III will result in systems with far greater processing capabilities than ECOSat-II. It will be using a Xilinx zynq system on chip which contains a combination of an ARM processor running VX Works and an FPGA fabric for communications digital signal processing as well as payload image compression.

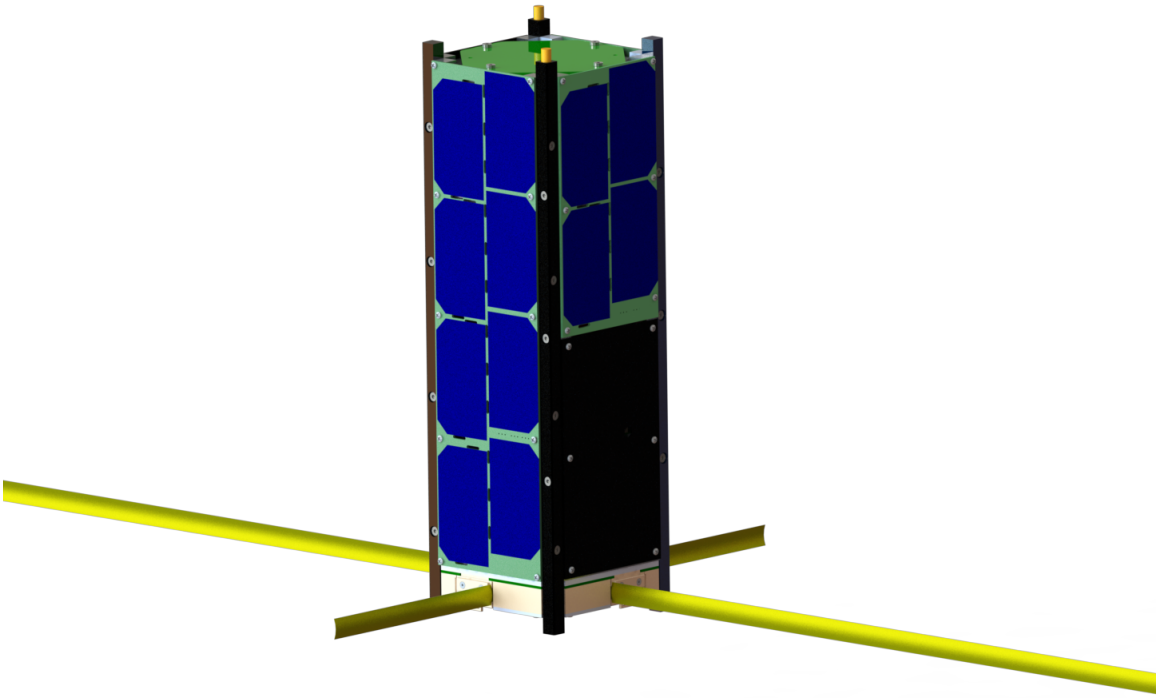

Figure 1.1: The ECOSat-2 Cube Satellite

1.1.3 Cube Satellite Success rates

While cube satellites and other micro satellite platforms continue to provide a low cost entry into space for academic and other small organizations, the development and launch of a cube satellite still cost on the order of USD$100k-$400k. While the cost of development and launch of a micro satellite is much lower than the millions of dollars required to launch a traditional large satellite bus, it is important to ensure that the mission will provide successful and useful scientific or technological outcomes.

Cube satellites have shown historically that first missions have a greater than 1 in 2 chance of not fully completing their missions. A database compiled by Michael Swartwout from Saint Louis University [2] provides a listing of missions status and results of cube satellites originating from both academic and industrial missions starting in the year 2000 to present. From this database, the chance of full success of an entitys first cube satellite is only 44.1%, and with experience of a first mission entities have shown that a second mission typically has a 62% chance of success.

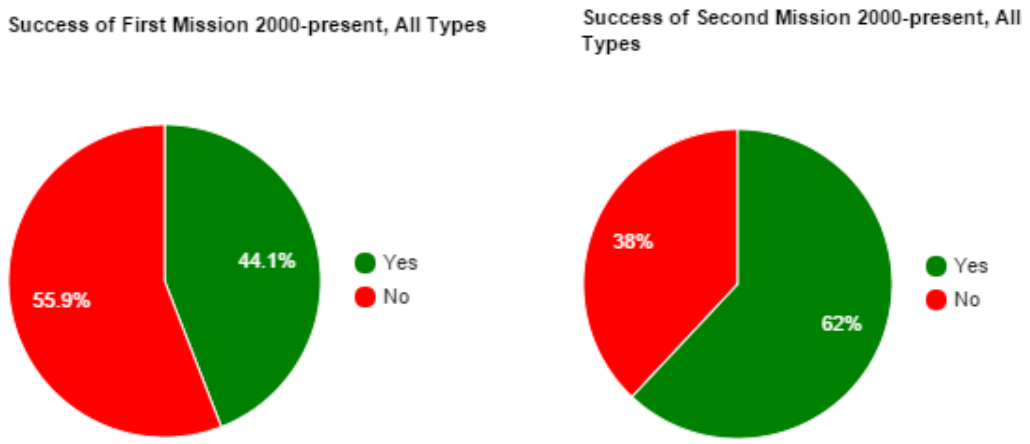

(a) First Mission Success (b) Second Mission Success

Figure 1.2: Cube Satellite mission success [2]

Separating academic and corporate mission results in two very different chances of success. Likely due to the experience of the engineers involved in the projects as well as differences in budget and organizational structure, industry and government agencies have demonstrated a much higher chance of success than universities.

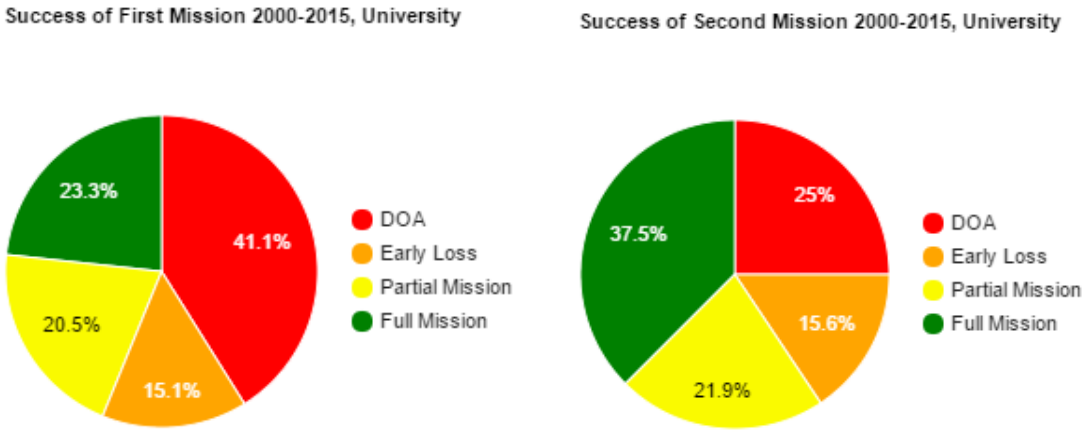

(a) First Mission Success (b) Second Mission Success

Figure 1.3: Academic Cube Satellite mission success [2]

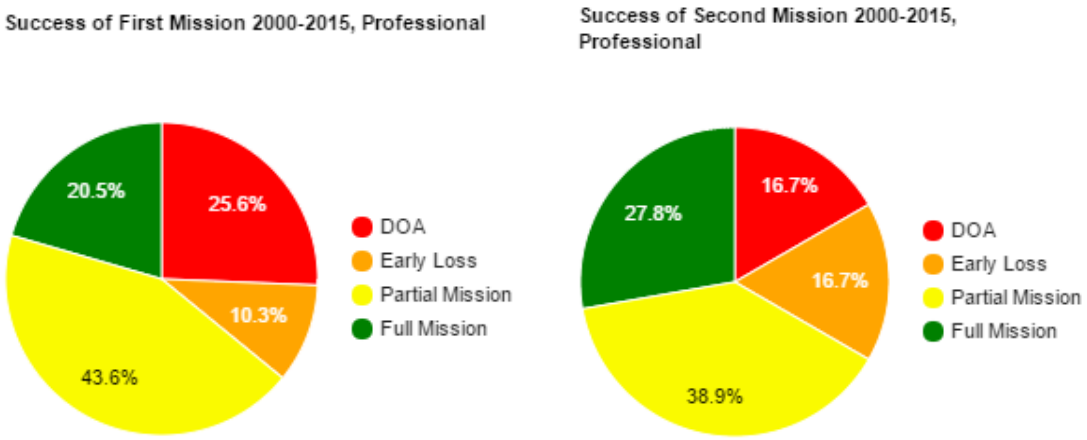

(a) First Mission Success (b) Second Mission Success

Figure 1.4: Professional Cube Satellite mission success [2]

1.2 Thesis Goals and Organization

This thesis aims to help understand and increase the probability of mission success by providing a means of using a combination of physics of failure models to predict an estimate of the reliability of EEE components and systems. Using reliability modeling helps identify sections of an electrical system that may require more redundancy to meet an acceptable level of risk at the end of a target mission duration. The effort of this research is to increase the chance of mission success and continued operation at the end of life of a micro satellites and any other space-based electrical system. Additionally, this thesis also aims to present background information on the effects of the space environment on satellite systems as well as highlight the importance of verification and testing often looked over within academic projects.

This thesis is divided into three main sections. First, chapters 1 and 2 present the motivation behind the work; chapters 3, 4 and 5 discuss the reliability model created and the design methodology developed; and chapter 6 discusses their use in the reliable design of the ECOSat project as a case study.

- **Chapter 2:** Background information on the space environment and its effects on a satellite
- **Chapter 3:** Models for estimating the reliability of EEE components
- **Chapter 4:** Redundancy schemes and their effect on reliability
- **Chapter 5:** Design Methodology
- **Chapter 6:** Reliability analysis and design comparisons using models discussed within Chapter 3
- **Chapter 7:** Conclusions and Future Work

Chapter 2

The Space Environment

2.1 Summary

Designing systems and materials for operation in space introduces many unique difficulties not experienced by applications operating in water, on the ground, or in the air. There are six environments of interest to satellite systems design with two causing the primary source of stress on the components. The main environments focused on for reliability are the vacuum environment and its effects on thermal cycling as well as the radiation environment and the total ionizing dose as well as single event effects caused by it. The remaining four environments include the vibrational environment experienced during launch which last a very short time in relation to the mission as well as the debris environment, plasma environment, and neutral environment.

2.2 Introduction

This section aims to provide background information on the effects that the space environment has on components and materials used in the constructions of a satellite. The orbital environment is presented as six separate environments in this chapter:

- The Vacuum Environment;
- The Neutral Environment;
- The Plasma Environment;
- The Radiation Environment;
- The Debris Environment; and,
- The Vibrational Environment

These environments and how they effect satellite systems will be discussed as background information to help describe the motivation behind the work into reliability prediction and reliable design of electrical satellite systems.

2.3 Vacuum Environment

The term vacuum environment will be used to describe all effects on a satellite caused by its operation in a near vacuum. Three main effects are caused by operating in a vacuum. First is the lack of any exterior pressure, the pressure on a structure at sea level is approximately 101.325 kPa, this means that any structure intended to maintain an interior compartment at sea level pressure needs to be designed to contain 101.325 kN of force per square meter of internal container wall. The Second major effect is thermal management, in a vacuum all input and output thermal energy is transferred radiantly causing large temperature extremes and variations through an orbit, the absorptivity and emissivity can be affected by both contamination and solar UV radiation, some of these thermal effects will be discussed more in the neutral environment section. The final effect of concern in vacuum is out gassing of materials in which through a number of different processes such as random thermal motion, molecules can separate from a material reducing its mass and potentially building up as contamination on sensitive surfaces such as optics. The build up of contaminants can increase the absorbency of the surface to thermal energy, thus increasing the thermal issues related to operating in a vacuum.

Pressure differentials

As mentioned the vacuum environment can create stresses on the structure of any satellite in orbit with pressurized sections. A compartment pressurized to sea level (101.325kPa) will experience a force of 101.325kN per square meter on the interior of the structure, this can be much worse for pressurized fuel, oxidizer, or propellant tanks. However, this effect is well known and not much different than it is for pressurized containers at sea level. A bigger focus by the designers should be on the proper venting of gazes from non pressurized sections such that the gases are directed away from sensitive components and that the ventilation holes are adequately sized for the rate at which the external pressure decreases due to the launch profile.

Out-gassing

The essence of out-gassing is that through random thermal motion, volatile chemicals in a material can make their way to the surface and escape into the vacuum, in orbit these particles that escape from the material travel on straight trajectories and can build up on any surface in line of sight. There are three mechanisms that control out gassing, first Diffusion occurs from the random thermal motion of a volatile chemical in an organic material, the escape of a molecule through this mechanism generally requires 5-15 kcal/mole of energy. The second mechanism is desorption which is a release of molecules on the surface of a material requiring energies around 1-10 kcal/mole. Finally, decomposition can cause a complex compound to separate into multiple substances that can then escape the material through diffusion or desorption, this process generally requires energies on the order of 20-80 kcal/mole.

Diffusion is focused on during the design and analysis of satellite. Desorption can be fairly safely neglected as it is only dependent on the surface area of a material, while Decomposition can be prevented by not allowing materials that can decompose to be used in the design of the satellite. When reading out gassing data, tables generally give two values, one for the total mass loss as a percent (TML) and another value of the Collected Volatile Condensible Materials (CVCM), for example some values of Delrin, a thermoplastic similar to Teflon, and a number of other materials

used in electronics can be seen in the table below, FR4 is a common epoxy using in PCB manufacturing while AM28F020-150PC, 9618FBB is an IC encapsulate. The NASA guidelines specify that materials used for satellite should have a TML of less than 1% and a CVCM of less than 0.1%.

Out-gassing of materials is primarily a concern for its resulting contamination referred to as molecular contamination of other surfaces within the satellite. Another source of contamination occurs from the satellites manufacturing and launch called particulate contamination, μm sized particles from the air can build up on surfaces and if not cleaned can find their way onto optics of sensors effectively increase the signal to noise ratio as well as onto solar cells decreasing the panels efficiency, it has been shown that as a general approximation the power of a solar cell drops 2% per μm of contamination buildup.

UV degradation

$$E = \frac{hc}{\lambda}$$

Without the protective atmosphere surrounding Earth, materials in orbit are exposed to the full energy of ultraviolet radiation coming from the sun. The energy in a photon of UV light is enough to break some organic bonds. As an example a C-C bond can be broken by 3.47eV of energy or equivalently 0.36μm while a C-O bond can be broken by 7.77eV or equivalently a photon with a wavelength of 0.16μm. Most

Table 2.1: Out gassing of some common materials used on ECOSat2 [3]

Material Description	Outgassing Reference	%TML	%CVCM
Delrin II 100NC10	GSFC16847	0.34	0.01
Delrin II 500NC10	GSFC16850	0.28	0.01
Delrin II 900NC10	GSFC16855	0.29	0.01
Delrin 100 NC10	SRI9201	0.58	0.06
FR-4 Epoxy Resin	-	0.32	0.01
AM28F020-150PC, 9618FBB	-	0.28	0.05

other organic bonds require energies that fall between C-C and C-O to be broken. The ultra violet spectrum ranges from 0.122μm with energies of 10.25eV to 0.4μm with energies of 3.1 eV. The degradation of materials from UV radiation can cause darkening of materials effectively increasing the absorbance of the material. This increase in absorbance can cause problems for thermal management over the life of the satellite.

Thermal Management

Operating in a vacuum environment poses a difficult problem for thermal management, without an atmosphere surrounding the satellite the total thermal energy in and out is radiant and follows the two equations below. where α_s is the solar absorbance of the material, A_{in} is the total surface area exposed to the solar flux S and ϵ is the emittance of the material, A is total surface area, σ is the Boltzmanns constant and T is the satellite temperature in kelvin. All thermal energy absorbed by the sun and Earth albedo as well as thermal energy generated by electronics must be radiated using radiator panels or other external surfaces.

$$Q_{in} = \alpha_s \alpha_{in} S(Watts) \quad Q_{out} = \epsilon A \sigma T^4 (Watts) \tag{2.1}$$

Through the contamination of outer surfaces and the darkening of materials through UV degradation α_{in} of the satellite can increase over its mission life time. Due to contamination a thermal management system may be insufficient at the end of satellites mission life, one approach is to create radiator panels designed for the end of life thermal characteristics with larger heaters used during the beginning of life.

Table 2.2: Absorbance and Emittance of common structural surface materials

Material	α	ϵ
Aluminum	0.1	0.05
Black Paint	0.97	0.87
Kapton	0.48	0.81

2.4 Neutral Environment

While in low Earth orbit, earths atmosphere is vacuum like ($1.56x10^{-13}\frac{kg}{m^3}$ at 600km [4]), however enough remaining particles exist to interact with the satellite. The Neutral environment is only of major concern to satellite operating in low Earth orbit (within the Thermosphere) as the major particle here is atomic oxygen, for satellite operating in medium to high Earth orbit (Exosphere) the extremely low density and He particles that are contained as the major component can cause sputtering but at very low rates such that the neutral environment effects can be effectively ignored. The atmosphere is broken into a number of regions based on altitude and major constituent, these regions are listed in the table below. Within the Thermosphere molecular oxygen and ozone are broken down into atomic oxygen through chemical reactions and radiation.

Aerodynamic Drag

Interactions between particles in the remaining atmosphere and a satellite can create aerodynamic drag forces, these forces can effect attitude control, orbital control, and the eventual de-orbit of satellite in low Earth orbit. From simplified kinetic gas theory it can be seen that for an atmospheric mass density of ρ, a differential area dA of the satellite at an angle of θ to the direction of travel will experience a drag force dF.

Table 2.3: Atmospheric Regions [5, p. 74]

Region	Altitude	Major Constituent
Troposphere	$0 \rightarrow$ 11-12km	N_2
Stratosphere	11-12km $\rightarrow$ 45km	N_2
Mesosphere	45km $\rightarrow$ 80-85km	N_2
Thermosphere	80-85km $\rightarrow$ 1000km	O
Exosphere	1000 $\rightarrow$	He

$$dF = \rho v^2(1 + f(\theta))dA \quad f(\theta) : \frac{initial \quad momentum}{recoil \quad momentum} \tag{2.2}$$

By convention the formula replaces $2(1 + f(\theta))$ with C_d for a flat plate, where C_d is the coefficient of drag, in practice $f(\theta)$ can not be determined as it is impossible to accurately predict if a particle will adhere to the surface or bounce off after a collision, what happens in this situation depends on many variables such as speed, temperature, material, and others. Due the difficulty in accurately simulating the drag force exerted on a satellite typically approximations from past experiments on the same materials are used.

The total drag force on a satellite is then simply the surface integral over the front facing surface of the satellite using approximations of drag coefficients of simple shapes.

$$F = \frac{1}{2}\rho v^2 \oint C_d dA \tag{2.3}$$

To get a more accurate estimation of the drag force, the thermal velocity of atomic oxygen in low Earth orbit needs to be considered. The thermal velocity of atomic oxygen in LEO is on the order of $\tilde{1}$km/s while this is lower than orbit velocity it is significant enough that the force from lateral impacts needs to be considered. Similarly the coefficient of drag of the lateral side is calculated as $C_{d,ls} = (1 - f(\theta))cot\theta$, this is added with the front facing coefficient to get a more accurate estimation.

Table 2.4: Drag Coefficients of various shapes [6]

Shape	C_d
Flat Plate	$2(1 + f(\theta))$
Cone	$2(1 + f(\frac{\pi}{2} - \phi))$
Truncated Cone	$2(1 + f(0))(\frac{b}{a})^2 + 2(1 + f(\frac{\pi}{2} - \phi))(1 - (\frac{b}{a})^2)$

$$C_D = c_d + d_{d,ls}\frac{A_{ls}}{A} \quad F = \frac{1}{2}\rho v^2 \oint C_D dA \tag{2.4}$$

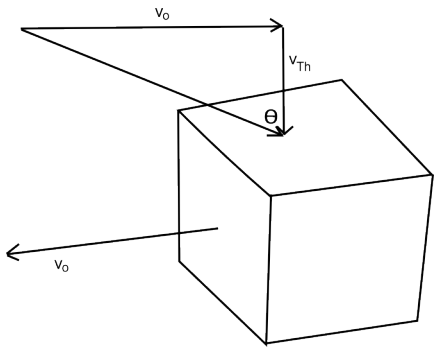

Figure 2.1: lateral impact contribution to aerodynamic drag

Physical Sputtering

As mentioned briefly in the aerodynamic drag section, particles in the neutral environment have significant large relative velocities on impact and as such have non-negligible energies during their collision with the satellite. It is possible for these collisions to break chemical bonds of surface atoms if the energy of the collision is higher than the surface atoms bond. When surface atom bonds are broken by the energy of a collision the process is called sputtering.

The threshold energy for sputtering to occur, that is the lowest energy impact that will allow for sputtering to occur can be modeled with the equations below [7], where U is the binding energy of the surface atom, m_t is the mass of the surface atom,

Table 2.5: Impact Energies of particles in the Thermosphere [5, p. 92]

		eV/atom					
Altitude	Velocity	H	He	O	N_2	O_2	Ar
200km	7.8km/s	0.3	1.3	5.0	8.8	10.1	12.6
400km	7.7km/s	0.3	1.2	4.9	8.6	9.8	12.2
600km	7.6km/s	0.3	1.2	4.7	8.3	9.5	11.8
200km	7.8km/s	0.3	1.1	4.5	7.9	9.0	11.2

and m_i is the mass of the incident atom.

$$\frac{m_t}{m_i} < 3: \quad E_{th} = 8U(\frac{m_t}{m_i})^{-\frac{1}{3}} \tag{2.5}$$

$$\frac{m_t}{m_i} > 3: \quad E_{th} = U[\gamma(1-\gamma)] \quad \gamma = \frac{4m_t m_i}{(m_t + m_i)^2} \tag{2.6}$$

Without the effects of satellite charging, sputtering yields are typically too small to effect material properties of materials on satellite operating for only a few years. As discussed in the vacuum environment section, sputtering instead is a concern for contamination of sensors, the degradation of thermal characteristics and solar panel efficiency.

Atomic Oxygen Attack

Atomic oxygen can chemically interact with coatings of materials effectively removing atoms from its surface. Since coatings are typically generated extremely thin, the contribution of atomic oxygen to the degradation can be significant over the life time of a satellite causing thermal issues similar to those discussed along with the vacuum environment. The mass loss of a material with an area dA over a differential amount of time dt caused by an atomic oxygen flux of ϕ in $atomcm^{-2}s^{-1}$ can be modeled as the following equation [5, p. 95-96] where ρ_t is the density of the target material in gcm^{-3} and RE is reaction efficiency of atomic oxygen and the target material, for example the RE of silver is 10.5.

$$dm = \rho_t RE\phi dAdt \tag{2.7}$$

Table 2.6: Sputtering yield of Al from incident energy of 100eV[5, p. 95]

	H	He	O	N_2	O_2	Ar
Al	0.01	0.02	0.026	0.06	0.076	0.11

$$\frac{dx}{dt} = RE\phi \tag{2.8}$$

Spacecraft Glow

Spacecraft glow is still not a very well understood effect. Many satellite in low Earth orbit have observed optical glow of surfaces which is believed to be linked to the neutral environment. The main concern associated with satellite glow is the negative effect on optical sensors, any surface in view of a sensor that begins to glow will effectively add noise into the sensor. While the mechanism that causes satellite glow to occur is not well understood some testing has shown a relation between the brightness of the glow B in units of Reyleighs to the altitude H in km [5, p. 100] and can be seen below.

$$logB = 7 - 0.0129H$$

2.5 Plasma Environment

The plasma environment includes the effects of all relatively low energy charged particles (on the range of keV's in comparison to charged particles in the radiation environment on the order of MeV's). Materials exposed to a plasma can be charged to very large electrical potentials. Different materials will charge at different rates and therefor to different electrical potentials when introduced to the same plasma due to different surface resistances, the major concern of the plasma environment is when two surfaces charge to different potentials with a great enough difference to cause arcing between the two materials along outer surfaces. Arcing can cause physical damage to the materials and structure as well as electrical damage in the form of ESD strikes to the power system and sense circuitry.

In a low Earth orbit, solar UV radiation ionizes nitrogen and oxygen atoms in earths atmosphere generating the majority of the plasma environment. Due to its

generation by solar UV, the plasma environment is partially dependent on local time and the current solar cycle. Density of the plasma peaks at an orbital altitude of about 300km, at higher altitudes the plasma density is lower but has a much higher energy. Since a charged particle's motion is constrained to move along magnetic field lines without any interfering electric fields, the high energy plasma present at high altitudes moves to much lower altitudes near the magnetic poles. This causes satellite in low Earth orbital altitudes but high inclinations to require considerations of the higher energy plasmas.

Plasma is greatly effected by the magnetic field it is in and as such is effected by the compression of earths magnetic field by solar wind. As the interface between earths magnetic field and the suns (known as the magnetopause) is compressed down forcing plasma into lower orbits. As solar activity changes the magnetopause fluctuates (severe events are referred to as geomagnetic storms) plasma is forced down to lower orbits. Due to the motion of charged particles in a magnetic field the fluctuation of the magnetopause forces electrons and ions in opposite directions, this causes a satellite between midnight and 6am local time to be surrounded by an excess of electrons. Due to the relative density of electronics compared to ions, satellite typically do not experience a similar effect caused by the more energetic ions forces down by the magnetopause fluctuations as the electrons cancel them out, the energetic electrons forced down are harder to be canceled by ions due to a lower density of ions and the slower velocity of ions due to their greater mass.

Spacecraft Charging and Arcing

From basic electromagnetics any unbiased object will be charged to a floating potential V_{fl} with respect to the surrounding plasma according to the following formula, where A_i is the area collecting ions on the front facing surface of the satellite, A_e is the area collecting electrons, v_o is the orbital velocity, n_o is the plasma density and $V_{e,Th}$ is the thermal velocity of electrons [5, p. 129-138]..

$$V_{fl} = \frac{kT_e}{e} ln(\frac{4v_o A_i}{V_{e,Th} A_e}) \tag{2.9}$$

$$I_i = en_o v_o A_i \quad I_e = \frac{1}{4} en_o exp(\frac{eV}{kT_e}) V_{e,Th} A_e \tag{2.10}$$

Objects charge to a different potential with respect to the satellite ground need to be analyzed differently. This typically only applies to solar panel arrays where each cell and interconnect is at a different potential than the reference ground. To simplify the situation the following equations only consider the portion of a surface that is charged to a lower electrical potential than that of the impacting ion or electron noted as ϕ.

$$I_i = en_o v_i \frac{f v_a - \phi_i}{v_a} A_i \quad I_e = en_o v_{e,Th} \frac{(1-f) f v_a - \phi_e}{v_a} A_e \tag{2.11}$$

The major factor in satellite charging in low Earth orbit is the ratio of A_e and A_i this is due to the large differences in their thermal velocity, the velocity of ions is low compared to the orbital velocity causing them to primarily interact with the front facing surface area with respect to the motion of travel, the thermal velocity of electrons on the other hand are high and can collide with the side surfaces providing more room to accumulate charge. At high altitudes the thermal velocity of ions is not longer much lower than the orbital velocity, this means that satellite charging is more depended on the plasma properties than it is on to ratio of A_e and A_i.

As can be seen from the equations, it is important to factor in the bias of the surface with respect to the satellite ground, this means that the type of grounding implemented is important to the analysis and the severity of plasma effects. Since solar arrays are typically the only biased surfaces on a satellite their connection is used to define the type of grounding used. There are three different types of grounding that can be used. Negative ground in which the satellite ground is referenced to the end of the solar array that floats negatively with respect to the plasma. Positive ground where the structure is connected to the end of the solar array that floats above the plasma potential. Finally, the floating ground method where the satellite structure is isolated from the solar array.

A negatively grounded satellite structure will collect ion current and push the solar

array bias with respect to the plasma higher, this typically causes a greater increase in electron current. A positively grounded satellite structure will collect electron current and cause the solar array to be come negatively biased with respect to the plasma and collect ion current. Finally, a floating grounded satellite structure has no effect on the bias of the solar array and does not increase collection currents.

Due to the density of electrons and ions, positively grounded and floating ground satellite will maintain the structure and solar array biases with respect to the plasma at a lower differential. Due to the low relative electric potential when using positively or floating ground satellite are preferred. Due to implementation issues negatively grounded satellite are more common as they can be implemented with fewer electrical concerns compared to floating and positive ground methods.

The main concern of satellite charging is not in the absolute value of the satellites potential with respect to the plasma but in the potential difference between different surfaces that when large enough can lead to arcing. When the potential difference of two surfaces becomes great enough an arc between the two surfaces can occur. There are 6 types of arcs defined by the MIL-HDBK-263 handbook as listed below.

- Thermal secondary breakdown
- Metalization melt
- Bulk breakdown
- Electrostatic discharge
- Dielectric breakdown
- Surface breakdown

Electrostatic and dielectric breakdown are typically focused on due to the potential differences surfaces on a satellite can charge too. Solar arrays are the main vulnerability of a satellite to arcing caused by satellite charging due to the proximity of dielectrics used on the cell and the metal interconnects between them. Arcing causes both physical damage as well as electromagnetic interference (EMI) effecting

sensitive electronics, communications, and data handling. The ESD strike can also carry large spikes of current into the power system causing damage to the batteries and regulation systems. Dielectric breakdown occurs when the potential difference across a material becomes greater than the dielectric breakdown characteristics of the material, this is typically on the scale of $10^5 V/cm$.

Induced Potentials

Another issue can occur that effects electrical systems on a satellite, the effect of induced potentials is not directly caused by the plasma environment but is related to satellite charging and electrical issues related to it. Induced potentials is an effect of the magnetic field. Due to the fact that an electron in a conducting material moving through a magnetic field has a force applied to it, the structure of a satellite will generate a potential voltage following the below equation. In low Earth orbit induced potentials create a voltage over the structure of approximately 0.3V/m, for large satellite this must be accounted for when designing communication lines and sensor lines.

$$V = (\vec{v} \times \vec{B}) \bullet \vec{l} \tag{2.12}$$

2.6 Radiation Environment

The radiation environment consists of very high energy particles on the order of MeV's to GeVs, the radiation environment shares many of the same particles that compose the plasma environment but on a much higher energy level, for example electrons in the plasma environment (on the order of keVs) can contribute to satellite charging while electrons in the radiation environment ($\sim$ 1MeV) can cause electrical faults within the interior of the satellite. There are many sources of radiation contributing to the radiation environment in space, the two major sources come from the sun directly in the form of galactic cosmic rays and streams of charged particles

expelled by solar particle events, the second is from high energy particles trapped in earths magnetic field in two main regions known as the Van Allen belts. The five sources of radiation that make up the majority of the radiation environment are listed below.

- Van Allen Belts (Trapped radiation belts)
- Galactic Cosmic Rays
- Solar Particle Events
- Atmospheric Neutrons
- Electronics and Packaging (Radioisotope thermo electric generators, Radioisotope Heating Units, etc)

For satellite operating in Earth orbit the main concern is the effect of the Vann Allen belts on electronics. The Vann Allen belts consist primarily of highly energetic electrons and protons trapped in earths magnetic field much like those that define the plasma environment. Due to the suns interaction with earths magnetic field the radiation belts are not static in their altitude and location. The belts are compressed down by the magnetopause during local day time and extend back out during local night. The radiation belts are also effected by the offset of earths magnetic and geographic poles which creates a region of lower magnetic field strength over the south Atlantic [5, p. 158], the lower magnetic field strength allows for higher energy particles to lower in altitude effectively increasing the flux at low altitudes in that region. There are two belts surrounding Earth that make up the trapped radiation belts, the inner belt consists of electrons and protons peaking at an altitude of 3000km, while the outer belt consisting of highly energetic electrons peaking at about 25000km.

Galactic cosmic rays also referred to as galactic cosmic radiation consists of 1MeV to >100GeV ionizing particles that fill our galaxy. Galactic cosmic rays consist primarily of photons, neutrons, and charged particles all with a low total flux of about 4 particles/cm^{2}s. The total flux of galactic cosmic rays has been shown to be depended on solar activity. With such low flux galactic cosmic radiation contributes mostly to single event effects in electronics than it does to total ionizing dose effects.

Another source comes from the sun in the form of solar particle events (more often referred to as coronal mass ejections), these events occur periodically in which the sun emits large amounts of protons, alpha particles, and other heavy ions. Solar particle events can last a wide range of durations from hours to a few weeks. In high orbits the absorbed dose and flux from a solar particle event may be high. In low altitude orbits the protection of the earths magnetic field deflects a majority of the charged particles, this deflection is caused from the force a perpendicular magnetic field exerts on a moving charged particle. At high latitudes near the magnetic poles this effect of shielding the satellite does not happen, here the particles ejected from the solar particle event travels parallel to the magnetic field lines and can reach much lower altitudes.

A minor source of concern for satellite in orbit are atmospheric neutrons that are generated when solar particle events and galactic cosmic radiation interacts with particles in the upper atmosphere. many of the products produced by the interaction interact quickly and only the neutrons are left to cause problems. These atmospheric neutrons have very low flux at low latitude and typically don't cause problems for satellite during launch.

During the design of deep space probes that will require the use of radioisotope thermoelectric generators (RTG) and radioisotope heating units (RHU) a source of radiation is introduced by the satellite itself. As an RTG or RHU is introduced as a design decision its source of gamma rays and neutrons from the decay of its nuclear source material must be characterized and accounted for.

Ionizing radiation

As charged particles in the radiation environment move through a material they exert a force on electrons in the materials atoms through the interaction of their electric fields. From electrostatic force, the force exerted by a charged particle of charge Z (C) and an electron with charge e at a distance of r away from each other can be calculated as F below. Similarly, it is also possible to formulate the amount of kinetic energy T transferred to the atomic electron as a charge particle passes in

terms of the charged particles velocity or in terms of its energy.

$$F = \frac{1}{4\pi\epsilon_o}\frac{Ze}{r^2} \tag{2.13}$$

$$T = \frac{p^2}{2m_e} = \frac{Z^2e^4}{8\pi^2\epsilon_o^2 a^2 m_e v^2} = \frac{Z^2e^4}{16\pi^2\epsilon_o^2 a^2 E} \quad [5, p.\ 170] \tag{2.14}$$

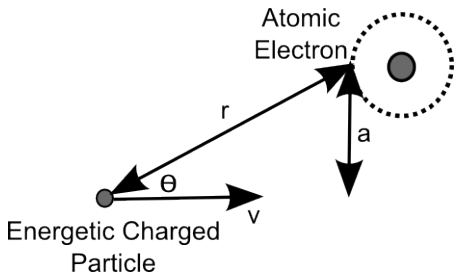

Figure 2.2: Ionizing radiation impact

As a charged particle passes through a material there are two measures of the amount of ionizing energy it transfers. The linear energy transfer (LET) is the change in kinetic energy per unit path ($\frac{dT}{dx}$) while the total ionizing dose (TID) is the kinetic energy transfer per unit mass ($\frac{dT}{dm}$). The values of TID and LET are dependent on both the materials density and a stopping cross section parameter σ_{stop} which is basically the probability of removing ΔT kinetic energy from a charged particle moving through an area of dA. The depth (also called range) a charged particle can penetrate into a material is then equal to R as seen below.

$$\sigma_{stop} = \int \Delta T dA \tag{2.15}$$

$$R = -\int_T^0 \frac{dT}{n\sigma_{stop}} \tag{2.16}$$

The stopping cross section is primarily dependent on the density of the material and while some methods of modeling it are available it is preferred to use empirical values from lab testing. The most common approach to protecting a satellite from ionizing radiation is to design shielding such that the range of a charged particle in the expected mission environment is less than the shield thickness.

The calculations above only work if relativistic effects are negligible, this is true for protons on the order of MeVs and electrons on the order of 0.5MeV in energy. For the much higher energy charged particles in galactic cosmic radiation or those that are ejected from the sun during solar particle events which have energies on the order of GeVs, the relativistic effects of their velocities needs to be taken into account. For charged particles on the order of GeV energy levels, the particle has to lose additional energy in the form of energetic photons for conservation of energy and momentum. The release of energetic photons is called bremsstrahlung radiation.

Energetic photons mainly x-ray (photons on the order of keV's) and gamma-ray (photons on the order of MeV's) energy photons can also cause damage to materials by altering its properties during a collision. the absorption of photons occur from one of three processes: the photoelectric effect, the Compton effect, or pair production. The photoelectric effect occurs when an atomic electron in the material absorbs the kinetic energy of the incident photon and is then given enough energy to break away from its atom. The Compton effect occurs when an electron deflects an incident photon and absorbs energy in the transfer of momentum. The final process, pair production occurs when an electron proton pair is created when the photon interacts near a nucleus. The three processes occur more frequently at different energies. While charged particles have a finite range, the decay of photons as they pass through a material is exponential and therefore there is no finite amount of shielding that can be used to completely remove the effect of high energy photons on the satellite.

Total Ionizing Dose

The total ionizing dose (TID) is a measure of the total amount of radiation causing ionization, this is separated from the displacement damage (DD) used to refer to the

Table 2.7: Photon absorption processes [5, p. 174]

Process	Energy Range
Photoelectric effect	<0.5MeV (Ultraviolet to X-ray)
Compton effect	0.5MeV - 5MeV (Gamma)
Pair production	>1.022MeV (Gamma)

total amount of displacement damage caused to the material. The amount of radiation absorbed is dependent on type of radiation and the material being affected, typically for electronics this is Silicon. For electronics values are typically measured with the unit Rad ($10^{-2}\frac{J}{Kg}$) rather than the SI unit of Grey ($1\frac{J}{Kg}$). At a geostationary orbit (35,800km, 0^o) a satellite experiences about 0.7 Rad/day, while at a low earth orbit the international space station (400km, 51.6^o) experiences only about 0.1 Rad/day, these values of course fluctuate following the fluctuations of the trapped radiation belts.

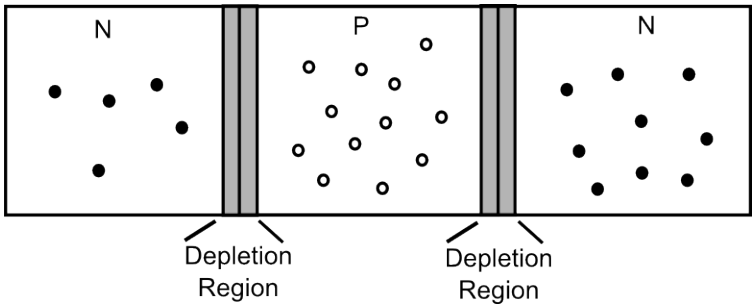

Figure 2.3: NPN Transistor

Large scale integrated electronics are created through the use of doping highly ordered silicon lattices into n-type (phosphorus, adding electrons), and p-type (boron, adding holes). An important concept in semiconductor physics is the energy band of a region, while in the valance band there are extra holes which prevents the flow of current, while in the conductive band there is an excess of electrons). The amount of dopant's, and the conductivity of each region, and the absence of contaminates (non silicon, phosphorus, or boron atoms) is very important to the operation of the circuit.

Displacement damage will cause the displacement of atoms in the silicon lattice which can change the dopant levels and change conductivity of the material. Ionizing radiation causes ionization of the material introducing excess charge carriers, this can increase the conductivity of dielectrics such as silicon dioxide creating leakage currents which can accumulate to cause major damage to the surrounding PN junctions. In silicon the electron hole pairs created by the ionization do not instantly recombine, the majority carrier (electrons in N type, and holes in P type) typically has a much higher mobility, if the majority carrier is given enough energy by the incident ionizing radiation then it may escape leaving the minority carrier, this excess minority carrier

effectively reduces the dopant level and makes it harder for the majority carriers to travel through the region.

Single Event Effects

Single event effects are a result of ionizing radiation much like total ionizing dose. As an energetic charged particle passes through a material electron-hole pairs are created in its wake, if the incident charged particles passes through the N-P junction of a transistor in silicon then a single even effect is likely to occur. Neutrons and heavy ions in radiation can also contribute to single event effects through the products of its interaction with the surrounding materials, when a neutron collides with some materials energetic charged particles can be released adding to the ionizing radiation from the trapped radiation belts, galactic cosmic radiation, and solar particle events.

Single event effects are classified into 3 types of soft errors and 3 types of hard errors. Soft errors do not cause long lasting damage to the effected transistor and are named: Single event upset (SEU), Single event transient (SET), and Single event functional interrupt (SEFI). Hard error will cause permanent damage and include: Single event latch up (SEL), Single event burnout (SEB), and Single event gate rupture (SEGR) [8].

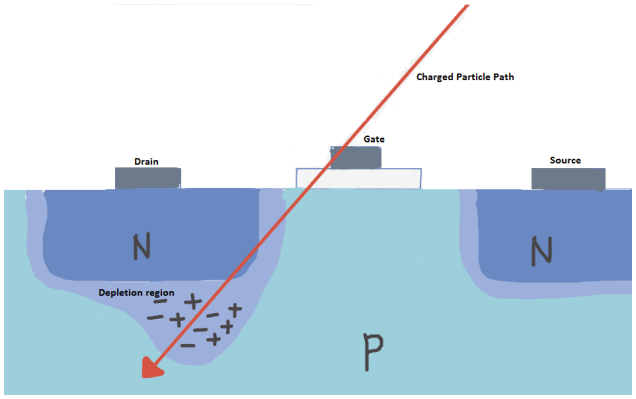

Figure 2.4: Single Event Effect impact

A SEE is caused by the ionization track created as a charged particle with significant energy collides with a transistor in the silicon substrate. When charged particles

strike silicon they transfer charge into the material along their path in the form of electron-hole pairs. If energy transferred into the silicon by the charged particle is significant enough with respect to the feature size of the transistor it can create voltage pulses throughout circuitry and has the potential to permanently change the state of the transistor. The amount of energy left behind by a collision is referred to as the linear energy transfer (LET). When a charged particle strikes the depletion region of an N-P junction in silicon the LET can inject charges as large as picocoulombs this charge is what can cause transient voltage and currents and has the potential to overpower the junction.

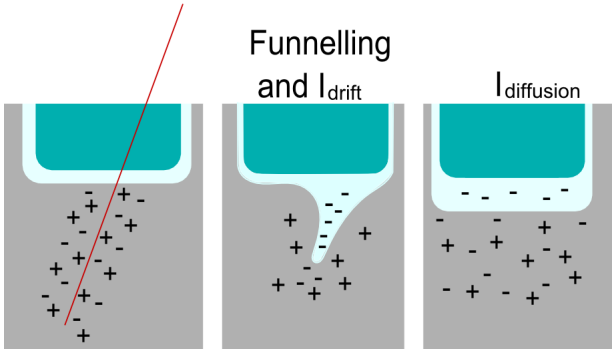

Figure 2.5: Single Event Effect across an N-P Junction

A Single Event Upset (SEU) is a classification of any SEE where the value stored in a memory element is changed by a either the propagation of a single event transient or the direct interaction of a charged particle striking the depletion region of an N-P junction. The charge required for the change of state to occur is referred to as the Q_{crit} of the element and similarly the energy transfer from a charged particle that is required for that charge to accumulate is $LET_{threshold}$. The $LET_{threshold}$ required to cause a SEU to occur is primarily dependent on the feature size (widths of doping regions in the silicon substrate) and clock speed. For flash based memories the $LET_{threshold}$ is commonly larger than 120MeV and as discussed earlier effectively immune to SEU errors as extremely few things can transfer this amount of energy into silicon or GaAs. In SRAM based memories SEU errors remain an issue that needs to be considered in a design. As the area of doping regions shrink, core voltage levels drop, and clock speeds increase with new technology the $LET_{threshold}$ of SRAM devices continues to decreases, this has caused more modern memory devices to become more susceptible to single event effects while becoming more resilient to total

dose effects.

Similar to an SEU a Single Event Transient (SET) is a sub classification of a soft error created when a charged particle strikes the depletion region of an N-P junction within a transistor, only transient pulses in combinational logic are considered SETs. Once an SET error propagates into a memory cell it is considered an SEU error. The temporary change in state created by the SEE can create voltage pulses up to 750ps in length in some devices and cause propagating errors through potentially critical data paths as well as Phase Lock Loops (PLL) and charge pumps. The length of transient error pulses is dependent on feature size, supply voltages, and other environmental factors.

Single Event Functional Interrupts (SEFI) occur in Field Programmable Gate Arrays (FPGA) and Complex Programmable Logic (CPLD) devices where functional configuration of signal connections and logic blocks are saved in some form of configuration memory. Configuration memory for many common FPGA devices is saved in SRAM cells. A SEFI error occurs when SEU errors occur in configuration memory. The change in configuration memory can change the functional operation of the device. SEFIs can manifest in numerous ways such as broken or shorted signal nets, modification of look up tables which can change the logic operation of a block, changing of embedded peripheral blocks such as memories, clock controllers and others, as well as changing the state of IO blocks.

Typically, hard errors cannot be corrected once they have occurred, however for single event latchups it is sometimes possible to recover by removing all power from the circuit and restarting it. A Single event latch up occurs when a charge particle creates a parasitic current loop in a transistor effectively causing it to be stuck in one state. Single event burnouts occur in when an energetic charged particle forward biases a power MOSFET, if the rush of current is large enough (ie exceeds the breakdown voltage of the MOSFET) the circuit can be burned out causing a permanent failure of the circuitry. Finally, single event gate ruptures occur when the incident charge particle injects enough charge into the gate oxide layer of the transistor that it ruptures causing permanent failure of the transistor.

Displacement Damage

A major concern for large scale integrated circuits and electronics is displacement damage. Displacement damage occurs when a neutron, proton, or other heavy ion collide with a nucleus of silicon in the circuits die the lattice can be altered which will change the electrical properties of the effected area. For an incident particle with significant energy the displaced atom may absorb enough energy to cause a cascade of displaced atoms as it strikes adjacent atoms. It is also possible for the nucleus of an atom to absorb the energy of the incident energetic particle causing it to become excited into a nuclear state, when the nucleus decays to its original energy level, an alpha, beta, or gamma ray will be emitted causing ionizing radiation effects along their paths.

Table 2.8: Reaction products caused by neutrons striking silicon [8]

Product	Threshold Energy (MeV)
$^{25}Mg + \alpha$	2.75
$^{28}Al + p$	4.00
$^{27}Al + d$	9.70
$^{24}Mg + n + \alpha$	10.34
$^{27}Al + n + p$	12.00
$^{26}Mg +^{3} He$	12.58
$^{21}Ne + 2\alpha$	12.99

In contrast to the penetration depth of energetic charged particles or energetic photons where a denser material will have a shorter range, neutrons have a much higher chance of being absorbed by materials with low densities.

2.7 Debris Environment

The debris environment is simply a convenient grouping of effects that can arise from the presence of large particles ($> 1\mu m$) or even visible objects in space. In orbit around Earth there are both naturally occurring micrometeorites as well as human introduced debris in the form of dead satellite, left over components and parts

from inter-stages, and solid rocket motor exhaust particles. The vast majority of the individual particles/parts that make up both the naturally occurring micrometeorites and man made orbital debris are typically $<$ 1cm, while this may seem small in comparison to a satellite, any particle at orbital velocities has significant kinetic energy.

Micrometeorites

The flux of micrometeorites around Earth is not constant throughout the year, when Earth's orbit intersects with the orbit of a cloud of debris left over from the breakup or collision of comets and asteroids the amount of micrometeorites in Earth orbit increase, these times of intersection are when meteorite showers occur.

Table 2.9: Approximate dates of meteorite showers [5, p. 200]

Meteorite shower name	Date
Quantrantids	January 1 - 6
Lyrids	April 19 - 24
Eta Aquarids	May 2 - 7
Delta Aquarids	July 15 - August 15
Perseids	July 27 - August 17
Orionids	October 12 - 16
Taurids	October 26 - November 25
Geminids	December 7 - 15

The flux of micrometeorites experienced by a satellite orbiting Earth is affected by earths gravitational field. A lot of work has gone into modeling the micrometeorite environment of the solar system, a closed form expression of the interplanetary micro meteorite flux in $m^{-2}yr^{-1}$ [9] can be seen in equations 2.17 to 2.19. As Earths gravity pulls micrometeorites towards itself the flux of micrometeorites (F_{MM})on the space facing sides of a satellite are amplified by the factor F_{grav}, additionally through the exact same process the Earth facing sides of a satellite are expected to see a lower flux of micrometeorites and experience a factor of F_{shield}, the final factor that reduced the experience micrometeorite flux expected on a satellite for a specific mass m of micrometeorites can be calculated as the product of the gravitational shielding, focusing, directional effects (F_{dir}), and background flux.

$$F_{MM} = 3.56x10^{7}(A^{-4.38} + B + C), \quad F_{grav} = 1 + \frac{R_E + 100km}{R_E + h} \tag{2.17}$$

$$F_{dir} = \frac{1.8 + 3\sqrt{1 - (\frac{R_E+100km}{R_E+h})^2}}{4}, \quad F_{shield} = \frac{1 + cos\eta}{2} \tag{2.18}$$

$$F_{total} = F_{MM}F_{grav}F_{shield}F_{dir} \tag{2.19}$$

The parameters for the above equations can be calculated with the following formulas. Within the formulas, R_E is used to denote the radius of the Earth in km and h is used to denote the altitude of the satellite.

$$A = 15 + 2.2x10^{3}m^{0.306} \tag{2.20}$$

$$B = 1.3x10^{-9}(m + 10^{11}m^2 + 10^{27}m^4)^{-0.306} \tag{2.21}$$

$$C = 1.3x10^{-16}(m + 10^{6}m^2)^{-0.85} \tag{2.22}$$

$$\eta = sin^{-1}(\frac{R_E + 100km}{R_E + h}) \tag{2.23}$$

Orbital Debris

Man made debris added to the environment due to rocket launches and satellites that define the orbital debris typically have much lower kinetic energy then that of micrometeorites (orbital debris typically has velocity on the order of 8km/s, ie the orbital velocity in LEO). Due to their lower but not insignificant kinetic energies they mainly interact with the ram side (front facing side in direction of velocity) of a satellite rather than from all directions like micrometeorites. The orbital debris environment is still widely unknown as only objects greater than 10 cm are tracked, although the environment is not well understood some approximations can be made to estimate the total flux of objects less than 10 cm. The numerical models available show a logarithmic increase in flux from 300km to 1000km in altitude as aerodynamic drag helps to clear up the debris in the lower altitudes, the model shows that the flux then levels out between 1000km and 2000km [10].

2.8 Vibrational Environment

The vibrational environment effecting a satellite occurs in very distinctive stage. The most violent of stages of a satellite in terms of vibration effects occur during the launch and de-orbit. During the launch of a satellite the launch vehicle introduces acoustic vibrations into the satellite. The actual vibration experienced by components of the satellite are dependent on not just the vibrational environment of the launch vehicle but on the physical design of the satellite. Space craft are typically designed to withstand a qualification-level random vibration spectrum rather than the exact spectrum of a single launch vehicle.

The second source of large vibrational effects occurs during the de-orbit or re-entry phase of a satellites mission, typically this is not an issue as for satellites the mission has ended and the intention is for the satellite to burn up on re-entry. However, for a satellite with sample return missions or for crewed satellite the vibration environment of re-entry should be evaluated.

A much smaller addition to the vibration environment occurs from mechanical components on board the satellite. Electrical motors used for sun tracking solar panels in the power system or torque wheels used in attitude control add small vibrations to the structure of the satellite. While the small vibrations introduced by on board components do not cause component failures like those of the launch and re-entry vibrations, they may cause noise in sensitive sensors or oscillators used in processors or sensors of very sensitive electronics.

Chapter 3

Reliability modeling of components

3.1 Summary

Using standards and other sources for reliability modeling, the failure rates of EEE components will be separated into two main characteristics for the purposes of discussion within this chapter. Intrinsic, extrinsic, and over stress failures caused by thermal mechanical effects will be calculated using IEC-TR-62380 [11] to determine λ_{TM}, the thermal mechanical failure rate of the component. Extrinsic failures caused by the effects of radiation will be used to determine λ_{SEE} and λ_{TID}, the failure rates casued by single event effects and total ionizing dose effects respectively, by building off of the work of N.M. Khamidullina, et al [12]. The combination of these failures rates will be used for the reliability of components R(t) considered during the design of systems. The combination of these models result in a constant hazard rate characteristic and an increasing hazard rate characteristic that allows for the estimation of reliability to be calculated is in equation 3.1.

$$R(t)_{IC} = e^{-(\lambda_{TM}+\lambda_{SEE})t} e^{-(\frac{\lambda_{TID}t}{\beta})^{\beta}} \tag{3.1}$$

The reliability of each component R(t) is used in the equations to calculate the

reliability of systems as discussed in chapter 4.

The printed circuit board that components are attached to is considered a component of the system in series redundancy of the other components in the system. Equation 3.3 shows the formulation of the hazard rate of the PCB as defined by the IEC standard [11].

$$R(t)_{PCB} = e^{-\lambda_{PCB}t} \tag{3.2}$$

$$\lambda_{PCB} = 5*10^{-3}\pi_t\pi_c\left[N_t\sqrt{1+\frac{N_t}{S}}+N_p\frac{1+0.1\sqrt{S}}{3}\pi_L\right]\left(1+3*10^{-3}\left[\sum_{i=1}^{j}(\pi_n)_i(\Delta T_i)^{0.68}\right]\right) \tag{3.3}$$

3.2 Introduction

To allow us to move towards the goal of reducing the probability of mission failure due to environmental factors for small satellite systems, it is important that we can provide an estimate of reliability for an individual component operating in a predictable and/or modeled environment. The goal of the models and equations introduced in this section are not to provide extremely accurate reliability results, but instead to provide rough estimates that can assist in the design process as will be discussed in chapter 5. This section will discuss the selected reliability models and the failure modes they incorporate.

Types of failure are classified into three different categories: Intrinsic failures classify all sources of failure within the system or component such as electron migration; extrinsic failures classify all sources of failure sourced from outside the system or component such as thermal cycling; and failures caused by over stress classify all sources of failure from improper design.

A Weibull distribution is used for each contributing effect to the reliability model, this allows for a variable hazard rate for each phase of a mission. The shape parameter

β is only used for increasing hazard rate failure sources while constant hazard rate failure sources use a β value of 1 making the reliability distribution exponential to match the IEC-TR-62380 standards results [11] for thermal mechanical reliability of electrical components.

$$R(t) = 1 - \int_0^t f(t)dt = exp(-(\frac{\lambda t}{\beta})^{\beta}) \tag{3.4}$$

3.3 Modeling Component Failure Rates

The simplified component reliability model proposed in this thesis uses a Weibull distribution to represent the probability that no errors occurred after time t in hours. This distribution relates to a constant hazard rate when the shape parameter β is 1, which works well for the modeling of single event effect radiation and other random failures and can approximate failures due to fatigue by increasing the value of β. It is important to remember that the goal of this reliability model is not to accurately predicate the time of failure of a component or system but to provide a tool for estimating reliability of components that can then be used for design comparisons and acceptance.

$$R(t) = e^{-(\frac{\lambda t}{\beta})^{\beta}} \tag{3.5}$$

The different sources of failure considered within this model and as outlined briefly early in this chapter will be considered as mutually exclusive probabilistic events with the probability of no failure occurring at time t to be R(t). The use of a Weibull distribution allows us to estimate the failure rates of each individual source of failure and use the sum of the failure rates as the failure rate of the component. A more in depth review of the math behind statistics and different distributions used in reliability models can be found in Appendix A.

Using standards and other sources for reliability modeling the failure rates of components will be separated into two for the purposes of discussion within this chapter. Intrinsic, extrinsic, and over stress failures caused by thermal mechanical effects will

be calculated using IEC-TR-62380 [11] to determine λ_{TM} of the component. Extrinsic failures caused by the effects of radiation will be used to determine λ_{SEE} and λ_{TID} building off of the work of N.M. Khamidullina, et al [12]. The combination of these failures rates will be used for the reliability of components R(t) considered during the design of systems.

$$R(t) = e^{-(\lambda_{TM}t + \lambda_{SEE}t + \frac{(\lambda_{TID}t)^{\beta}}{\beta})} \tag{3.6}$$

3.3.1 Thermal Mechanical Effects

For thermal mechanical failure effects the standard IEC-TR-62380 [11] titled "universal model for reliability prediction of electronics components, PCB's, and equipment" was selected. Failure rates predicted by the 62380 standard assume a constant failure rate allowing the use of an exponential distribution of component and system reliability. The standard aims to include factors for reliability caused by thermal mechanical, over stress, and other sources of failure caused by aging and fatigue. While the standard does provide a suggestion for calculating the reliability of an electrical system as an exponential distribution with the failure rate of $\lambda_{IEC-TR-62380}$, the resulting model indicates the failure of the system as any single failure within it. While a model for first failure is useful for predicating maintenance requirements, for spacecraft systems designs we want to have the ability to account for the redundancy designed into a system, therefor the reliability model for individual components will be used from the standard but not the model for overall system reliability, the calculation of system reliability will be discussed in more detail in chapter 4.

$$\lambda_{IEC-TR-62380} = \sum \lambda_{SurfaceComponents} + \sum \lambda_{ThroughholeComponents} + \sum \lambda_{Connectors} + \lambda_{PCB} \tag{3.7}$$

For individual components the failure rate λ_{TM} of an integrated circuit is calculated in three parts, the thermal effects, electrical over stress (EOS) of the die as

well as the thermal mechanical effects on the package. The majority of factors can be simplified from package type, thermal environment and age, the IEC-TR-62380 handbook provides the majority of these factors in tables within the standard. The failure rate λ_{TM} of passive components such as inductors, capacitors, resistors or connectors is much simpler as there are fewer intrinsic failures to consider. The failure rates of passive components such as resistors and capacitors can typically be ignored as the result in failures rates a few orders of magnitude lower than primary integrated circuit packages.

$$\lambda_{TM(IntegratedCircuit)} = (\lambda_{thermalEffects} + \lambda_{EOSeffects})_{die} + (\lambda_{thermalmechanicalEffects})_{package} \tag{3.8}$$

The environment the component operates in is of course extremely important, the environment as summarized by IEC-TR-62380 can be seen summarized in table 3.1. Since the primary observed failure of electrical components are from thermomechanical factors relating to failure of the electrical components package, the temperature range, humidity, vibration environment, and cycling are critical. As defined by the 62380 standard a systems environment is broken into multiple phases, typically permanently working phases, permanently dormant phases, and duty cycle phases. The type of phase effects the values of τ used in the estimation of intrinsic failures.

Table 3.1: IEC-TR-62380 Mission Environment parameters

Parameter	Note
$(t_{ae})_i$	Ambient temperature surrounding the equipment or system
$(t_{ac})_i$	Ambient temperature of the PCB near the component
τ_i	Ratio of time the system is in the permanently on phase
τ_{on}	Ratio of time the system is in the working phase of a duty cycle phase
τ_{off}	Ratio of time the system is in the dormant phase of a duty cycle phase
n_i	Number of thermal cycles experienced by the system during the i_{th} phase
ΔT_i	Average thermal cycle range experienced by components in the i_{th} phase $\Delta T_i = [\frac{\Delta T_j}{3} + (t_{ac})_i] - (t_{ae})_i$

From thermal modeling of a spacecraft the value of ΔT_i can be determined from

simulation and the Ambient temperature parameters $(t_{ae})_i$ and $(t_{ac})_i$ are unnecessary as it is more important to obtain t_c the average case temperature which can be approximated as the average printed circuit board temperature. The values of τ and n_i are factors of mission planning and are results of target orbit and concept of operations, these along with an initial power budget are important for thermal simulations.

The expanded equation for estimated failure rate of an integrated circuit in IEC-TR-62380 can be seen below in number of failures per billion hours. For the value used within the reliability model the result is scaled by 10^{-9} to get failures per hour.

$$\lambda_{TM} = \lambda_{TM\_die} + \lambda_{TM\_package} + \lambda_{EOS\_effects} \tag{3.9}$$

$$\begin{aligned}\lambda_{TM} =& \lambda_1 N e^{-0.35\alpha} + \lambda_2)\left(\frac{\sum_{i=1}^{y}(\pi_t)_i\tau_i}{\tau_{on}+\tau_{off}}\right) \\ &+ (2.75*10^{-3}\pi_\alpha)(\sum_{i=1}^{Z}(\pi_n)_i(\Delta T_i)^{0.68})\lambda_3) + (\pi_I\lambda_{EOS})\Bigg) x10^{-9}/hr\end{aligned} \tag{3.10}$$

The failure rate associated with intrinsic failures within the die are incorporated into the model through the sum of λ_1 and λ_2 scaled by the temperature factor created from π_t and the duty cycle. The base failure rate λ_1 is the base per transistor failure rate of the integrated circuit technology, values for λ_1 can be found tabulated within the standard. The failure rate λ_1 is multiplied by the number of transistors N and the factor $e^{-0.35\alpha}$ where α is the year of manufacture of the component minus 1998. The failure rate λ_2 is a failure rate related to the technological mastery of the integrated circuit technology, values for λ_2 are used as tabulated within the standard. The scaling factor π_t uses the Arrhenius equation (a representation of the temperature dependence of chemical reactions) to represent the temperature dependence on aging of the component. The factor π_t can be calculated based on the average junction temperature as seen below, the values A and E_a for low voltage BiCMOS ICs is 3480 and 0.3eV respectively, similarly for a high voltage BiCMOS IC the values of A and

E_a are 4640 and 0.4eV respectively.

$$\pi_t = e^{A(\frac{1}{B} - \frac{1}{273+t_j})} \tag{3.11}$$

$$t_j = t_c + PR_{jc} \tag{3.12}$$

The second element of the sum incorporates the effects of the components package. The coefficient of thermal expansion (CTE) factor π_a accounts for the effect on package reliability due to thermal cycling, as the temperature changes the package of the IC and the PCB expand or contract at different rates which can crack solder joints. α_s (substrate) represents the coefficient of thermal expansion of the PCB, for the most common material called FR4, the value is equal to 16ppm/C, for PTFE glass the value is equal to 20ppm/C. α_c (case) represents the coefficient of thermal expansion of the IC package, for a plastic component this is equal to 21.5ppm/C while ceramic is 6.5ppm/C. From these it can be seen that the most reliable combination would be a PTFE glass substrate with plastic package components resulting in a coefficient of thermal expansion mismatch of only 1.5ppm/C, the most common value would be an FR4 substrate with a plastic component case resulting in a CTE mismatch of 5.5 ppm/C. The values of CTE can be determined from initial decisions made in the systems engineering phases and component choices early in the design phase.

$$\pi_a = 0.06(|\alpha_s - \alpha_c|)^{1.68} \tag{3.13}$$

The failure rate due to thermal expansion and solder cracking is also dependent on the number of cycles, range of thermal cycling, and the type of component package. The factor π_n incorporates the number of thermal cycles of amplitude ΔT per year as a function of n_i, this information can be determined from the orbital parameters and thermal simulation of the mission. The base failure rate of the component package type is denoted as λ_3 and can be determined from a table of functions (table 17a in [11]) which relate package type and dimensions to a base failure rate that is then scaled by the previously discussed π_n,π_a, and ΔT factors.

$$\pi_n = \begin{cases} n_i^{0.76}, & n_i \leq 8760 \\ 1.7 * n_i^{0.60}, & n_i > 8760 \end{cases} \tag{3.14}$$

The final element of the sum simplifies the effect of electrical over stress on a component by relating the type of interface the component has to the external environment to typical failure rates from past products. For a component with any type of external interface the value of pi_I is 1 while for an all electrical environment the value is 0. A few examples of π_I and λ_{EOS} include values such as 1 and 10 respectively for a computer, 1 and 20 for civilian avionics, 1 and 40 for power supplies, etc. For a satellite the majority of circuitry and components are in an all electrical environment with the exception of telemetry and battery charge ports, the most common value used for these factors will be 0.

Factors that affect failure rates caused by the influence of special stresses dependent on the type of component are also factored into the standard. For example, π_a is used to factor in the effect of current pulses on aluminum capacitors, while π_i is used to factor in the effect of current intensity on connectors.

For components other than integrated circuits the main difference is in the first element which determines the failure rate of the die. Diodes for example replace the factor $(\lambda_1 N e^{-0.35\alpha} + \lambda_2)$ with $\pi_U \lambda_0$ where π_U is the use factor and λ_0 is the base failure rate of the diode type as found tabulated in the IEC-TR-62380 standard. Transistors, opto-couplers, capacitors, and other types of components are similarly calculated with values obtainable within the standard.

As discussed earlier the failure rate of PCB's and hybrid circuits in IEC-TR-62380 are calculated from two main sources, source A incorporates the failure rates of connections and components on the PCB while source B incorporates the failure rates of the board itself. The failure rate A is the summation of all components and connectors on the printed circuit board, this provides the failure rate of the PCB as a system as the first failure of any component on the board, therefore we will drop the factor A and focus on the factor B as the failure rate of the printed circuit board

itself.

$$\lambda_{PCB\_IEC} = (A + B)x10^{-9}/hr \tag{3.15}$$

$$A = \sum \lambda_S + \sum \lambda_f + \left(1 + 3.10^{-3}\left[\sum_{i=1}^{j}(\pi_n)_i(\Delta T_i)^{0.68}\right]\right)\sum \lambda_d \tag{3.16}$$

$$B = 5.10^{-3}\pi_t\pi_c\left[N_t\sqrt{1+\frac{N_t}{S}} + N_p\frac{1+0.1\sqrt{S}}{3}\pi_L\right]\left(1 + 3.10^{-3}\left[\sum_{i=1}^{j}(\pi_n)_i(\Delta T_i)^{0.68}\right]\right) \tag{3.17}$$

The thermal cycle influence factor π_n is equal to $n_i^{0.76}$ for $n_i \leq 8760$ cycles per year and $1.7n_i^{0.6}$ when $n_i < 8670$ cycles per year. The failure rates of the miscellaneous connectors are depended on the manufacturing and their connection type, the 62380 standard uses the following estimations for λ_d: 0.5 for a manual solder joint, 0.5 for connected with insulating transfer, 0.3 for a crimp connection, 0.01 for a wrapped connection, and 0.006 for a press fit connection. From the failure rate factors from the PCB π_t is used to factor in the temperature environments effect on the trace and via failure rates, π_c is used to factor in the influence of number of layers used (π_c = 1 for layers $\leq$ 2, and $0.7\sqrt{numberoflayers}$ for layers > 2). The factors N_p, N_t and S represent the total number of tracks, total number of vias, and the board size respectively. To factor in the effect of track width π_L is used. The π_L factor increases as track width decreases, starting from a value of 1 for a predominant track width of 0.56mm and increases to a value of 8 at a track width of 0.08mm. For the purposes of this work we will use the following failure rate for PCBs as a component for a design.

$$\lambda_{PCB} = 5.10^{-3}\pi_t\pi_c\left[N_t\sqrt{1+\frac{N_t}{S}} + N_p\frac{1+0.1\sqrt{S}}{3}\pi_L\right]\left(1 + 3.10^{-3}\left[\sum_{i=1}^{j}(\pi_n)_i(\Delta T_i)^{0.68}\right]\right) \tag{3.18}$$

The reliability of a component due to thermal mechanical effects on the package and die can then be determined as seen in equation 3.19. The parameters required for evaluation of equation 3.10 have been summarized in table 3.2.

$$R(t) = e^{-\lambda_{TM}t} \tag{3.19}$$

Table 3.2: Thermal mechanical Component Reliability parameters

Parameter	Note
	Obtained from tables or equations within the IEC-TR-62380 standard [11]
λ_1	per transistor base failure rate of the IC family
λ_2	failure rate related to type of technology
α	year of manufacturing - 1998
N	Number of transistors of the IC
$(\pi_t)_i$	i^h temperature factor related to the i^{th} junction temperature
π_a	Influence of coefficient of thermal expansion difference
λ_3	base failure rate of the IC
π_I	influence factor related to the use of the IC
λ_{EOS}	failure rate related to electrical over stress.
	Obtained from Mission parameters and/or simulation
τ_i	i^{th} working time ratio
τ_{on}	Total woking time ratio
τ_{off}	Total dormant time ratio
$(\pi_n)_i$	i^{th} influence factor related to the annual thermal variations
ΔT_i	i^{th} thermal cycle range
t_c	Average PCB temperature near component

3.3.2 Radiation Effects

The effects of radiation on a component pose a difficult problem for physics of failure based modeling of reliability. Standard design approaches relate the total ionizing dose (TID) failure level as a value of total accumulated dose that will cause a component to fail, from an orbital simulation the total mission dose is determined and only components with a higher TID tolerance than the total dose are selected or shielding is added to reduce the total accumulated dose at the component to a safe level. For the modeling of reliability being developed for this research we would like to determine a constant hazard rate based on average orbital flux of protons and other heavy ions to add into the thermal mechanical failure model discussed so far such that the effects of total dose failures and single event failures can be considered.

To account for the effect of radiation environmental effects on satellite components, models of component reliability were created by building off of the work of N.M. Khamidullina, et al [12]. The equations created attempted to incorporate the failure rates of total dose as well as single event effects from both heavy ions, protons, and electrons as functions of cross sectional flux, linear energy transfer and cross sectional probability of an interaction between an incident ion or proton and the sensitive region of the component. The failure rate λ_R as suggested by N.M. Khamidullina, et al [12] is calculated in three parts, the first element $\lambda_{TID/DD}$ incorporates the probability of total ionizing dose failure while the second and third elements of the sum incorporate the probability of hard single event effect errors from occurring first from the sum of the heavy ions present in the radiation environment and lastly from the high energy protons present in the environment.

$$\lambda_R* = \lambda_{TID/DD} + \lambda_{SEE,ion} + \lambda_{SEE,proton} \tag{3.20}$$

$$\lambda_{TID/DD*} = K_{TDF}\Big(\sum_i \int L_i(E) * F_i(E,t) * dE\Big)^n \tag{3.21}$$

The failure rate $\lambda_{TID/DD}$ for the effect of total dose incorporates all charged particles i, including trapped electrons, trapped protons, solar protons and high energy heavy ions from galactic cosmic rays (GCR) in the environment where $L_i(E)$ is the Linear Energy Transfer (LET) dependence in $MeVcm^2/g$, and $F_i(E,t)$ is the differential energy spectrum of charged particle flux for the i^{th} charged particle flux in n/cm^2MeVs, for protons and electrons the value of $L_i(E)$ is often called stopping power instead of linear energy transfer which specifies the amount of energy lost by a particle as it travels through a specific material at energy level E which is the same as the amount of energy transferred from the particle into the material. The integral $\int L_i(E) * F_i(E,t) * dE$ is the total ionizing dose rate of the i^{th} charged particle in units of MeV/g. The exponent n is used in N.M. Khamidullina [12] to help scale the sensitivity of the manufacturing process and equals 0.94 for CMOS and 0.88 for bi-polar devices. The factor K_{TDF} is effected by design of the circuit, packaging, and technology size and can be calculated from radiation total ionizing dose testing at a proton beam test facility or from past tests.

Values for $F_i(E,t)$ for the heavy ions H through Ni as well as for solar and trapped protons, electrons, and neutrons can be obtained using the SPENVIS on-line tool [13]. It is important that values of $F_i(E,t)$ be evaluated at the interior of the satellite, close to the components being evaluated, the equivalent aluminum shielding caused by the solar panels and structural components can greatly effect the results, potentially increasing or decreasing the dose rate as lower energy particles are stopped and higher energy particles can lose enough energy to begin transferring larger amounts of energy into a target device. Similarly, there are tools available to evaluated the linear energy transfer of heavy ions such as B N L Tandem Van de Graaff Accelerator TVDG LET Calculator [14] as well as the stopping power of protons and neutrons in silicon such as ESTAR and PSTAR [15].

The total ionizing dose (TID) of a component is very difficult to predict as it results in a slow degradation of component parameters, the rate that degradation occurs is dependent on many design, manufacturing and environment factors such as temperature, electrical bias, dose rate, and manufacturing variability. Typically, TID values for a component should be lot tested, that is components from the same manufacturing lot as the components to be used in flight testing should be used, this is however very expensive and approximations can be made from similar components or old testing of the same component being evaluated.

The model suggested by N.M. Khamidullina, et al [12] uses the parameter n to try and help scale a constant hazard rate (exponential distribution) reliability model, this however provides extremely poor estimates of reliability at low total doses. In figure 3.1 the reliability of three lots of the same component tested at different dose rates in 1988 by G.J. Brucker [16] can be seen, the exponential decay function is the result of applying the previous model to the average TID of 6750 rad. It is clear that this model provides a poor estimation for low dose values and will result in a system being evaluated as unsuitable for short missions in comparison to the components TID.

To better represent the increasing hazard rate of failures caused by total ionizing dose we can utilize the shape parameter β from the Weibull distribution. The model of reliability for the component from total ionizing dose effects will be then formated as seen in equation 3.22. In figure 3.1 the results of dose rate testing at 1.64 mrad/s

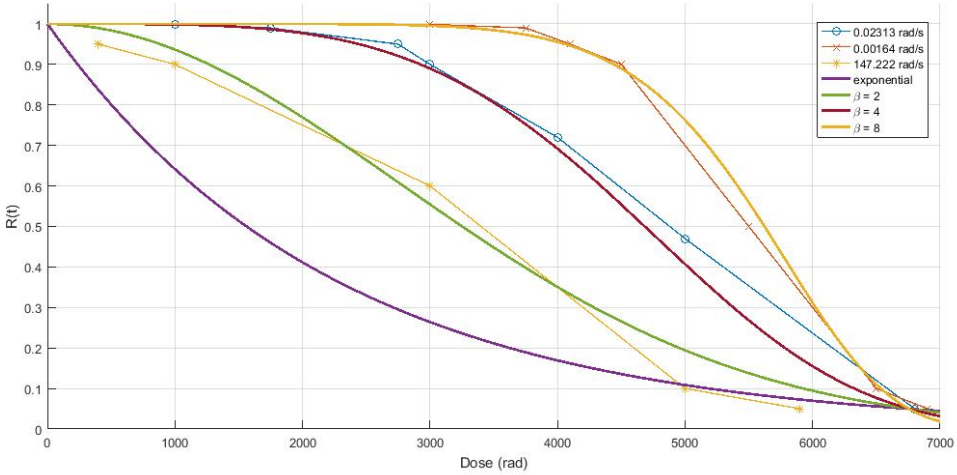

Figure 3.1: Matching shape parameter to TID failure rate [16]

(27 component samples), 23.13 mrad/s (23 component samples), and 147.222 rad/s (27 component samples) [16] can be seen with Weibull distributions showing much better representation of the reliability at low accumulated dose.

$$R(t)_{TID/DD} = e^{\left(-\left(\frac{K_{TDF}(\sum_i \int L_i(E)*F_i(E,t)*dE)t}{\beta}\right)^{\beta}\right)} \tag{3.22}$$

Since we know that $\left(\sum_i \int L_i(E)*F_i(E,t)*dE\right)t$ is the total absorbed dose at time t, we can determine the K_{TDF} as a function of D_{TID} the dose indicated by TID failure testing, and β a shape parameter based on dose rate. Values reported in radiation testing are listed in values of rad, for these equations the values of absorbed dose will be interpreted as $\frac{MeV}{g}$ therefore results used from external testing need to be scaled by equation 3.24. By fitting a basic power function to the shape parameters estimated for the three dose rates tested by Brucker [16] the value of the shape parameter β as a function of dose rate D_r in units of $\frac{MeV}{gs}$ can be determined by equation 3.26. By determining the values of β and K_{TDF} the model of reliability in 3.22 can better represent the low absorbed dose reliability of the component.

$$R(D)_{TID/DD} = e^{-\left(\frac{K_{TDF}*D}{\beta}\right)^{\beta}} \tag{3.23}$$

$$1rad = 6.2415x10^{7}\frac{MeV}{g} \tag{3.24}$$

$$K_{TDF} = \frac{\beta(-ln(0.05))^{\beta}}{D_{TID}} \tag{3.25}$$

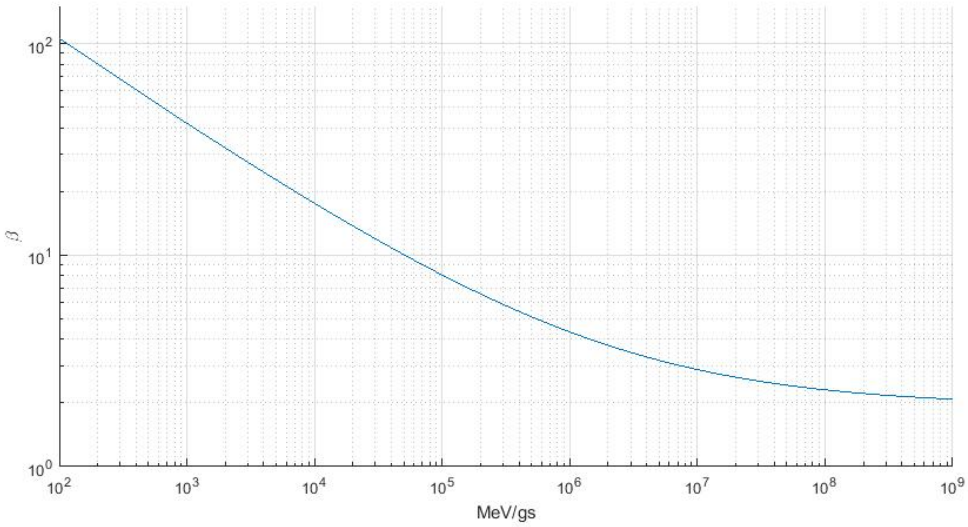

Figure 3.2: Basic power function fit of shape parameter β vs dose rate

$$\beta = 670.5(D_r)^{-0.408} + 1.942 \tag{3.26}$$

Single event effects are calculated similarly using the same shielded flux distributions $F_i(E)$ as evaluated for the total dose effects for protons and heavy ions. The flux of electrons are typically ignored for SEE rates as individually particle collisions of electrons through a component do not transfer significant amounts of energy to overcome the linear energy transfer threshold for most components SEE cross-sections. Failure rates suggested by the work of N.M. Khamidullina, et al [12] define failures rates for both ion induced single event effects and proton induced single event effects as follows.

$$\lambda_{SEE} = \lambda_{SEE,ion} + \lambda_{SEE,proton}$$

$$\lambda_{SEE,ion} = 2\pi \sum_{i} \int \int \sigma_i(E,\theta) F_i(E,t) dE sin\theta cos\theta d\theta \tag{3.27}$$

$\lambda_{SEE,ion}$ represents the heavy ion induced single event effects where σ_i is the cross section of single event effects caused by the i^{th} type of heavy ions (H through Ni) and $F_i(E,t)$ is the differential energy spectrum of the i^{th} type ion flux. Similarly the upset rates caused by proton induced events can be estimated by equation 3.28.

$$\lambda_{SEE,proton} = 4\pi \int \int \sigma_p(E,\theta) F_p(E_p,t) dE dE_p \tag{3.28}$$

Where σ_p is the double differentiated cross section of single event effects from protons. The integration of F_p and F_i for single event effects should be integrated over energy levels for Linear energy transfer levels from $LET_{threshold}$ to ∞ in the target material where $LET_{threshold}$ is the minimum energy transfer that can cause a single event to occur (denoted LET_T in equations). To clarify the use of LET in the model, equation 3.29 is used and the product of $\eta(E)$ and $F(E)$ is integrated over all energy values. The cross section of proton induced single events are tricky as protons themselves typically do not transfer enough energy to cause a SEE but the secondary particles caused by the interaction of protons with the component material can. Similar to the units for fluency used in the model for total ionizing dose the values of F_p and F_i that are simulated or calculated in per steradian units require the factor of 2π to account for all possible directions around the component, some models of radiation fluency already account for this and would require the factor to be removed. Assuming that the cross section of single events are approximately level for LET values from $LET_{threshold}$ to ∞ we will pull them out of the integral to simplify the model.

$$\eta(E) = \begin{cases} 1 & LET \geq LET_{threshold} \\ 0 & LET < LET_{threshold} \end{cases} \tag{3.29}$$

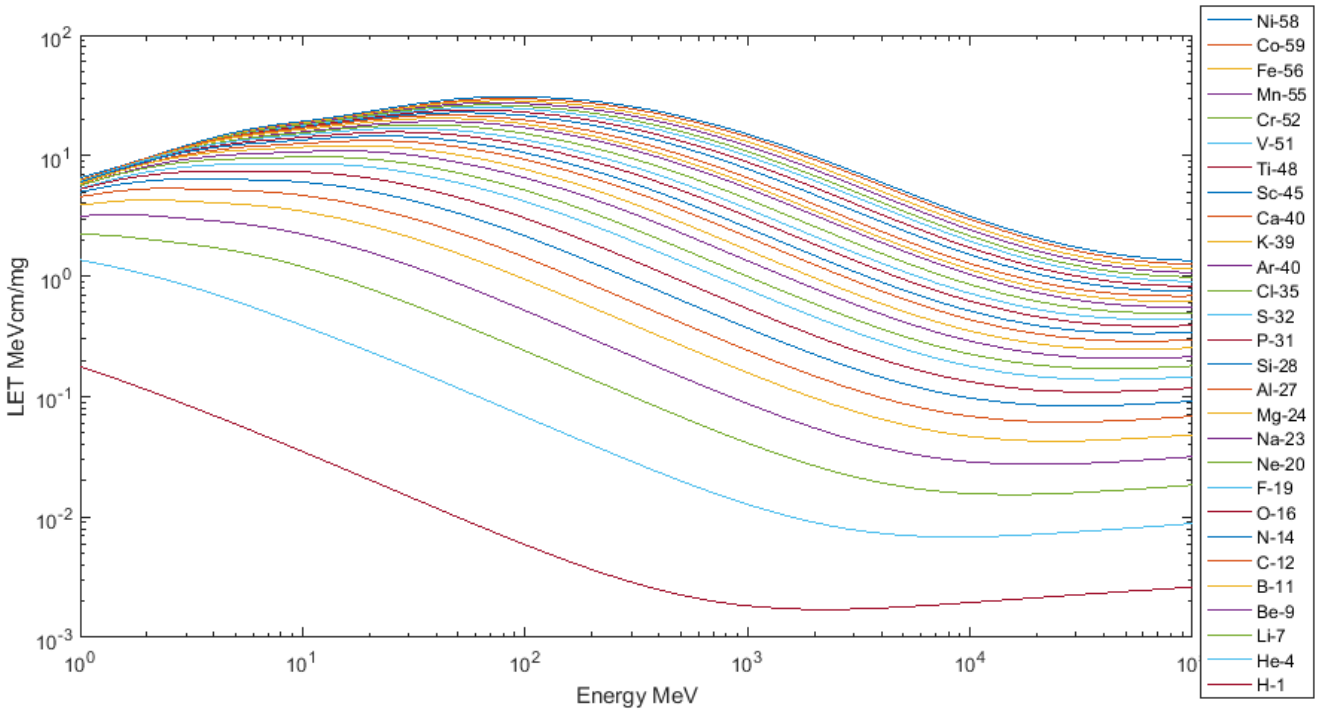

Figure 3.3: Linear Energy Transfer of Heavy Ions in Silicon [14]

If σ_p can not be obtained from testing, J Barak [17] proposes a simplified model of σ_p from values of σ_i based on the results of an analytical micro dosimetry model. From the work of J Barak [17], we can use equations 3.31 and 3.32 to calculate σ_p where L_C is the LET at which σ_i reaches 0.25 of its saturation value σ_i (the value used when approximating the cross section as a step function as we have done in this model). Comparisons of this model for σ_p based on experimental results of heavy ions and experimental results of proton cross sections are within a factor of 2.5 and agree well for the purposes used in the simplified reliability model discussed in this chapter.

$$P_0(E_p, L) = 4.0x10^{-6} e^{[-(0.134+\frac{9}{E_p})L]} \tag{3.30}$$

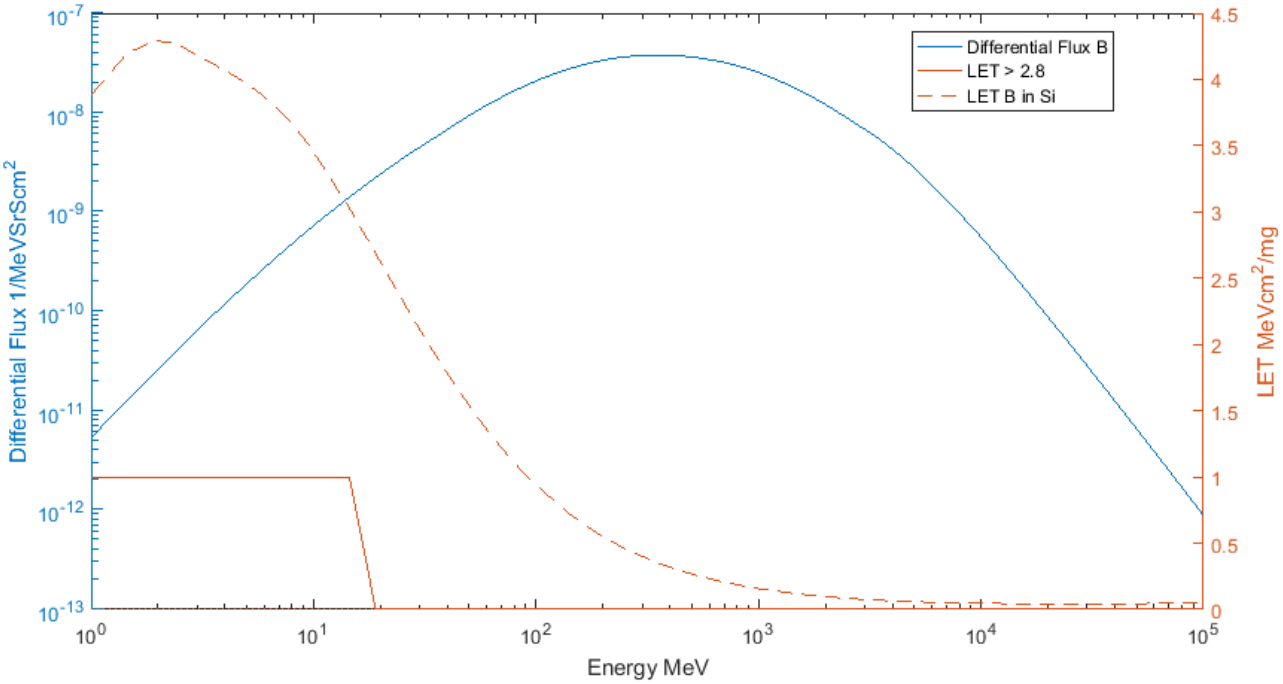

Figure 3.4: LET Example

$$P(E_p, L) = \begin{cases} 1.503x10^{-5}L^{-1.425} + P_0 & L < 1MeVcm^2/mg \\ 1.58x10^{-5}L^{-2.56} + P_0 & 1MeVcm^2/mg \leq L < 5MeVcm^2/mg \\ P_0 & L \geq 5MeVcm^2/mg \end{cases} \tag{3.31}$$

$$\sigma_p(E_p) = P(E_p, L_C)\sigma_i \tag{3.32}$$

The rate of ion and proton induced single event effects can then be approximated as seen in equations 3.33 and 3.34.

$$\lambda_{SEE,ion} = 2\pi \sum_i \sigma_i \int \eta_i(E) F_i(E,t) dE \tag{3.33}$$

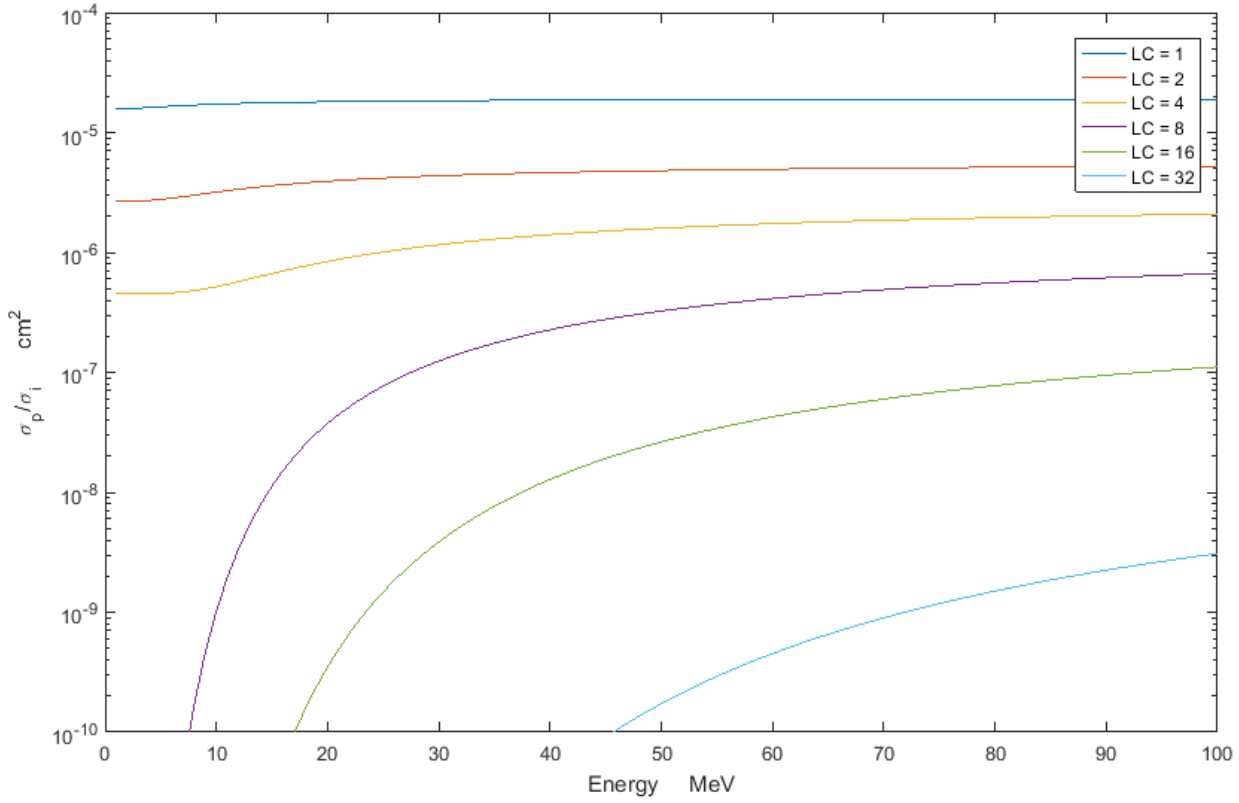

Figure 3.5: $\sigma_p(E_p)$ for different L_C values with $\sigma_i = 1$

$$\lambda_{SEE,proton} = 2\pi \int \sigma_p(E_p) F_p(E_p, t) dE \tag{3.34}$$

For single event effects the exponential distribution represents the constant hazard rate well. It is important to note that for determining the reliability of a component due to single event effects values of σ and $LET_{threshold}$ need to be for hard single event effects or functional interrupt events. The same model can be used with cross section values for soft errors such as single event transient errors or single event upset errors in memory when evaluating information reliability but the values of σ and $LET_{threshold}$ will differ. The reliability of a component due to single event effects can then be determined as seen in equation 3.35.

$$R(t) = e^{-\left(\lambda_{SEE,ion}+\lambda_{SEE,proton}\right)t} \tag{3.35}$$

Table 3.3: Radiation Component Reliability parameters

Parameter	Note
D_{TID}	Total ionizing dose failure level
σ_i	cross section of single event failures induced by the i^{th} ion (H through Ni)
σ_p	cross section of single event failures induced by protons

Table 3.4: Radiation Environment parameters

Parameter	Note
F_i	Fluency of the i^{th} ion (H through Ni) near the component
F_p	Fluency of protons near the component
F_e	Fluency of electrons near the component

3.3.3 Combined Model for Simplified Reliability Estimation

By using the estimations of reliability discussed within this chapter so far the reliability of a EEE component over time in a orbital environment can then be calculated using the assumption that the effects of thermal mechanical stress, single event radiation effects, and total ionizing dose effects are mutually independent. For the three independent effects the total reliability of the component can then be calculated as the product of them as in equation 3.36.

$$R(t)_{EEE} = R(t)_{TM}R(t)_{SEE}R(t)_{TID/DD} \tag{3.36}$$

Since the models for $R(t)_{TID/DD}$ and $R(t)_{SEE}$ developed hazard rates in units of per second and the values for $R(t)_{TM}$ hazard rate calculated using IEC-TR-62380 [11] are in units of per hour a factor of 3600 is required. By using the equations 3.19, 3.22 and 3.35 the reliability of a EEE component can be calculated as equation 3.37.

$$R(t) = e^{\left(-\lambda_{TM}t\right)} e^{\left(-3600*(\lambda_{SEE,ion}+\lambda_{SEE,proton})t\right)} e^{-\left(\frac{3600*\lambda_{TID/DD}t}{\beta}\right)^{\beta}} \tag{3.37}$$

Which can be combined further into equation 3.38.

$$R(t) = exp\big(-(\lambda_{TM} + 3600(\lambda_{SEE,ion}+_{SEE,proton}))t - \big(\frac{3600 * \lambda_{TID/DD}t}{\beta}\big)^{\beta}\big) \tag{3.38}$$

Where the values of λ_{TM}, $\lambda_{SEE,ion}$, $\lambda_{SEE,proton}$ $\lambda_{TID/DD}$ and β can be calculated as below.

$$\begin{aligned}\lambda_{TM} =& \lambda_1 N e^{-0.35\alpha} + \lambda_2)\left(\frac{\sum_{i=1}^{y}(\pi_t)_i\tau_i}{\tau_{on}+\tau_{off}}\right) \\ &+ (2.75*10^{-3}\pi_\alpha)(\sum_{i=1}^{Z}(\pi_n)_i(\Delta T_i)^{0.68})\lambda_3) + (\pi_I\lambda_{EOS})\Big)x10^{-9}/hr\end{aligned} \tag{3.39}$$

$$\lambda_{SEE,ion} = 2\pi\sum_i \sigma_i \int \eta_i(E, LET_{threshold})F_i(E,t)dE \tag{3.40}$$

$$\lambda_{SEE,proton} = 2\pi \int \sigma_p(E)F_p(E_p,t)dE \tag{3.41}$$

$$\lambda_{TID/DD} = -K_{TDF}(\sum_i \int L_i(E) * F_i(E,t) * dE) \tag{3.42}$$

Where the parameters of each have been discussed earlier in this chapter. From this combined model and the discussions so far we can see that the required parameters to gather for the reliability of each component are listed in table 3.5. The parameters that can be determined from the environment simulation can be seen

listed in table 3.6.

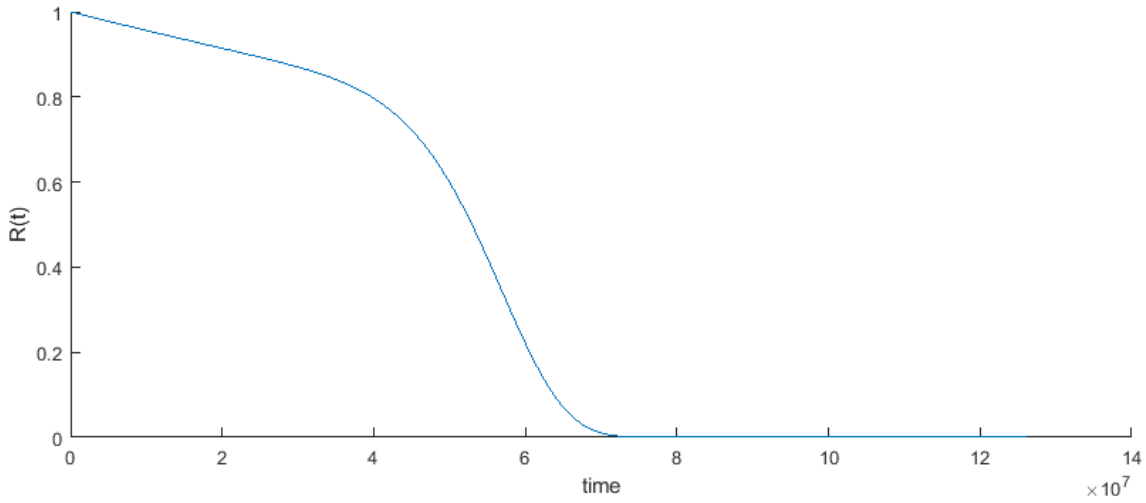

Figure 3.6: Example Reliability shape over time of the combined reliability model (time in hrs)

Table 3.5: Required Component Reliability parameters

Parameter	Note
	Obtained from tables or equations within the IEC-TR-62380 standard [11]
λ_1	per transistor base failure rate of the IC family
λ_2	failure rate related to type of technology
α	year of manufacturing - 1998
N	Number of transistors of the IC
$(\pi_t)_i$	i^h temperature factor related to the i^{th} junction temperature
π_a	Influence of coefficient of thermal expansion difference
λ_3	base failure rate of the IC
π_I	influence factor related to the use of the IC
λ_{EOS}	failure rate related to electrical over stress.
	Obtained from Radiation testing or databases
D_{TID}	Total ionizing dose failure level
$\sigma_{i,\infty}$	cross section of single event failures induced by the i^{th} ion (H through Ni)
$LET_{threshold,i}$	LET threshold value for ion induced hard Single event effects
$LET_{threshold,25\%}$	LET threshold value for proton induced hard Single event effects
τ_i	i^{th} working time ratio
τ_{on}	Total woking time ratio
τ_{off}	Total dormant time ratio

Table 3.6: Required Environment parameters

Parameter	Note
$(\pi_n)_i$	i^{th} influence factor related to the annual thermal variations
ΔT_i	i^{th} thermal cycle range
t_c	Average PCB temperature near component
F_i	Fluency of the i^{th} ion (H through Ni) near the component
F_p	Fluency of protons near the component
F_e	Fluency of electrons near the component

Chapter 4

Reliability of Systems

4.1 Summary

The reliability of each component within an electrical system has an effect on the reliability of the system in different ways. In situations with redundancy the failure of a single component does not always cause the failure of the entire system, this is the fundamental idea behind the addition of redundancy to a design. Reliability block diagrams can be used to visually display the relations between components and the redundancy they provide. This section aims to present the basic forms of redundancy as well as reliability between dependent components as well as the equations that represent them.

4.2 Introduction

This chapter aims to discuss the math used for combining the reliability of individual components into an entire systems reliability. In the IEC TR 62380 [11] failure of a system is defined as the first failure of any component within the system, the use of redundancy allows for a system to operate well past the first failure. Connections

are in terms of reliability or dependence and not in terms of physical connection or schematic, for example in a shared (parallel connected devices) communication bus, if the common failure mode of a device connected to the bus is to short to positive or negative rather than enter high impedance the reliability block diagram would organize the components in series as a failure of any single component causes all connected components to fail.

4.3 Redundancy Schemes

When attempting to predict the reliability of a system comprised of multiple components, the system is first represented with a reliability block diagram. For example, two components in a system with failure rates of λ_i and λ_k can be arranged with dependencies with respect to each other in parallel or series, where parallel represents a redundancy between the two with the failure of one not effecting the other and series representing the direct dependency where failure of one causes failure of the other. Considering the system hazard rates of the two component as constant, the system hazard rate will be equal to the sum $(\lambda_i + \lambda_k)$ when in series. In the series configuration the reliability of the system is essentially the product of the probability of a failure not occurring in each component $(R_{series} = (1 - R_i)(1 - R_j))$, another way of looking at it is that probability of failure of the system is equal to the probability that component i or component j have failed $(R_{series} = (1 - (F_i)(F_j))$. For a system composed of two parallel and active components j and k, the probability of system failure is equal to the probability of component i and component j failing, in terms of reliability functions the reliability of the system is equal to the probability that component i or component j survives $(R_{parallel} = R_i + R_j - R_i R_j)$, this equation comes from the probability of two independent variables under the or operation. Equations 4.1 and 4.2 [18] show in general the relation for reliability of components in series or in active redundancy.

$$R_{SeriesSystem} = \prod_{i=1}^{n} (1 - R_i) \tag{4.1}$$

$$R_{ActiveRedundancy} = 1 - \prod_{i=1}^{n}(1 - R_i) \tag{4.2}$$

Figure 4.1: Reliability of Series connected components

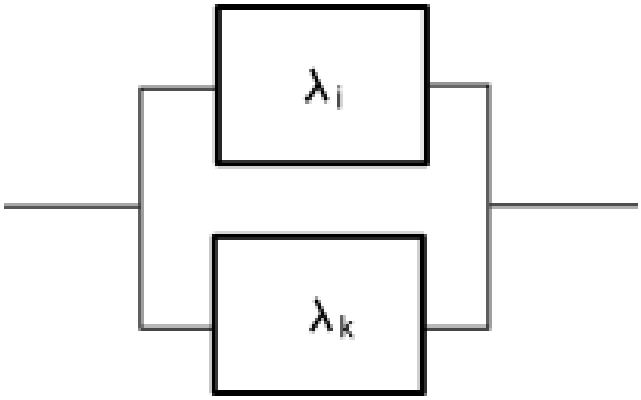

Figure 4.2: Reliability of Parallel connected components

In many situations parallel redundancy is better represented by m out of n redundancy, the difference being that in m out of n redundant systems a minimum of m systems must remain working for the system to work. For example, on a very small scale like the redundancy of simple circuits, if only dual redundancy is used and a single component fails it may become impossible for supervisory circuitry to determine which one is broken, in this situation the added redundancy may actually reduce the reliability of the system. More commonly used in electronics is triple redundancy in which the output of the three systems are voted upon to determine the majority and assume it is correct, in this situation two out of the three systems must fail for the system to fail making it a 2 out of 3 redundancy configuration.

$$R_{m/nRedundancy} = 1 - \sum_{i=0}^{m-1} \left(\begin{array}{c} n \\ i \end{array} \right) R^i (1-R)^{n-i} \tag{4.3}$$

Figure 4.3: Reliability of 2 out of 3 connected components

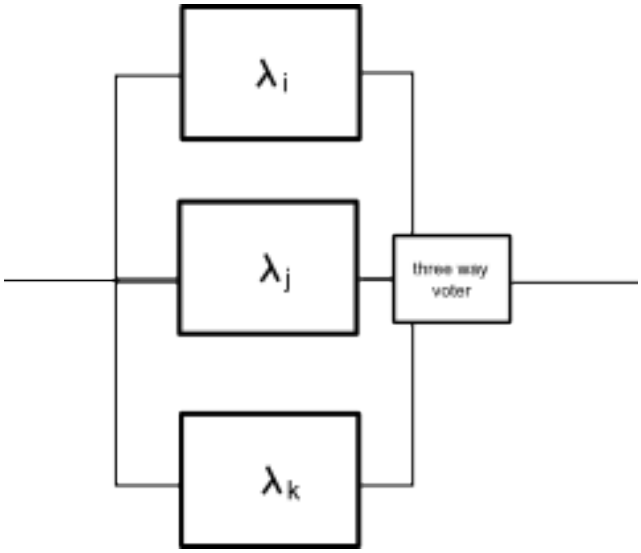

Another form of redundancy can come from a number of components in standby (called standby redundancy or cold redundancy), these components are maintained in an off or disconnected state until another component has had a detected fault.

$$R_{standbyRedundancy} = exp(-\lambda t) \sum_{i=0}^{n-1} \frac{(\lambda t)^{ia}}{i!} \tag{4.4}$$

An important factor to consider when designing redundancy into systems is common mode failures. A common mode failure is a failure that will effect all paths of a redundant system, this should be added as a failure point in series with the redundancy. Due to the nature of series components, common mode failures have a very large effect on the total reliability of the system, if a common mode failure can be identified it should be kept an order of magnitude lower than that of the rest of the system.

4.4 Redundancy in Information

Systems can also be looked at from the perspective of information. The reliability of information within a system can be interpreted as the probability that all of the stored information can be reconstructed without error, in a binary system this would imply that no 0's have erroneously changed to 1's and vice versa. The most common approach to protecting information for storage is the use of linear block codes.

Linear block codes take an input grouping of k symbols and encode them into a code word of length n symbols to create a **(n,k,d)** code where d is called the minimum distance of the code. The minimum distance d is equal to the minimum number of symbols that are different between any two potential code words generated by the code. A linear block code with minimum distance d can correct $\lfloor \frac{d-1}{2} \rfloor$ errors (which will be denoted t from now on) and detect up to $d-1$ errors [19]. Given that more than t errors must occur for the information to be decoded incorrectly or a failure to decode can occur, a linear block code can be seen as an (t+1)/n redundant system. We can then develop a equation for the reliability of the redundancy scheme by defining the probability that a single symbol has been corrupted as R_{symbol} and using equation 4.3 as the equation 4.5.

$$R_{information}(t) = 1 - \sum_{i=0}^{t} \left(\begin{array}{c} n \\ i \end{array} \right) R_{symbol}(t)^i (1 - R_{symbol}(t))^{n-i} \tag{4.5}$$

For the most common situation where the symbols are binary (0,1) and the source

of corruption is from single event upsets, a type of single event effect where the interaction of a charge particle causes a memory element to flip value, we can use the model for single event effects (equation 3.35) as discussed in chapter 3. We can then write a function for R_{symbol} over time as equation 4.6, where the values of σ_p and σ_i are the cross sections for single event upsets per bit of the memory from SEE testing.

$$\begin{aligned} R_{bit}(t) &= e^{-\lambda_{SEU}t} \\ &= e^{-(\lambda_{SEU,ion}+\lambda_{SEU,proton})t} \\ &= e^{-(2\pi\sum_i \sigma_i \int_{LET_T,i} F_i(E,t)dE + 2\pi\sigma_p \int_{LET_T,p} F_p(E_p,t)dE)t} \end{aligned} \tag{4.6}$$

A large difference in the failure or corruption of information from the failure of components discussed so far is that information can be corrected. Any code word read from a storage containing $\leq t$ errors can be re-encoded and written back to storage cleaning that information of the SEU's, this practice is called memory scrubbing. It is clear that the reliability of the information is then also dependent on rate at which the information is cleaned of errors. We will denote the amount of time paused between each reading, correcting, and re-writing cycle of a codeword in storage as t_s the scrubbing period. The probability that the system can not recover the encoded information from a code is the probability that more than t errors have occurred at time t_s, the reliability of the code can then be determined as one minus the sum of the probabilities that each uncorrectable error pattern have occurred (greater than t errors) equation 4.7.

$$R_{code} = R_{code}(t_s) = 1 - \sum_{i=t+1}^{n} \left(\begin{array}{c} n \\ i \end{array} \right) R_{bit}(t_s)^{n-i}(1 - R_{bit}(t_s))^i \tag{4.7}$$

The reliability of the system is then the probability that no code in the entire used memory of size N has encountered an uncorrectable amount of errors.

$$R_{information}(t_s) = (1 - R_{code}(t_s))^{\lfloor \frac{N}{n} \rfloor} \tag{4.8}$$

Chapter 5

Design Methodology

5.1 Summary

Following a consistent design methodology that incorporates rigorous verification and the use of reliability estimation is very important in ensuring mission success. The design methodology discussed in this section is targeted at the design of electrical systems between the preliminary and critical design review stages of a satellite program. The methodology starts with software in loop testing of primary system algorithms given the requirements and target environment. With verified algorithms, the requirements on actuator, sensors as well as processing power can be refined and a minimal functional system can be developed. The minimal system is then evaluated for estimated reliability as discussed in chapters 3 and 4, if the system reliability at end of life is acceptable the system can be built and move forward to hardware in loop testing. hardware in loop testing follows two main stages, first functional testing ensures that the system operates as expected to commands and error states, the second set of testing is refereed to as burn in testing where the system runs from the simulated environment for one week and one month tests.

5.2 Introduction

To address the risk of mission failure two main sources have been discussed as potential causes, first the environment and its effect on component failures has been described and a simplified model for evaluating an estimate on an electrical systems reliability at the end of mission. A second and equally important factor affecting the high failure rates of small satellites is lack of verification. It is clear that proper verification and testing would solve this but on the time constraints and budget often available to academic and young companies or organizations steps are often skipped. It is then obvious that a design methodology that can be followed to address both primary sources of mission failures needs to be followed.

The majority of small satellite projects follow a flow of design process of three major milestones, first the preliminary design review (PDR) which outlines mission application and concept of operations, orbital and attitude control plans, the requirements of each system, communication, mass and power budgets as well as the mechanical structure. After PDR has been accepted systems are designed to the outlined requirements and the mechanical structure is finalized. The critical design review (CDR) reviews the detailed electrical sub system, mechanical design and concept of operations. When the CDR is accepted the small satellite moves through the assembly, integration, and testing before finally being subjected to environment testing through vibration and thermal vacuum tests. It is often during the review processes that small teams miss or skip strict validation of a systems design. The design process outlined in this chapter aims to removed opportunity for design errors propagating to the flight hardware of a finished satellite.

5.3 Design

The design methodology for electrical systems proposed can be seen at a high level in figure 5.1, this methodology was developed for the ECOSat team so that a consistent process could be followed that would ensure testing and environmental considerations where followed. The methodology focuses on the design of electrical

subsystems which have been assumed to be the primary failure point for small satellite missions where there are typically very few moving components and very simple mechanical and thermal structures. The design process relies on proper mission design and concept of operations to have been completed and aims to assist the design of systems in between the preliminary design review and critical design review stages. It is important to have knowledge of the target orbit, attitude control plans, mechanical structure and mechanical mounting of electronics such that the environments that effect component reliability can be estimated.

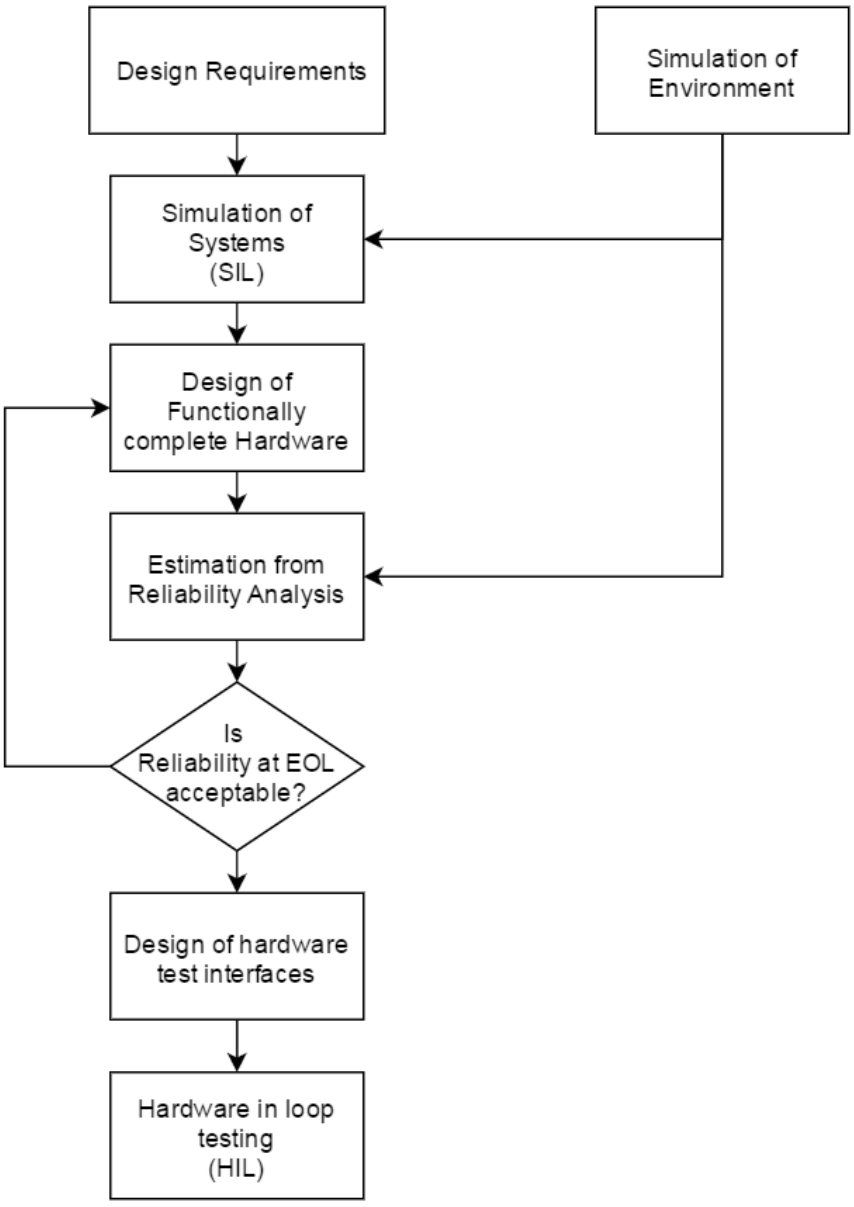

Figure 5.1: System Design Methodology

The first step in reliable system design is a good understanding of the environment the system will be operating in, it is especially important to determine the thermal and radiation environments of the electrical circuit board being designed given its location in the satellite and the target orbit from the preliminary design review. Figure 5.2 shows the basic flow of information required to obtain environmental data for reliability estimation. The evaluation of radiation information can be obtained from knowledge of the target orbit and structural shielding of the systems location within the satellite, SPENVIS [13] an on line tool created by the ESA for running radiation models, can be used to determine the flux values of protons, electronics, and heavy ions required for the models discussed in chapter 3 for a given shielding in equivalent aluminum thickness, sectored shielding analysis can be used for significantly non uniform amounts of metal around the target system. For the thermal environment, first the structure, attitude control plan, and orbit can be used to develop an initial power budget based on available power generated by the structural size and fill factor as well as attitude planning and its affect on solar angle to each solar panel through a simulated orbit. The initial power budgeting available to each subsystem is then used for thermal generation in a thermal model. A simple orbit simulation and power budget which takes into account the attitude and panel orientation on power generation was developed for the ECOSat team in excel, more information can be found in appendix C. With the initial thermal information, a simulation software such as Siemens NX [20] or Thermal Desktop [21] can be used to model the structure and simulate the thermal cycling of the electronics using the available power as a heating load to the system.

The second step focuses on simulation of the system and software in loop testing. Software in loop testing within this stage is intended to identify any errors in the initial planning and requirements of primary system algorithms and design. The primary focus should be on verification of the attitude and orbital control, communication, as well as on board command and data handling systems. Simulation of the attitude, orbit, and power generation should to be created such that sensors and actuators along with communication between the simulated satellite position and a ground station can be evaluated. Software in loop test cases should provide full coverage of typical operating conditions as well as input failure cases and error state cases.

After the completion of software in loop testing when primary algorithms for sys-

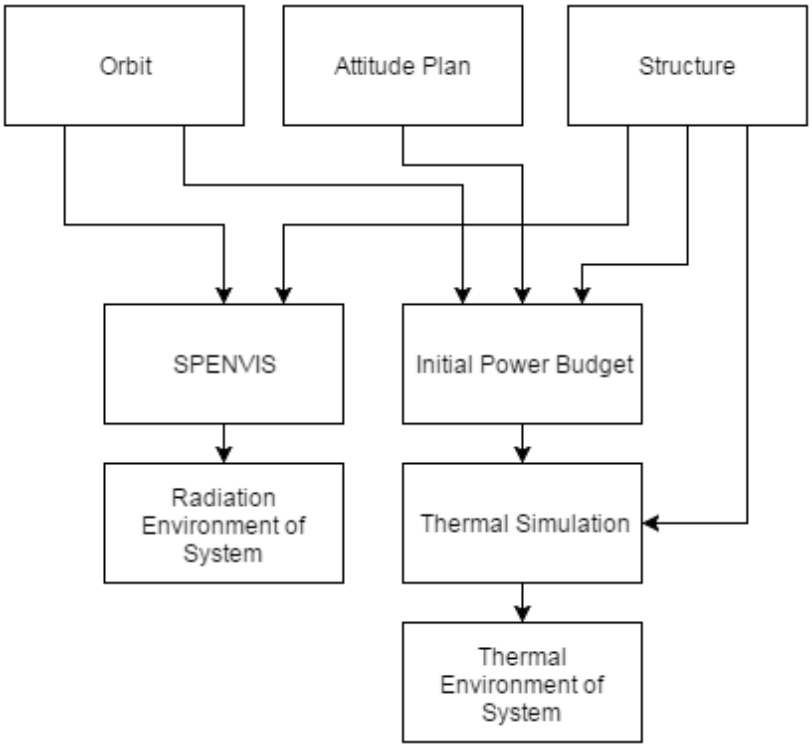

Figure 5.2: Environment Simulation

tems have been verified, functionally complete hardware can be designed. Functionally complete refers to the idea that the first version of the systems electronics should contain the minimum number of components to accomplish subsystems requirements to reduce complexity and power. The main idea of a functionally complete system is the same as minimum viable product used in project management, in this design methodology the goal is to add no redundancy into the design at this stage, that will be done later where needed. At this stage all electrical components should be selected and schematics or system block diagrams made with components selected.

Once a functionally complete system has been completed and reviewed, the reliability of components selected can be estimated using the models discussed in chapter 3 using environment data evaluated for the target orbit and location of the system in the satellite structure. It is at this stage that the reliability at the end of life (EOL), or target mission duration can be evaluated, if the reliability of the system at this stage is less than some acceptable level ϵ then the reliability of each component can be compared to find weak points in the design. From here systems with unaccept-

able amount of reliability at EOL can be modified to add redundancy, the results from the reliability estimation can be used to determine if thermal or radiation is the primary cause. For systems with low reliability due to radiation, possible solutions include adding shielding, changing component selection or implementing redundancy schemes discussed in chapter 4. For components with low thermal mechanical reliability, changes in the thermal control or design of the structure can be made or a change on package type can be made, for example changing the selection of the QFP package in an old ECOSat-2 design to the BGA package reduces the width of a chip enough to increase the reliability by reducing the effect of thermal cycling on coefficient of expansion miss match, Figure 5.3.

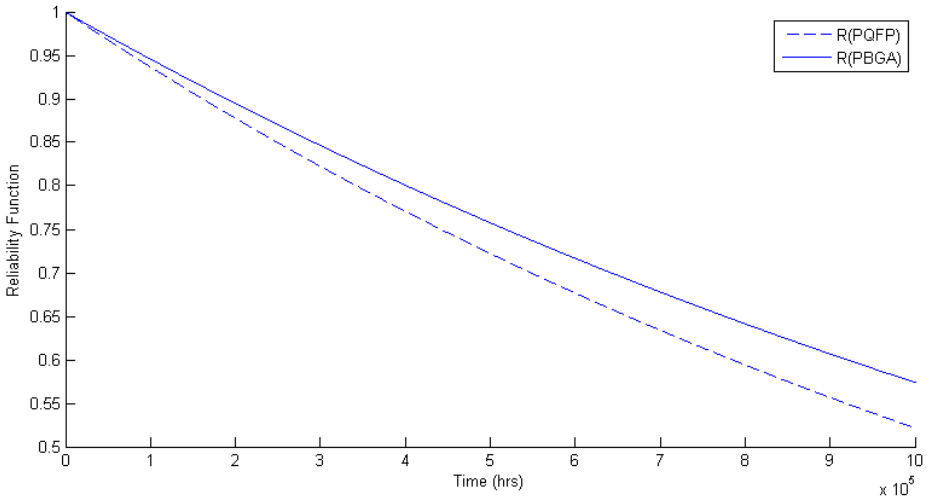

Figure 5.3: BGA and QFP thermal mechanical reliability in same environment parameters

If the reliability is acceptable then the system can be constructed and hardware in loop testing can be started. Test interfaces should be made to allow the environmental simulation that was used to test the system algorithms during the software in loop stage access to conduct the same tests in real time.

5.4 Verification

The goal of verification is to identify errors caused by implementation and manufacturing. Test interfaces for hardware in loop testing such as the ones developed for ECOSat-2 seen in figure 5.4 should be developed to allow the system to operate from simulated command and sensor inputs while providing telemetry and testing information back to the test computer.

Two main style of testing should be focused on. First functional testing should be defined such that the full set of tests cover every command and response over different operational states. Functional testing allows for basic errors in firmware and hardware to be identified. The second style of testing can be refereed to as burn in testing and should be conducted after functional testing passes in which the system is left to operate on simulated inputs as it would on orbit. Two types of burn in testing should be conducted, first one week tests should be defined such that simple concept of operation procedures can be tested. The one week tests allow for testing of change of state, telemetry and file management, response to loss of contact for multiple days and that basic automation works without deadlocks. Once one week tests pass a one-month test should be conducted that follows the full concept of operations of the satellite systems from deployment to operation.

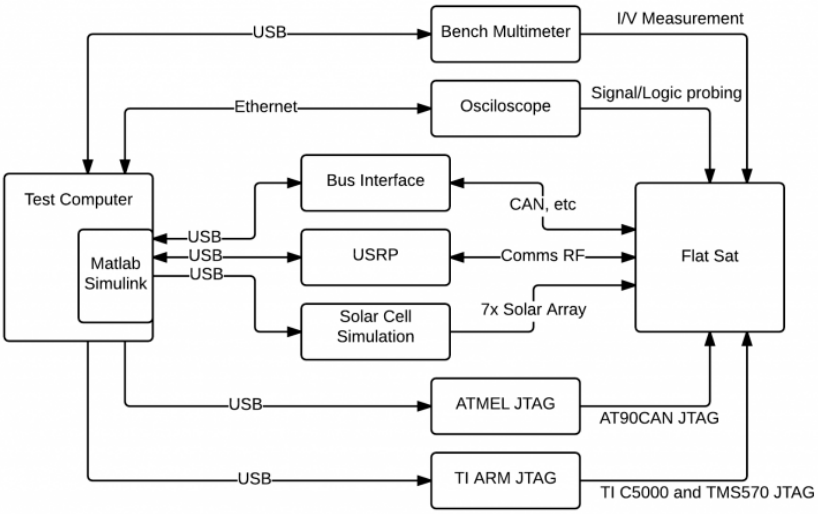

Figure 5.4: Hardware in loop testing

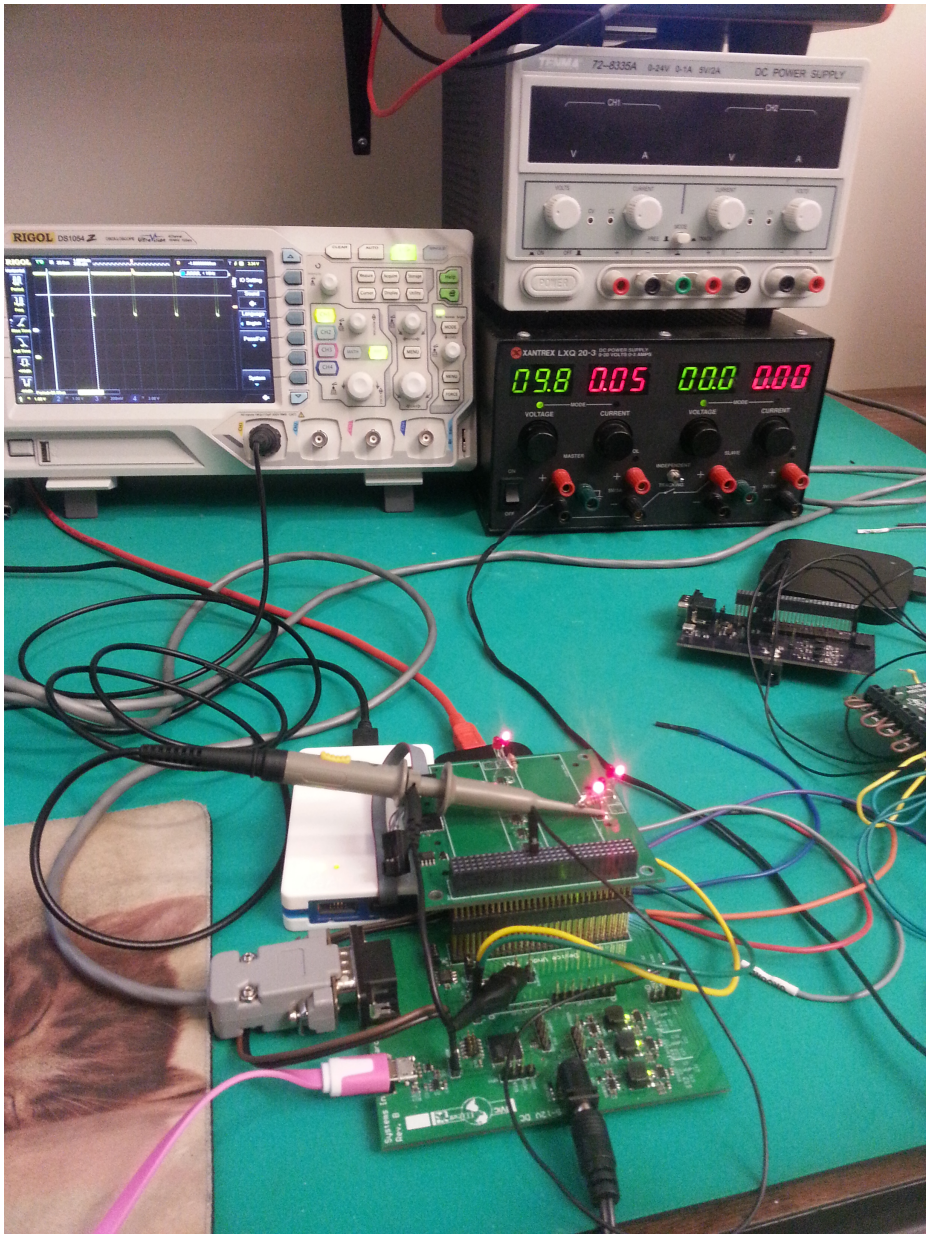

Figure 5.5: Example of the ECOSat-2 Test Interface with the ACS system during functional testing

Chapter 6

Case Study, ECOSat-II on board command and data handling

6.1 Summary

Discussed so far reliability models that depend on the thermal and radiation environment of a target orbit have been developed for use in reliable design of electrical systems. To obtain the environmental parameters required for reliability estimation Siemens NX has been used to create a model of the ECOSat-II satellite that will be used for thermal mechanical simulation. The Space Systems Thermal FEA application [20] within Siemens NX was used such that a thermal analysis could be conducted to provide thermal cycling and average temperature data for each printed circuit board within the satellite. For the radiation environment parameters required, an on-line tool called SPENVIS [13] has been used to obtain shielded flux values for heavy ions, protons, and electrons near the components within the satellite. Applying these environmental parameters and component parameters to the reliability models discussed so far, the reliability of the on board command and data handling system within the EOCSat-II cube satellite was estimated as a case study resulting in a reliability of 92.5% in a 600km sun synchronous orbit for a targeted mission time of 2 years. The reliability of information within the main memory has also

been evaluated providing results that shows the current standard for error coding in which triple modular redundancy is used is not acceptable for large memory spaces, a reed-solomon code has been designed to provide a greater than 95% reliability of information over a 1GB memory space for the 2 year target mission.

6.2 Environment Modeling

To obtain environmental parameters of the satellite required for the reliability models discussed in chapter 3, thermal and radiation models where computed for a 600km sun-synchronous orbit having a noon local time at the ascending node. The 600km sun-synchronous orbit was selected for use in modeling the reliability of systems design by the ECOSat team as it is the target orbit for ECOSat-2 both for magnetic field requirements of the science payload and increased coverage for the amateur radio relay, in addition to ECOSat-2, ECOSat-3 will target this orbit for coverage requirements of imaging Canada. A new model had to be created as the original model of the satellite in Solid Works used by the ECOSat team was outdated from the current electrical stack, battery configuration as well as being in a difficult form to transfer to another program for environment modeling. The environmental parameters for the thermal mechanical effects will be obtained through the use of Siemens NX Space Systems Thermal while the radiation environment where computed through SPENVIS an online tool hosted by the European Space Agency. Using this tool av-

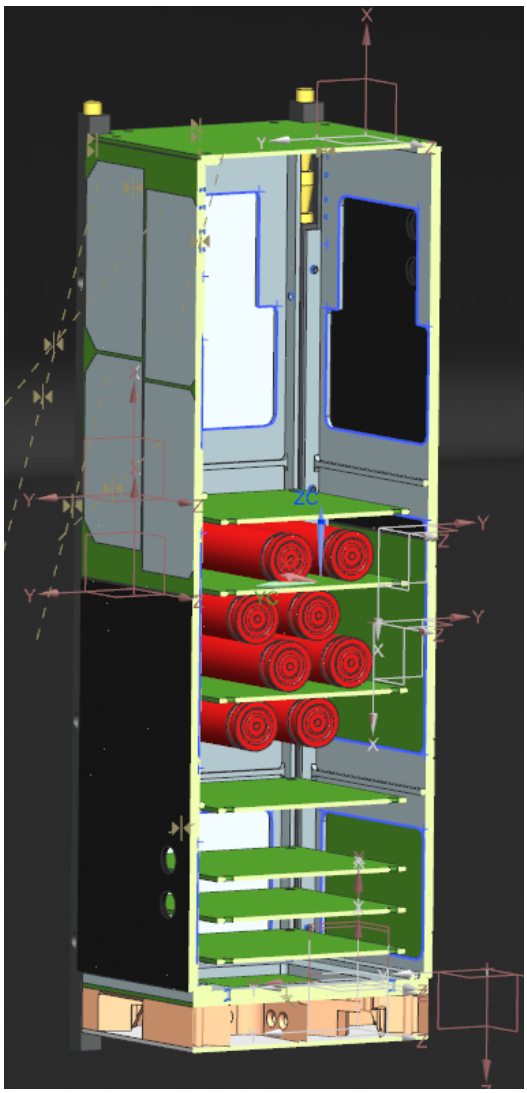

Figure 6.1: ECOSat-2 Siemens NX model

erage fluxes of protons, electrons, and other heavy ions as well as cumulative values of total does can be calculated for a given altitude or orbit.

6.2.1 Thermal FEA

NX Space Systems Thermal

Thermal data was collected for each electronics board through the creation of an FEA model developed by first modeling the structure in Siemens NX and creating both an FEA model for NASTRAN (NASA structure analysis) Simulation of vibrational modes as well as another FEA model for the NX Space Systems Thermal Simulation.

Initial CAD work through this project focused on efficiently recapturing the design of ECOSat-2 done by Justin Curran [22] and other ECOSat members in Solid Works into Siemens NX where better Vibrational and Thermal analysis could be done. This work was intended to make the future use of NX for simulation much easier as Solid Works was unable to provide adequate simulations tools for on orbit thermal simulation as well the industry preferred use of NASTRAN for vibrational analysis.

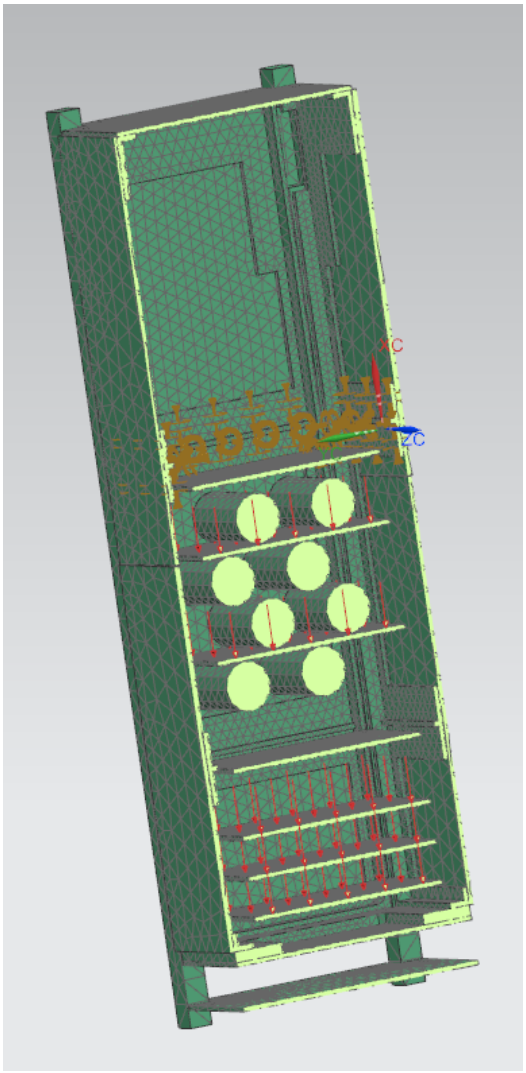

Figure 6.2: Mesh created for thermal modal

A cutout of the assembly created for thermal simulation can be seen in figure 6.1, The primary changes to the model from the initial work of the ECOSat team was the redesign of the structure to accommodate the launch requirements of new Nano Rack Standards that have been since added to the design integration and environmental testing requirements [23]. The changes to the structure are focused on the deployment pins which now provide up to 8 isolation switches in comparison to the original 2 on opposite corners. The new deployment switch positions allow for redundancy in all three required isolation points (at the ground of the batteries and two in series between the battery positive and load) previously only one switch was required between the battery positive and load which was duplicated for redundancy in the original design. The second difference is the update to the electronics stack to accurately represent the new systems in development, the most important being the reduced communications stack from three printed circuit boards to one and the update of the battery boards from the old design using 14650 lithium ion cells to the new design using 18650 sized lithium ion cells.

Two different meshes were created, one for vibrational analysis where 1D connections were created with the bolt wizard and another for thermal analysis where 1D connections were created with the simplified thermal connection models. A cut-out of the thermal mesh can be seen in figure 6.2. the red arrows seen on each board show the thermal energy generated by the electronics. The thermal analysis is run in both a cold case and hot case, parameters of the two situations can be seen in tables 6.2 and 6.1. The hot cases assumes maximum solar flux and maximum power consumption of electronics while the cold case assumes minimum solar flux and minimum operating power consumption. After initial runs it was found that the battery heaters would only activate in the cold case and were not used during the hot case simulations as the control system for them while operating correctly would not turn them on.

Standoffs between printed circuit boards as well as the thermal connections through bolts and screws where added to the simulation with the use of simplified thermal coupling simulation elements. The thermal conductivity of each standoff was based on aluminum and Delrin standoffs as required in the design with the start and end points of the connection being the interior of the standoff holes as seen in figure 6.3. Similar to the standoffs, the thermal conductivity through the structural bolts, electrical stack mounts, as well as the battery clips used to hold the individual battery

cells were simplified as thermal coupling model elements.

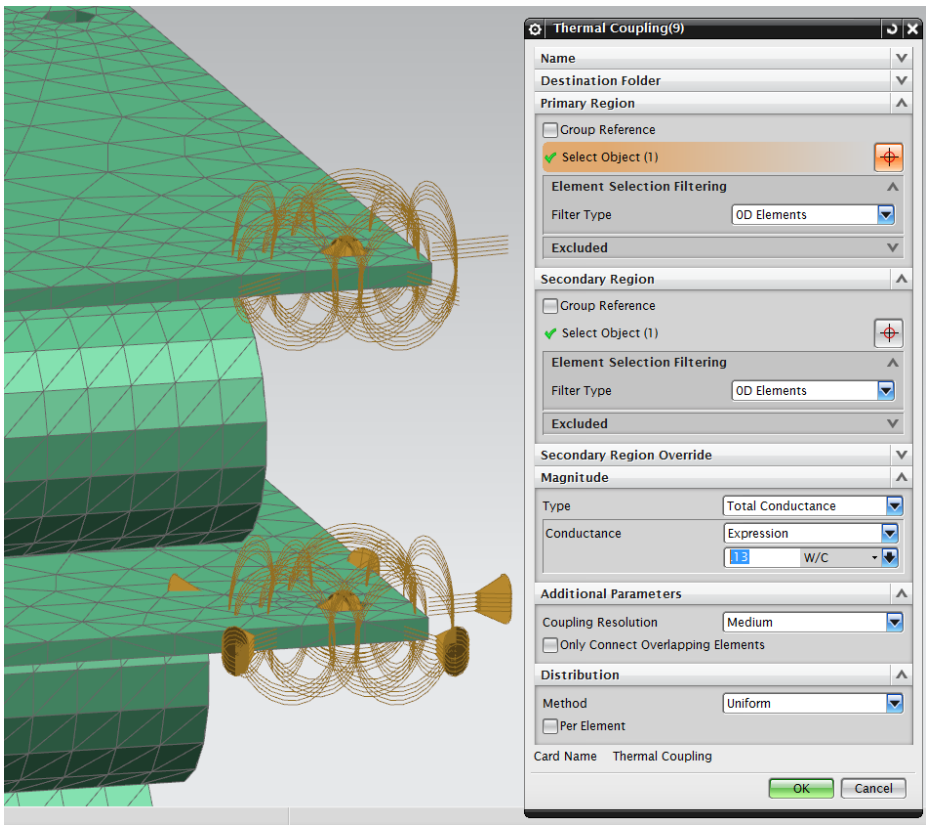

Figure 6.3: Thermal transfer through standoffs

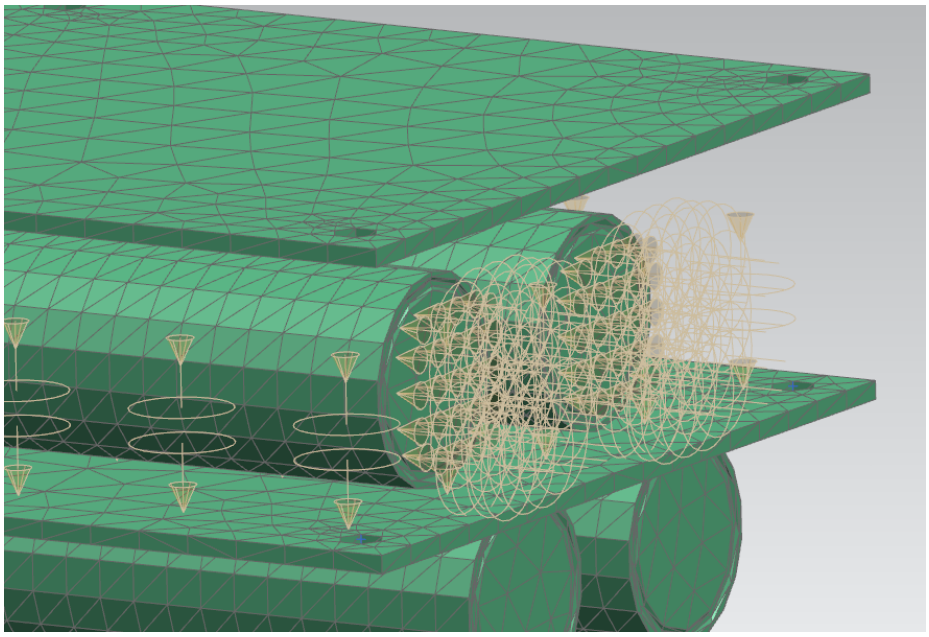

Figure 6.4: Battery Clip thermal transfer

The power listed in the heating sections of the cold case and hot case parameter tables show the total power generated by each system, to simplify and increase the speed of the simulation the heating was spread across the boards equally and the individual electrical layout was not considered, the assumption made during the modeling and simulation is that for a properly designed system, a clean ground plane (solid layer without and cuts) connects and allows for efficient spreading of heat throughout the board. The thermal impedance of each printed circuit board in the x-y plane was set to be equal to a single 1oz copper layer within the plane, this is about $79.4^oC/W$ in comparison to $2620^oC/W$ of FR4 for a typical 6 thou (mil) layer [24]. ECOSat-II is unpressurized and for internal connections only conductive thermal transfer was used, during early simulations it was found that the radiative transfer between boards was much smaller than the transfer through the aluminum standoffs and afterwards ignored as it greatly increased simulation time.

Using the Siemens NX Space Systems Thermal Analysis the thermal simulation was run for the solar flux and orbits as listed in the cold case and hot case parameter tables. The radiative transfer into the satellite structure as well as the radiative cooling of the satellite structure configured for the simulation was set to calculate through 16 locations around the sun synchronous orbit, the ability to specify orbital

Table 6.1: Thermal Analysis Hot Case Parameters

Orbital Parameters	Solar Flux ($\frac{W}{m^2}$) :	1412.73
	Orbit :	600km Sun Synchronous, 12:00:00 Ascending time
	Period (sec) :	5792.407
Heating	Batteries (μW) :	21
	OBC (W) :	1.216
	Payload (W) :	0.256
	ACS (W) :	1.024
	Communications (W) :	2
	ADM (mW) :	64
	Regulation (mW) :	100

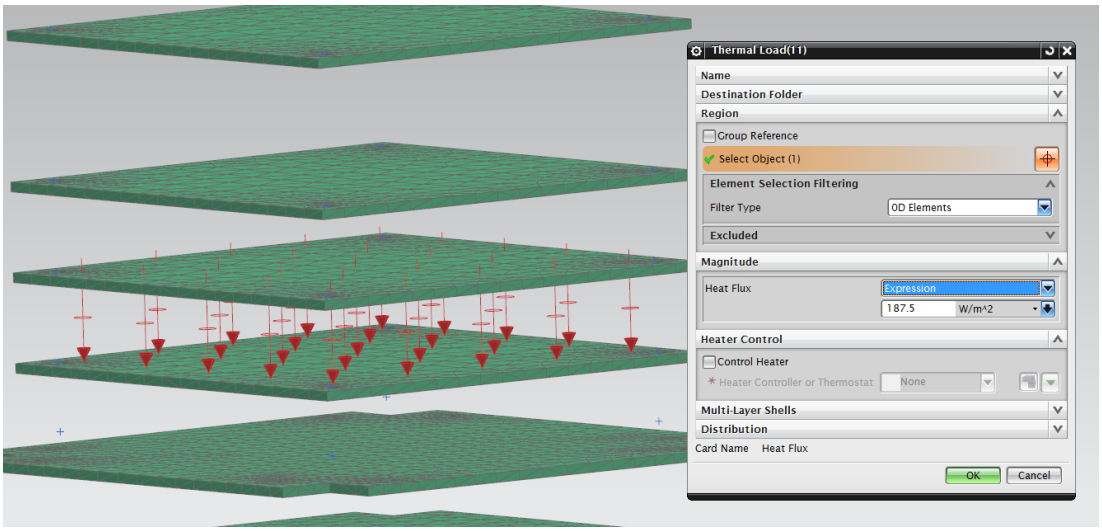

Figure 6.5: Thermal Loads added

parameters for a transient simulation was the primary feature that caused Siemens NX to be selected for both vibrational and thermal analysis.

Table 6.2: Thermal Analysis Cold Case Parameters

Orbital Parameters	Solar Flux ($\frac{W}{m^2}$) :	1322.47
	Orbit :	600km Sun Synchronous, 12:00:00 Ascending time
	Period (sec) :	5792.407
Heating	Batteries (μW) :	5
	Battery Heaters (mW) :	100
	OBC (W) :	0.24
	Payload (W) :	0
	ACS (W) :	0
	Communications (W) :	0.7
	ADM (mW) :	64
	Regulation (mW) :	50

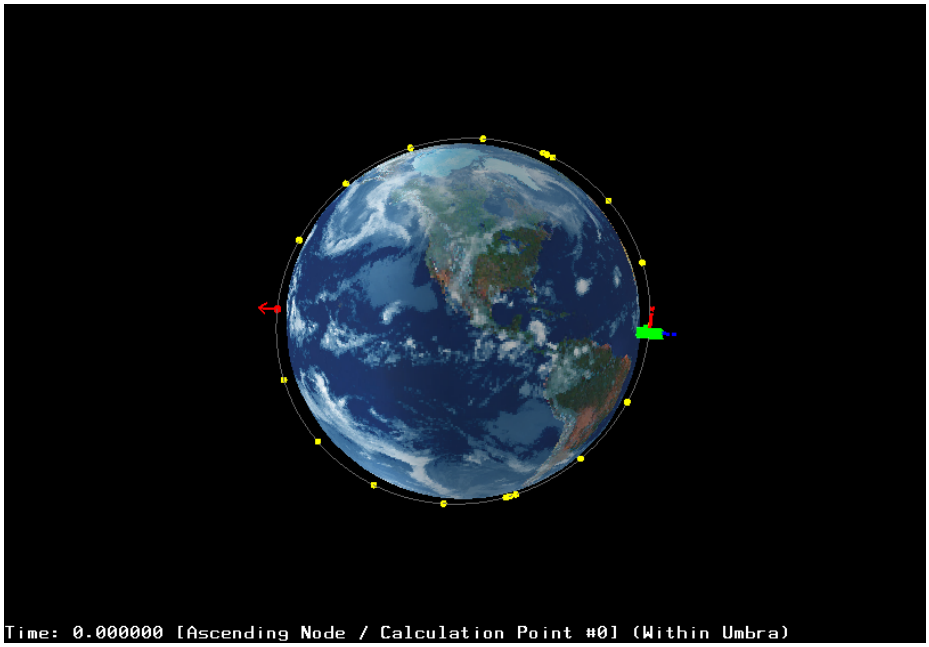

Figure 6.6: Orbital locations for calculation in the Space Systems Thermal Analysis setup

Thermal Cycling Results

For the reliability model discussed in chapter 3 it is important to gather the thermal cycle range to determine the reliability of solder joints and other thermal mechanical failure causes. From the thermal simulation the temperature range of each printed circuit board was determined as the temperature cycle of the average temperature of all nodes on each specific board, or of all nodes within the batteries. A snapshot of the transient analysis can be seen in figure 6.7.

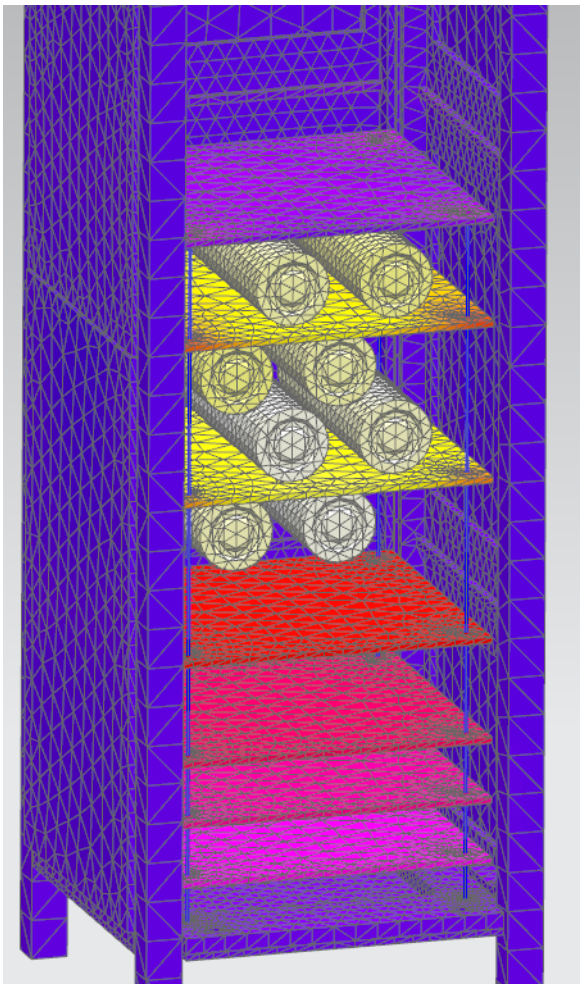

Figure 6.7: Simulation Result snapshot

After allowing the transient simulation to come to a dynamic equilibrium over a few orbits the temperature of the structure was found to cycle between -14.85^oC to 36.88^oC in the hot case (51.73Δ^oC), and -21.16^oC to 28.75^oC in the cold case (49.91Δ^oC). Graphs of the average node temperature of the structure in both the hot case and cold case can be seen in figure 6.8. While the structural temperature range is high for electronics, the aluminum structure is well within its tolerances.

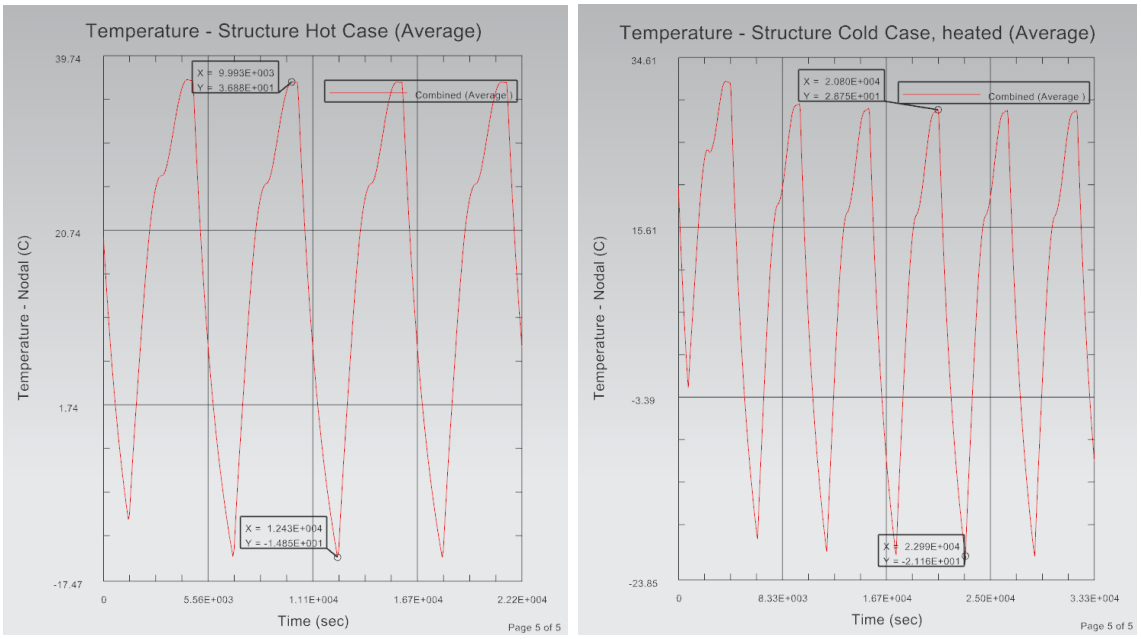

(a) Structural temperature in the Hot Case (b) Structural temperature in the Cold Case

Figure 6.8: Structural temperature results

After allowing the transient simulation to come to a dynamic equilibrium over a few orbits the temperature of the solar panel printed circuit boards was found to cycle between -14.85^oC to 36.82^oC in the hot case (51.67Δ^oC), and -21.28^oC to 29.38^oC in the cold case (50.66Δ^oC). Graphs of the average node temperature of the solar panels in both the hot case and cold case can be seen in figure 6.9.

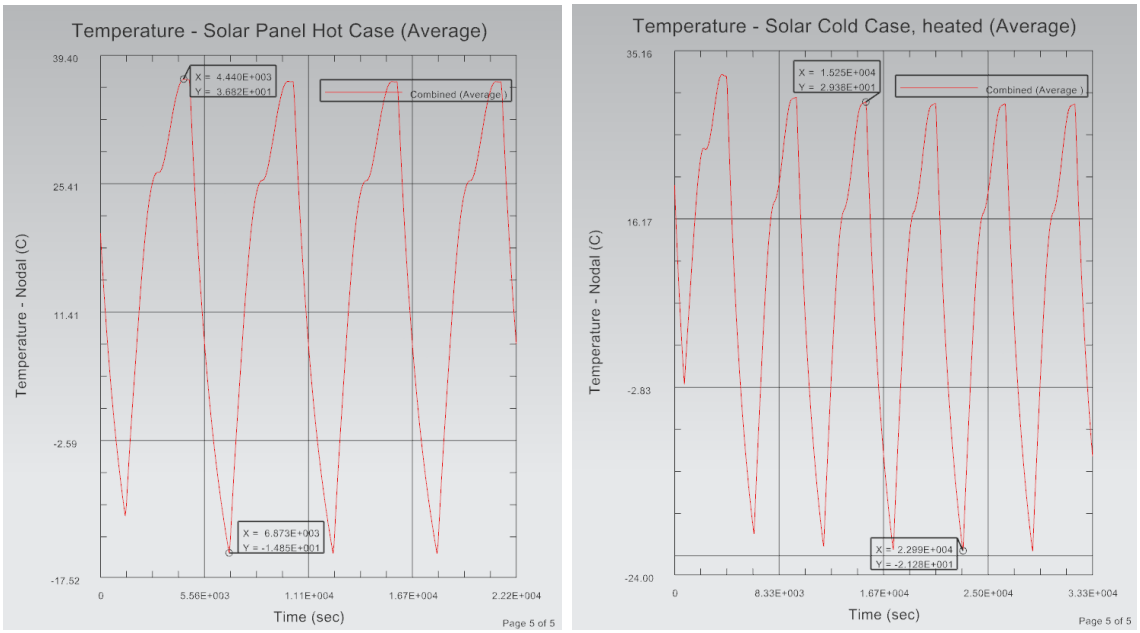

(a) Solar Panel temperature in the Hot Case (b) Solar Panel temperature in the Cold Case

Figure 6.9: Solar Panel temperature results

While the minimum and maximum values of temperature differ between the hot and cold situations that absolute temperature change remains similar. For a typical orbit the temperature cycle should operate somewhere between these two values and so a ΔT of 51.67^oC will be used for reliability modeling of any component located on the solar panels.

After allowing the transient simulation to come to a dynamic equilibrium over a few orbits the temperature of the regulation printed circuit board as part of the power system was found to cycle between -1.58^oC to 36.5^oC in the hot case (38.08Δ^oC), and -11.35^oC to 25.09^oC in the cold case (36.44Δ^oC). Graphs of the average node temperature of the regulation PCB in both the hot case and cold case can be seen in figure 6.10. While the minimum and maximum values of temperature differ between

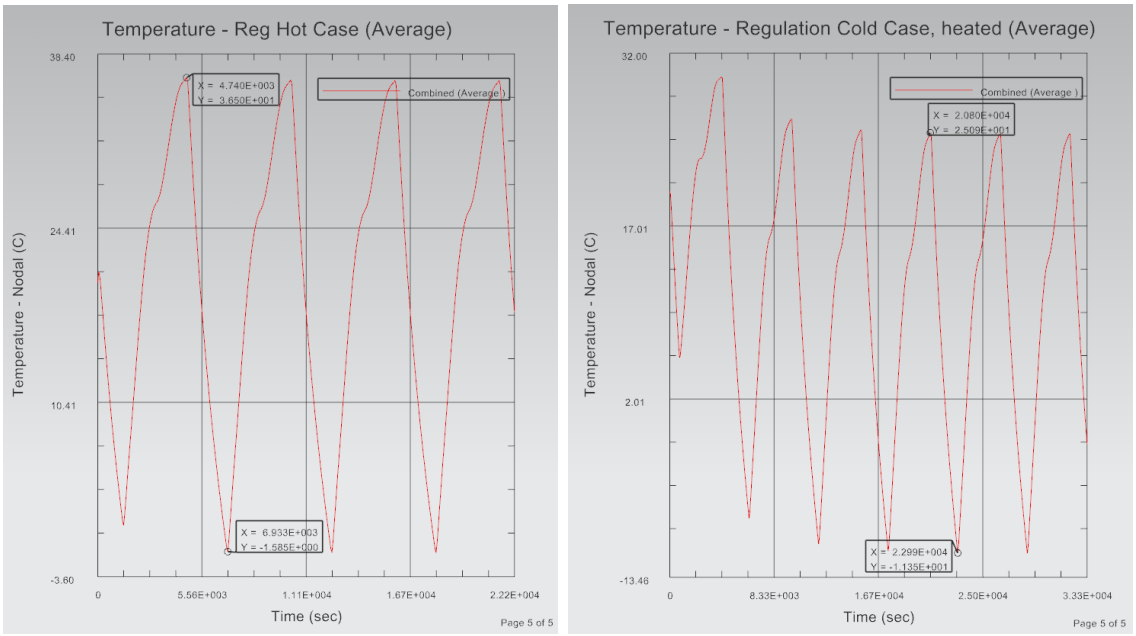

(a) Regulation temperature in the Hot Case (b) Regulation temperature in the Cold Case

Figure 6.10: Regulation temperature results

the hot and cold situations that absolute temperature change remains similar. For a typical orbit the temperature cycle should operate somewhere between these two values and so a ΔT of 38.08^oC will be used for reliability modeling of any component located on the regulation board.

After allowing the transient simulation to come to a dynamic equilibrium over a few orbits the temperature of the payload control printed circuit board was found to cycle between 13.31^oC to 27.57^oC in the hot case ($14.26\Delta^oC$), and 2.137^oC to 15.76^oC in the cold case ($13.623\Delta^oC$). Graphs of the average node temperature of the payload control PCB in both the hot case and cold case can be seen in figure 6.11. While the minimum and maximum values of temperature differ between the hot and

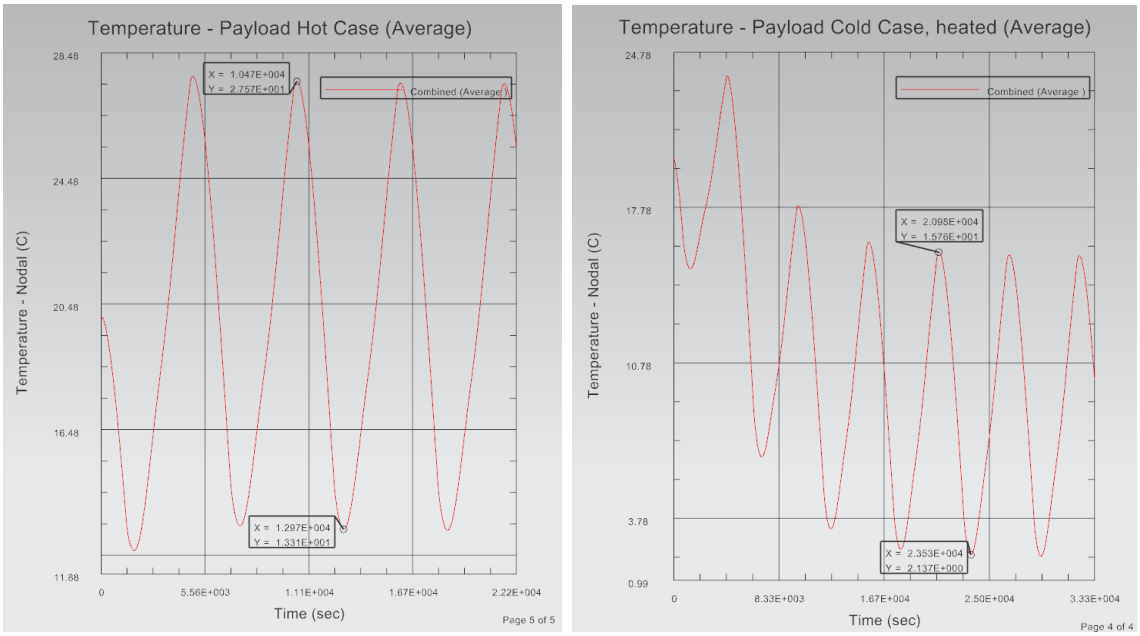

(a) Payload temperature in the Hot Case (b) Payload temperature in the Cold Case

Figure 6.11: Payload temperature results

cold situations that absolute temperature change remains similar. For a typical orbit the temperature cycle should operate somewhere between these two values and so a ΔT of 14.26^oC will be used for reliability modeling of any component located on the payload board.

After allowing the transient simulation to come to a dynamic equilibrium over a few orbits the temperature of the on board computer printed circuit board was found to cycle between -5.002^oC to 37.84^oC in the hot case (42.842Δ^oC), and -14.28^oC to 26.91^oC in the cold case (41.19Δ^oC). Graphs of the average node temperature of the on board computer PCB in both the hot case and cold case can be seen in figure 6.12. While the minimum and maximum values of temperature differ between the hot and

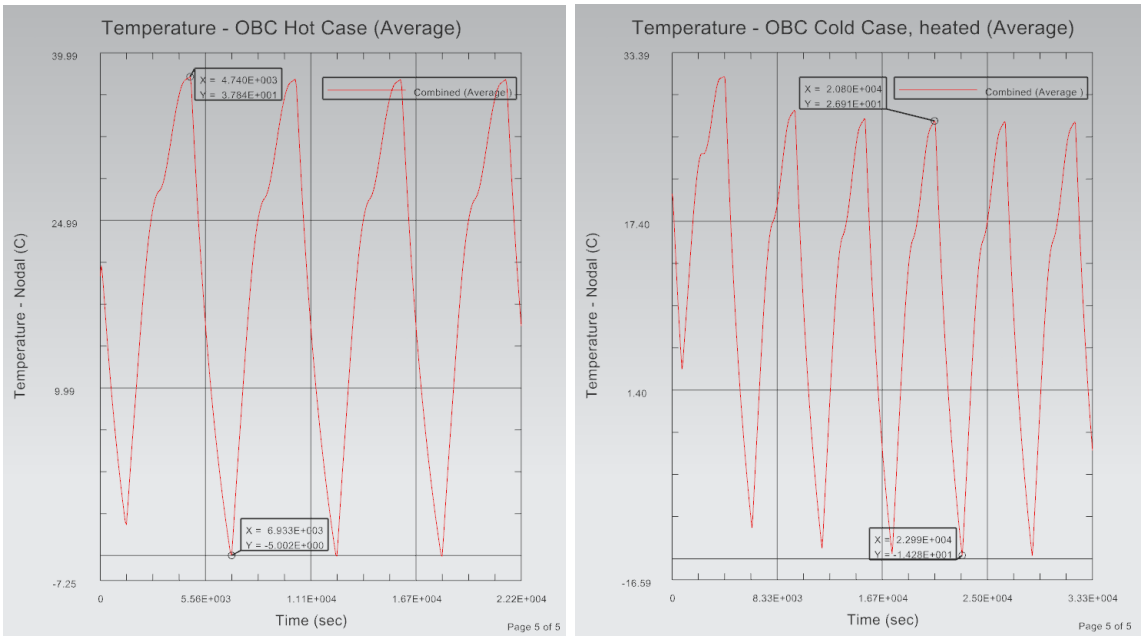

(a) OBC temperature in the Hot Case (b) OBC temperature in the Cold Case

Figure 6.12: On Board Computer temperature results

cold situations that absolute temperature change remains similar. For a typical orbit the temperature cycle should operate somewhere between these two values and so a ΔT of 42.842^oC will be used for reliability modeling of any component located on the on board computer board.

After allowing the transient simulation to come to a dynamic equilibrium over a few orbits the temperature of the modem printed circuit board as part of the communication system was found to cycle between -9.032^oC to 38.65^oC in the hot case (47.682Δ^oC), and -17.31^oC to 28.69^oC in the cold case (46Δ^oC). Graphs of the average node temperature of the modem in both the hot case and cold case can be seen in figure 6.13. While the minimum and maximum values of temperature

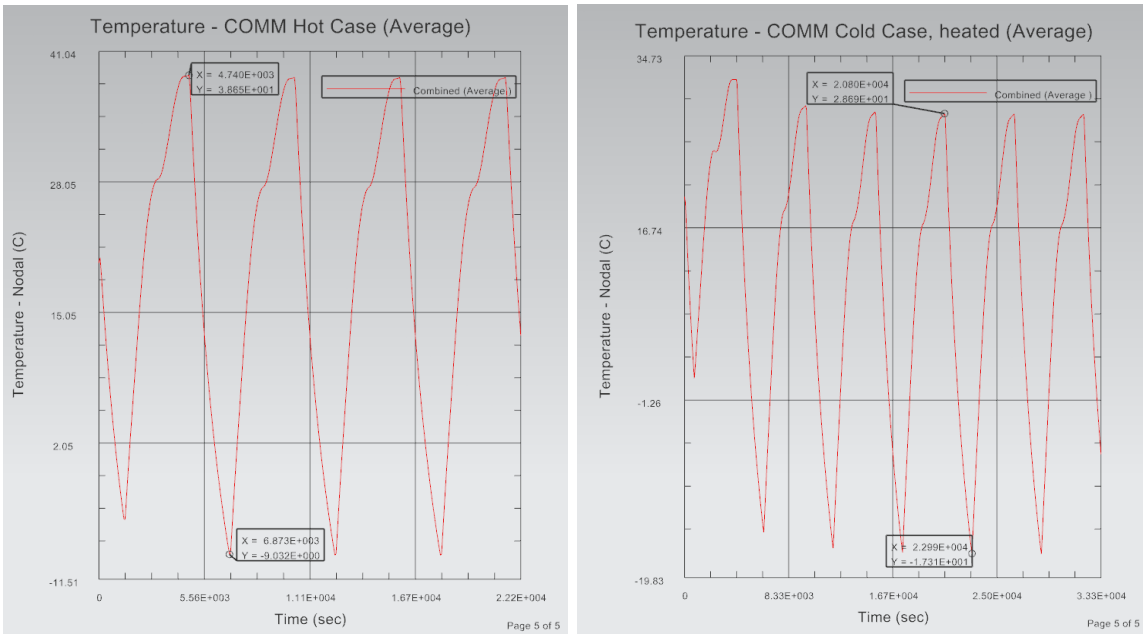

(a) COMM temperature in the Hot Case (b) COMM temperature in the Cold Case

Figure 6.13: Communications Modem temperature results

differ between the hot and cold situations that absolute temperature change remains similar. For a typical orbit the temperature cycle should operate somewhere between these two values and so a ΔT of 47.682^oC will be used for reliability modeling of any component located on the modem board.

After allowing the transient simulation to come to a dynamic equilibrium over a few orbits the temperature of the batteries was found to cycle between 13.57^oC to 27.64^oC in the hot case ($47.682\Delta^oC$), and 2.263^oC to 15.68^oC in the cold case ($13.417\Delta^oC$) Graphs of the average node temperature of the batteries in both the hot case and cold case can be seen in figure 6.14. While the minimum and maximum values

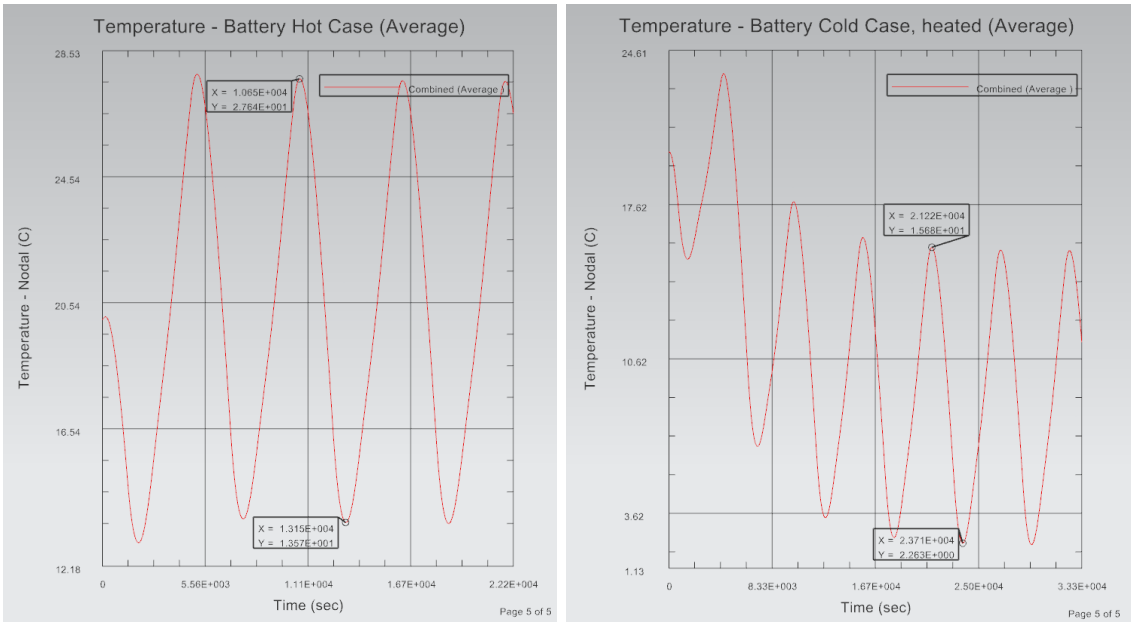

(a) Battery temperature in the Hot Case (b) Battery temperature in the Cold Case

Figure 6.14: Battery temperature results

of temperature differ between the hot and cold situations that absolute temperature change remains similar. For a typical orbit the temperature cycle should operate somewhere between these two values and so a ΔT of 14.07^oC will be use for reliability modeling of the batteries.

After allowing the transient simulation to come to a dynamic equilibrium over a few orbits the temperature of the antenna deployment board was found to cycle between -14.58^oC to 37.12^oC in the hot case (51.7Δ^oC), and -21.04^oC to 28.76^oC in the cold case (49.8Δ^oC) Graphs of the average node temperature of the batteries in both the hot case and cold case can be seen in figure 6.15. While the minimum

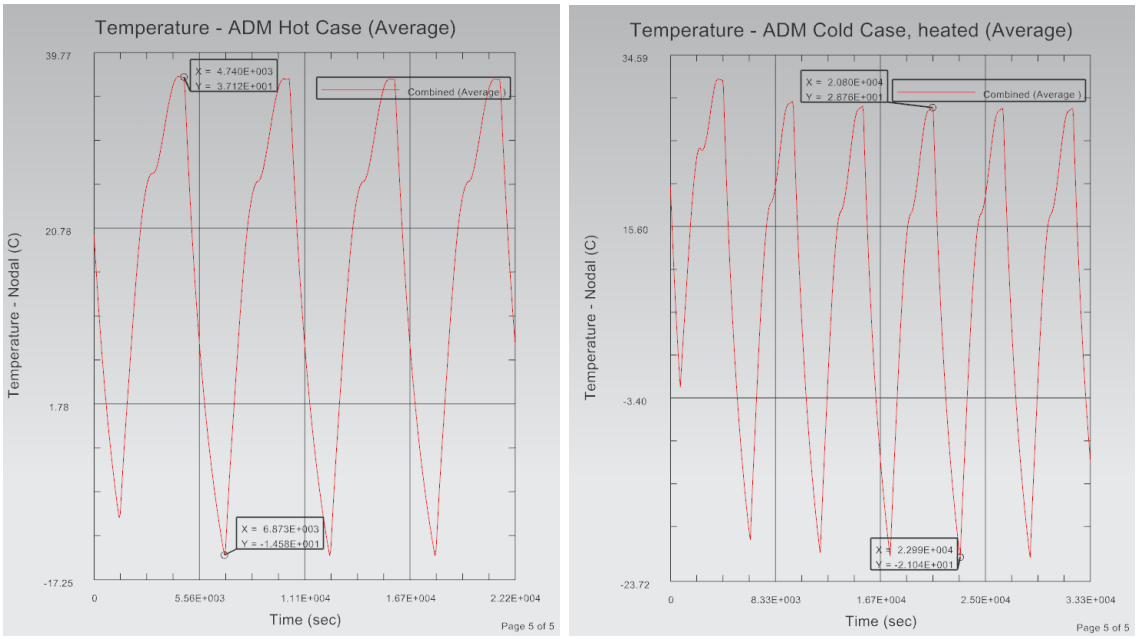

(a) ADM temperature in the Hot Case (b) ADM temperature in the Cold Case

Figure 6.15: Antenna Deployment Module temperature results

and maximum values of temperature differ between the hot and cold situations that absolute temperature change remains similar. For a typical orbit the temperature cycle should operate somewhere between these two values and so a ΔT of 51.7^oC will be use for reliability modeling of components on the antenna deployment board.

After allowing the transient simulation to come to a dynamic equilibrium over a few orbits the temperature of Attitude Control System Board was found to cycle between 5.798^oC to 34.14^oC in the hot case (28.342Δ^oC), and -5.506^oC to 21.51^oC in the cold case (27.016Δ^oC) Graphs of the average node temperature of the Batteries in both the hot case and cold case can be seen in figure 6.16. While the minimum

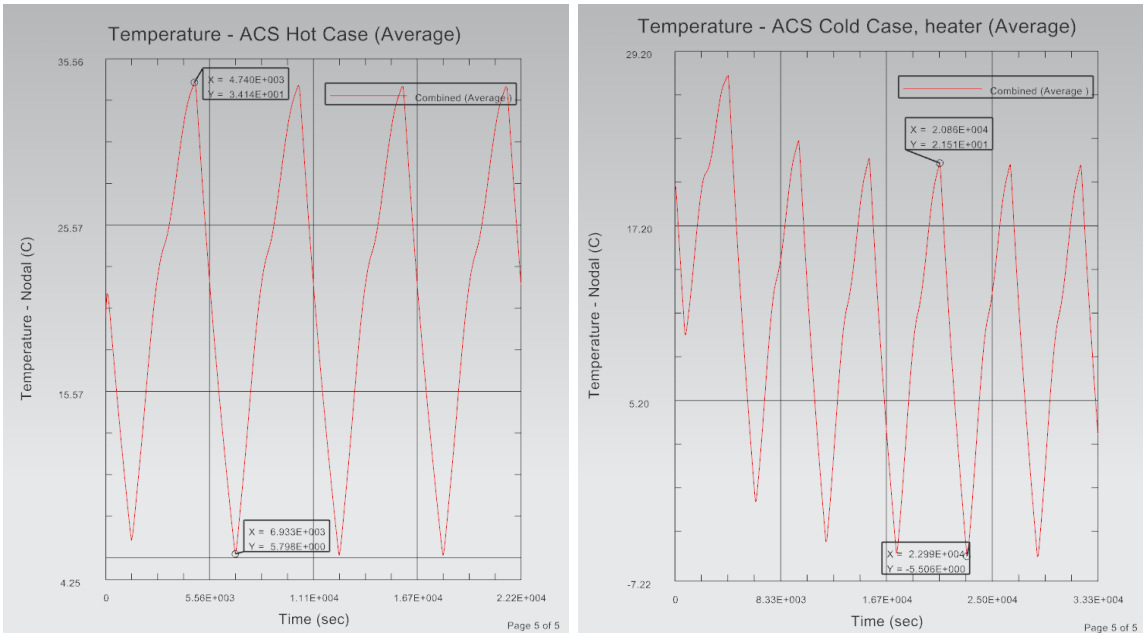

(a) ACS temperature in the Hot Case (b) ACS temperature in the Cold Case

Figure 6.16: Attitude Control System temperature results

and maximum values of temperature differ between the hot and cold situations that absolute temperature change remains similar. For a typical orbit the temperature cycle should operate somewhere between these two values and so a ΔT of 28.342^oC will be use for reliability modeling of components on the attitude control board.

6.2.2 Radiation Environment

Modeling the radiation environment for the 600km sun synchronous orbit used for reliability evaluation is important for the required environmental parameters of the models discussed in chapter 3. The radiation environment models selected for use focused on maximum values. To calculate the selected models, the online tool SPENVIS [13] created by the European Space Agency was used for Differential fluxes and shielding flux spectrums. Values for Linear energy transfers into Silicon where determined from the LET Calculator [14]. The data collected focuses on the maximum values of proton, electron, and heavy ion fluxes through the target orbit as well as total accumulated ionizing dose for a 2-year mission given different shielding thicknesses. Shielded flux values where obtained for a shielding thickness of 2mm equivalent aluminum to account for the satellites solar panels and structure.

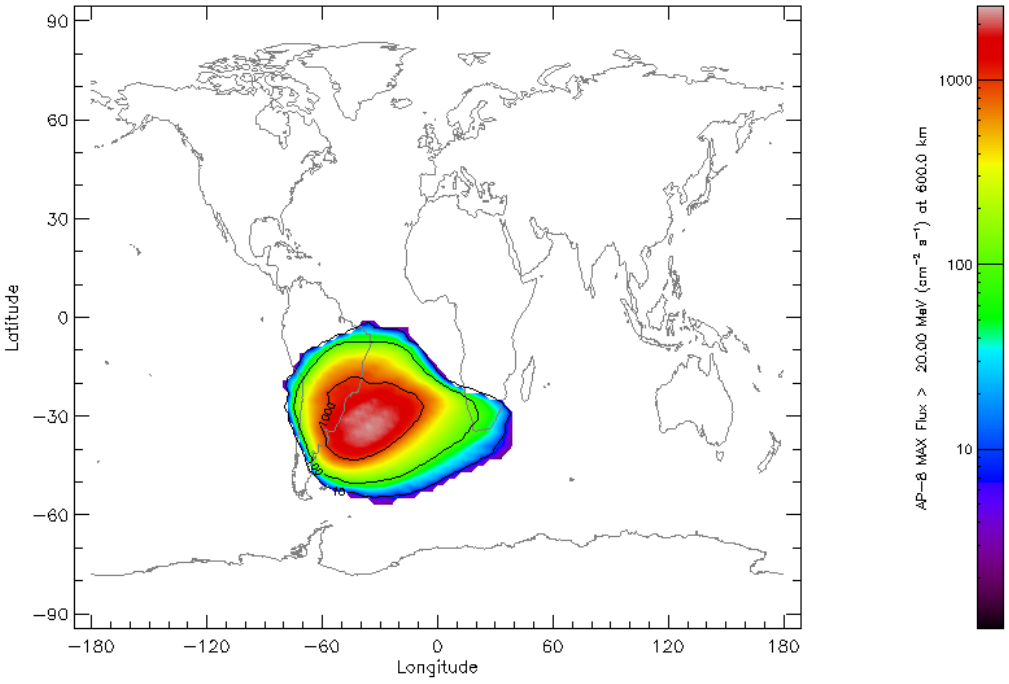

Figure 6.17: >20MeV Proton flux at maximum in the 600km orbit

At an altitude of 600km Earth's magnetic field still greatly protects the satellite from solar flare particles and cosmic ray effects in comparison to missions targeting the geo-synchronous belts. The primary sources of ionizing radiation for the evaluation

orbit are sources from the Van Allen belts and the South Atlantic Anomaly (SAA). The effect of the SAA on proton flux can be seen in figure 6.17 where the integral flux of protons greater than 20MeV can be seen overlapped on a map of earth. From a combination of the solar panels and aluminum structure there is an equivalent of about 2mm of aluminum shielding reducing the energy of incoming heavy ions, protons, and electrons.

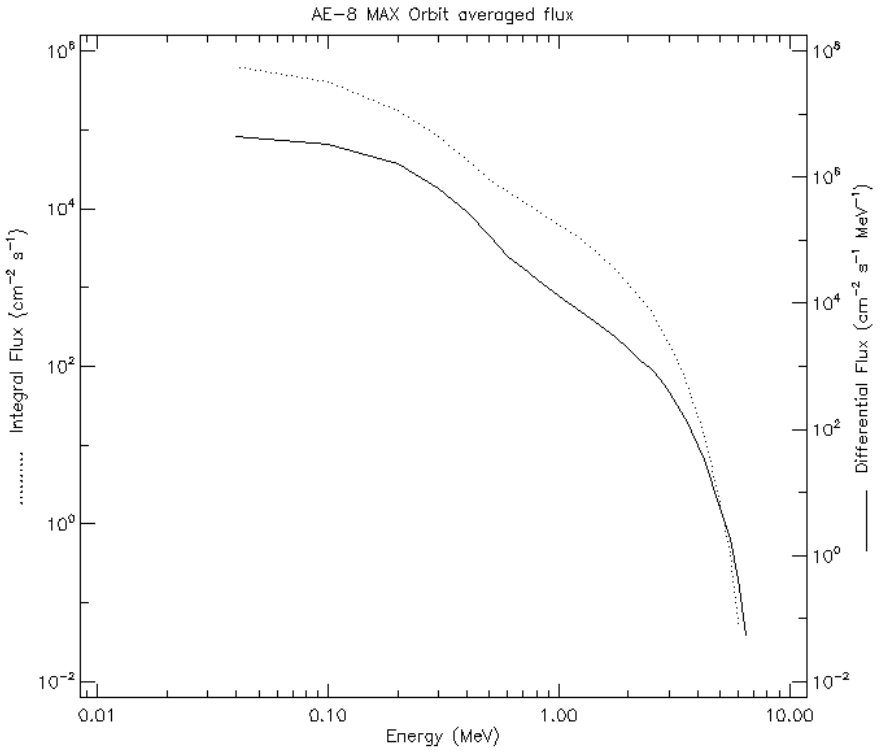

Figure 6.18: Electron flux Power Spectral Density

In figure 6.18, the average electron flux for the targeted evaluation orbit can be seen. The maximum integral flux of electrons greater than 0.04MeV can be seen to be around $8 * 10^5 \frac{1}{cm^2 s}$. For the average flux of protons in the environment figure 6.19 shows an integral value of approximately $9 * 10^5 \frac{1}{cm^2 s}$.

Individual heavy ion fluxes are many orders of magnitude less than electron and proton fluxes but the combination of them add a significant amount to TID and SEE error rates that they need to be accounted for. Shielded heavy ion fluxes evaluated for this orbit can be seen in figure 6.20. The fluxes of each heavy ion from H to Ni in the environment individually can be seen in Appendix B.

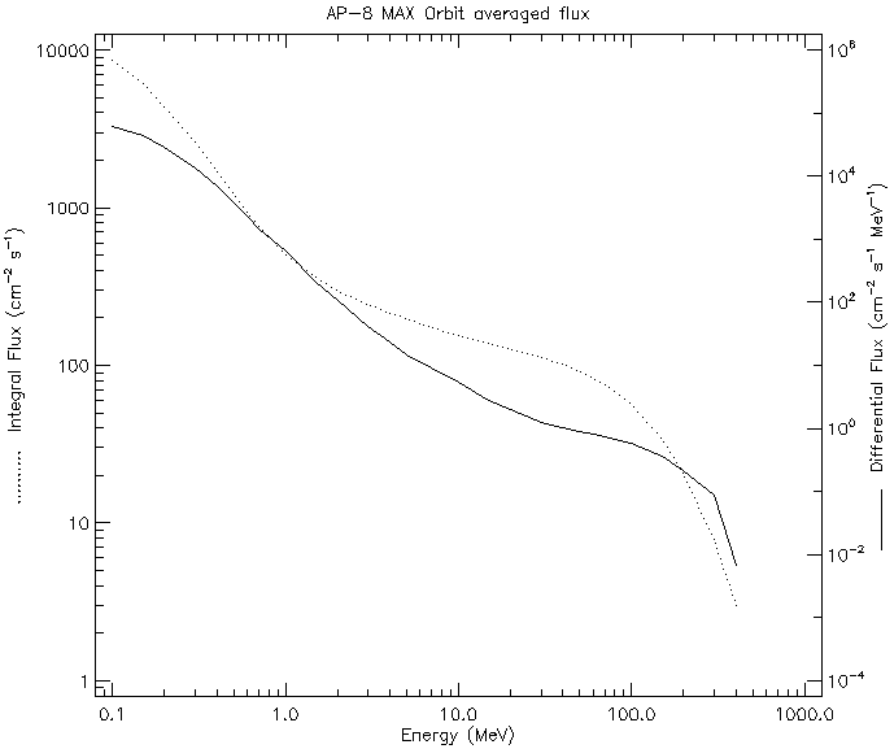

Figure 6.19: Proton flux Power Spectral Density

The total mission dose at two years evaluated by SHIELDDOSE2 [13] for a 2mm shielding thickness, which only calculates dose from electrons and protons, is 2411 rad. The value obtained from SHIELDDOSE2 is close to the total dose evaluated within the reliability model (using the integral of the product of electron and proton shielded flux spectrums with their stopping powers) which results in 2345 rad ignoring heavy ions and 2824 rad considering the heavy ion flux.

Table 6.3: Total mission dose (2 years) vs shielding thickness

Thickness of Aluminum Shielding (mm)	total mission dose (rad)	Solar protons
0.001	1.480E+06	1.480E+06
1.000	5.070E+03	5.070E+03
2.000	2.411E+03	2.411E+03
3.000	1.516E+03	1.516E+03
4.000	1.074E+03	1.074E+03
5.000	8.067E+02	8.067E+02
6.000	6.471E+02	6.471E+02

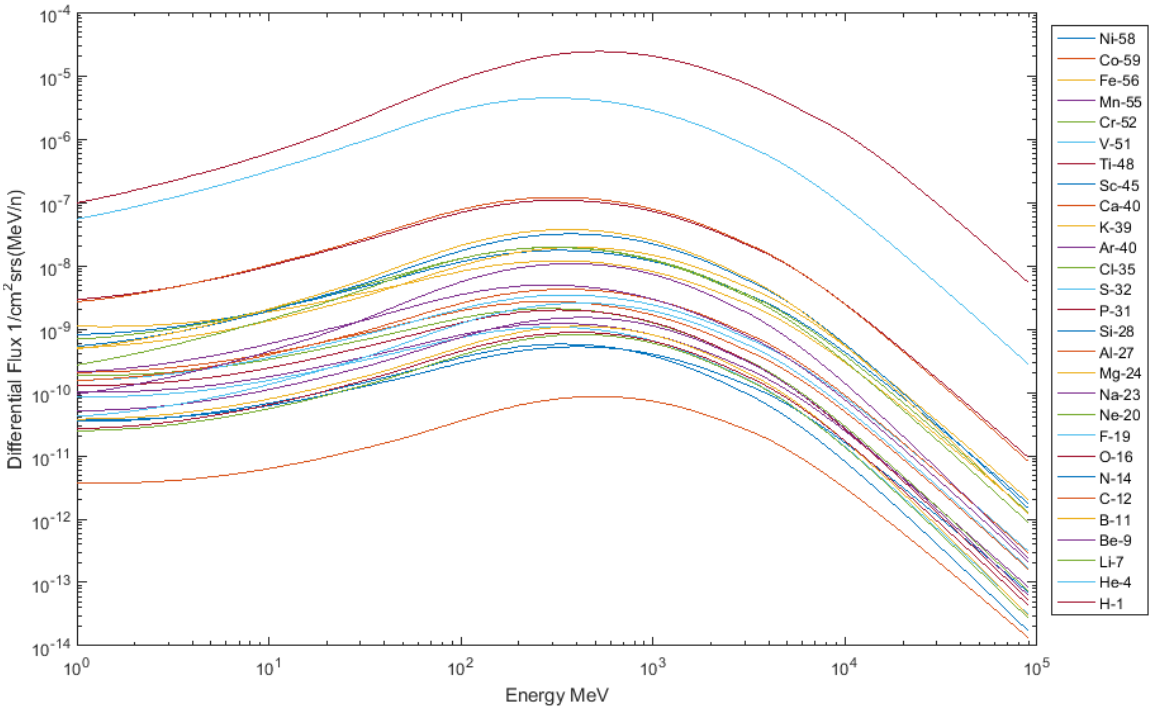

Figure 6.20: Shielded Heavy Ion Differential Flux Spectrum

Calculating Dose Rate and SEE rates

With shielded flux values for protons, electrons, and heavy ions obtained from SPENVIS [13] and linear energy transfer functions for heavy ions from the LET calculator [14] and proton and electron stopping powers from [15] the dose rate $2\pi * \sum_i \int L_i(E) * F_i(E,t) * dE$ was calculated in Matlab for the total ionizing dose failure rate. Additional functions for evaluating $\eta(E, LET_{threshold})$ and K_{TDF} where created.

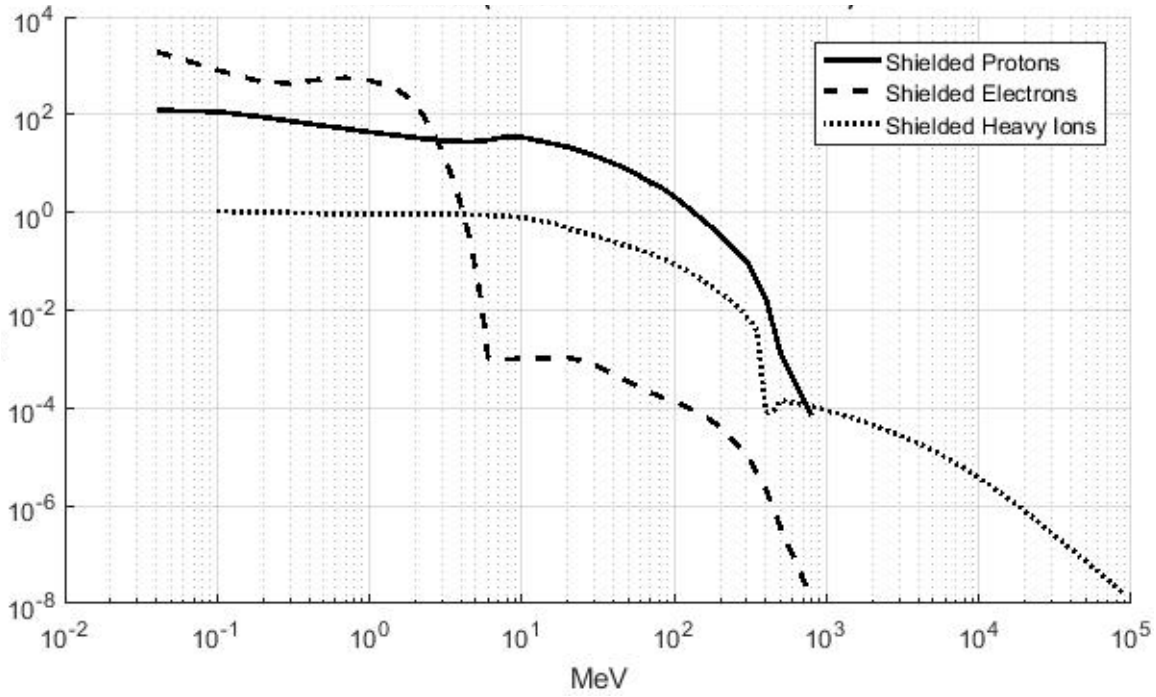

Figure 6.21: Differential Dose Rate of Electron, Proton, and Heavy Ions

For the 600km evaluation orbit targeted by ECOSat-II, the total dose rate has been calculated as $2794.8 MeV cm^2/g$. The total dose rate consists of 474.1912 caused by the sum of heavy ions, 962.1174 from total electrons, and 1358.5 from total protons. The total dose for a two year mission in this environment would then be only 2.82 krad.

$$2\pi * \sum_i \int L_i(E) * F_i(E,t) * dE = 2794.8 MeV cm^2/gs$$

$$2\pi * \sum_i \int L_i(E) * F_i(E,t) * dE = 4.4778x10^{-5} rad/s$$

A function for $\eta(E, LET_{threshold})$ as defined in chapter 3 equation 3.29 was created in Matlab to allow for SEE rate calculations to be made. Using the LET values of heavy ions in silicon the differential flux of each heavy ion such that the LET transferred into the target is greater than $LET_{threshold}$ can be calculated and then integrated. As an example the product of $\eta_i(E, 2.8) * F_i(E)$, ie the fluxes of heavy ions with an LET greater than 2.8 can be seen in figure 6.22.

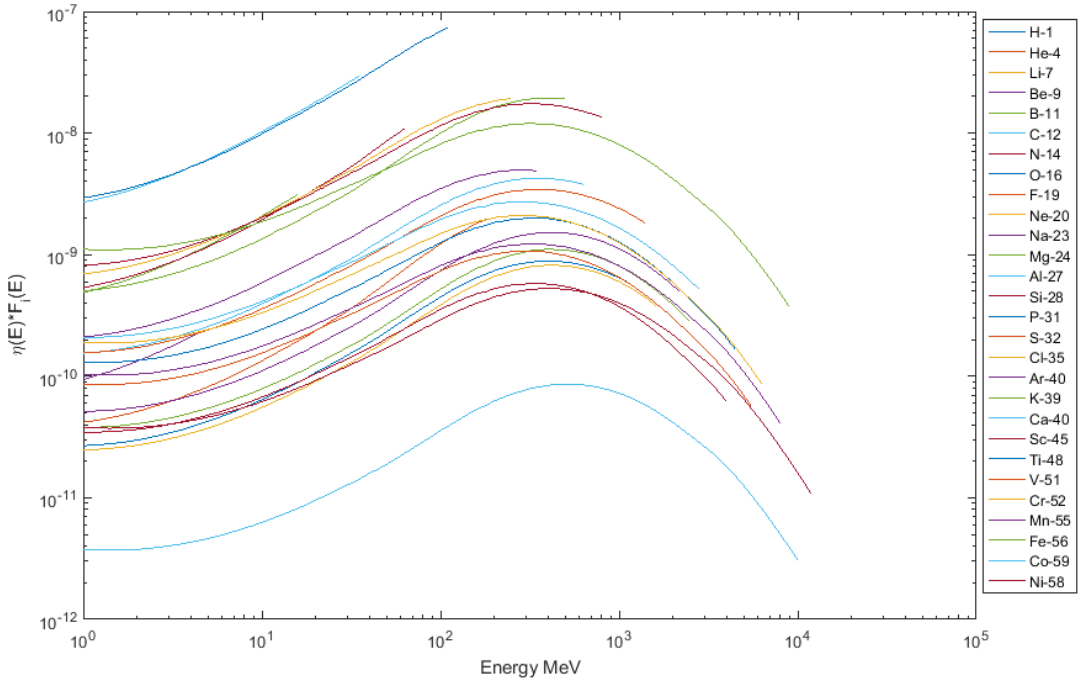

Figure 6.22: Example Heavy Ions for $\eta_i(E, 2.8) * F_i(E)$

This was then used to calculated values of $\int \eta(E, LET_{threshold}) F_(E,t)$.

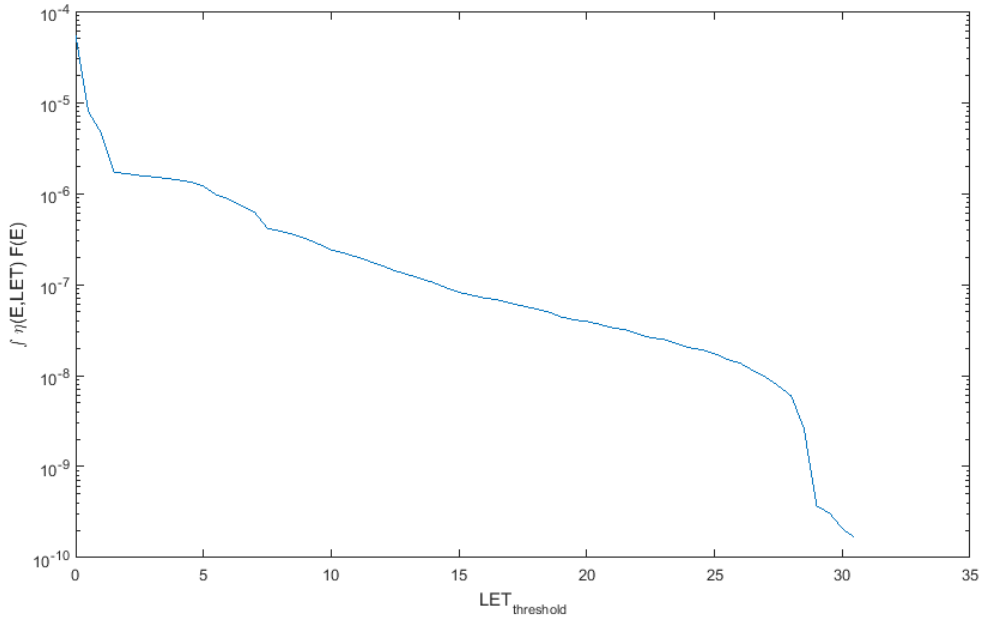

Figure 6.23: $\int \eta_i(E, LET_{threshold})F_i(E_i, t)$ vs $LET_{threshold}$ for evaluation orbit

6.3 ECOSat-2 Command and Data Handling

The ECOSat-2 on board computer (OBC) is responsible for all command and data handling as well as baseband communications. Its three primary functions include Attitude Determination and Control (ADCS), Telemetry monitoring and communications baseband as well as command processing. The overall electrical system design of ECOSat-II implemented a decentralized approach to telemetry and control in which a dedicated micro-controller handles each individual system (Power, Attitude Control, and payload) actuator and sensor gathering as well as low level control loops. To accomplish reliable command and data handling between the on board systems the controller area network (CAN) bus protocol was selected as the physical layer. CAN has many advantages over a centralized network of I2C or SPI sensors and actuators such as built in noise immunity from its differential data lines, robust built in bit error detection and bus arbitration, as well as multi master communications. An additional advantage to the use of the CAN bus physical layer is its wide availability in automotive grade components allowing for selection of higher operating temperature ranges.

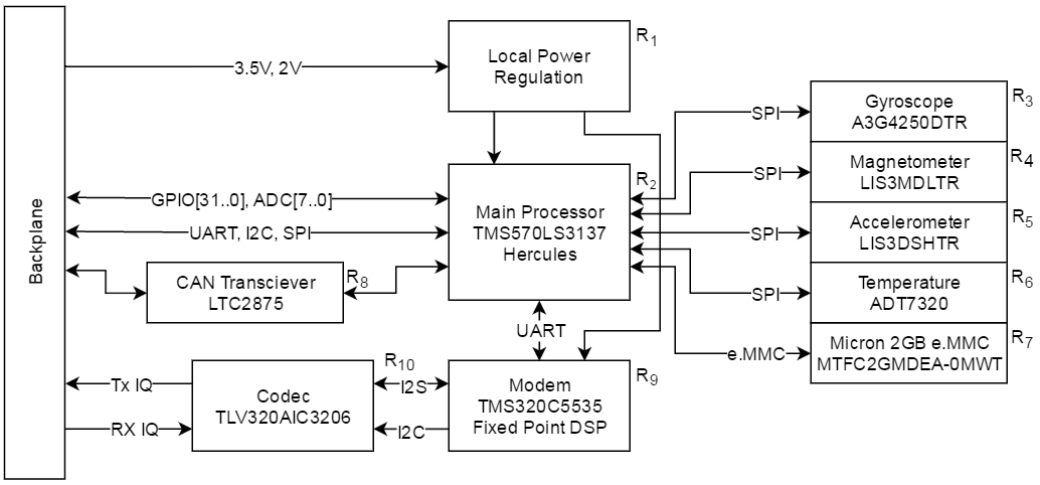

Figure 6.24: ECOSat-2 On Board Command and Data Handling

The on board computer contains 4GB (reduced to 2GB) of on board memory of which 1GB is planned for file storage for firmware, telemetry files, and payload data, 2GB of parity (later reduced to 0.5GB later in this chapter), and 1GB of spare memory as well as OBC firmware such that the OBC can be reprogrammed on air before the RTOS starts through an SPI (simplified e.MMC interface) interface. The

storage of firmware data allows the on board computer to periodically check the flash memory of the decentralized sensor and actuator nodes for single event upsets and reprogram them over CAN bus as well as conduct on air updates of firmware in which updates to firmware code can be loaded onto micro-controllers after launch. A dedicated software defined radio chip is used for baseband communications allowing for flexible modification as well as multiple channels within a limited bandwidth.

The communications functionality uses a TLV320AIC3205 audio frequency front end for transmit (Tx) and receive (Rx) IQ signals which are then routed through the backplane as differential pairs. Software Defined Radio implementation is processed by a TMS320C5535 fixed point digital signal processing (DSP) micro-controller which provides translation from the baseband IQ signals to a standard asynchronous serial communication to the main processor. The main processor uses a TMS570LS3137 Hercules safety line micro-controller which contains built in ECC RAM protection, a redundant CPU core, and a built in self test module. As the majority of communications involve file transfers of some form, the main memory is also important to the reliability of the communications subsystem, a 2GB Micron e.MMC was selected (MTFC2GMDEA-0MWT) as radiation test data is available for Micron flash memories showing a good tolerance between the mission total dose and the tolerance of other Micron memories. Control of amplifiers and front end components as well as the collection of telemetry such as temperature and faults is controlled through CAN bus using the LTC2875 CAN bus transceiver and a micro-controller on the front end subsystem board. The Reliability of the communications functionality within the on board computer is then the product of these components reliability.

Attitude Determination and Control algorithms are processed on the main processor (TMS570LS3137). Attitude determination operates by taking magnetic (LIS3MDLTR), gyroscopic (A3F4250DTR), and acceleration (LIS3DSHTR) sensor data on board the on board command and data board as well as magnetic map data from the main memory to determine current attitude (orientation). Actuation of magnetorquer and potentially momentum or reaction wheels are controlled by sending control values over CAN bus to a dedicated micro-controller that controls the low level control loops and telemetry of the actuators and their control circuitry. The reliability of the attitude determination and control system within the on board command and data handling board is the product of these components reliabilities as no redundancy is present in

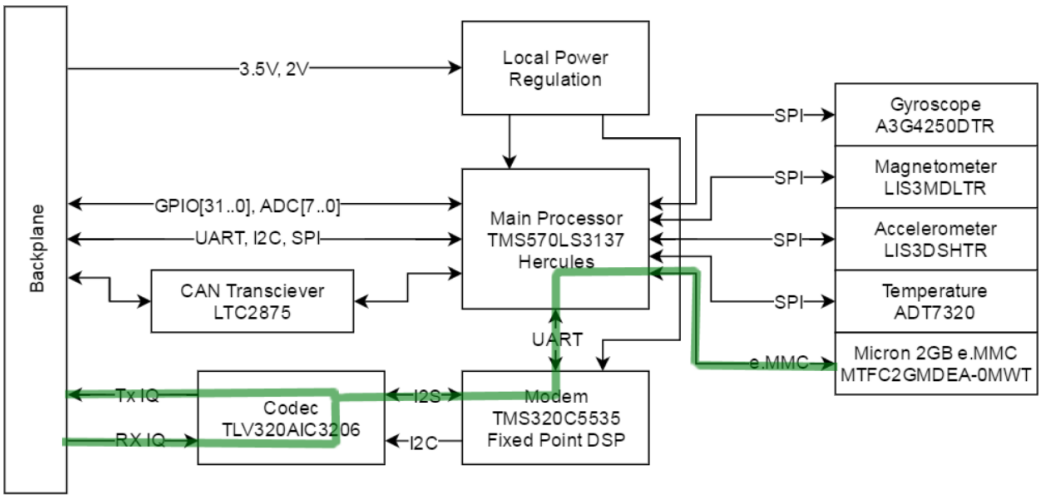

Figure 6.25: Communications components

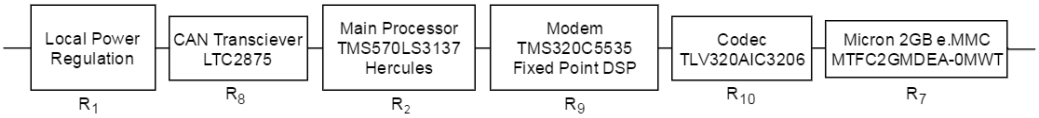

Figure 6.26: Functionally complete Communications reliability

the design until the first reliability analysis has been conducted.

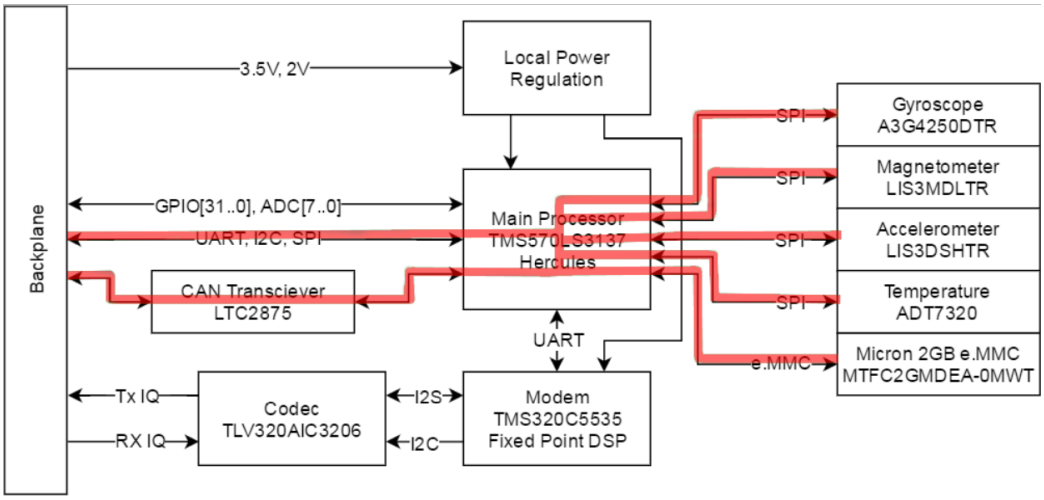

Figure 6.27: Attitude Determination and Control components

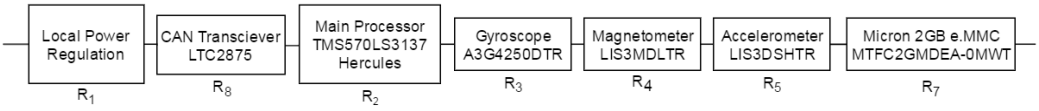

Figure 6.28: Functionally complete ADCS reliability

The telemetry system simply collects satellite telemetry from the ADCS control algorithms and communication statistics internally in the main processor as well as temperatures, battery charge state, and power consumption as well as generation from the rest of the satellite. These values are saved to a comma delimited telemetry file for each day and saved in the main memory.

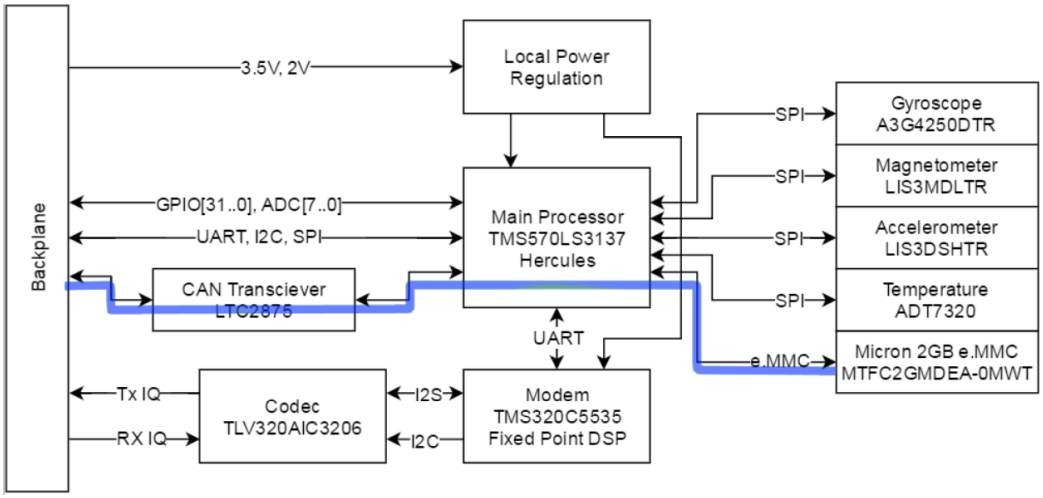

Figure 6.29: Telemetry components

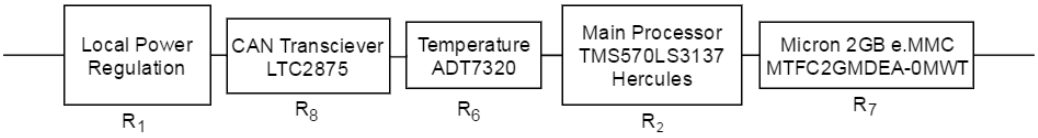

Figure 6.30: Functionally complete Telemetry reliability

6.3.1 Evaluating Hardware Reliability

Reliability of the individual components are calculated in this section using the environmental data simulated earlier and the models discussed in chapter 3. Many of the parameters needed to conduct these evaluations can be obtained directly from companies that develop the components under a non disclosure agreement (NDA). Due to the nature of the non disclosure agreements, specifically the ones for Texas Instruments in which the information can not be released or used in any academic publication, many of the component parameters used in this section are estimations used as an example. For application of these models internally in an organization without the need to publish the results it is important to obtain the more accurate parameters directly from the manufacturers.

From the environmental simulations discussed so far we can calculate a few parameters common to all components on the on board computer PCB. For temperature values our worst case thermal environment is the hot case with an average temperature of 16.419^oC and a thermal cycle of 42.842^oC. For the 600km sun synchronous orbit we get 5558.4 seconds per orbit resulting in 5673 cycles per year, since this is $\leq$ 8760 we can calculate π_n to be 712.6852 from the equations discussed in chapter 3.

Table 6.4: Environment parameters for components on the On Board Computer PCB

Parameter	Note
$(\pi_n)_i$	712.6852
ΔT_i	42.842^oC
t_c	16.419^oC
F_i	See Appendix B
F_p	See Appendix B
F_e	See Appendix B

There are a few other shared component parameters that can be calculated once for all of the components. As all components currently selected use an epoxy package and are mounted to the same FR4 printed circuit board the value of π_a is shared between them all. The shape parameter for total ionizing dose failure is also the same for each component in this example as no component in the design has additional shielding.

$$\pi_a = 0.006(|\alpha_s - \alpha_c|)^1.68 = 1.0519 \tag{6.1}$$

$$\beta = 670.5(D_r)^{-0.408} + 1.942 = 28.2619 \tag{6.2}$$

The Printed Circuit Board

The connections on the printed circuit board as well as the lamination of the layers they are contained on is equally important to the reliability of the systems as the components contained on it, the de-lamination or breakage of a copper trace can cause failure of the system dependent on that signal or power. As discussed in chapter 3, the reliability of the printed circuit board will be treated as a component in series with the rest of the system in terms of reliability dependencies with its reliability modeled as a constant hazard rate ($\beta = 1$) focused on the thermal mechanical effects with no radiation effects.

$$\lambda_{PCB} = 5*10^{-3}\pi_t\pi_c\left[N_t\sqrt{1+\frac{N_t}{S}}+N_p\frac{1+0.1\sqrt{S}}{3}\pi_L\right]\left(1+3*10^{-3}\left[\sum_{i=1}^{j}(\pi_n)_i(\Delta T_i)^{0.68}\right]\right) \tag{6.3}$$

The parameters required can be calculated as seen below. The calculations will use the average temperature of the board obtained from the thermal simulation of 16.419^oC as well as the thermal cycling of 42.842^oC along with the total thermal cycles per year of 5673.

$$\pi_t = e^{17540(\frac{1}{303}-\frac{1}{273+16.419})} = 0.7638 \tag{6.4}$$

$$\pi_c = 0.7\sqrt{Num\ layers} = 0.7\sqrt{6} = 1.7146 \tag{6.5}$$

Estimations of number of vias (signal connections between layers) and holes used by the components result in a value of 250 for N_t and 200 traces for N_p. As every board is standardized to an 80mm by 80mm format for the electrical stack the value S of PCB area in cm^2 is equal to 64. With a planned minimum trace width of 5 mil (thousandth of an inch) the value of π_L can be obtained from [11] as 4. Using all of these parameters and the previously calculated π_n we can find in figure 6.31 that the probability that the PCB has not failed at the planned EOL of 2 years is 98.3%.

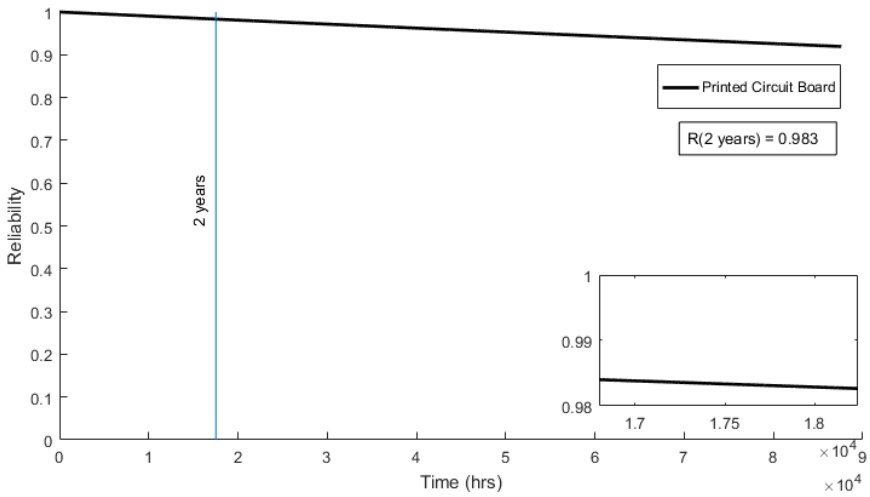

Figure 6.31: Reliability over time of the Printed Circuit board and its connections

Main Processor

The TMS570 Hercules safety line micro-controller has many advantageous features for space applications. The processor operating on a clock frequency up to 180MHz contains 3MB of flash and 256KB of RAM protected from bit errors by a built in ECC peripheral, the memory and RAM can be expanded on an external memory interface for applications that require it. The CPU core hardware has a redundant copy operating in lock step, a method of detecting errors where each instruction is processed by the two CPUs one clock cycle out of phase so that transient errors can be detected and not accepted as correct, this helps add additional protection against soft single event radiation errors from causing software errors. Detection of errors occurs when the result of the two lock step processors is different, when this happens and interrupt occurs and the program counter can be stepped back to re execute the

command. Communications peripherals available allow for direct control of CAN bus, SPI, I2C, and Serial without the need for additional controller interface component.

The main processor is responsible in ECOSat-II for interfacing with sensors and actuators for attitude determination and control systems using SPI, I2C, CAN bus as well as the main memory to access world magnetic map data. It is also responsible for command handling of messages received over the communications system, these messages typically deal with file transfers, for updates of firmware the main processor is also responsible for handling the firmware update procedure in which the new firmware is saved to memory, the satellite is put into safe mode, the system to be updated is then held in reset and the new firmware is loaded over CAN bus with the main processor as the controller. Telemetry is collected over CAN bus and saved into main memory by the Hercules processor as well.

Table 6.5: TMS570LS3137 Package Thermal Parameters [25]

Package	Ambient	Board	Junction
(PQFP) 144 pins	$R\theta_{jA} = 39^oC/W$	$R\theta_{jB} = 26.3^oC/W$	$R\theta_{jC} = 6.7^oC/W$
(PBGA) 337 balls	$R\theta_{jA} = 18.8^oC/W$	$R\theta_{jB} = 14.1^oC/W$	$R\theta_{jC} = 7.1^oC/W$

First we can calculate the thermal parameters π_a π_n and π_t, two of which have already been calculated as the are common to all components. For π_t we need to first find the junction temperature, in table 6.5 we can find the thermal resistance from junction to board which can be used with the average power consumption of the component to find junction temperature, as the component is operating in vacuum and does not have additional heat sinking attached to the package the values of thermal resistance between junction and ambient ($R\theta_{jA}$) and the thermal resistance between junction and package/case ($R\theta_{jC}$) are not used. Average power consumption is estimated at 96mW using the equations in [25]. A 50% duty cycle will be used to estimate the on off cycling of sleep and operating modes of the ADCS and telemetry tasks that will take up the majority of the components time.

$$t_j = t_c + (Power)(R\theta_{jB}) = 16.419 + 0.098(14.1) = 17.801 \tag{6.6}$$

$$\pi_t = e^{(\frac{3480}{328})(\frac{1}{273+17.801})=1.0372} \tag{6.7}$$

The base failure rates λ_1 and λ_2 can be taken from table 16 in [11] while λ_3 can be calculated as follows.

$$\lambda_3 = 0.073 * D^{1.68} = 0.073 * (\sqrt{16mm^2 + 16mm^2})^{1.68} = 13.776 \tag{6.8}$$

Since Radiation data for Texas Instruments components can not be used academically estimated values based on similar components will be used, A Microchip PIC24F256GA110 tested by NASA's Jet Propulsion Lab [26]. Total ionizing dose and single event latch up data from the PIC24F256 will be used as an example for the TMS570, for proper evaluation of the systems reliability the correct data should be obtained from Texas Instruments under their NDA. Total ionizing dose results show a failure level of 10 krad biased and 15-20 krad unbiased (cold spare conditions), in the initial design without added redundancy the biased results need to be used. Testing of single event latch up cross section values show a saturation cross section of approximately $\sigma_{i,\infty,SEU} = 8 * 10^{-3}$ with an ion LET threshold of approximately 2 $MeVcm^2/mg$ and a LET at 25% of saturation of approximately 15 $MeVcm^2/mg$.

What we are interested in is the single event functional interrupt (SEFI) cross section of the device rather than the single event upset (SEU) or single event latch up (SEL) cross sections. We can use the results from SEU or SEL data though to estimate the cross section of SEFI for the component. From the results of ESA's report "TID Influence on the SEE sensitivity of Active EEE" [27] it can be seen the cross section of SEFI events are typically on the range of 10^-4 to 10^-6 smaller than the values of SEL and SEU cross sections. Therefor from the value of $\sigma_{i,\infty,SEU} = 8 * 10^{-3}$ we will use $\sigma_{i,\infty} = 8 * 10^{-7}$ as the saturation cross section, this lower value will be used to calculate the proton cross section.

The value of K_{TDF} calculated from 10krad first transfers the units to MeV resulting in a total dose factor of $6.2415 * 10^{11}$, using the previously computed value for β the scaling parameter K_{TDF} can be calculated as follows.

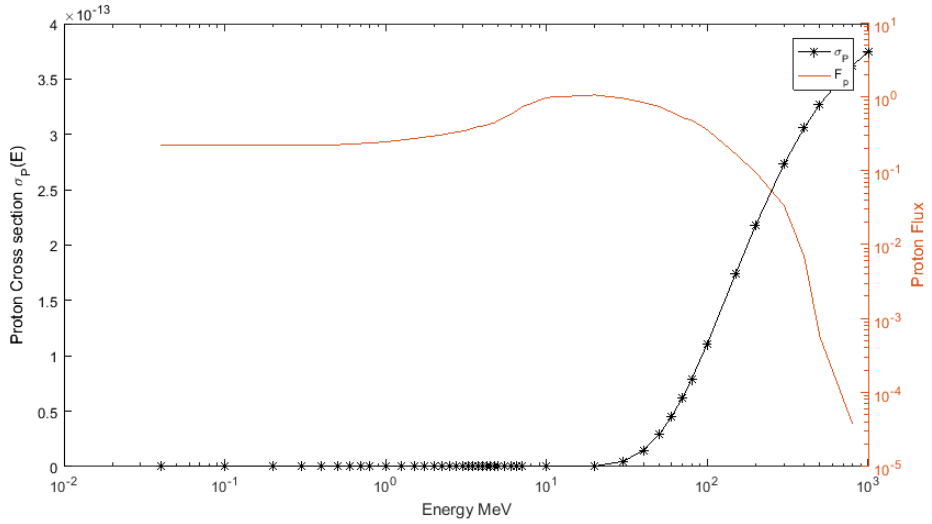

Figure 6.32: Proton Cross Section calculated for the TMS320C25 [28] Data

$$K_{TDF} = \frac{28.2619(-ln(0.05))^{28.2619}}{6.2415 * 10^{11}} = 4.4796 * 10^{-9} \tag{6.9}$$

A summary of the component parameters used to calculate the component reliability for the TMS570LS3137 can be seen in table 6.6. These parameters are used by the matlab functions listed in appendix D to generate reliability versus time data for Thermal mechanical, Single Event Effect, Total Ionizing Dose as well as total (product of TM,SEE and TID).

Table 6.6: Hercules Reliability parameters

Parameter	Note
λ_1	$3.4 * 10^{-6}$
λ_2	1.7
α	2014 - 1998 = 16
N	10^8
$(\pi_t)_i$	1.0372
π_a	1.0519
λ_3	13.776
π_I	0
λ_{EOS}	0
D_{TID}	10krad
$\sigma_{i,\infty}$	$8 * 10^{-7}$
$LET_{threshold,i}$	2 $MeVcm^2/mg$
$LET_{threshold,25\%}$	15 $MeVcm^2/mg$
τ_i	0.5
τ_{on}	0.5
τ_{off}	0.5

Matlab code used for simulation and computation of reliability models can be seen in appendix D. These models resulted in a reliability of 0.985 for the TMS570LS3137 by itself at the end of the 2 year planned mission in the 600km sun synchronous target orbit discussed in the environment modeling section.

Main Memory

The main memory is implemented by a 2GB e.MMC by Micron (MTFC2GMDEA-0MWT) [29]. The memory package is a 156 ball BGA package with dimensions 11.5mm x 13mm. The memory interface allows for single data line control over SPI or for larger data bus widths of 4 or 8 to be used with an MMC interface up to 52MHz clock speed. The reliability of data stored within the memory will be discussed later in this chapter, first the hardware reliability will be determined.

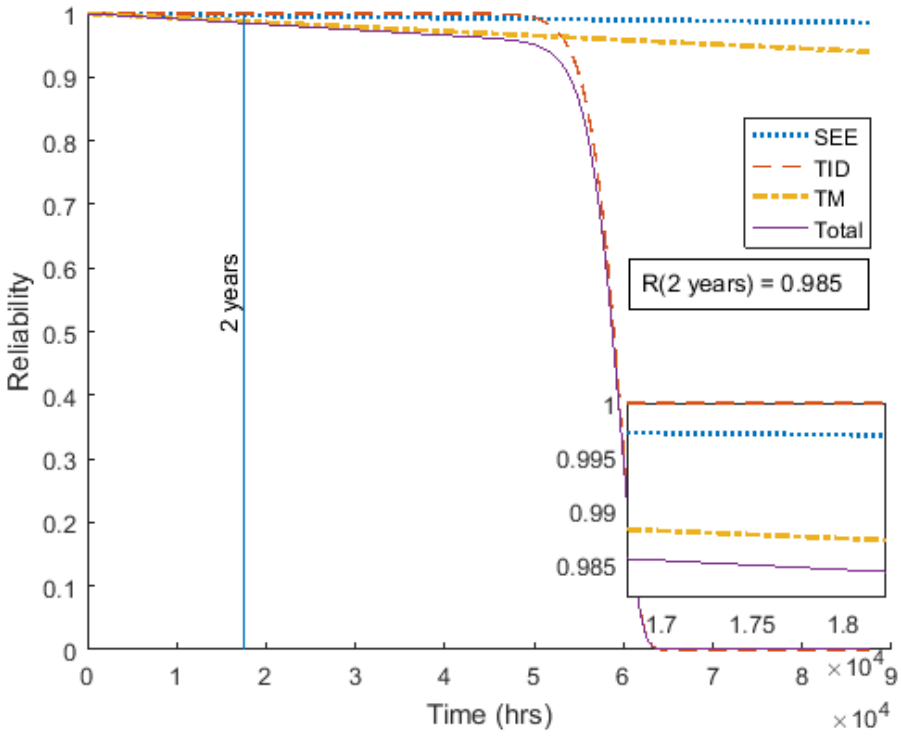

Figure 6.33: Reliability over time of the Hercules TMS570LS3137

First we can calculate the thermal parameters π_a π_n and π_t, two of which have already been calculated as the are common to all components. Since the thermal resistance between junction and board is not specified in the available data sheet, the thermal resistance can be calculated from the number of balls S using the equation in table 12 of [11].

$$R\Theta_{jB} = 0.4(6.6 + \frac{1.1 * 10^6}{S^2}) = 0.4(6.6 + \frac{1.1 * 10^6}{156^2}) = 20.72^oC/W \tag{6.10}$$

Assuming a 10% access time based on payload coverage and telemetry rates currently planned the memory will consume 23.1mW (for 70mA @ 3.3V active, 110uA @ 3.3V standby, 10% duty) resulting in a junction temperature of 16.898^oC.

$$t_j = t_c + (Power)(R\theta_{jB}) = 16.419 + 0.0231(20.72) = 16.898 \tag{6.11}$$

$$\pi_t = e^{(\frac{3480}{328})(\frac{1}{273+16.898})=1.0373} \tag{6.12}$$

The base failure rates λ_1 and λ_2 can be taken from table 16 in [11] while λ_3 can be calculated as follows. The value of N for flash memory is calculated as number of programmable points or blocks in the case of the Micron flash MMC this is per byte resulting in a value of N of $2 * 10^9$.

$$\lambda_3 = 0.073 * D^{1.68} = 0.073 * (\sqrt{11.5mm^2 + 13mm^2})^{1.68} = 8.823 \tag{6.13}$$

While radiation data of the 2GB memory is unavailable, TID and SEE testing of similar flash memories made by Micron for 4Gb, 8Gb, and 16Gb flash memory sizes has been conducted [30] [31] [32]. Test results of the previously mentioned components show fairly similar results with approximate total ionizing dose failure levels of 75krad and SEFI cross sections per device of approximately $3 * 10^{-7} cm^2$ with a LET threshold of $9 MeV cm^2/mg$ and an LET at 25% of saturation cross section of approximately $30 MeV cm^2/mg$.

The value of K_{TDF} calculated from 75krad first transfers the units to MeV resulting in a total dose factor of $4.6811 * 10^{12}$, using the previously computed value for β the scaling parameter K_{TDF} can be calculated as follows.

$$K_{TDF} = \frac{28.2619(-ln(0.05))^{28.2619}}{4.6811 * 10^{12}} = 6.2764 * 10^{-12} \tag{6.14}$$

A summary of the component parameters used to calculate the component reliability for the 2GB Micron e.MMC can be seen in table 6.7, these parameters are passed into Matlab code that provides reliability versus time data for Thermal mechanical, Single Event Effect, Total Ionizing Dose as well as total (product of TM,SEE and

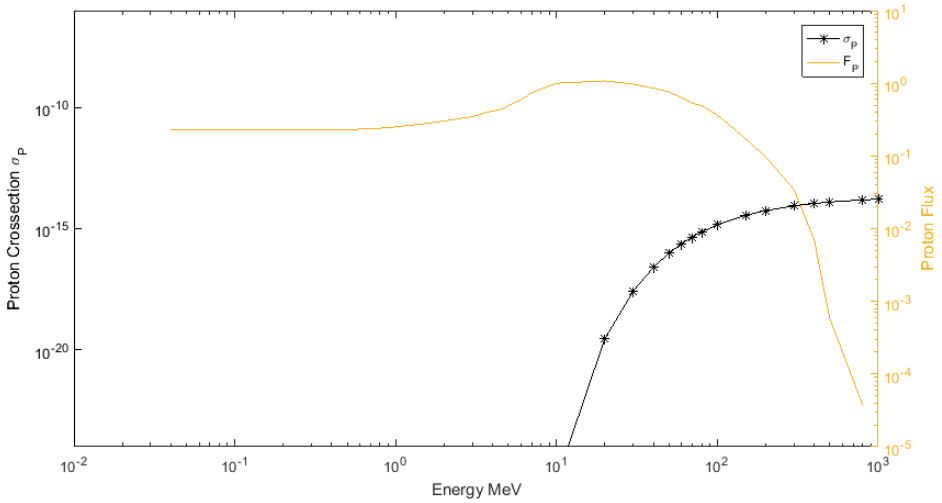

Figure 6.34: Proton Cross Section calculated for Micron Flash Memory TID).

Table 6.7: Micron Reliability parameters

Parameter	Note
λ_1	$2.6 * 10^{-7}$
λ_2	34
α	2015 - 1998 = 17
N	$2 * 10^9$
$(\pi_t)_i$	1.0373
π_a	1.0519
λ_3	8.823
π_I	0
λ_{EOS}	0
D_{TID}	75krad
$\sigma_{i,\infty}$	$3 * 10^{-7} cm^2$
$LET_{threshold,i}$	$9\ MeVcm^2/mg$
$LET_{threshold,25\%}$	$30\ MeVcm^2/mg$
τ_i	0.1
τ_{on}	0.1
τ_{off}	0.9

Matlab code used for simulation and computation of reliability models can be seen in appendix D. These models resulted in a reliability of 0.993 for the 2GB Micron Memory by itself at the end of the 2-year planned mission in the 600km sun synchronous target orbit discussed in the environment modeling section.

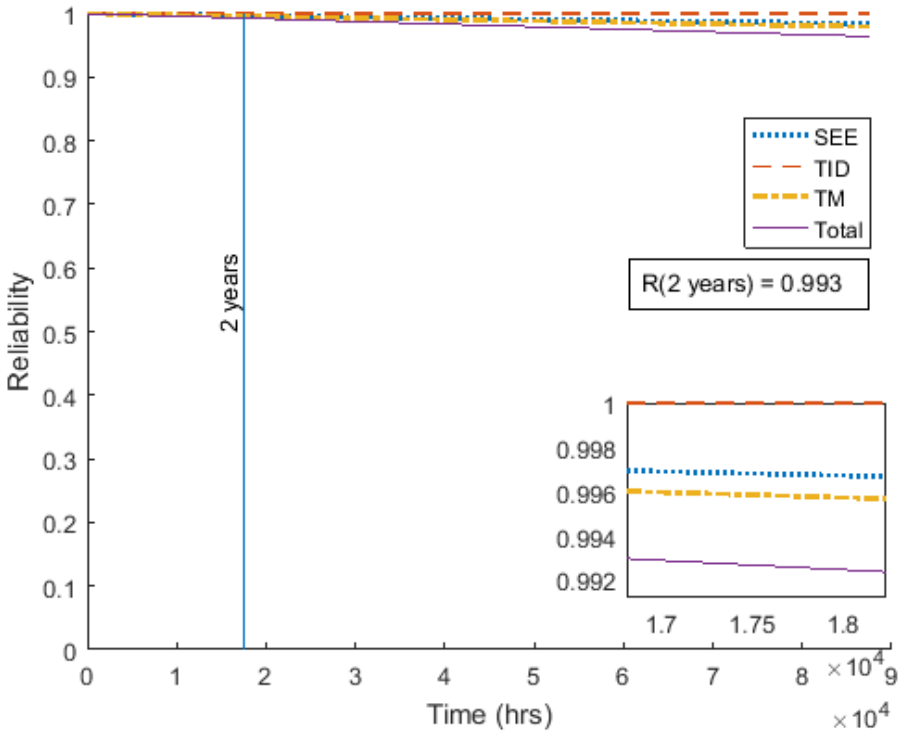

Figure 6.35: Reliability over time of the Micron MTFC2GMDEA-0MWT

CAN Bus

A Linear Technologies LTC2875 High Speed CAN Bus transceiver is used to translate the differential shared CAN bus signal lines spread throughout the satellite electrical bus to logic level I/O for the main processor to receive and transmit over. The LTC2875 allows for up to 4MHz baud rates and features $\pm 60V$ input voltage protection, 25KV ESD protection low power standby modes as well as operating temperature ranges in the military grade ($-55^oCto125^oC$) [33]. ECOSat-II will use the 3mm by 3mm DFN package.

First we can calculate the thermal parameters π_a π_n and π_t, two of which have

already been calculated as the are common to all components. From linear Technologies Package Thermal Resistance Table reference [34] the $R\Theta_{jB} = 5.5$ Assuming a 2% Duty cycle based on a 1MHz baud rate bus and the planned telemetry rate the LTC2875 CAN transceiver will consume 8.59mW without using the shut down power mode.

$$t_j = t_c + (Power)(R\theta_{jB}) = 16.419 + 0.00859(5.5) = 16.466 \tag{6.15}$$

$$\pi_t = e^{(\frac{3480}{328})(\frac{1}{273+16.466})=1.0373} \tag{6.16}$$

For mixed linear and digital circuits λ_1 and λ_2 can be taken from table 16 in [11] as $2.7 * 10^{-3}$ and 20 respectively. The value of λ_3 can be calculated as follows.

$$\lambda_3 = 0.024 * D^{1.68} = 0.024 * (\sqrt{3mm^2 + 3mm^2})^{1.68} = 0.272 \tag{6.17}$$

Since the LTC2875 is a relatively new component, open radiation data is not yet available. To estimate the reliability of the CAN transceiver, radiation data of a similar transceiver for RS-485 communications (same physical layer as CAN bus) from Analog Devices (ADM3485) will be used. Radiation testing of the similar component resulting in a total ionizing dose starting from 9krads (first parameter out of specification) to 20krads (functional failure of the component) for reliability of the component we will use the TID value that resulted in functional failure [35]. The results for single event latch up testing showed no events up to a linear energy transfer of 55.9 $MeVcm^2/mg$, this will result in a failure rate of 0 from single event effects.

To value of K_{TDF} calculated from 20krad first transfers the units to MeV resulting in a total dose factor of $1.2483 * 10^{12}$, using the previously computed value for β the scaling parameter K_{TDF} can be calculated as follows.

$$K_{TDF} = \frac{28.2619(-ln(0.05))^{28.2619}}{1.2483 * 10^{12}} = 1.8735 * 10^{-11} \tag{6.18}$$

A summary of the component parameters used to calculate the component reliability for the CAN bus transceiver can be seen in table 6.8, these parameters are passed into Matlab code that provides reliability versus time data for Thermal mechanical, Single Event Effect, Total Ionizing Dose as well as total (product of TM,SEE and TID).

Table 6.8: LTC2875 Reliability parameters

Parameter	Note
λ_1	$2.7 * 10^{-3}$
λ_2	20
α	2015 - 1998 = 17
N	200
$(\pi_t)_i$	1.0373
π_a	1.0519
λ_3	0.272
π_I	0
λ_{EOS}	0
D_{TID}	20krad
$\sigma_{i,\infty}$	0
$LET_{threshold,i}$	55.9 $MeVcm^2/mg$
$LET_{threshold,25\%}$	55.9 $MeVcm^2/mg$
τ_i	0.02
τ_{on}	0.02
τ_{off}	0.98

Matlab code used for simulation and computation of reliability models can be seen in appendix D. These models resulted in a reliability of approximately 1 for the CAN transceiver by itself at the end of the 2-year planned mission in the 600km sun synchronous target orbit discussed in the environment modeling section.

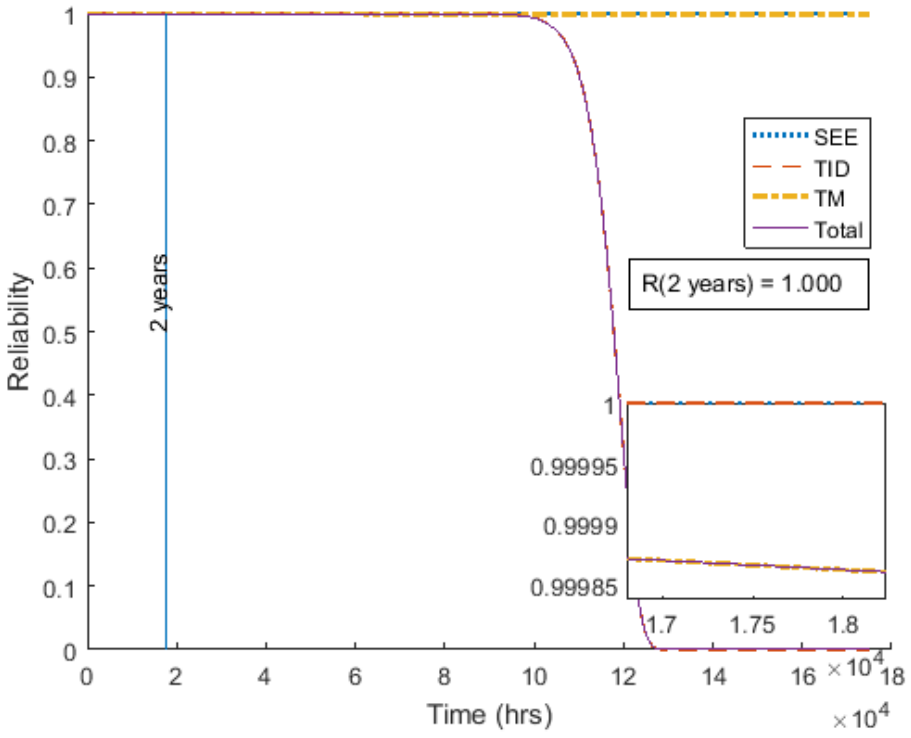

Figure 6.36: Reliability over time of the Linear Technologies LTC2875

Communications Processor

The Texas Instruments TMS320C5535 fixed point DSP is responsible for processing the software defined radio algorithms that take serial data from the main processor for down link, process relay channels in the amateur radio sub channels and decode and synchronize data in the uplink sub channel, the digital wave forms of these are output and input to the DSP as baseband (audio frequency) IQ signals through the codec which converts them to analog signals that can be mixed up to the 2m band for downlink and down from the 70cm band for uplink. There are three channels within a 192kHz bandwidth, one data channel for command and telemetry, one FM voice relay channel for OSCAR operations, and one linear relay channel for OSCAR operations [36]. The TMS320C55x family of DSP processors contains dedicated fixed point arithmetic units designed to increase the efficient of signal processing instructions allowing for up to 200 million Multiply-Accumulate per second. In addition to the dedicated arithmetic for digital signal processing, the processor also contains a Fast Fourier Transform (FFT) co-processor and 64kB dual access RAM for buffers

and a 256kB RAM for software dynamic memory.

Table 6.9: TMS320C55xx Package Thermal Parameters [37]

Package	Ambient	Board	Junction
(PBGA) 144 balls	$R\theta_{jA} = 50^oC/W$	$R\theta_{jB} = 38^oC/W$	$R\theta_{jC} = 12.53^oC/W$

To determine reliability of the component first we can calculate the thermal parameters π_a π_n and π_t, two of which have already been calculated as the are common to all components. For π_t we need to first find the junction temperature, in table 6.9 we can find the thermal resistance from junction to board which can be used with the average power consumption of the component to find junction temperature, as the component is operating in vacuum and does not have additional heat sinking attached to the package the values of thermal resistance between junction and ambient ($R\theta_{jA}$) and the thermal resistance between junction and package/case ($R\theta_{jC}$) are not used. A 100% duty cycle will be used to estimate the on off cycling as the receive chain will always need to be left on requiring constant processing, it is possible to use geo fencing to turn off the Rx chain over the poles and oceans but this is not a current design specification. Assuming a 100MHz clock speed the typical power consumption expected during active mode is 28.6 mW running on a 1.3V core voltage.

$$t_j = t_c + (Power)(R\theta_{jB}) = 16.419 + 0.0286(38) = 17.5058 \tag{6.19}$$

$$\pi_t = e^{(\frac{3480}{328})(\frac{1}{273+17.801})=1.0372} \tag{6.20}$$

The base failure rates λ_1 and λ_2 can be taken from table 16 in [11] while λ_3 can be calculated as follows for a ball grid array package.

$$\lambda_3 = 0.073 * D^{1.68} = 0.073 * (\sqrt{12mm^2 + 12mm^2})^{1.68} = 8.496 \tag{6.21}$$

as the Radiation data for Texas Instruments components can not be used academ-

ically, estimated values based on similar components will be used. A Texas Instruments TMS320C25 using a similar arm core but on a different process was tested by the European Space Agency [28], values of total ionizing dose and cross sections will be used as an example for the TMS320C5535. Results from total ionizing dose show a failure level of approximately 6.5krad. To obtain the values for ion cross section, LET threshold, and LET at 25% of the saturation cross section we must fit the SEE testing results to the equation 6.22 [38] resulting in a LET threshold of approximately 3.5 $MeVcm^2/mg$, LET at 25% of 5.2$MeVcm^2/mg$, and a $\sigma_{i,\infty,SEU} = 7.38 * 10^{-3}$ for SEUs within the processor.

$$\sigma(E) = \sigma_{\infty}(1 - exp(-\frac{E - LET_{thresh}}{W}^{s})) \tag{6.22}$$

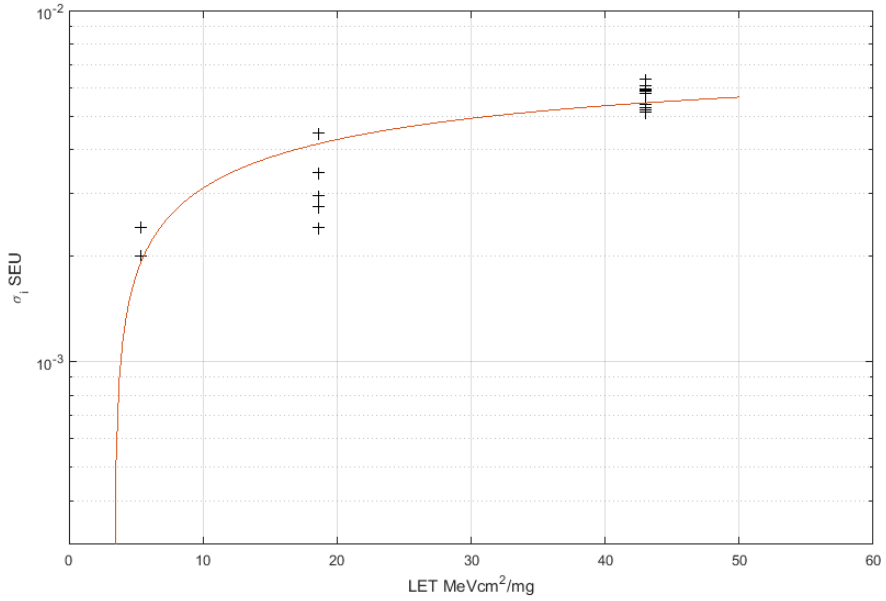

Figure 6.37: Fit of Cross Section data for the TMS320C25 [28]

What we are interested in is the single event functional interrupt (SEFI) cross section of the device rather than the single event upset (SEU) or single event latch up (SEL) cross sections. We can use the results from SEU or SEL data though to estimate the cross section of SEFI for the component. From the results of ESA's report "TID Influence on the SEE sensitivity of Active EEE" [27] it can be seen the cross section of SEFI events are typically on the range of 10^-4 to 10^-6 smaller than the values of

SEL and SEU cross sections. Therefor from the value of $\sigma_{i,\infty,SEU} = 7.38 * 10^{-3}$ we will use $\sigma_{i,\infty} = 7.38 * 10^{-7}$ as the saturation cross section, this lower value will be used to calculate the proton cross section.

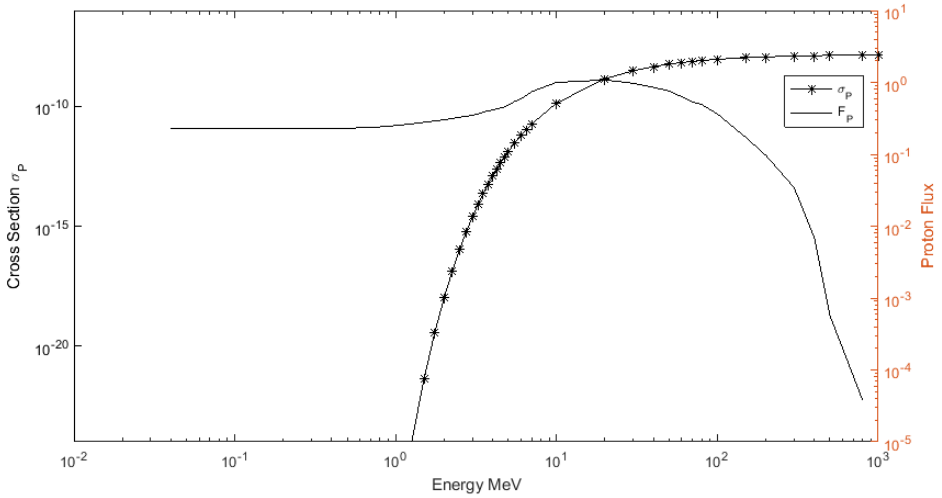

Figure 6.38: Proton Cross Section calculated for the TMS320C25 [28] Data

To value of K_{TDF} calculated from 6.5krad first transfers the units to MeV resulting in a total dose factor of $4.0570 * 10^{11}$, using the previously computed value for β the scaling parameter K_{TDF} can be calculated as follows.

$$K_{TDF} = \frac{28.2619(-ln(0.05))^{28.2619}}{4.0570 * 10^{11}} = 6.8917 * 10^{-9} \tag{6.23}$$

A summary of the component parameters used to calculate the component reliability for the TMS320C55x DSP can be seen in table 6.10, these parameters are passed into Matlab code that provides reliability versus time data for Thermal mechanical, Single Event Effect, Total Ionizing Dose as well as total (product of TM,SEE and TID).

Table 6.10: TMS320C55x DSP Reliability parameters

Parameter	Note
λ_1	$3.4 * 10^{-6}$
λ_2	1.7
α	2015 - 1998 = 16
N	10^8
$(\pi_t)_i$	1.0372
π_a	1.0519
λ_3	8.496
π_I	0
λ_{EOS}	0
D_{TID}	6.5krad
$\sigma_{i,\infty}$	$7.38 * 10^{-7}$
$LET_{threshold,i}$	3.5 $MeVcm^2/mg$
$LET_{threshold,25\%}$	5.2 $MeVcm^2/mg$
τ_i	1
τ_{on}	1
τ_{off}	0

Matlab code used for simulation and computation of reliability models can be seen in appendix D. These models resulted in a reliability of 0.952 for the DSP processor by itself at the end of the 2-year planned mission in the 600km sun synchronous target orbit discussed in the environment modeling section.

Baseband Codec

The TLV320AIC3206 stereo codec from Texas Instruments is an ultra-low power audio front end responsible for converting digital signals to audio analog signals and audio to digital for the IQ. The TLV320 contains a digital to analog converter (DAC) capable of output frequencies from mono 8kHz up to stereo 192kHz, for SDR applications the stereo mode is used with the left audio channel allocated to the in phase signal and right audio channel allocated to the quadrature signal. Similarly, for the

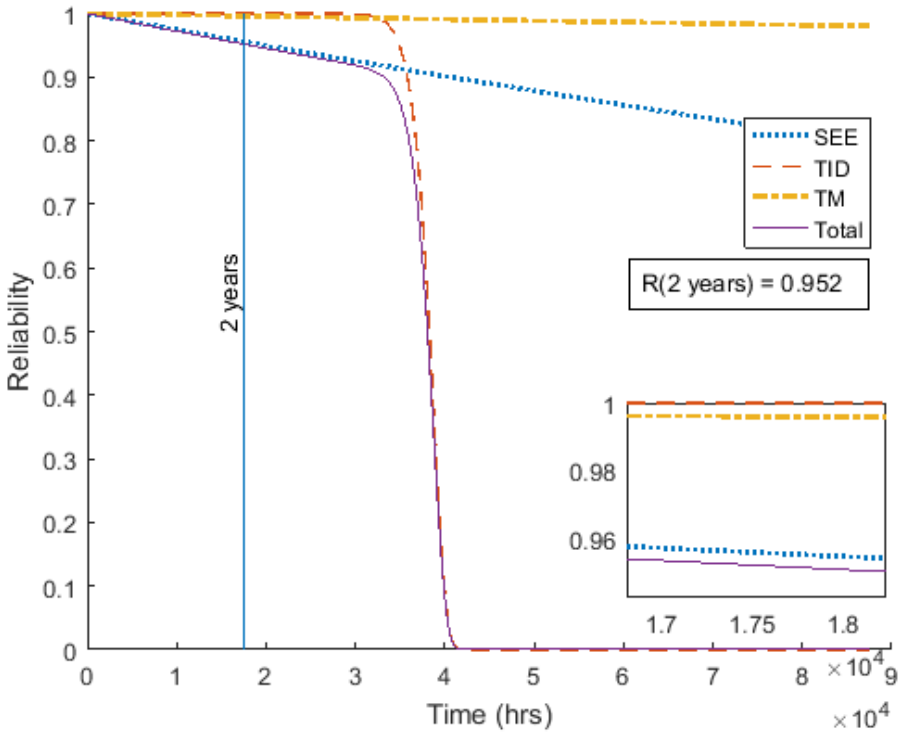

Figure 6.39: Reliability over time of the Texas Instruments TMS320C5535

uplink channel, the TLV320 contains an analog to digital converter (ADC) capable of the same frequency ranges of 8kHz to 192kHz and features optional built in DSP filters [37].

Table 6.11: TLV320AIC3206 Package Thermal Parameters [37]

Package	Board
(QFN) 40 pins	$R\theta_{jB} = 6.1^oC/W$
(DSGBA) 42 balls	$R\theta_{jB} = 7.7^oC/W$

Based on the expected usage (100% receive, 25% transmit duty cycles) the codec will consume an average of 24.725mW, using the QFN package the thermal mechanical parameters can be calculated starting with the thermal parameters. Given that the receive chain must remain on at all times as a requirement of the system the duty cycle used for the working time ratio for reliability will be used as 100%.

$$t_j = t_c + (Power)(R\theta_{jB}) = 16.419 + 0.024725(6.1) = 16.570 \tag{6.24}$$

$$\pi_t = e^{(\frac{3480}{328})(\frac{1}{273+16.570})=1.0373} \tag{6.25}$$

The base failure rates λ_1 and λ_2 can be taken from table 16 in [11] while λ_3 can be calculated as follows for a peripheral connection package based on package diameter.

$$\lambda_3 = 0.048 * D^{1.68} = 0.048 * (\sqrt{3.5mm^2 + 3.5mm^2})^{1.68} = 0.705 \tag{6.26}$$

Much like the other Texas Instruments components discussed so far in this example radiation data can be requested from Texas Instruments under a non disclosure agreement, the chip is relatively new and has yet to be tested independently. For this example, test result data from a Texas Instruments TLV5618A, an older TI ADC interface will be used. Radiation testing of the TLV5618A [35], with a LET threshold of 8 $MeVcm^2/mg$, SEL saturation cross section of $6 * 10^{-5}cm^2$, and a total dose of approximately 40krad the level that other Texas Instruments ADC digital interfaces begin to have read problems. Tabulated cross section results where not provided so the LET value at which the cross section reaches 25% of its saturation level is not available, a value of 11 $MeVcm^2/mg$ will be used for the example. Much like the other components used in this example the SEL cross section will be related to the SEFI cross section by a factor of 10^{-4}.

A summary of the component parameters used to calculate the component reliability for the baseband codec can be seen in table 6.12, these parameters are passed into Matlab code that provides reliability versus time data for Thermal mechanical, Single Event Effect, Total Ionizing Dose as well as total (product of TM,SEE and TID).

Table 6.12: TLV320AIC3206 codec Reliability parameters

Parameter	Note
λ_1	$2.7 * 10^{-4}$
λ_2	20
α	2015 - 1998 = 16
N	10^8
$(\pi_t)_i$	1.0373
π_a	1.0519
λ_3	0.705
π_I	0
λ_{EOS}	0
D_{TID}	40krad
$\sigma_{i,\infty}$	$6 * 10^{-9}$
$LET_{threshold,i}$	8 $MeVcm^2/mg$
$LET_{threshold,25\%}$	11 $MeVcm^2/mg$
τ_i	1
τ_{on}	1
τ_{off}	0

Matlab code used for simulation and computation of reliability models can be seen in appendix D. These models resulted in a reliability of 0.998 for the codec by itself at the end of the 2-year planned mission in the 600km sun synchronous target orbit discussed in the environment modeling section.

Gyroscope, Magnetic and Accelerometer

The A3G4250DTR is a 3 axis MEMS motion sensor is a three axis digital output gyroscope used to measure angular accelerations for telemetry and assist in attitude determination. The sensor provides a 16 bit output with ±245dps (degrees per second) full scale or approximately 7.5mdps per least significant bit over an SPI interface to the main processor [39]. The component is used in a 16 pin LGA/QFN package measuring 4mm by 4mm and consuming 20.13mW of power assuming constant op-

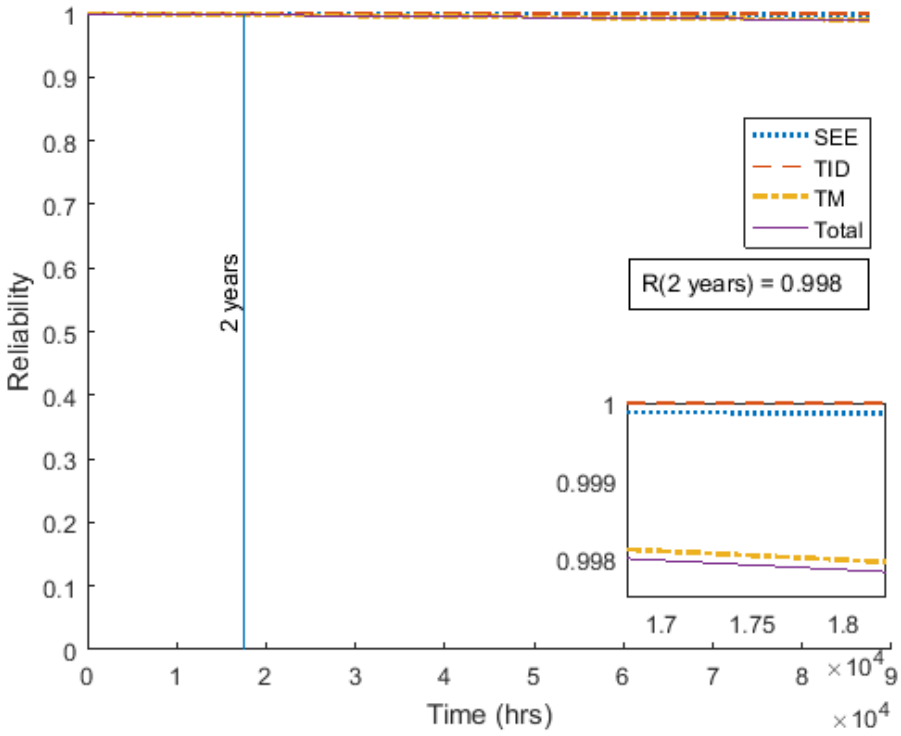

Figure 6.40: Reliability over time of the Texas Instruments TLV320AIG3206

eration. From the thermal package reference [34] the junction to case of $4.5^oC/W$. Much like the previous components parameters for the thermal mechanical reliability of the package will be obtained and summarized in table 6.13.

$$t_j = t_c + (Power)(R\theta_{jB}) = 16.419 + 0.02013(4.5) = 16.509 \tag{6.27}$$

$$\pi_t = e^{(\frac{3480}{328})(\frac{1}{273+16.509})=1.0373} \tag{6.28}$$

Since the LGA package reference from STM is a peripheral connected package the same formula for λ_3 that was used for the codec's QFN package can be used.

$$\lambda_{3,4x4} = 0.048 * D^{1.68} = 0.048 * (\sqrt{4mm^2 + 4mm^2})^{1.68} = 0.882 \tag{6.29}$$

The LIS3DH 3 axis accelerometer is a 16bit, $\pm 2g$ full range ($1 * 10^{-3}g$ per least significant bit) accelerometer used for measuring linear accelerations about the satellite body for use by the attitude determination system. The accelerometer comes in the same 16 pin LGA (QFN) as the A3G4250DTR gyroscope already discussed. Based on expected usage without any sleep periods the accelerometer will only consume approximately 6.6uW when operating at 1Hz on the 3.3V rail, this means the junction temperature at steady state can be approximated as the board temperature and the thermal resistance between junction and board does not have a noticeable effect on the reliability of the component. The LIS3MDL 3 axis magnetometer is capable of down to a full range of ± 4 gauss over a 16bit data register and comes in a 2mm by 2mm 12 pin LGA package. The typical power consumption of the magnetometer is only 0.7mW which will not effect the value of π_t within reasonable rounding.

$$\lambda_{3,2x2} = 0.048 * D^{1.68} = 0.048 * (\sqrt{2mm^2 + 2mm^2})^{1.68} = 0.2753 \tag{6.30}$$

Not many studies have yet been done on the radiation tolerance of specific types of MEMs sensors, the testing that has been done has shown that the MEMs structures themselves experience changes in calibration but no functional failure into the millions of rad total dose caused by increases in electric field near the MEMs structures as charge is deposited in insolation layers [40]. The few components that have been tested show TID values ranging from 10krad to 100krad in which the digital interfaces and/or analog sense circuitry has a functional failure, for this example a value of 20krad will be used, it is important to remember that these values are used as an example of the reliability calculation not as accurate results to be used for ECOSat-II, for the final ECOSat-II analysis data should be obtained under NDA and care taken that results are not published. To properly evaluate the single event functional interrupt rate of the sensor, SEE testing will need to be carried out by the ECOSat team, for this example a SEL cross section of $5 * 10^{-4} cm^2$ will be used with a LET threshold of 10 $MeVcm^2/mg$ and a LET at 25% of saturation cross section of 20 $MeVcm^2/mg$.

Table 6.13: A3G4250DTR, LIS3DH and LIS3MDL Reliability parameters

Parameter	A3G4250DTR	LIS3DH	LIS3MDL
λ_1	$2.7 * 10^{-4}$	$2.7 * 10^{-4}$	$2.7 * 10^{-4}$
λ_2	20	20	20
α	2013 - 1998 = 14	14	14
N	10^8	10^8	10^8
$(\pi_t)_i$	1.0373	1.0373	1.0373
π_a	1.0519	1.0519	1.0519
λ_3	0.882	0.882	0.2753
π_I	0	0	0
λ_{EOS}	0	0	0
D_{TID}	20krad	20krad	20krad
$\sigma_{i,\infty}$	$5 * 10^{-8}$	$5 * 10^{-8}$	$5 * 10^{-8}$
$LET_{threshold,i}$	10 $MeVcm^2/mg$	10 $MeVcm^2/mg$	10 $MeVcm^2/mg$
$LET_{threshold,25\%}$	20 $MeVcm^2/mg$	20 $MeVcm^2/mg$	20 $MeVcm^2/mg$
τ_i	1	1	1
τ_{on}	1	1	1
τ_{off}	0	0	0

Matlab code used for simulation and computation of reliability models can be seen in appendix D. These models resulted in a reliability of 0.999 for the gyroscope, accelerometer, and magnetometer by themselves at the end of the 2-year planned mission in the 600km sun synchronous target orbit discussed in the environment modeling section.

Magnetic and Accelerometer Sensors

The LIS3DH 3 axis accelerometer is a 16bit, $\pm 2g$ full range ($1 * 10^{-3}g$ per least significant bit) accelerometer used for measuring linear accelerations about the satellite body for use by the attitude determination system. The accelerometer comes in the same 16 pin LGA (QFN) as the A3G4250DTR gyroscope discussed in the last section. Based on expected usage without any sleep periods the accelerometer will

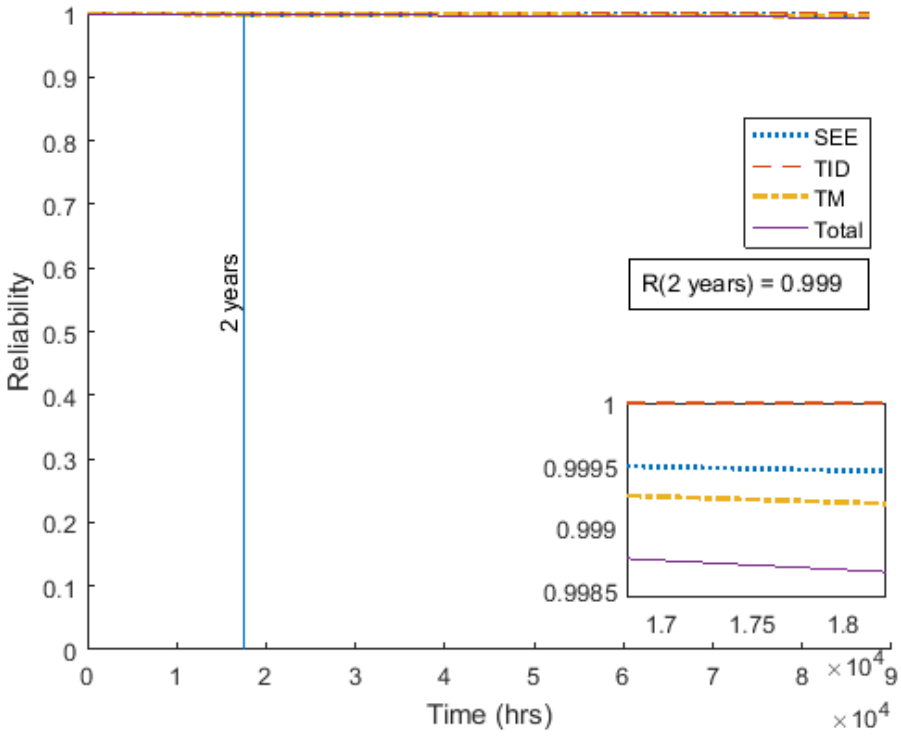

Figure 6.41: Reliability over time of the STM A3G4250DTR Gyroscope

only consume approximately 6.6uW when operating at 1Hz on the 3.3V rail, this means the junction temperature at steady state can be approximated as the board temperature and the thermal resistance between junction and board does not have a noticeable effect on the reliability of the component. The LIS3MDL 3 axis magnetometer is capable of down to a full range of ±4 gauss over a 16bit data register and comes in a 2mm by 2mm 12 pin LGA package. The typical power consumption of the magnetometer is only 0.7mW which will not effect the value of π_t within reasonable rounding.

Local Power Regulation

Power regulation local to the on board command and data handling board consists of two low drop out (LDO) regulators that generate the local 3.3V rail for IO and the 1.8V rail for the TMS570, TLV320, and TMS320 core processors voltages. A fixed 3.3V and fixed 1.8V regulator from the TPS735xx family from Texas Instruments are

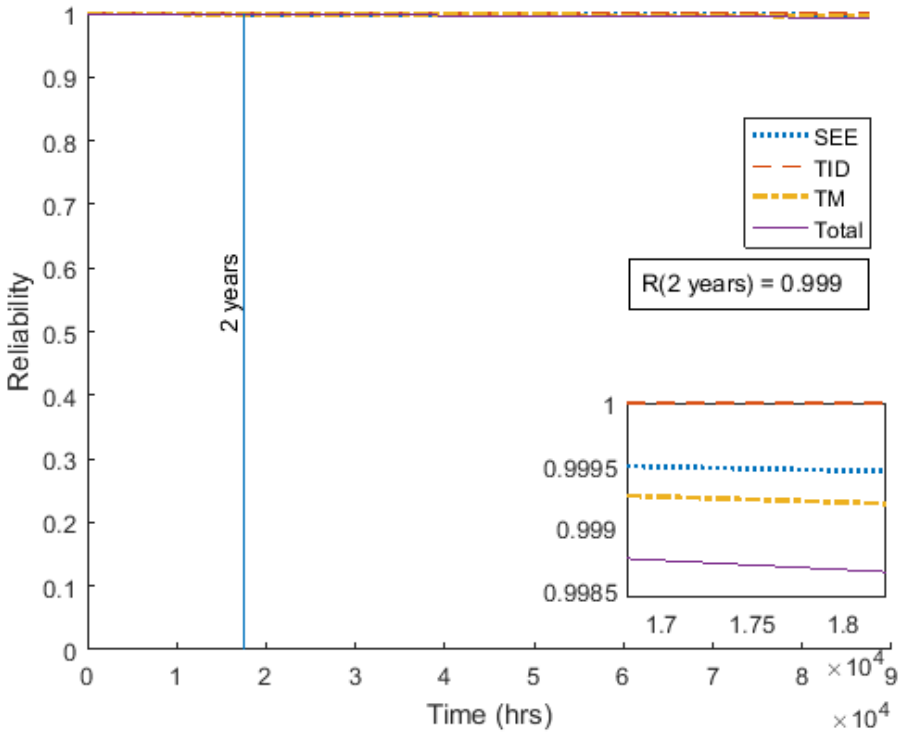

Figure 6.42: Reliability over time of the STM LIS3DH Accelerometer

used for voltage regulation [41]. Maximum power dissipation of the two regulators is 100mW peak and 38mW (1.8V), 20mW (3.3V) typical. The 8 pin DRB (SON) 3mm x 3mm package will be used for both which has a junction to board thermal resistance $R_{\Theta jB} = 18^oC/W$.

$$t_{j,1.8V} = t_c + (Power)(R\theta_{jB}) = 16.419 + 0.038(18) = 17.103 \tag{6.31}$$

$$t_{j,3.3V} = t_c + (Power)(R\theta_{jB}) = 16.419 + 0.02(18) = 16.779 \tag{6.32}$$

$$\pi_{t,1.8V} = e^{(\frac{3480}{328})(\frac{1}{273+17.103})=1.0372} \tag{6.33}$$

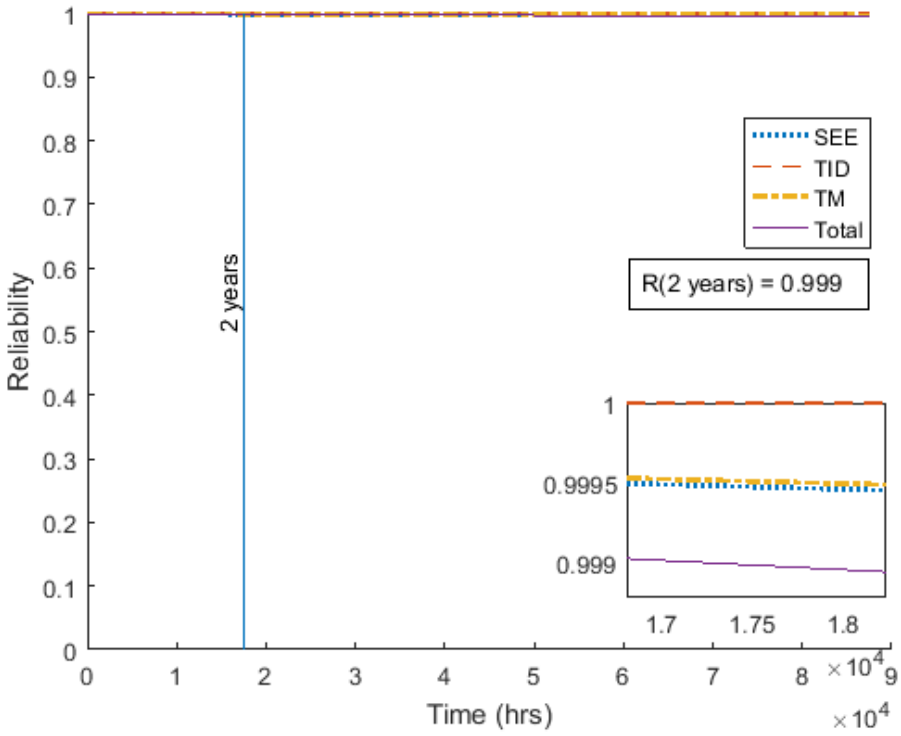

Figure 6.43: Reliability over time of the STM LIS3MDL Magnetometer

$$\pi_{t,3.3V} = e^{(\frac{3480}{328})(\frac{1}{273+16.779})=1.0373} \tag{6.34}$$

Since both use the same two row connection, λ_3 can be calculated for both as follows from table 17b in [11].

$$\lambda_{3,2x2} = 0.024 * D^{1.68} = 0.024 * (\sqrt{3mm^2 + 3mm^2})^{1.68} = 0.272 \tag{6.35}$$

Radiation testing of similar low drop out regulators for SEE resulting in now destructive failures up to a LET threshold of 120MeV [42] therefor the LDOs will be assumed to be functionally immune to permanent functional failure due to single event effects in the low earth orbit as the flux of ions with a linear energy transfer into silicon or silicon dioxide greater than 120MeV is extremely low. Typical total ionizing dose values for simple regulators range from 50krad to 100krad [43] so a value

of 50krad will be assumed until the component can be tested.

Table 6.14: TLV320AIC3206 codec Reliability parameters

Parameter	TPS73518	TPS73533
λ_1	$1 * 10^{-2}$	$1 * 10^{-2}$
λ_2	4.2	4.2
α	2015 - 1998 = 16	16
N	750	750
$(\pi_t)_i$	1.0373	1.0373
π_a	1.0519	1.0519
λ_3	0.272	0.272
π_I	0	0
λ_{EOS}	0	0
D_{TID}	50krad	50krad
$\sigma_{i,\infty}$	0	NA
$LET_{threshold,i}$	NA	NA
$LET_{threshold,25\%}$	NA	NA
τ_i	1	1
τ_{on}	1	1
τ_{off}	0	0

Matlab code used for simulation and computation of reliability models can be seen in appendix D. These models resulted in a reliability of effectively 1 for the two voltage regulators by themselves at the end of the 2-year planned mission in the 600km sun synchronous target orbit discussed in the environment modeling section.

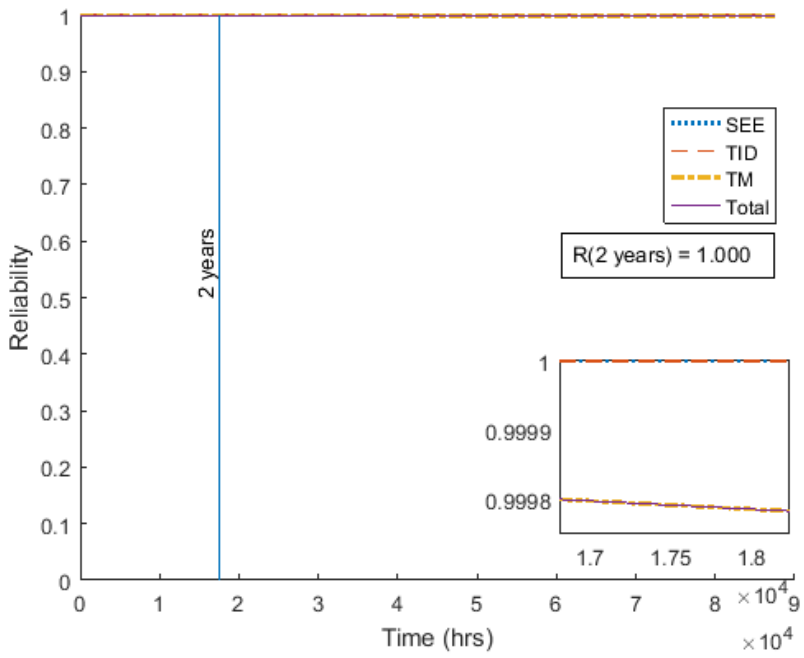

Figure 6.44: Reliability over time of the TI TPS73518

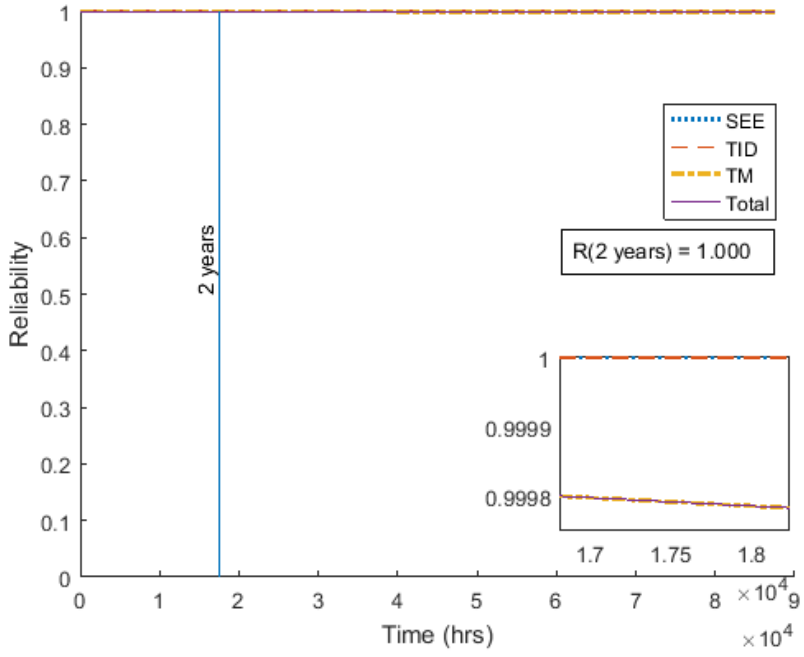

Figure 6.45: Reliability over time of the TI TPS73533

On Board Command and Data Handling Reliability

Now that the reliability of each individual component used in the functionally complete system design have been estimated we can determine the initial estimate for system reliability of the entire sub system as well as the individual functionalities. At this stage following the design methodology discussed in chapter 5 there is no added redundancy, this keeps the design lower volume, power and complexity while the actual reliability is not yet known, therefor the reliability of the system and its individual functionalities is just the product of the involved components. The reliability flow graphs of each required function can be seen in figures 6.26, 6.28 and 6.30.

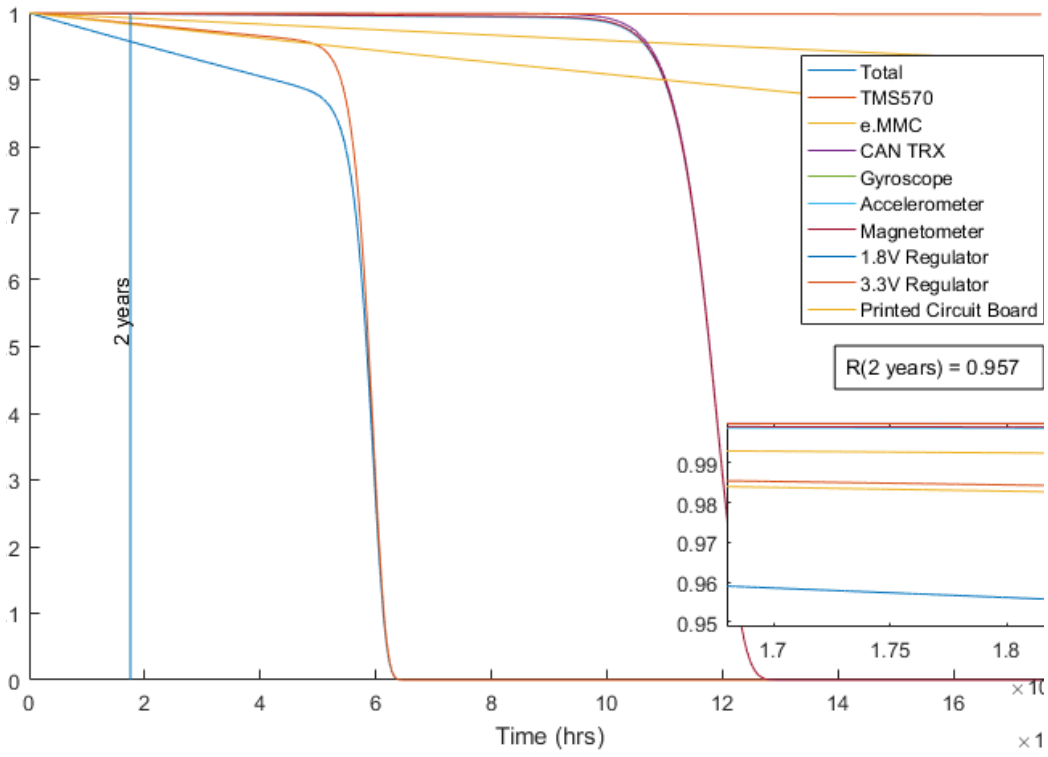

Figure 6.46: Reliability over time of the ADCS functionality within the command and data handling subsystem

By itself the ADCS functionality has a 95.7% chance of operating without hardware failure at the end of the two year planned mission, The reliability over time of the ADCS components from mission start to 20 years can be seen in figure 6.46 with

a zoomed section ranging from 30 days before the target EOL to 30 days after the target EOL. Assuming a 90% acceptable risk as discussed within the ECOSat team this functionality by itself does not need any additional redundancy added into it and in the design processor proposed in chapter 5 can move on to the design of test interfaces and hardware in loop testing.

The communications functionality requirement of the on board command and data handling hardware can be seen to have a reliability of 91.3% at the 2 year planned EOL with the reliability over time shown in figure 6.47. While this is still above the acceptable level of risk decided upon by the team it can be seen from the individual component reliabilities that the TMS320 digital signal processing component effected by single event effects is the main source of failure with a reliability at 2 years by itself of 95.2%, this could be increased with a cold spare (unbiased components typically have lower cross section) or by additional shielding around the component to reduce the LET of ions near the processor.

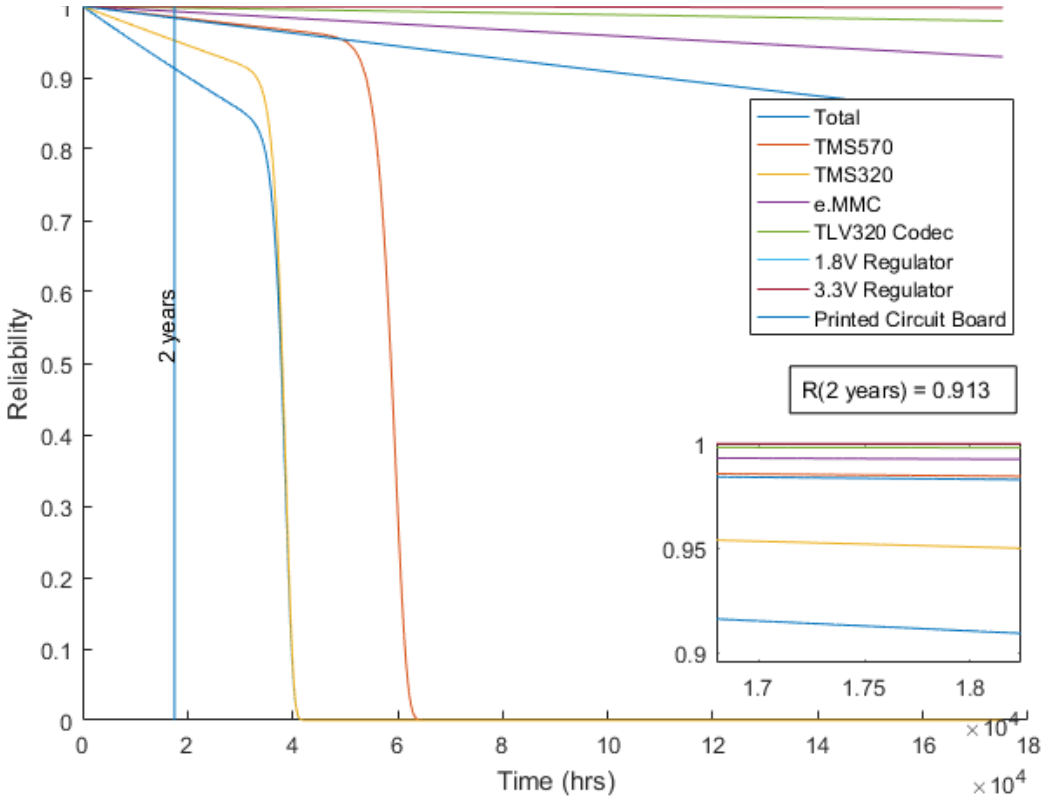

Figure 6.47: Reliability over time of the Communications functionality within the command and data handling subsystem

The final main functionality of the on board command and data handling hardware is the collection of telemetry, figure 6.48 shows that the main components responsible for the collection and storage of telemetry have a 96.1% chance of not having hardware failures at the planned EOL of 2 years. As this is well above the acceptable risk no additional redundancy is required, The reliability of the information within the memory will be discussed later in this chapter.

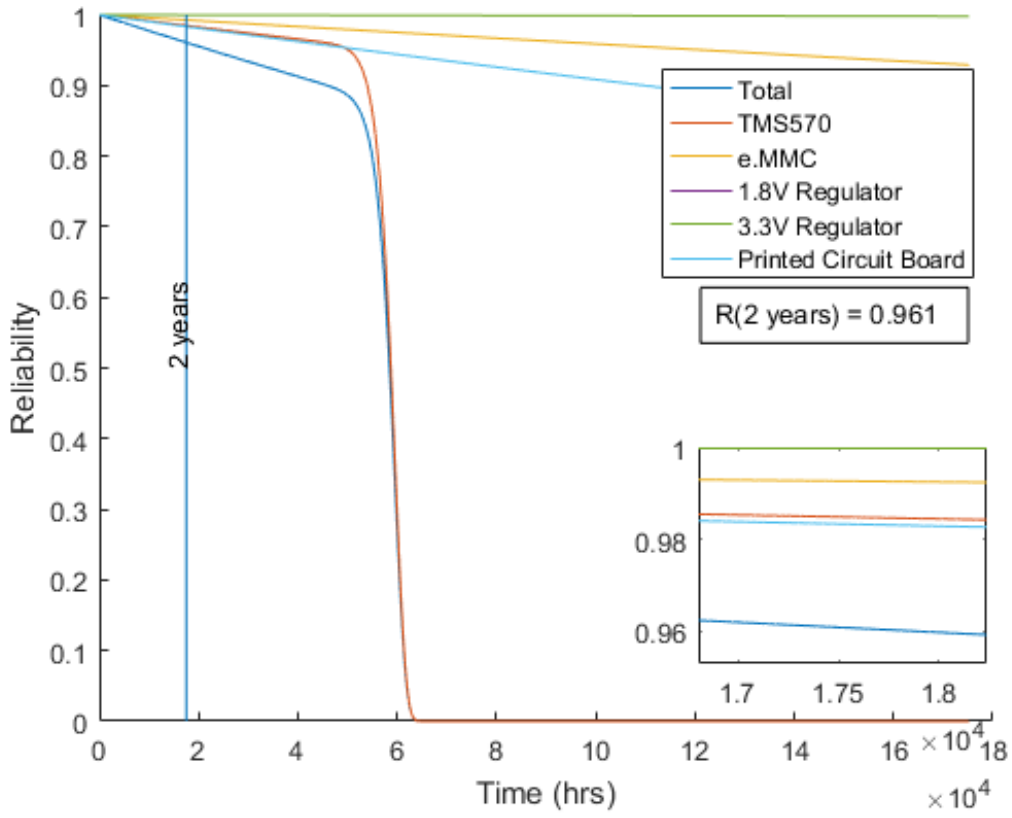

Figure 6.48: Reliability over time of the Telemetry functionality within the command and data handling subsystem

Overall the reliability of the entire system can be seen in figure 6.49 with a reliability at EOL of 90.9%. Since the reliability of the entire system remains above ECOSats acceptable risk the system designed does not require additional redundancy, component selection changes, or mechanical changes. Following the design process discussed in chapter 5 this system would then move forward into hardware in loop testing to verify software implementation. The three least reliable components are predictably the DSP processor, main processor and Micron flash memory in that

order, if a larger value was required as an acceptable risk the design could be improved by inspecting the main effects at EOL the reduce the individual components reliability and mitigation schemes such as physical redundancy, mechanical changes, or complete component reselection can be used and the reliability analysis restarted until the total reliability of the system matches the acceptable risk.

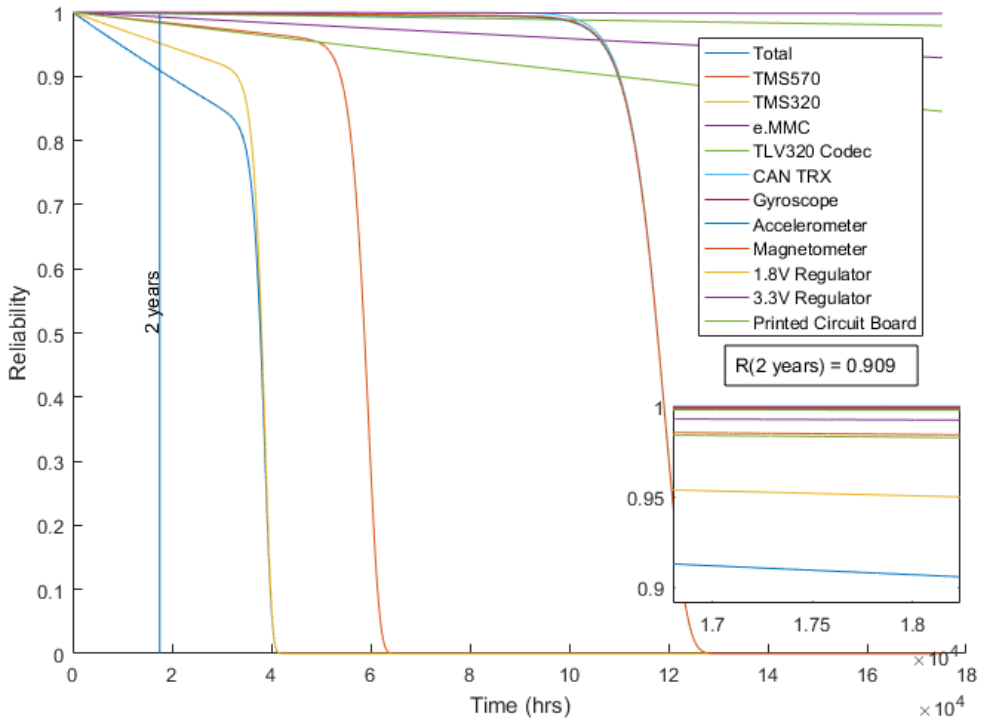

Figure 6.49: Reliability over time of the total command and data handling subsystem

6.3.2 Evaluating Information Reliability

The main memory for the ECOSat-2 on board computer was originally specified to use a triple redundancy code for memory protection without any written requirement for scrubbing period, this was to be implemented over 1GB of the 2GB memory to allow for spares that could replace addresses that experience hard errors. while triple modular redundancy is an easy and effective error correcting code in terms of processing it has a low coding rate (ratio of encoded information to parity information) as well as a small hamming distance. To determine a more acceptable code for ensuring the reliability of information in memory first the reliability of the information per bit needs to be evaluated using the equations from chapters 3 and 4, it is important that the cross sectional areas that we will use in this section are different than the ones that would be used for component reliability estimations as the focus is on single event upsets per bit rather than single event functional interrupts or other hard error single event effects of the entire device.

While test data of the 2GB e.MMC is unavailable, heavy ion test reports from the same family of NAND flash memories created by Micron are available for their 4GB [30], 8GB [31] and 16GB [32] components which match each other well. From these reports we can determine for SEUs σ_i is 10^{-10} per bit with an LET threshold value of approximately 9 $MeVcm^2/mg$ and an L value of approximately 30 $MeVcm^2/mg$ (the value where $\sigma_i(E)$ reaches 25% σ_i the cross section at ∞). We can then determine $\sigma_p(E)$ the proton cross section as seen in figure 6.50 from σ_i the heavy ion cross section using equations 3.31 and 3.32.

$$P(E) = P_0(E_p, L) = 4.0x10^{-6}e^{[-(0.134+\frac{9}{E_p})30]}$$

Matlab and the trapz function was used to integrate the product of the shielded proton flux and calculated proton cross section from the heavy ion cross section data. The integration of the two allows us to find the error rate caused by protons per hour in the target evaluation orbit as the following equation:

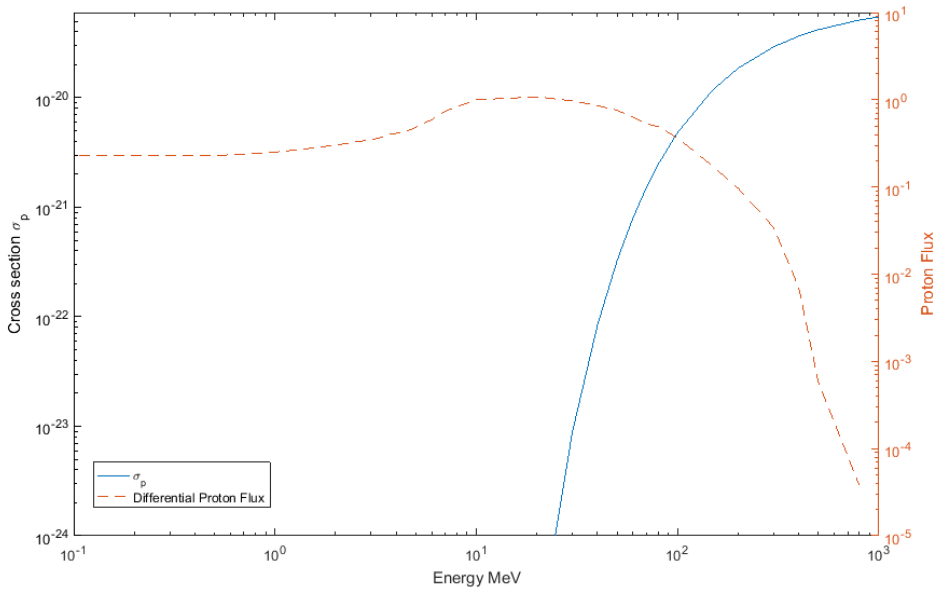

Figure 6.50: Proton cross section and flux for SEU in the Micron e.MMC

$$\lambda_{SEU,proton} = 3600 * 2\pi \int \sigma_p(E_p) F_p(E_p, t) dE = 1.0504e - 14$$

Similarly Matlab was used to calculated the filtering functions $\eta(E, i)$ as seen in figure 6.51 for each ion such that only the flux of heavy ions at energy's with linear energy transfer values into silicon larger than the linear energy transfer threshold are used.

Matlab was once again used to integrate the products of each heavy ions flux and filter function using the trapz function. Using the sum of the individual products together we can find that the hazard rate for ion induced SEUs in the target orbit is:

$$\lambda_{SEE,ion} = 3600 * 2\pi \sum_i \sigma_i \int \eta_i(E) F_i(E, t) dE = 9.0813e - 06$$

The reliability per bit over time is then shown in equation 6.36 where the effect of heavy ion flux is the dominant source of errors.

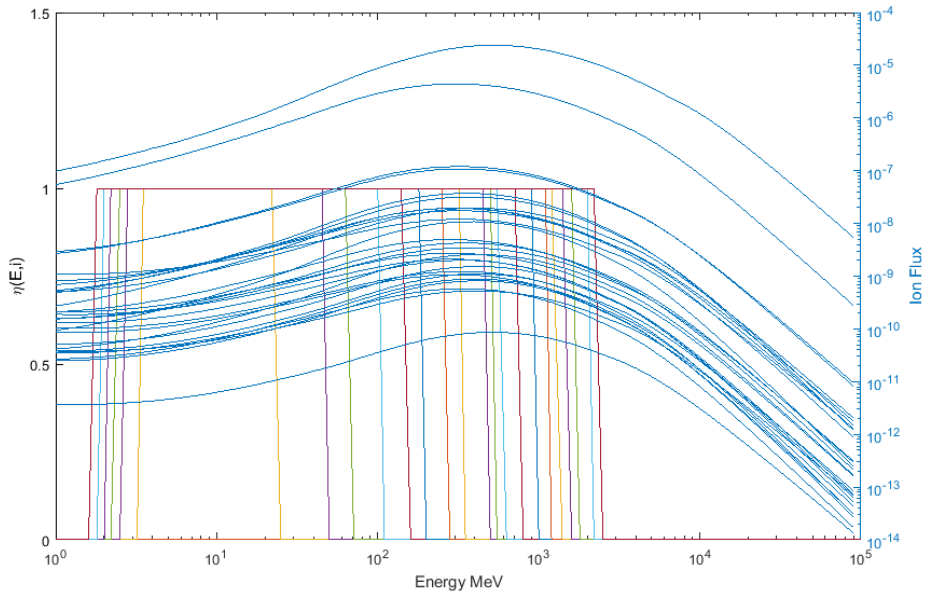

Figure 6.51: Ion fluxes and filters $\eta(E, i)$ for SEU in the Micron e.MMC

$$R_{bit}(t) = e^{-(9.0813e-6)*t} \tag{6.36}$$

Now that we have the probability that a bit has not failed we can use R_{bit} and equation 6.37 to determine the reliability of information that has been encoded by an error correcting code (ECC) of block length n and error correction capability t. The equation represents one minus the probability of all possible error patterns greater than t+1, which is then the probability that less than t+1 errors have occurred and the information can be corrected at time t_s.

$$R_{code}(t_s) = 1 - \sum_{i=t+1}^{n} \binom{n}{i} R_{bit}(t_s)^{n-i}(1 - R_{bit}(t_s))^i \tag{6.37}$$

Equation 6.37 works well to represent the reliability of linear block codes over binary symbols but for codes that are developed over larger bases such as Reed Solomon codes over 8 bit symbols we need to find the reliability that any error has occurred in a symbol of size 2^m to properly calculate the probability that a decoding

error has occurred in the code. The reliability of different symbol sizes within the micron memory and the 600km orbit can be seen in figure 6.52.

$$R_{symbol}(t) = (e^{-(9.0813e-6)*t})^m \tag{6.38}$$

$$R_{code,RS}(t_s) = 1 - \sum_{i=t+1}^{n} \begin{pmatrix} n \\ i \end{pmatrix} R_{symbol}(t_s)^{n-i}(1 - R_{symbol}(t_s))^i \tag{6.39}$$

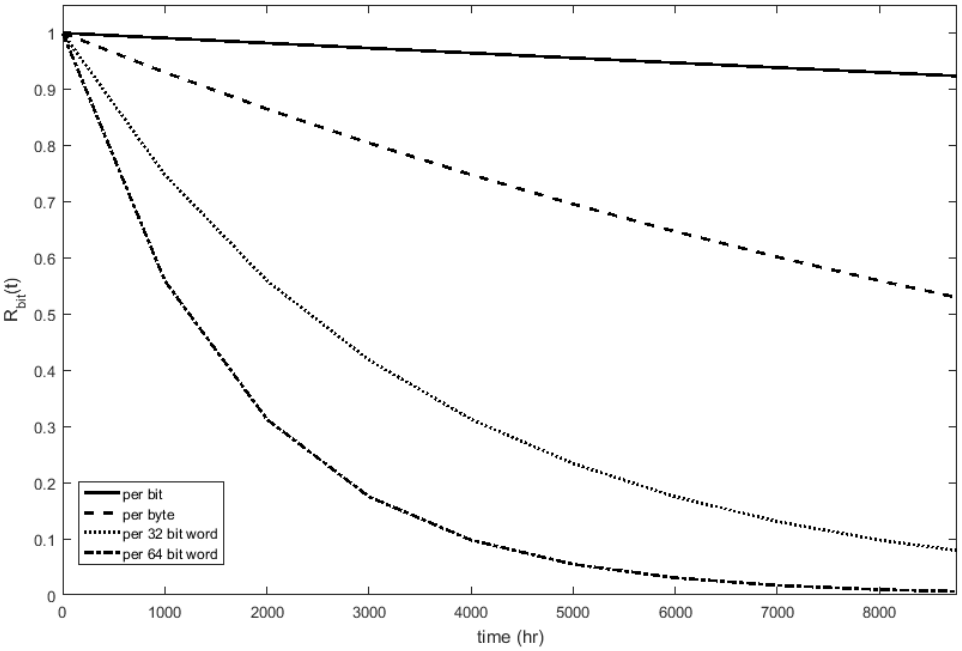

Figure 6.52: Reliability of a symbol for 1bit, 8bit, 32bit, and 64bit symbols

The Reliability of information in an N bit memory is then the probability that no code of length n over the entire memory space has developed greater than t+1 errors between scrubbing periods.

$$R_{information}(t_s) = (1 - R_{code}(t_s))^{\lfloor \frac{N}{n} \rfloor} \tag{6.40}$$

Using Equations 6.37, 6.39 and 6.40 we can determine contours of reliability versus block size and time to help determine acceptable boundaries on scrubbing time and code parameters. The figures 6.53, 6.54 and 6.55 below show contours of constant reliability for single, double, and triple error correcting linear block codes. For designed codes of block size n the contours show what scrubbing periods are required to keep the entire memory, 1GB (8Gb) in the figures, above an acceptable risk.

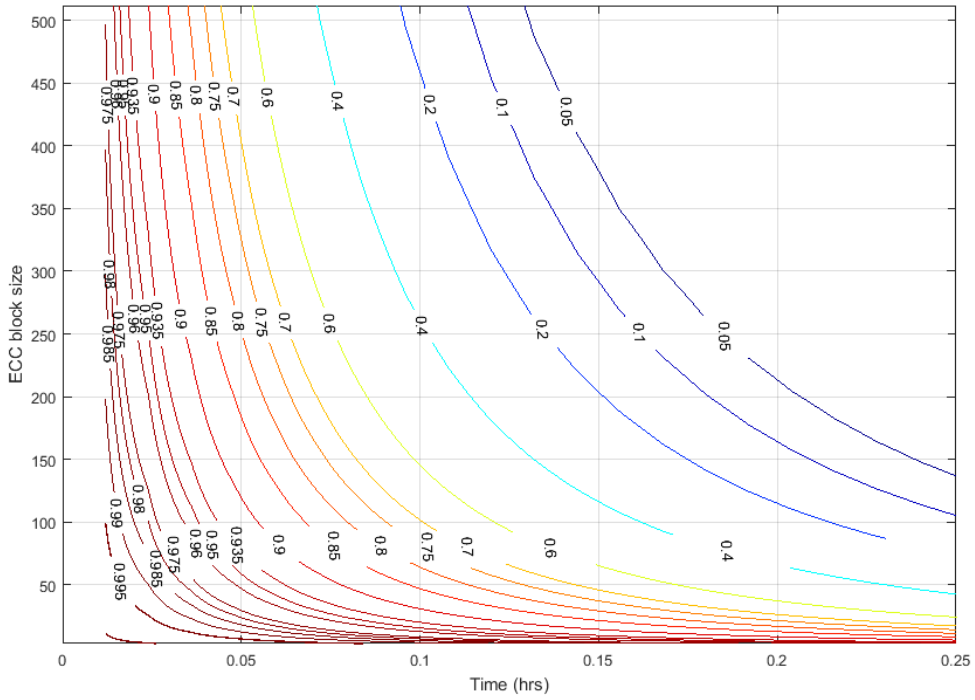

Figure 6.53: Reliability Contours for a t=1 s=1 linear block code, (block size in bits)

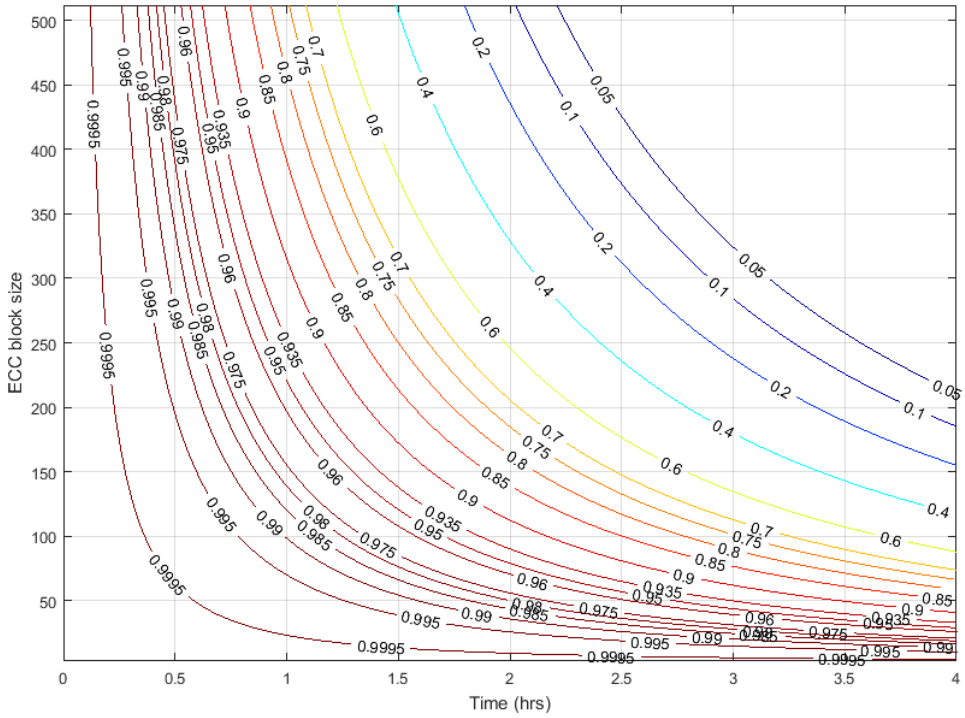

Figure 6.54: Reliability Contours for a t=2 s=1 linear block code, (block size in bits)

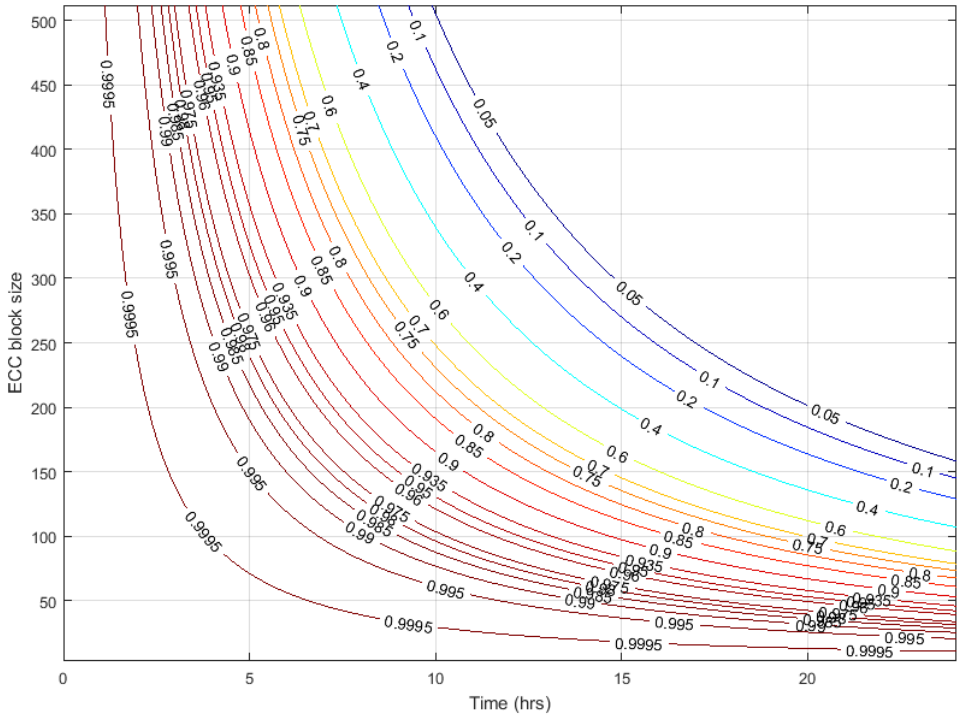

Figure 6.55: Reliability Contours for a t=3 s=1 linear block code, (block size in bits)

From the figure of single error correction, we can see that the scrubbing period would be very short, on the order of minutes. If we zoom in on a block size of three for the single error correcting code we can find the reliability that triple modular redundancy would have (shown in figure 6.56), from this we can see that the initial plan for error correction specified for Ecosat-2 would require scrubbing periods on the order of one to six minutes for the 1GB of planned used memory.

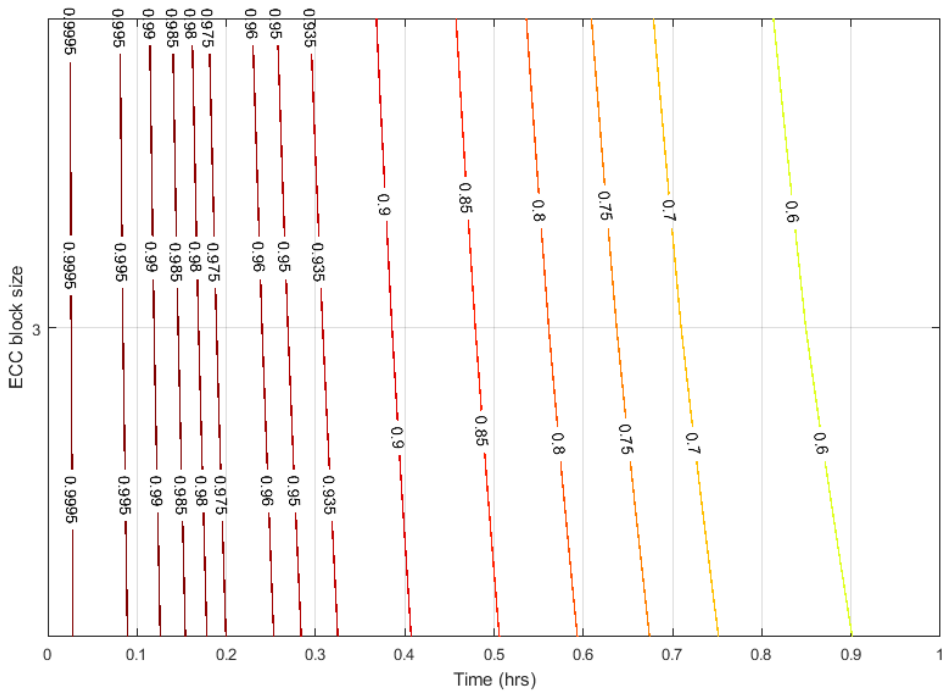

Figure 6.56: Reliability Contours for a Triple Modular Redundancy code, (block size in bits)

In a similar way we can look at the reliability of Reed Solomon codes over constant block sizes, since Reed Solomon codes are minimum distance separable [44] and their distance is always n-k+1 we can set the information block size as constant and find the reliability vs time for different error correction capabilities. Since the file system implemented has a minimum sector size of 512 bytes, codes with information lengths k of 512, 256 and 128 where evaluated for symbol correction capabilities from 1 to 3, the contours that resulted can be seen in figures 6.57, 6.58 and 6.59 below.

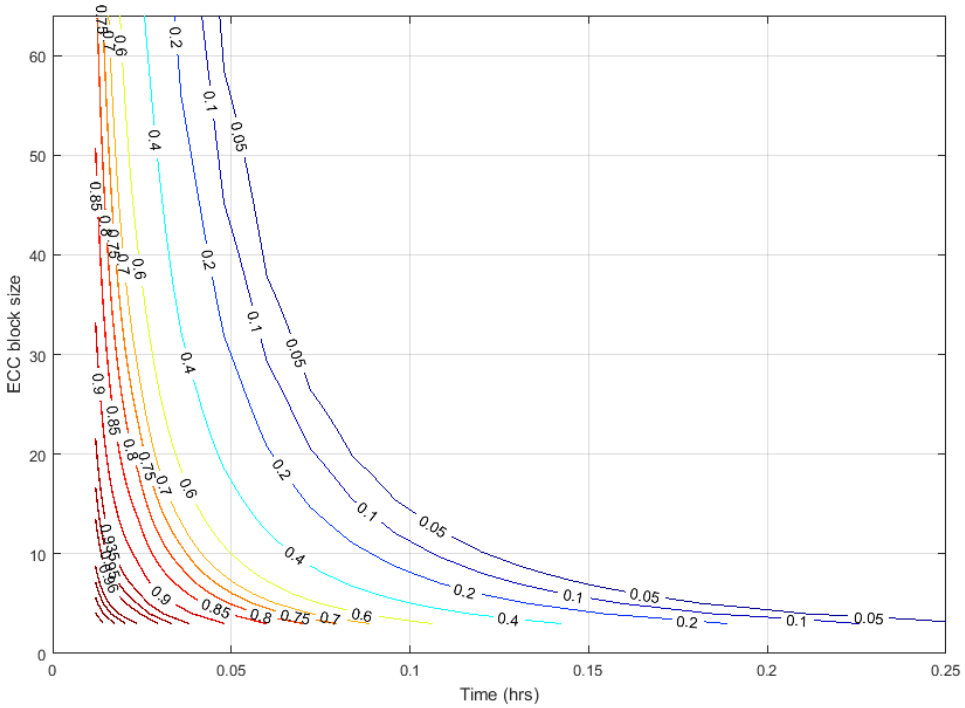

Figure 6.57: Reliability Contours for a t=1 s=8 Reed Solomon code, (block size in bytes)

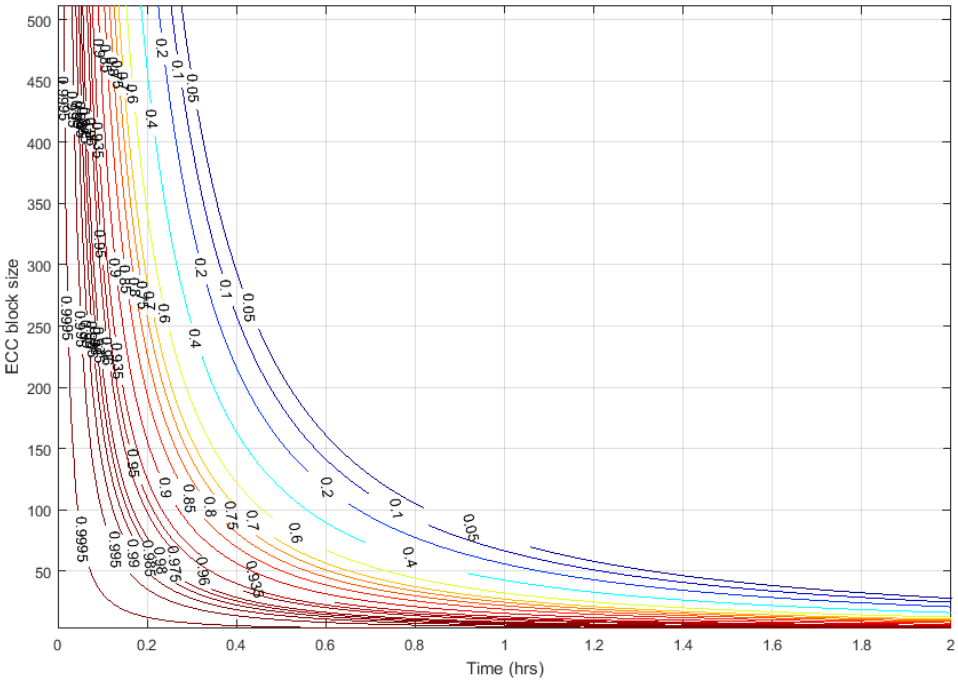

Figure 6.58: Reliability Contours for a t=2 s=8 Reed Solomon code, (block size in bytes)

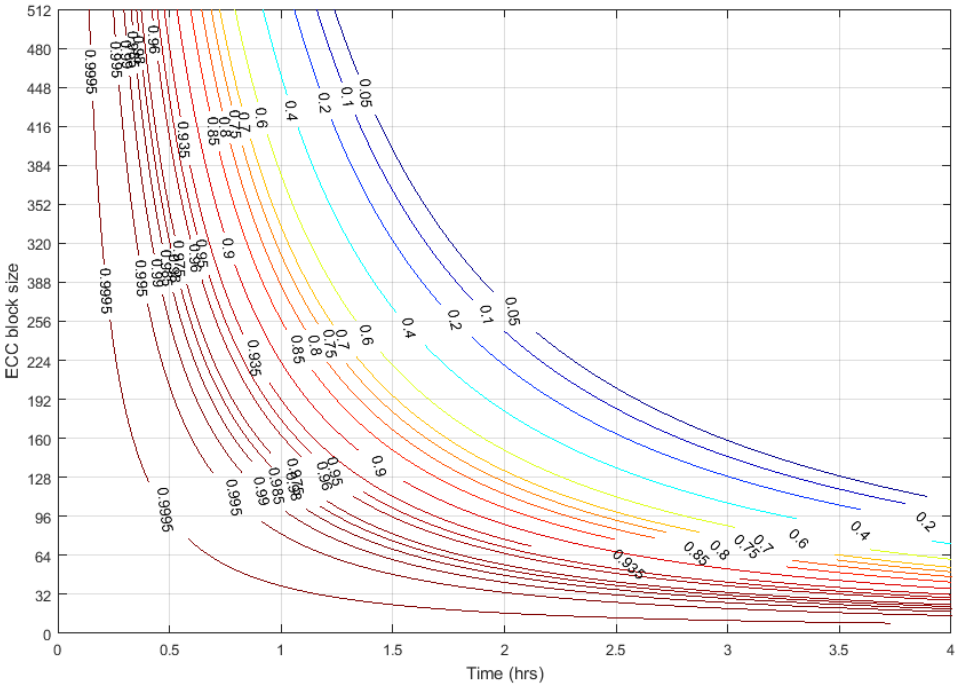

Figure 6.59: Reliability Contours for a t=3 s=8 Reed Solomon code, (block size in bytes)

From these plots we can determine that the original specification for triple modular redundancy would require an unacceptably high scrubbing rate to protect the entire planned available memory space of 1GB, it would be more reliable if only used memory was protected by scrubbing but the amount of this is not yet well defined. It was decided that the design of the error coding will aim to be used over the minimum sector size of 512 bytes and target a scrubbing period greater than one hour. As the decoding complexity of a Reed Solomon code is $O(n^2)$ and $O(nt)$ for BCH codes [45] the balance is then to select a code with a large enough error correction capability to increase the required scrubbing period but not so large that the decoding complexity increases the memory latency to an unacceptable amount.

A Reed Solomon code specified to have an error correction capability t of 3 (minimum distance 7) and a message length of 128 bytes such that 4 codes could be used to protect each minimum size sector of the file system. From the figures and analysis so far scrubbing this code once every 5 hours will provide a reliability greater than 0.995. Another option is to design a Reed Solomon error correcting code with sym-

bol correction capability of 2 and a scrubbing period 37min. These two codes both have advantages and disadvantages, the t=2 code provides much lower memory read latency as decoding is faster but requires a significantly shorter scrubbing period, the t=3 code provides longer memory read latency but is far more flexible in scrubbing period, up to 5 hours, which may provide longer sleep and safer shutdown modes of the satellite.

A simple Matlab simulation was made that computed the probability of error for small memory sizes to visualize the memory upsets. The simulation function took in code parameters, the SEU hazard rate and a memory size. For each time step each bit in the memory size was randomly set based on the hazard rate to provide the error patterns of each byte over time, at every scrubbing period interval each code in the memory was evaluated for number of symbol errors, if the number of errors exceeded the correctable amount of errors then every byte in the code was set to 10 for the visual simulation and for the time simulation the time at which failure occurred was output for a histogram. This simulation had a lot of trouble with large memory sizes and the entire 1GB of memory was not possible to simulate on typical office computers due to extremely long run times and large memory requirements. As an example of what this looks like, the t=2 linear block code was simulated with a scrubbing period of 3 hours over a 1KB memory and can be seen in figures 6.60 and 6.61. In figure 6.61 the SEU rate estimated for the memory was increased by a factor of 10, the first code failure can be seen at 189 hours with the second at 618 and third and fourth failures at 855, these plots are intended as an example only.

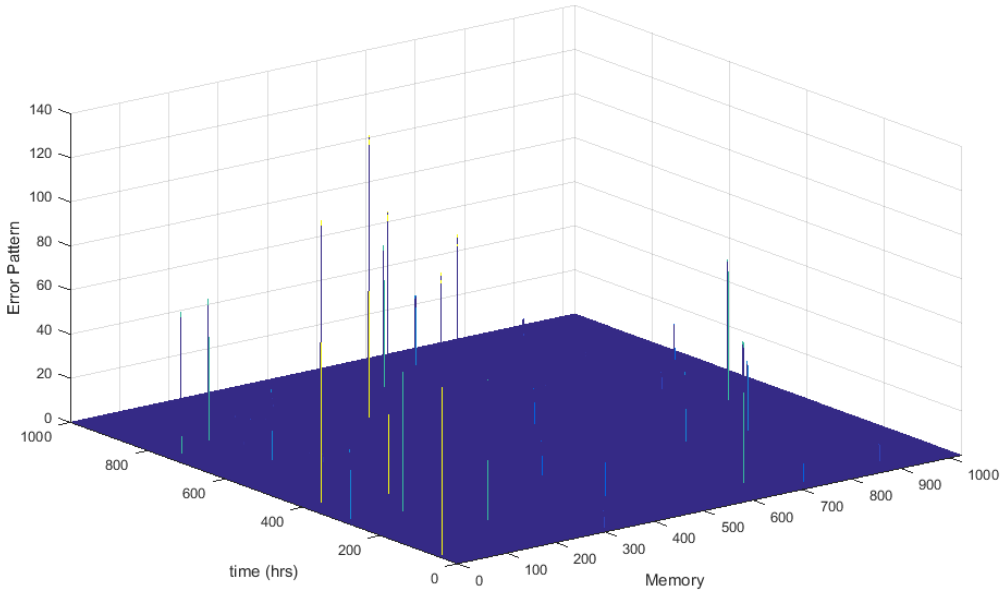

Figure 6.60: Bit errors in memory for a t=2, k=128B, t_s=3 hours at mission hazard rate

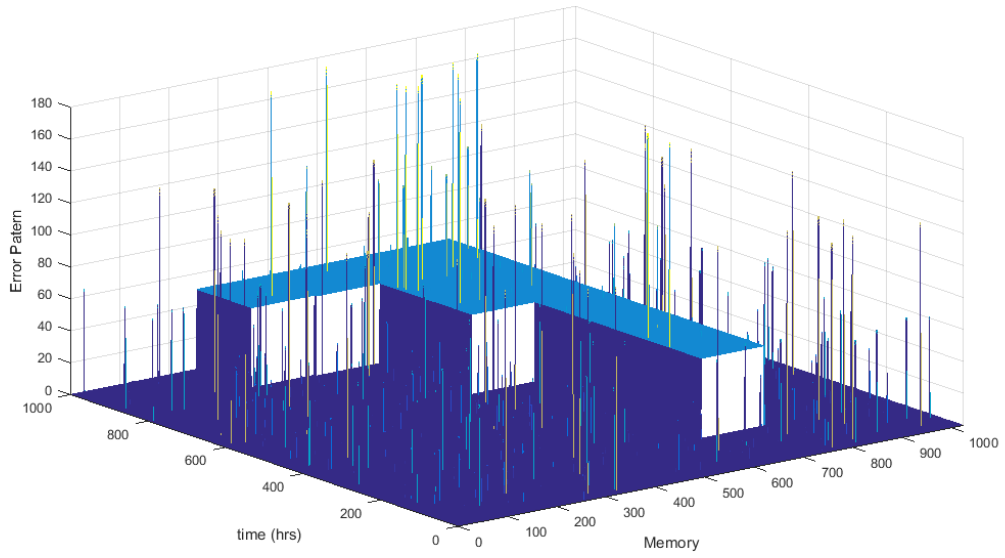

Figure 6.61: Bit errors in memory for a t=2, k=128B, t_s=3 hours at 10 times SEU FIT rate

A simulation was then run without the visualization greatly increases its speed. this simulation was run for 1000 trials for the triple modular redundancy scheme, and three reed solomon codes with information block sizes 16, 32, and 64 bytes each with a scrubbing period of 1 hour.

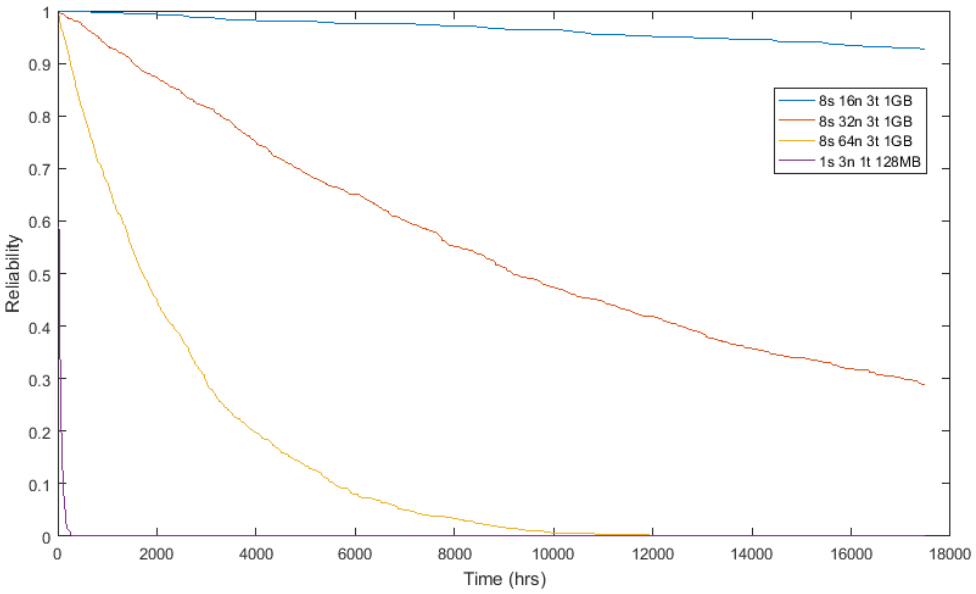

Figure 6.62: Reliability of the scheme over 1000 trials for s symbol size, n block size, 1 hour scrubbing, and 128MB or 1GB memory sizes

From these simulations we can see that the triple modular redundancy code selected even over only 128MB has an extremely low reliability for no code errors over the 2-year mission. Reed Solomon codes show much better results with a reliability that no errors have occurred at end of mission (2 years) greater than 95%. Similarly the **(72,64)** SECDED Hamming code that is used internally to protect ram and rom inside the Hercules main processor was evaluated to ensure no additional coding is required.

To design the code we will start with a **(255,249,7)** code and shorten it by 233 bytes to a **(24,16,7)** code (**(192,128,7)** in bits). The resulting code will have a code rate of approximately $\frac{2}{3}$ double that of the initial triple modular redundancy code specified for the on board computer. We will use the Reed Solomon code built from Galois Field GF(256) so that math can be done over bytes. Creating a narrow sense Reed Solomon code over the Galois Field GF(256) of design error correction t

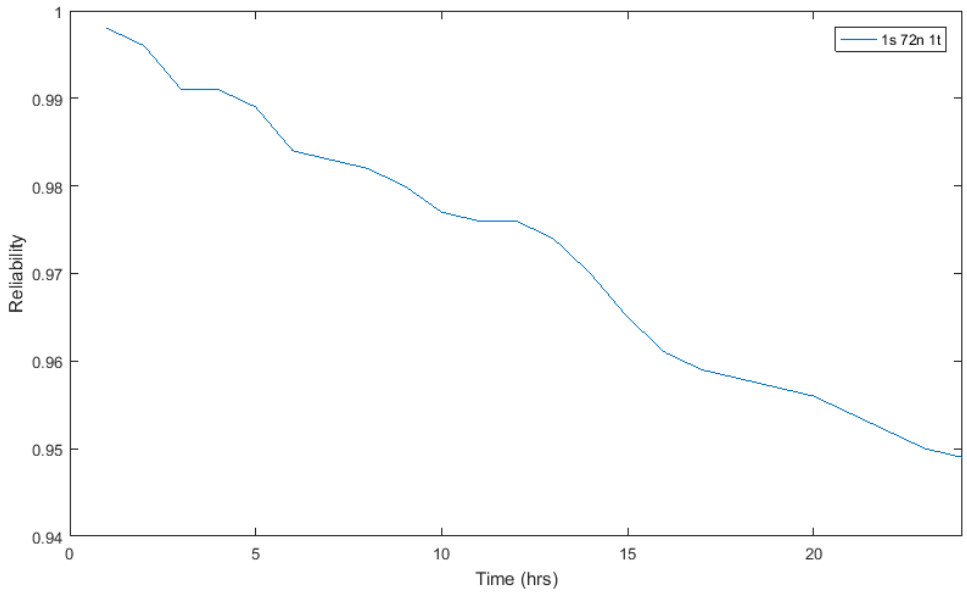

Figure 6.63: Reliability of the 72,64 Hamming code with a 6min scrubbing period inside the Hercules

requires 2t consecutive roots of the fields generator polynomial. let α be a root of the generator polynomial $p(x)$:

$$p(x) = x^8 + x^4 + x^3 + x^2 + 1$$

The generator polynomial g(x) of the **(255,249,7)** code can then be calculated as:

$$
\begin{aligned}
g(x) &= (x-\alpha)(x-\alpha^2)(x-\alpha^3)(x-\alpha^4)(x-\alpha^5)(x-\alpha^6) \\
&= (x^2-(\alpha+\alpha^2)x+\alpha^3)(x^2-(\alpha^3+\alpha^4)x+\alpha^7)(x^2-(\alpha^5+\alpha^6)x+\alpha^{11}) \\
&= (x^2-(\alpha^{25})x+\alpha^3)(x^2-(\alpha^{27})x+\alpha^7)(x^2-(\alpha^{29})x+\alpha^{11}) \\
&= (x^4-(\alpha^{30}+\alpha^{22})x^3+(\alpha^7+\alpha^{52}+\alpha^3)x^2-(\alpha^{32}+\alpha^{30})x+\alpha^{10})(x^2-(\alpha^{29})x+\alpha^{11}) \\
&= (x^4-(\alpha^{222})x^3+(\alpha^{54})x^2-(\alpha^{80})x+\alpha^{10})(x^2-(\alpha^{29})x+\alpha^{11}) \\
&= (x^6-(\alpha^{222}+\alpha^{29})x^5+(\alpha^{54}+\alpha^{251}+\alpha^{11})x^4-(\alpha^{80}+\alpha^{80}+\alpha^{233})x^3 \\
&+ (\alpha^3+\alpha^{109}+\alpha^{65})x^2-(\alpha^{39}+\alpha^{91})x+\alpha^{21})
\end{aligned}
$$

Resulting in the generator equation shown in power form in equation 6.41 and vector form in equation 6.42

$$g(x) = x^6 - \alpha^{57}x^5 + \alpha^{30}x^4 - \alpha^{233}x^3 + \alpha^{238}x^2 - \alpha^{180}x + \alpha^{21} \tag{6.41}$$

$$g(x) = x^6 + 126x^5 + 4x^4 + 1587x^3 + 58x^2 + 49x + 174 \tag{6.42}$$

Chapter 7

Conclusions and Future Work

7.1 Conclusions

The rapidly expanding micro satellite market has shown very promising results by reducing the barrier to entry to space for universities in comparison to the traditional satellite industry. While the applications of micro-satellites are very promising, the current success rate of cube satellite missions has shown to be very low. The success rate is only approximately 44% for the first mission, only increasing to a 62% chance of full mission success on a second try. The high failure rate of these missions has been attributed to two factors: first, the harsh thermal mechanical and radiation environment; and second, the lack of rigorous verification procedures conducted before launch. This thesis has proposed a combination of thermal, mechanical and radiation reliability models for EEE components. The goal was to address the effects of the orbital environment on mission assurance. Also, a design methodology has been proposed that incorporates hardware and software in loop testing to provide guidelines to prevent failures due to lack of testing. The physics of failure reliability models assists in identifying the most probably causes of failure in a design of each component. Using knowledge of which components and what factors reduce the reliability of a system to an unacceptable level, the proposed design process assists in reducing added redundancy to where it is needed most allowing for less complex and lower

power designs. The reliability model and design process as presented in this thesis is a valuable tool for design comparison. However, due to the simplifications and assumptions made of components as well as the variability of the orbital environment, it should not be used as an accurate means of determining exactly how long a system will last in orbit.

The case study conducted of the on-board command and data handling within the ECOSat-II cube satellite started with an environmental analysis conducted using SPENVIS for the radiation environment for component boards and a CAD model of the satellite created in Siemens NX so that a FEM analysis could be conducted to obtain the thermo-mechanical environment of each circuit board. The case study shows that the initial functionally complete hardware design, based on the proposed design methodology, has an acceptable reliability at the two-year targeted mission time. This shows an important contrast to the initial design that contained triple redundant sensors behind an I2C switch as a blind attempt at increasing the reliability of the system where it is not necessary. Another interesting result is in the study of information reliability within the main memory. The initial design requirements that specified a triple redundancy scheme for memory protection is shown to be extremely unreliable over large memory spaces. Even the second most popular error coding scheme (a 72,64 Hamming) is unsuitable for a 1Gb memory space. A Reed-Solomon code has been designed that provides greater than 95% reliability of the information stored within memory using the same physics of failure models as discussed for the single event effects used for hardware reliability, Reed-Solomon was selected over a normal cyclic or linear block code for its added protection against multiple bit errors caused by a single event.

7.2 Future Work

The parameters used for the radiation effects on failure of components within the case study where estimated from similar components. Moving forward, ECOSat should conduct Heavy Ion SEL or SEFI testing as well as total ionizing dose testing of candidate components. Additionally, laboratory experimentation should be carried out to further refine reliability prediction model parameters. This would provide valuable information to the ever growing small-satellite market. Further studies of the thermo-mechanical reliability, while operating in a vacuum, should also be conducted to verify and improve the current physics of failure model that uses values from the IEC standard that has been tested and verified for operation on the ground.

Appendix A

Review of Probability Distributions

In all systems there will be an inherent variability in the environment and events that effect the failure rate and error rates of components. For this reason it is important to understand the rules of statistics and the use of probability distributions. This section is intended as a basic summary of the probability distributions and concepts used in reliability analysis for readers who are unfamiliar with them or have not used them in a long time.

A.0.1 Basic rules of probability used in Reliability Analysis

When dealing with multiple components or multiple failure causes it is important to understand how to deal with multiple random variables. Any pair of random variables can be classified as dependent, independent or mutually exclusive. With two dependent variables, the outcome of each random variable is dependent on the result of the other, this is typical in situations where one failure can cause another. With two independent random variables the the outcome of each random variable has no effect on the other. Finally two Mutually exclusive random variables can not occur at the same time, for example a passive component on a circuit board can not

fail to a short circuit and an open circuit a the same time. Notation for

For two independent variables the following three relations for the probability of A and B occurring, the probability of A given B occurring and the probability of A or B occurring are shown below respectively.

$$P(AB) = P(A)P(B)$$

$$P(A|B) = P(A)$$

$$P(A+B) = P(A) + P(B) - P(A)P(B)$$

For two dependent variables the following three relations for the probability of A and B occurring, the probability of A given B occurring and the probability of A or B occurring are shown below respectively.

$$P(AB) = P(B)P(A|B)$$

$$P(A|B) = \frac{P(AB)}{P(B)}$$

$$P(A+B) = P(A) + P(B) - P(AB)$$

For two mutually exclusive variables the following three relations for the probability of A and B occurring, the probability of A given B occurring and the probability of A or B occurring are shown below respectively.

$$P(AB) = 0$$

$$P(A|B) = 0$$

$$P(A+B) = P(A) + P(B)$$

The actual distributions associated with the the probability of a random variable

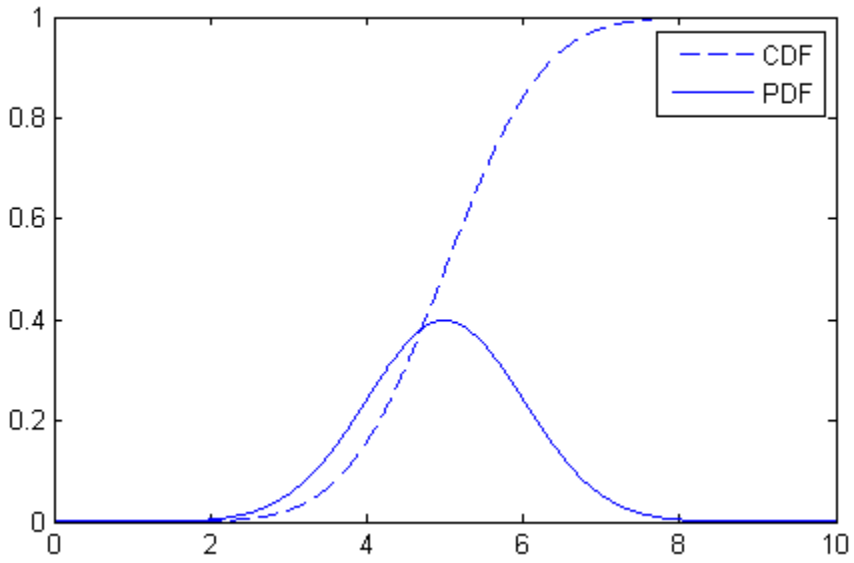

Figure A.1: Continuous normal probability density function and cumulative distribution function

can be discrete or continuous.A discrete probability distribution represents the probability of an event as it is depended on a discrete variable, such as number of cycles, etc. A continuous probability distribution represents the probability of an event as it is dependent on a continuous variable such as time or temperature. The Probability Density Function (PDF) represents the probability of the event occurring at the exact value of the dependent variable. Of more interest to reliability is the Cumulative Distribution Function (CDF) of the random variable, which is a representation of the probability that event has occurred at a given value of the dependent variable, for example the probability that a component has failed after 10 seconds would be equal to the value of the CDF at 10 seconds, or equivalently equal to the integral of all instantaneous probability that the component has failed from $-\infty$ to 10 seconds.

$$PDF = f(x), \quad \int_{-\infty}^{\infty} f(x)dx = 1$$

$$CDF = F(x), \quad \int_{-\infty}^{x} f(x)dx$$

A.0.2 Common distributions used in Reliability

There are many different types of distributions used to represent different random variables in statistics. Each type of distribution may be more or less accurate for a given situation than other failure modes. By far the most common distribution used in Reliability analysis is the Weibull distribution, this is due to its flexibility allowing for many different types of situations to be represented by changing its parameters.

Normal Distribution

While the normal distribution is fairly limiting in its shape it is important due to the central limit theorem. The central limit theorem states that as many probability distributions are added together their sum tends towards a normal distribution.

$$f(x) = \frac{1}{\sigma(2\pi)^{\frac{1}{2}}} exp\left[-\frac{1}{2}\left(\frac{x-\mu}{\sigma}\right)^2 \right]$$

Exponential Distribution

The exponential distribution is very important for reliability analysis as it describes a probability distribution with a constant hazard rate. The mean of the distribution or equivalently the mean time to failure (MTTF) of the component that the distribution represents is $1/\lambda$ with a constant hazard rate of λ. An example of a constant hazard rate situation would be that of hard errors caused by single event effects in a constant flux of ionizing radiation.

$$f(x) = \begin{cases} \lambda exp(-\lambda x) & x \geq 0 \\ 0 & x < 0 \end{cases}$$

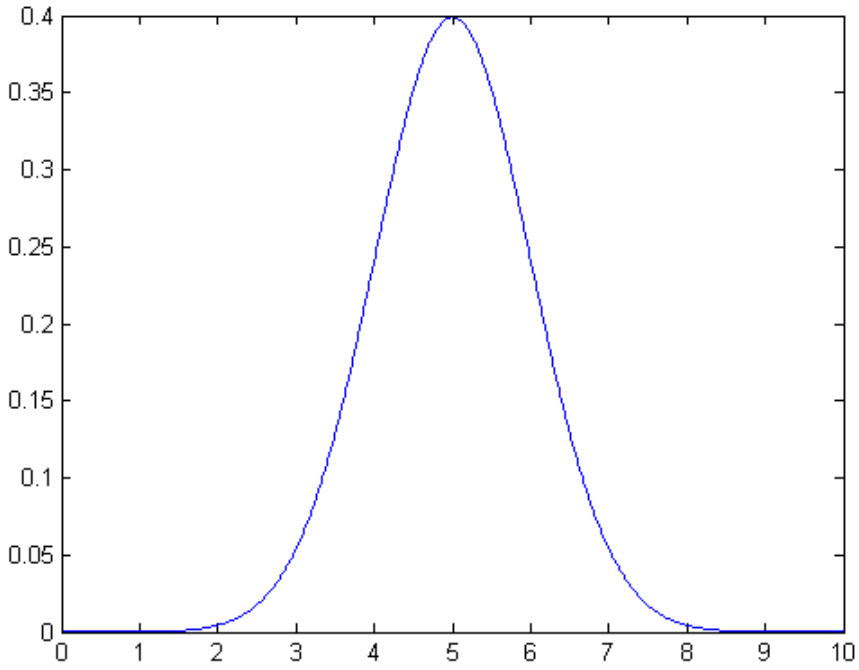

Figure A.2: Normal Distribution with mean = 5, standard deviation = 1

$$R(x) = 1 - \int_0^x f(x)dx = exp(-\lambda x)$$

Gamma Distribution

The gamma distribution can be used to represent the situation where partial failures can occur before the total failure of the component. For the gamma distribution, the parameter λ is used to measure the failure rate of the complete failure while α is used in the equations to denote the number of partial failures required for the complete failure to occur. The gamma distribution is essentially a way to represent the sum of α exponential distributions.

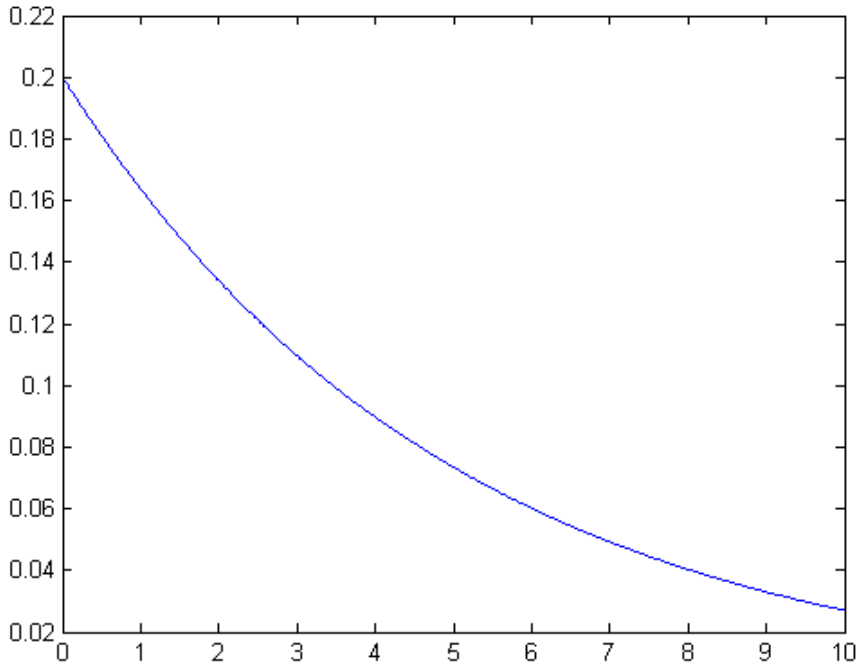

Figure A.3: Exponential Distribution with mean = 5

$$f(x) = \begin{cases} \frac{\lambda}{\Gamma(\alpha)}(\lambda x)^{\alpha-1} exp(-\lambda x) & x \geq 0 \\ 0 & x < 0 \end{cases}$$

where

$$\Gamma(\alpha) = \int_0^\infty x^{\alpha-1} exp(-x) dx$$

Weibull Distribution

As mentioned before the weibull distribution is by far the most common used as it offers the most control in fitting the distribution to experimental data. The parameter β is called the shape characteristic. When $\beta = 1$, the weibull distribution

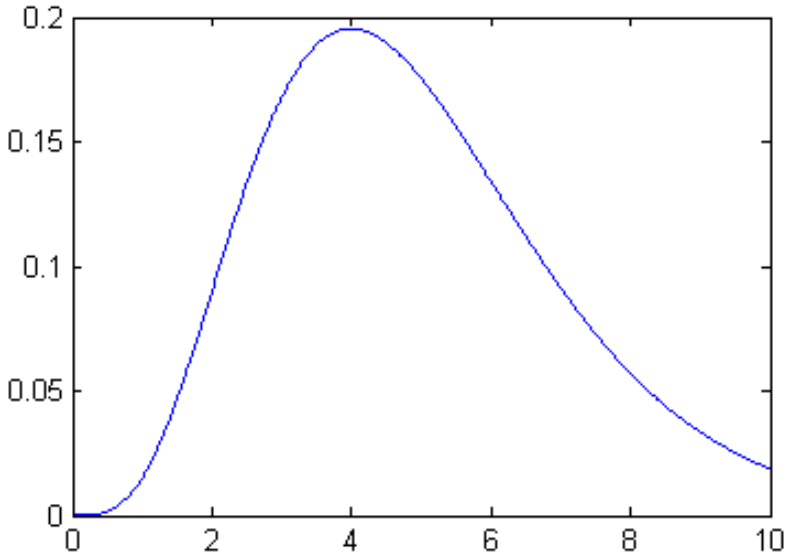

Figure A.4: Gamma Distribution with mean = 5, standard deviation = 2.2

becomes the exponential and represents a constant hazard rate $\eta = 1/\lambda$. For $\beta < 1$ the distribution represents an decreasing hazard rate and for $\beta > 1$ the distribution can be used to represent an increasing hazard rate situation. The parameter η is called the scale parameter. An additional parameter γ can be added to account for an error free time.

$$f(x) = \begin{cases} \frac{\beta}{\eta^\beta} x^{\beta-1} exp[-(\frac{x}{\eta})^\beta] & x \geq 0 \\ 0 & x < 0 \end{cases}$$

$$R(x) = exp[-(\frac{x}{\beta})^\beta]$$

$$h(x) = \frac{\beta}{\eta^\beta} x^{\beta-1}$$

$$f(x) = \begin{cases} \frac{\beta}{\eta^\beta} (x-\gamma)^{\beta-1} exp[-(\frac{x-\gamma}{\eta})^\beta] & x \geq 0 \\ 0 & x < 0 \end{cases}$$

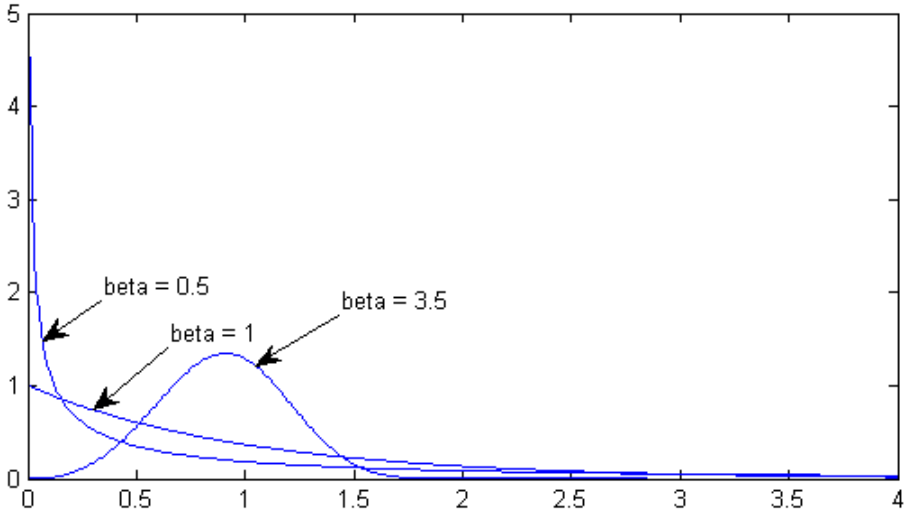

Figure A.5: Weibull Distribution with mean = 5, standard deviation = 2.2

Appendix B

Ion Flux distributions of GCR for ECOSat-2

Ion flux data used for SEE ion failure rates calculated for ECOSat-2 evaluation orbit (600km sun synchronous) are list in this appendix. These fluxes where generated using Spenvis.

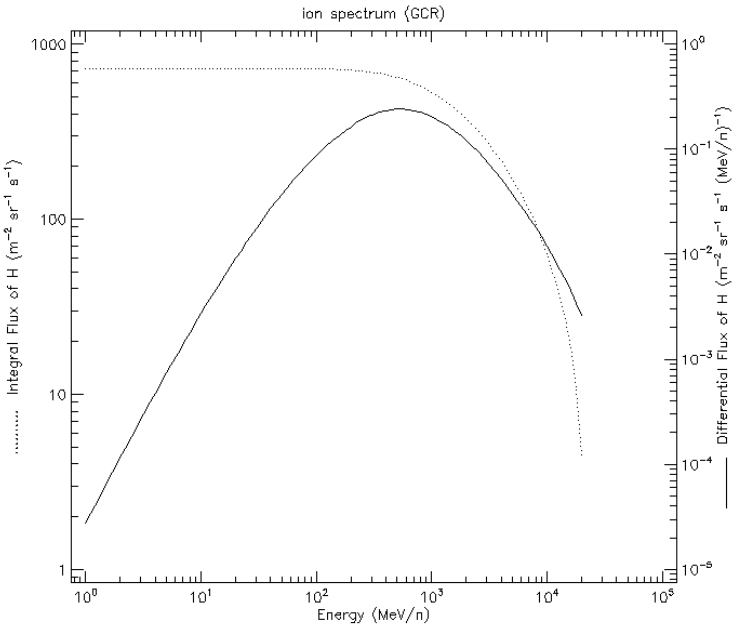

Figure B.1: H ion flux of GCR for ECOSat-2 evaluation orbit

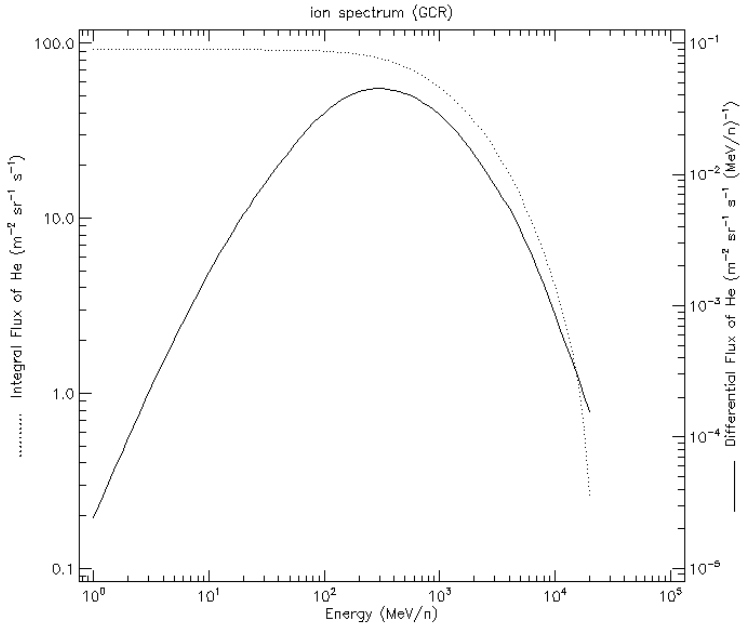

Figure B.2: He ion flux of GCR for ECOSat-2 evaluation orbit

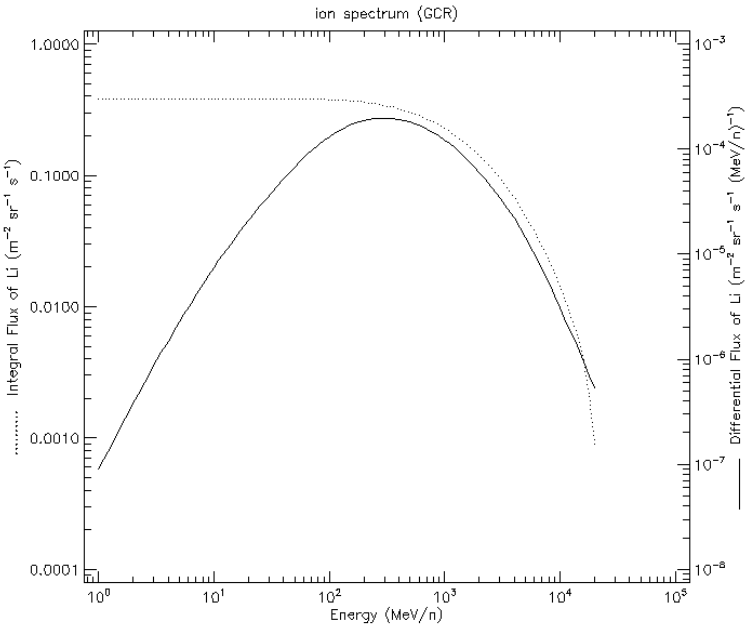

Figure B.3: Li ion flux of GCR for ECOSat-2 evaluation orbit

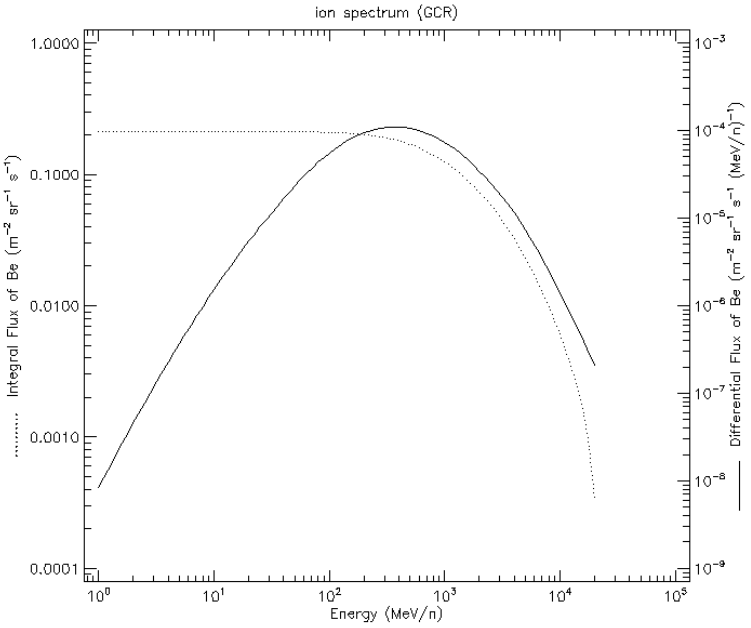

Figure B.4: Be ion flux of GCR for ECOSat-2 evaluation orbit

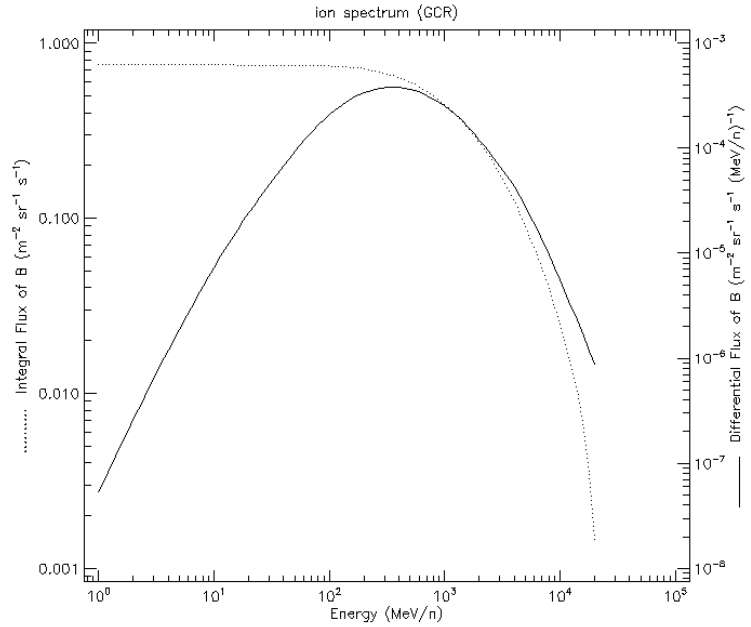

Figure B.5: B ion flux of GCR for ECOSat-2 evaluation orbit

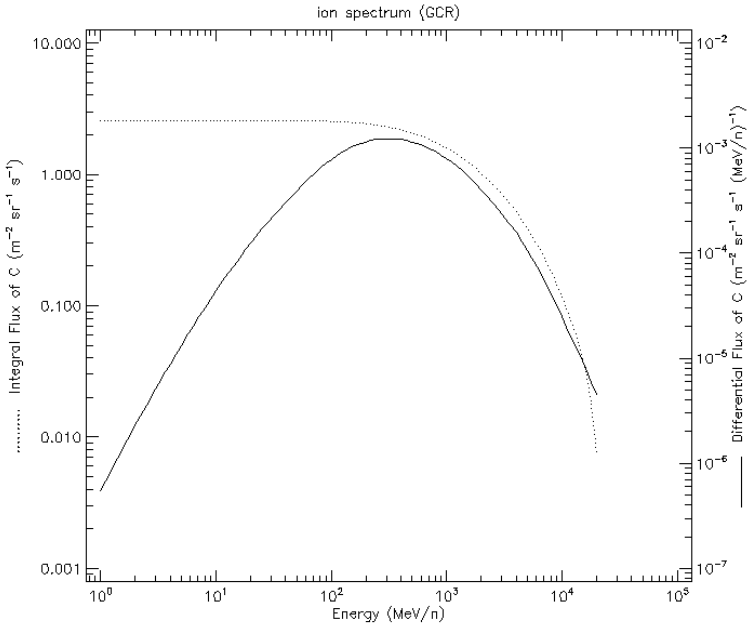

Figure B.6: C ion flux of GCR for ECOSat-2 evaluation orbit

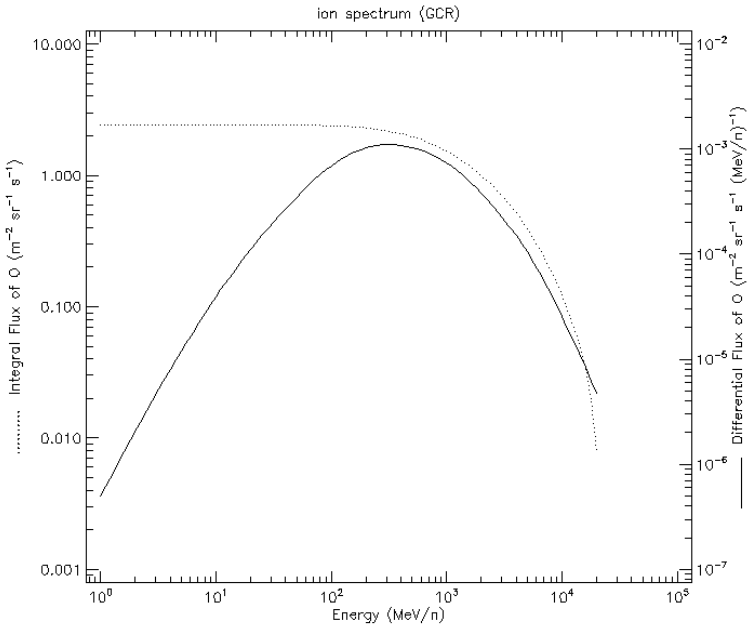

Figure B.7: O ion flux of GCR for ECOSat-2 evaluation orbit

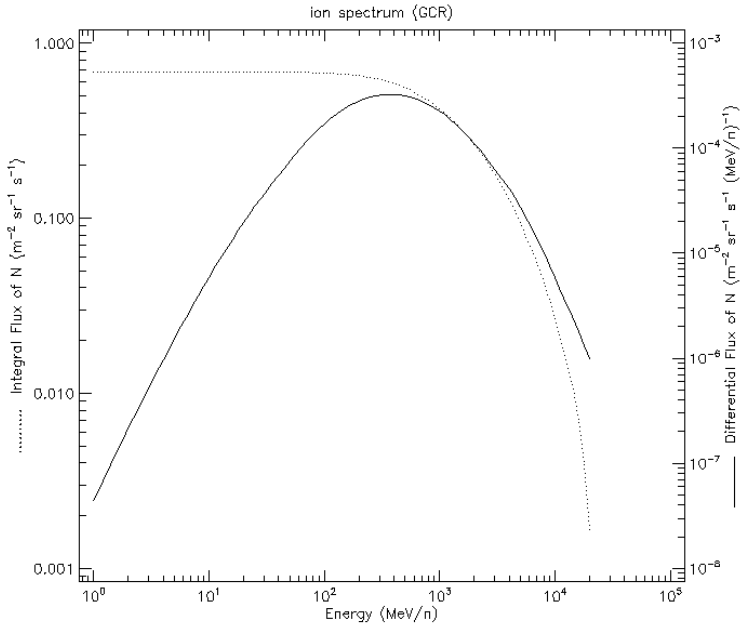

Figure B.8: N ion flux of GCR for ECOSat-2 evaluation orbit

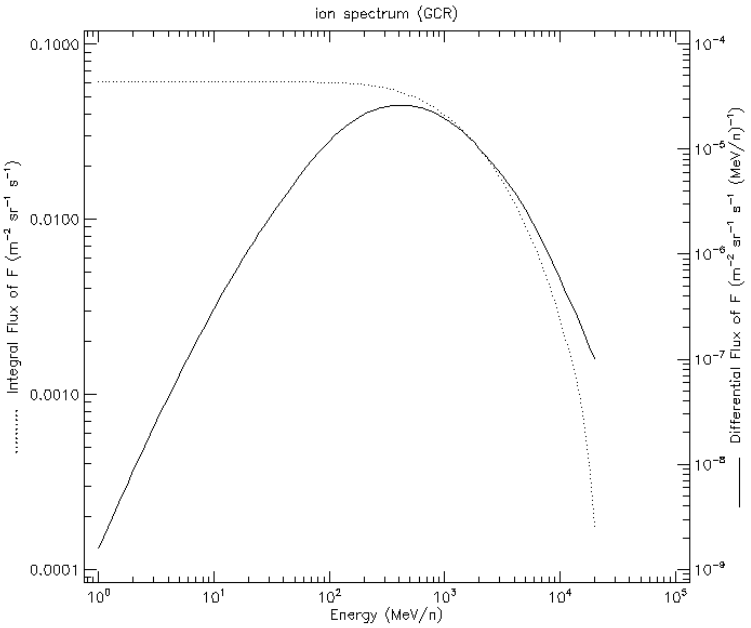

Figure B.9: F ion flux of GCR for ECOSat-2 evaluation orbit

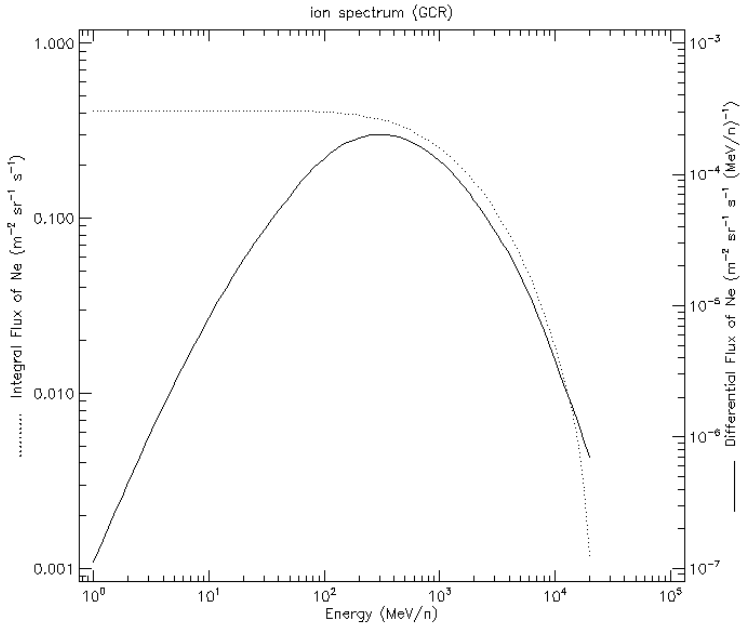

Figure B.10: Ne ion flux of GCR for ECOSat-2 evaluation orbit

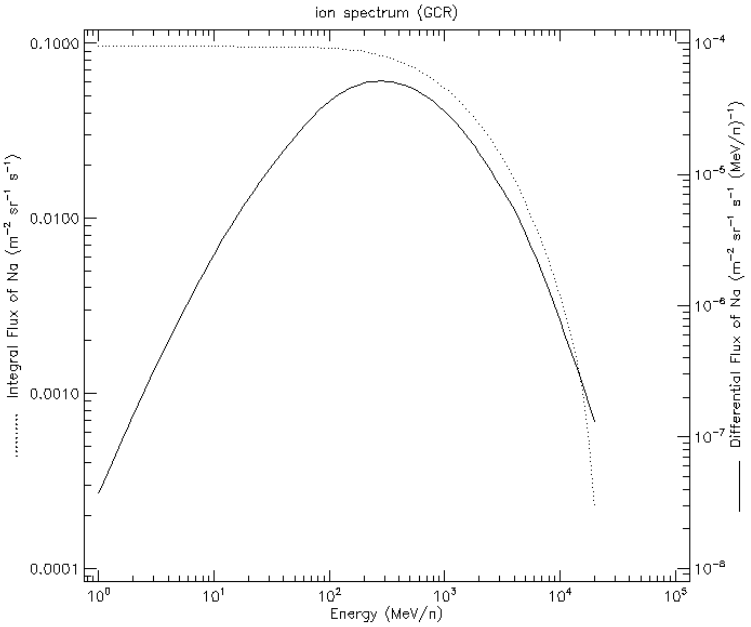

Figure B.11: Na ion flux of GCR for ECOSat-2 evaluation orbit

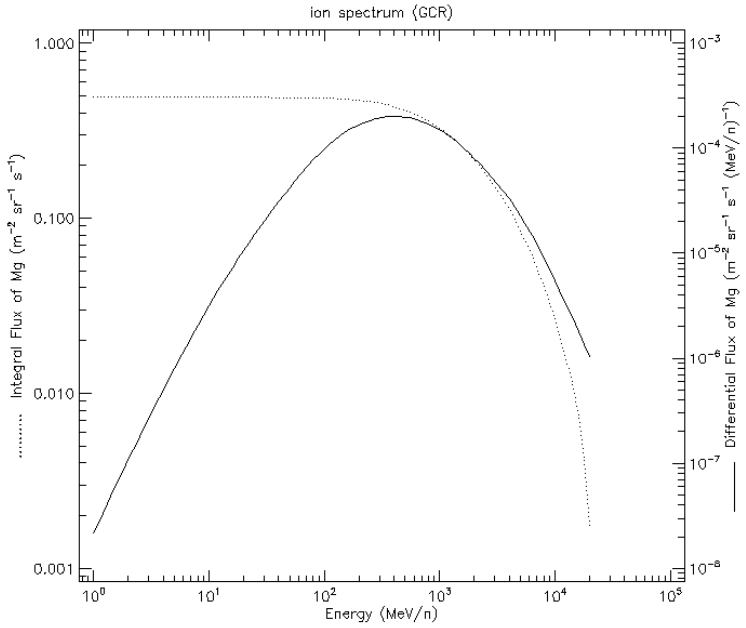

Figure B.12: Mg ion flux of GCR for ECOSat-2 evaluation orbit

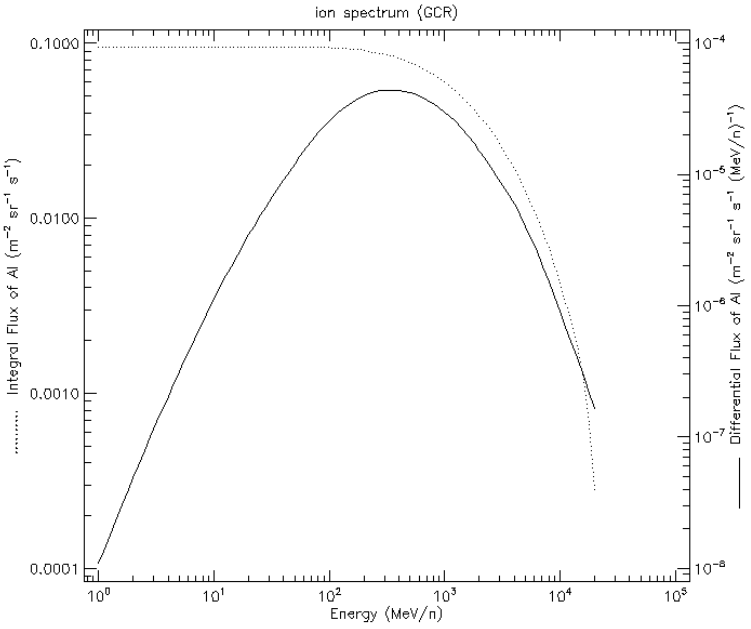

Figure B.13: Al ion flux of GCR for ECOSat-2 evaluation orbit

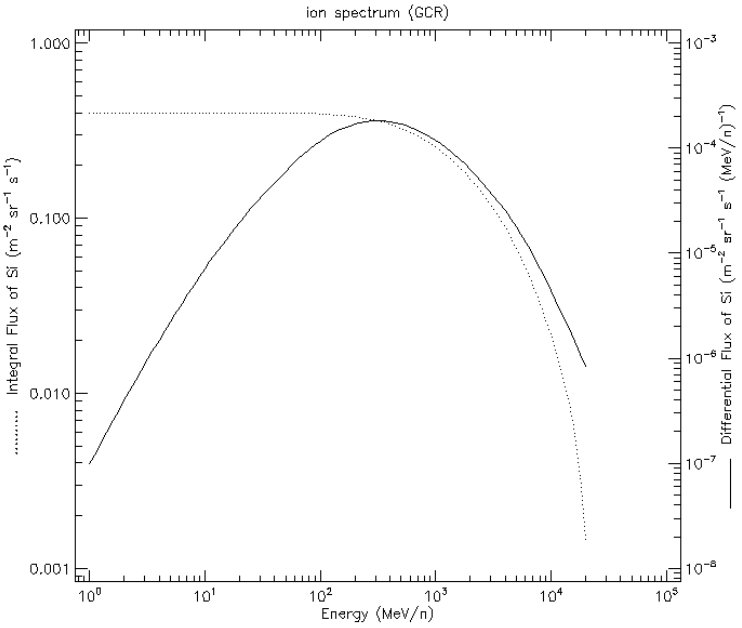

Figure B.14: Si ion flux of GCR for ECOSat-2 evaluation orbit

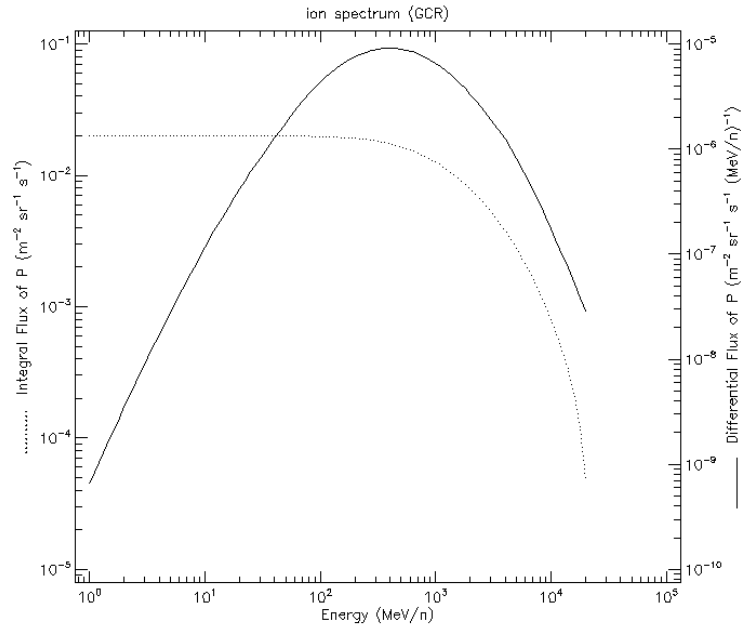

Figure B.15: P ion flux of GCR for ECOSat-2 evaluation orbit

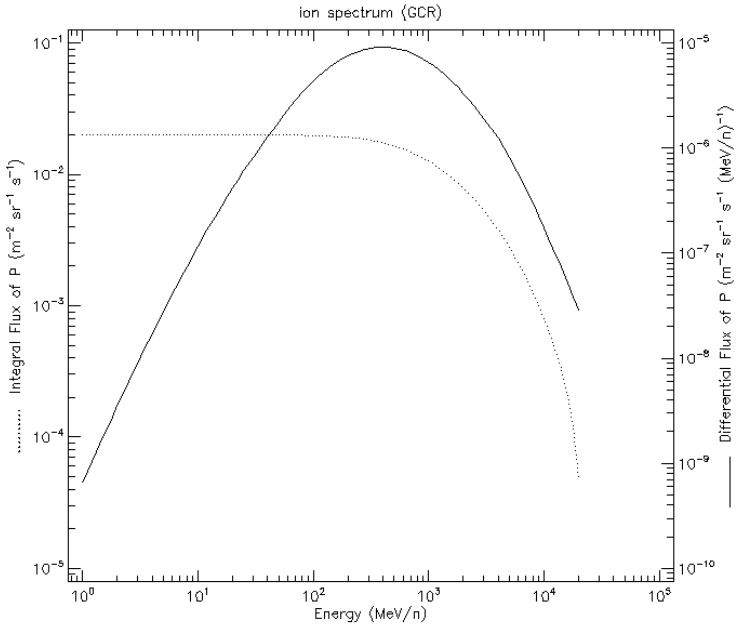

Figure B.16: S ion flux of GCR for ECOSat-2 evaluation orbit

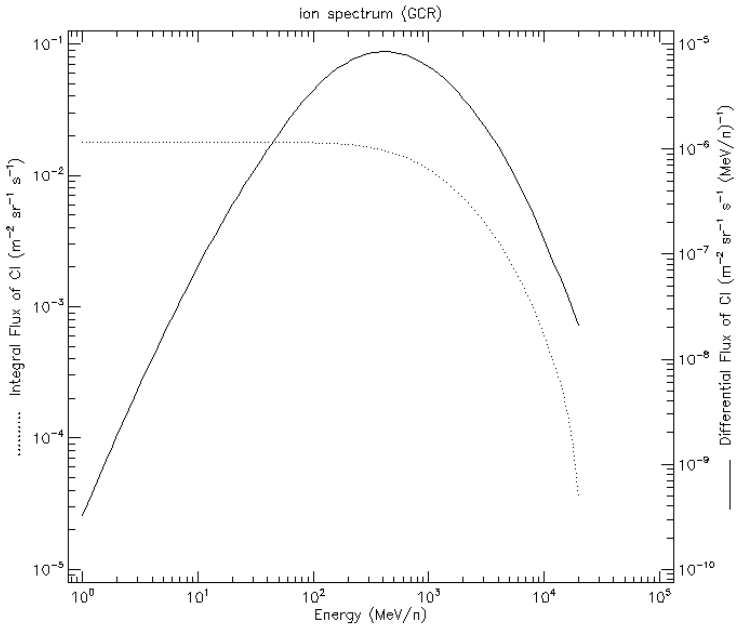

Figure B.17: Cl ion flux of GCR for ECOSat-2 evaluation orbit

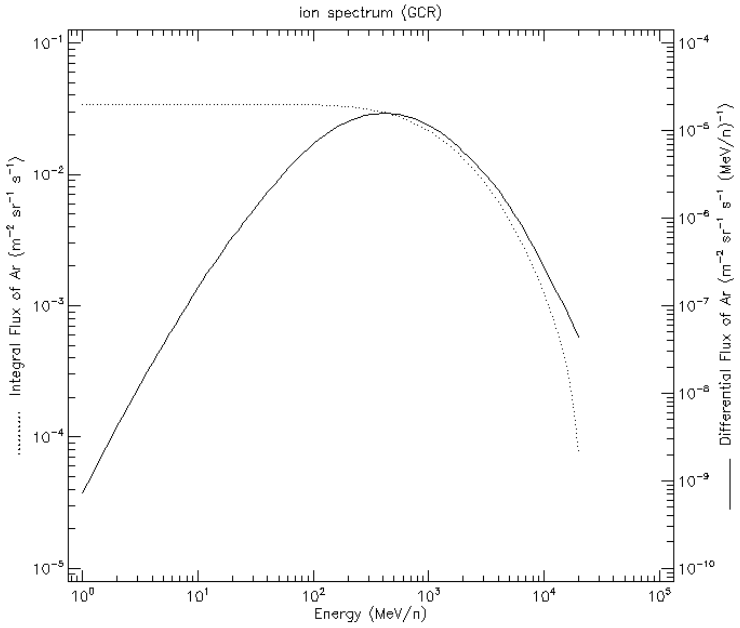

Figure B.18: Ar ion flux of GCR for ECOSat-2 evaluation orbit

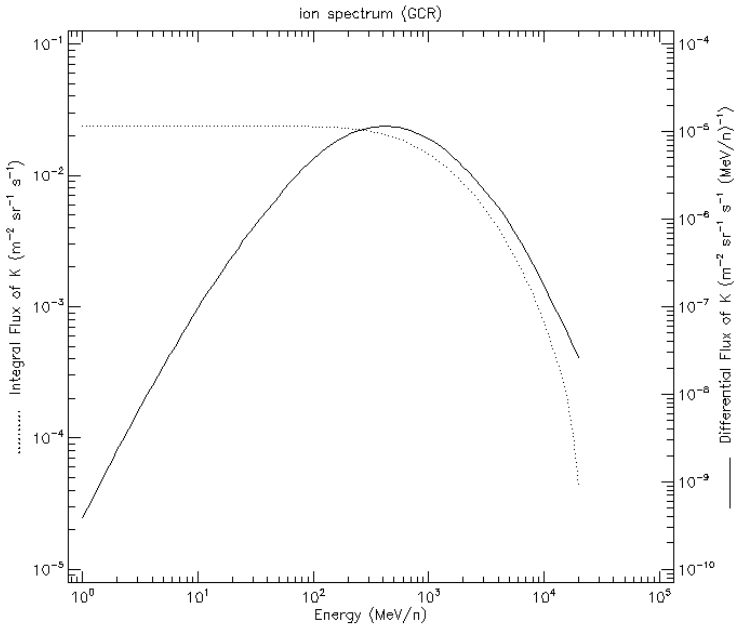

Figure B.19: K ion flux of GCR for ECOSat-2 evaluation orbit

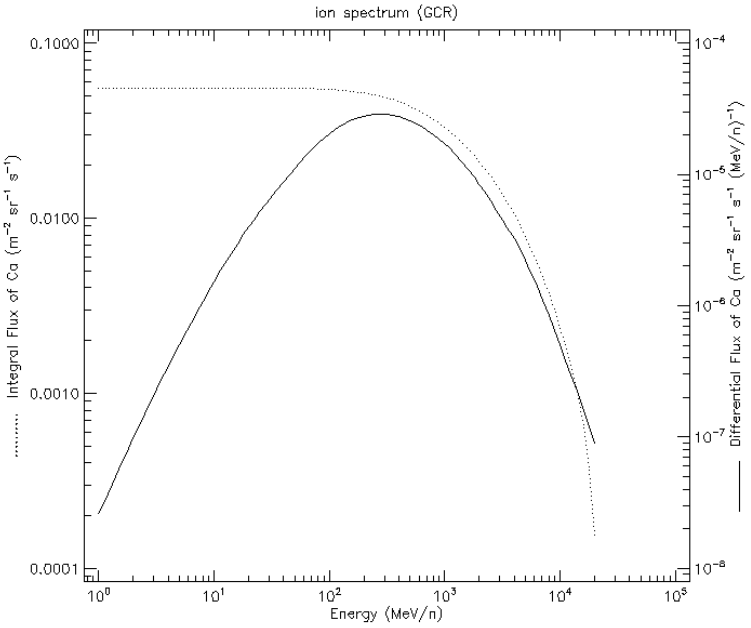

Figure B.20: Ca ion flux of GCR for ECOSat-2 evaluation orbit

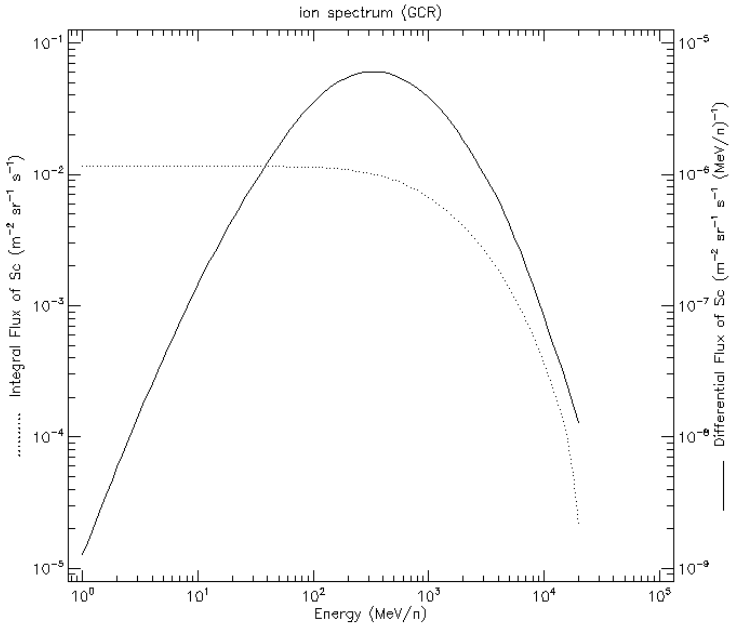

Figure B.21: Sc ion flux of GCR for ECOSat-2 evaluation orbit

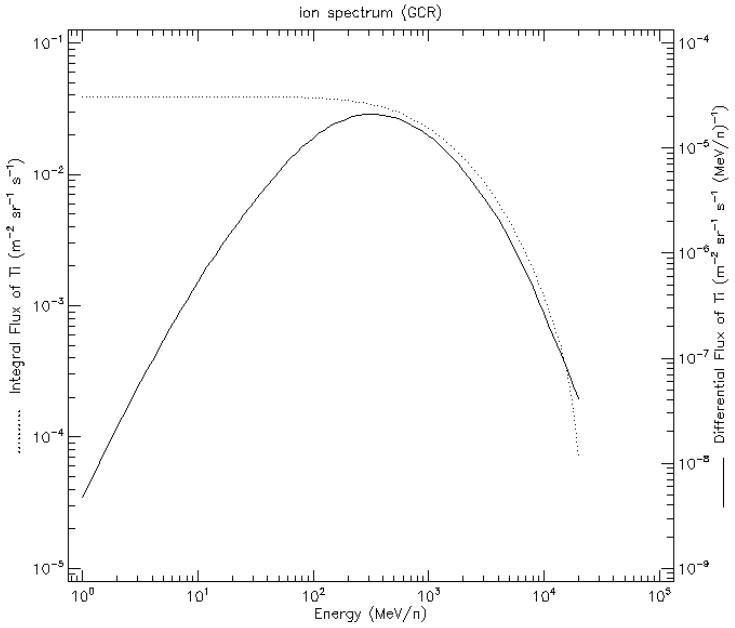

Figure B.22: Ti ion flux of GCR for ECOSat-2 evaluation orbit

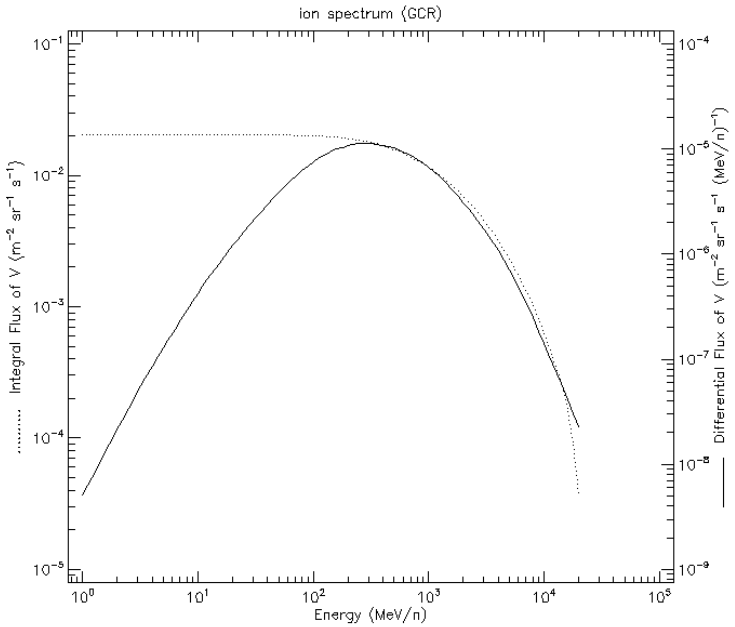

Figure B.23: V ion flux of GCR for ECOSat-2 evaluation orbit

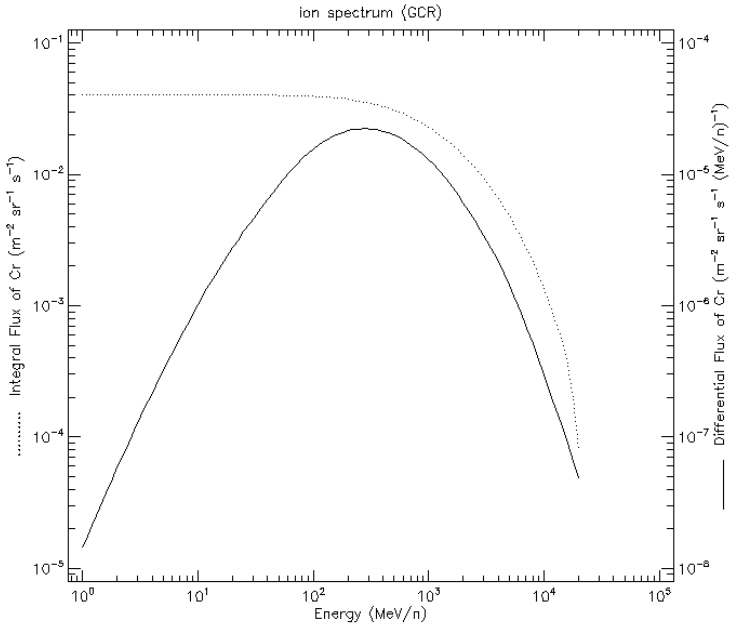

Figure B.24: Cr ion flux of GCR for ECOSat-2 evaluation orbit

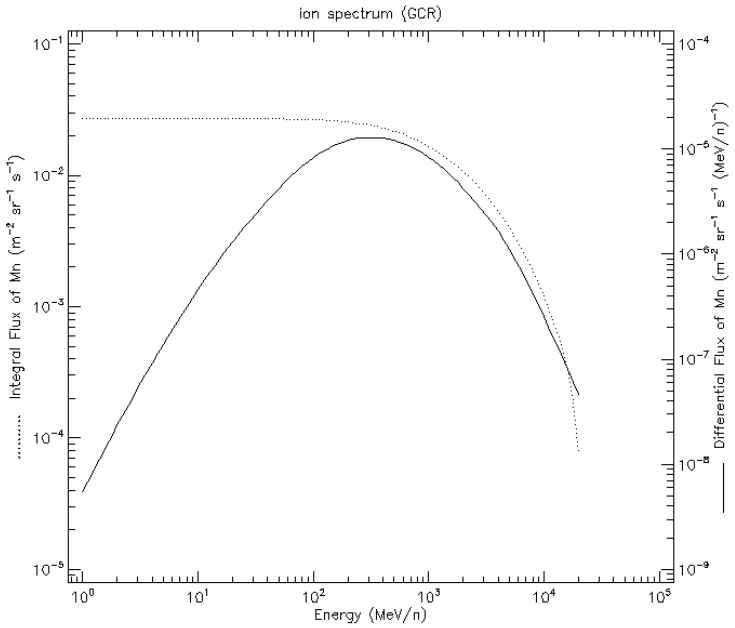

Figure B.25: Mn ion flux of GCR for ECOSat-2 evaluation orbit

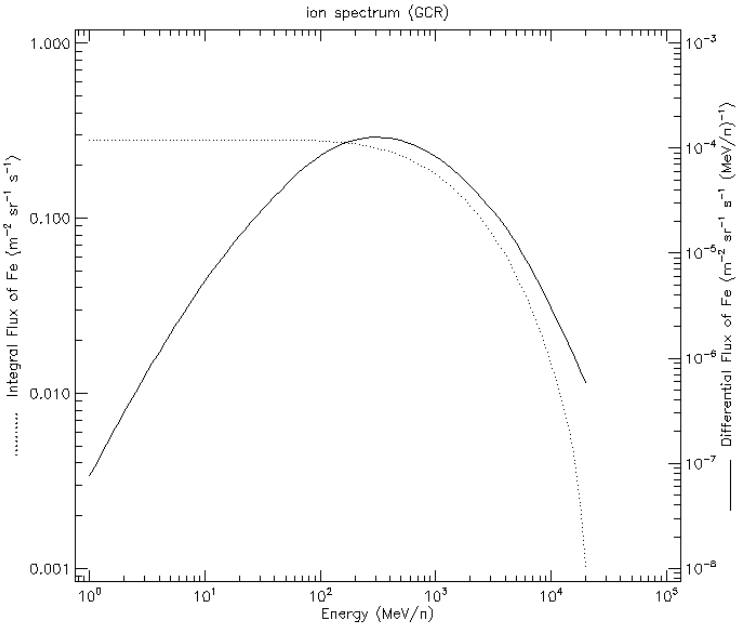

Figure B.26: Fe ion flux of GCR for ECOSat-2 evaluation orbit

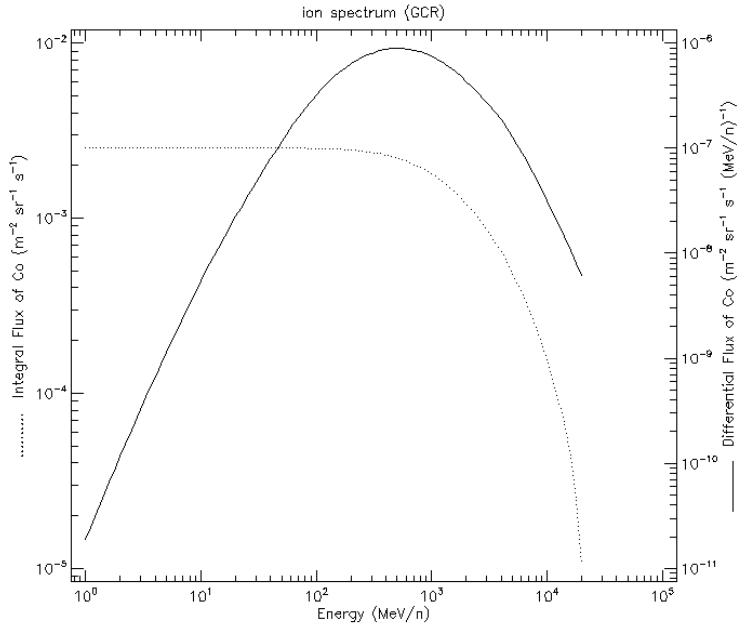

Figure B.27: Co ion flux of GCR for ECOSat-2 evaluation orbit

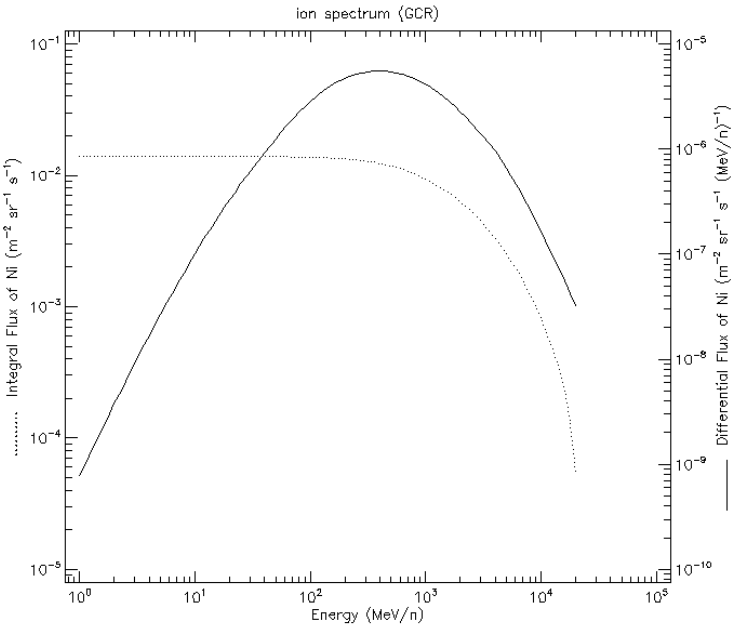

Figure B.28: Ni ion flux of GCR for ECOSat-2 evaluation orbit

Appendix C

Power Budget

Power Budget

File Name	C:\SVN\Budgets\Power Budget Cass.xlsx
Last Modified	11/16/2015 5:20:30 PM

Summary

Power Budget

Regulation Efficiency	90%	**%**
Average Consumption	3.38	**W**
Average Generation	3.49	**W**
Margin	2.97	**%**
Average Consumption Night	3.38	**W**

Nominal Case Orbit DOD:

Total Power Draw	3.04	**W**
Battery Energy Drained In Night Phase	2.00	**WHr**
Battery Energy Charged in Day Phase	2.16	**WHr**
Battery Margin	7.47	**%**
DOD	9.66	**%**

Consumption	Note	PWR(W)	Duty Cycle Scenario 1	Night	Average
Payload	total for estimate	0.511	0.1	Yes	0.0511
AC S	total for estimate	4.027	0.1	Yes	0.4027
ADS/OBC	total for estimate	1.2	0.5	Yes	0.6
Modem	total for estimate	0.5	1	Yes	0.5
Tx	total for estimate	4.7	0.2	Yes	0.94
Rx	total for estimate	0.5	1	Yes	0.5
Regulation	total for estimate	0.05	1	Yes	0.05
Heaters	100mW per board	0.2	0	Yes	0
0	0	0	0	0	0
0	0	0	0	0	0
0	0	0	0	0	0
0	0	0	0	0	0
0	0	0	0	0	0
0	0	0	0	0	0

Power Budget

Storage

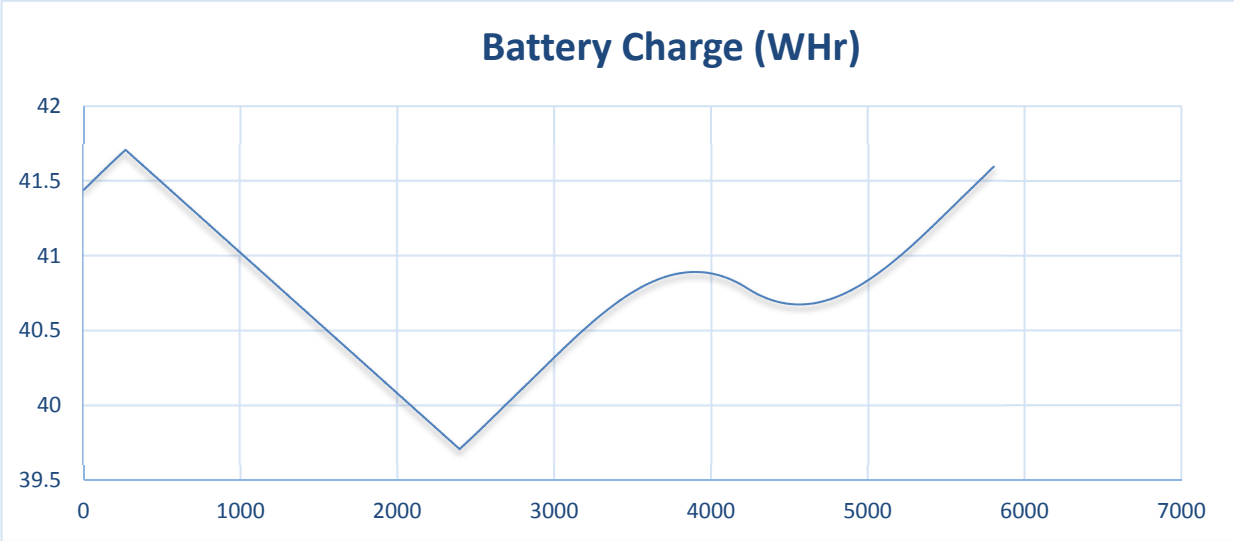

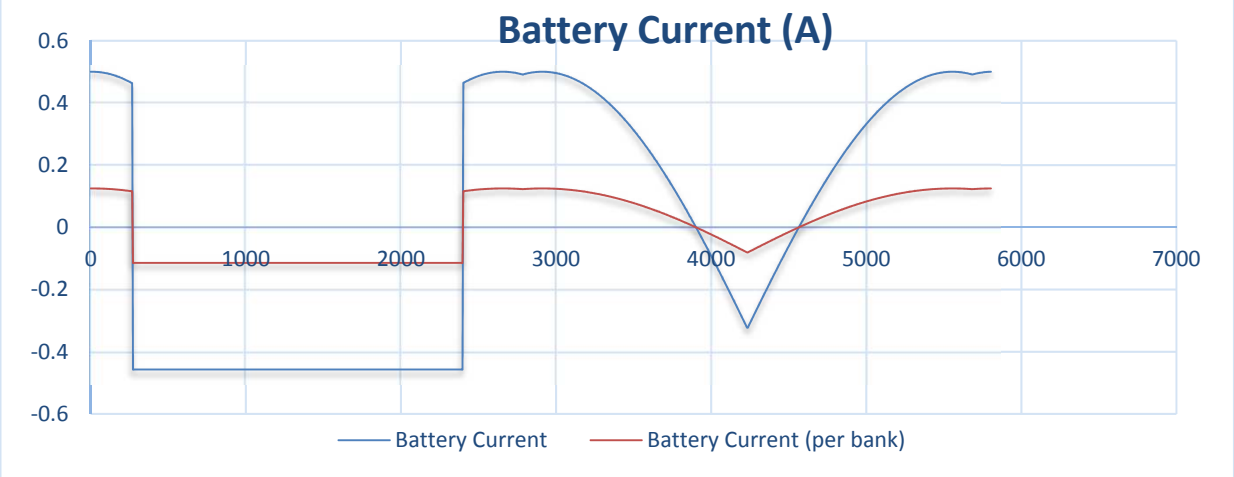

Battery Specs:

Total Cell Mass	0.026	**Kg**
Cell Energy Density	133	**W/Kg**
Nominal Cell Voltage	3.7	**V**
Nominal Capacity	2800	**mAh**
Capacity Per Bank	20.72	**WHr**
Total Capacity	82.88	**WHr**
Battery Life @ 10% DOD	20000	**Cl**
Battery Cycles	5433.911	**Cl/yr**
Expected Battery life	3.68059	**Years**

Nominal Case Orbit DOD:

Total Power Draw	3.38	**W**
Battery Power Used	2.00	**WHr**
Battery Power Charged	2.16	**WHr**
DOD per Battery Bank	9.66	**%**
DOD Full Battery System	2.41	**%**
Battery Margin	0.07	

Power Budget

Generation:

Panel	Surface Area	Fill Factor	Max Generat	Average (W)	Average(W/orbit)	Peak
1	300	0.7	7.01687448	0.027018416	0.156802855	0.39628268
2	100	0	0	0	0	0
3	300	0.7	7.01687448	0.310549808	1.802292798	0.97655627
4	100	0	0	0	0	0
5	300	0.7	7.01687448	1.580280899	9.171246652	7.01684715
6	300	0.7	7.01687448	1.567689019	9.098168988	7.01687068

Average	3.49	W
Peak	7.08	W

Cell Generation	37.88	mW/cm^2
Generation Efficiency	0.90	%
EOL Degredation	0.98	%

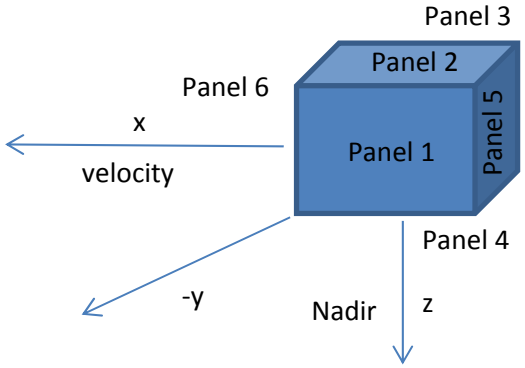

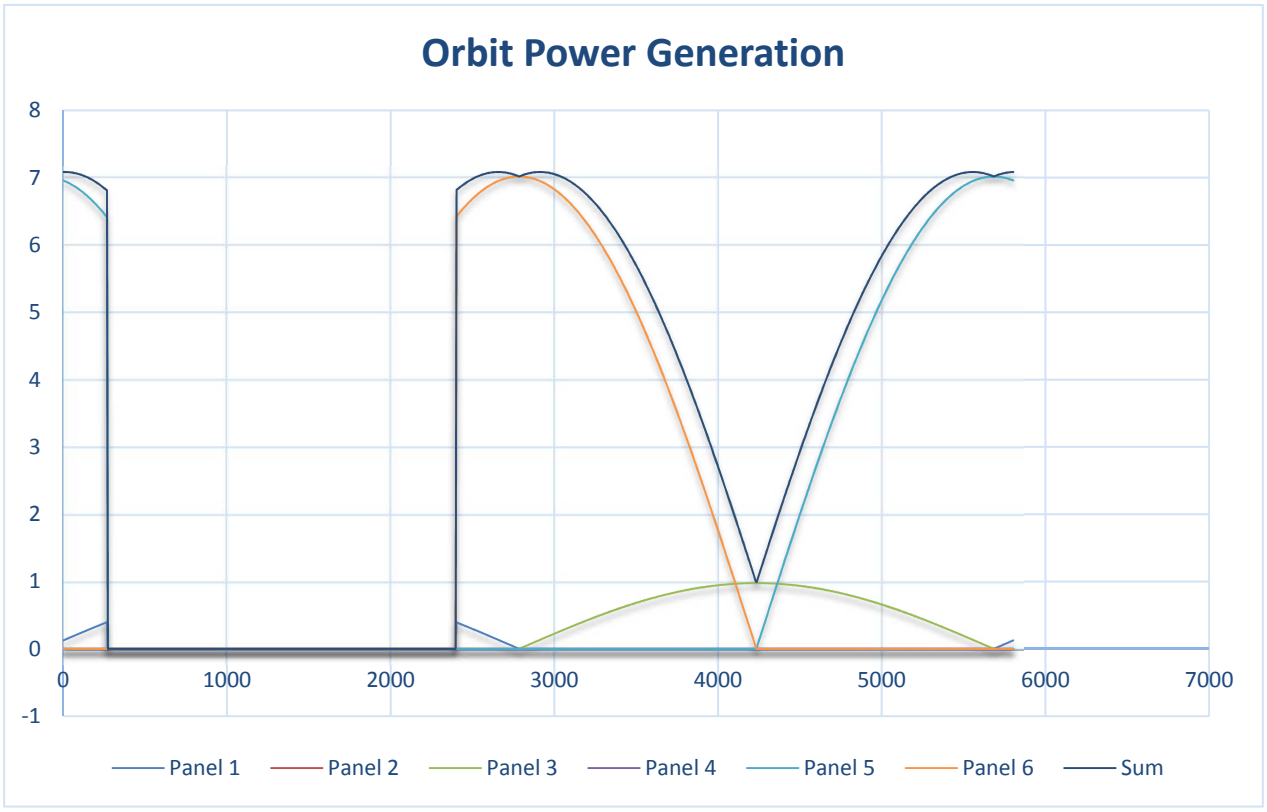

Power Budget

Orbit:

Inclination	98	degrees	Period	5803.555	s
Longitude of Assending Node	60	degrees	Inclination	1.710423	rad
Argument of perigee	114.575	degrees	Longitude of Assending Node	3.141593	rad
Eccentricity	0.000674	0	Argument of perigee	1.999711	rad
Semimajor Axis	6980	km	Mean Anomaly	2.127639	rad
Mean Anomaly at t0	128	degrees	Time Step	5.803555	s
Local Time at Longitude 0	20	0	perigee	595.2976	km
Attitude	Nadir Pointing		apogee	604.7024	km

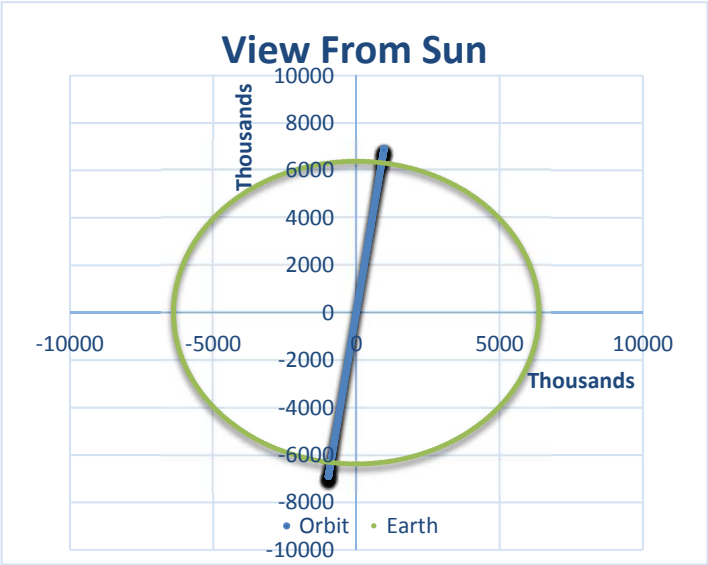

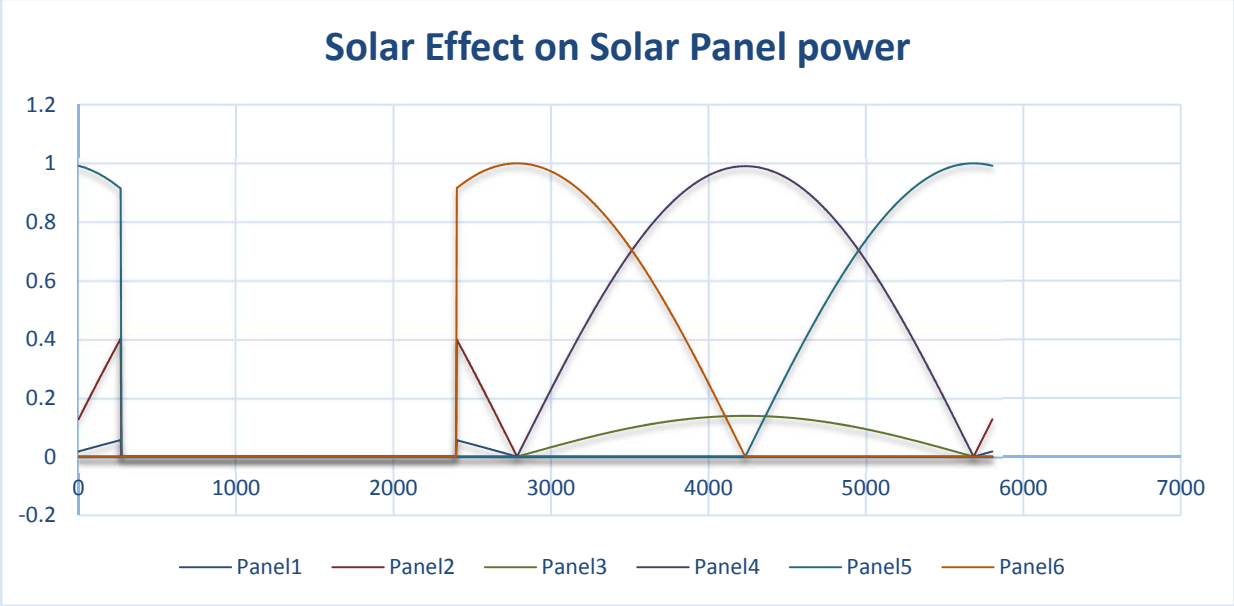

Power Budget

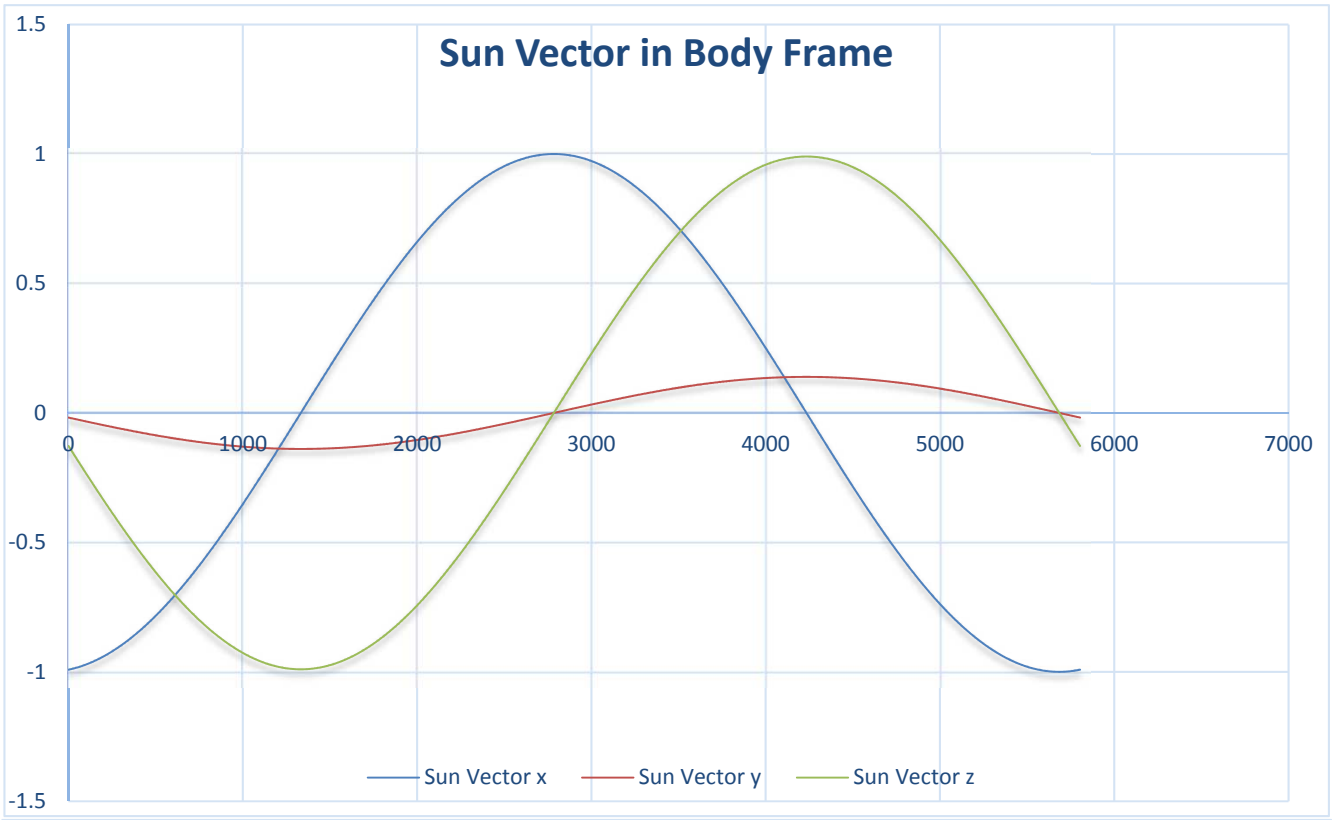

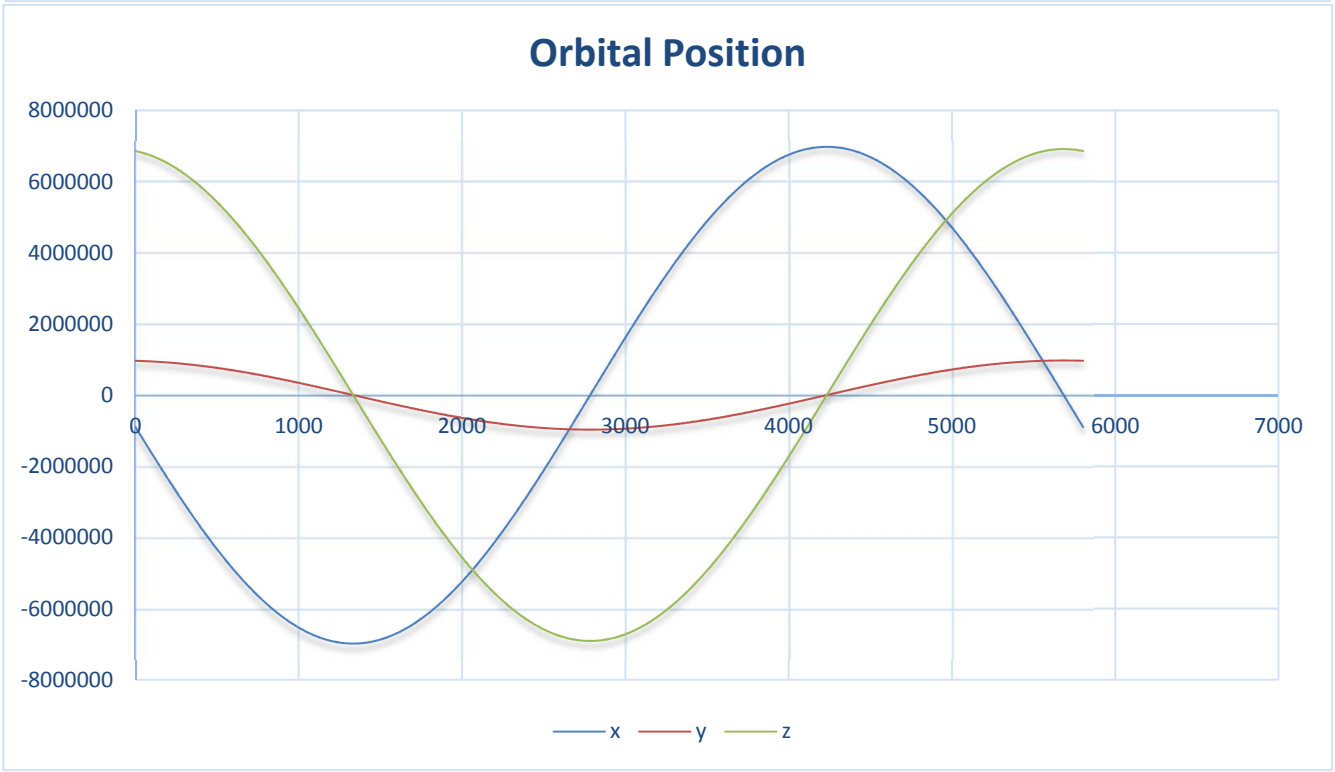

Appendix D

Matlab Code

This section contains matlab functions and scripts that where created to simplify the calculation of the reliability estimation models.

D.0.1 Hardware related scripts and functions

```
function [ lambda ] = SEEFailureRate( Fp, Fi, sigmai, LET, LET25 )
%UNTITLED7 Summary of this function goes here
%   Detailed explanation goes here

lambdaProton = 3600*2*pi*trapz(Fp(:,1),Fp(:,2).*sigmaP(Fp(:,1),LET25,sigmai));

lambdaIon = 3600*2*pi*etaF_ions(LET,Fi)*sigmai;

lambda = lambdaProton + lambdaIon;
end
```

```
function [ lambda ] = ThermalMechanicalFailureRate( lambda1, N, lambda2,
    yearManufacture, caseTemp, thermalCycle, Power, ThermalResistance,
    thernalCyclesPerYear, boardCTE, packageCTE, lambda3, PiI, lambdaEOS,
    tauon, tauoni, tauoff )
%UNTITLED4 Summary of this function goes here
%   boardCTE typical 16ppm/C FR4, 21.5ppm/C expoxy package
%   cycles per year = 365*24 / orbital period (hrs)   5673 for 600km SS
%   since systems are considered all electrical environments the interface
% PiI and lambdaEOS are 0

temp1 = ((lambda1*N*exp(-0.35*(yearManufacture-1998))+lambda2))*(PiT
    (3480,328,caseTemp,ThermalResistance,Power)*tauoni)/(tauon+tauoff);
temp2 = (0.00275*PiA(boardCTE, packageCTE)*(PiN(thernalCyclesPerYear)*
    thermalCycle^(0.68))*lambda3);
temp3 = PiI*lambdaEOS;

lambda = (temp1 + temp2 + temp3)*10^(-9);

end
```

```
function [ lambda ] = TIDFailureRate( TID, Beta, DoseRate )
%UNTITLED8 Summary of this function goes here
%   Dose Rate per hour
%   TID in MeV radToMeV() can be used
 K = KTDF(TID, Beta);

 lambda = K*DoseRate*3600;

end
```

```
function [ sigmaP ] = sigmaP( EP, LC, sigmai )
%UNTITLED6 Summary of this function goes here
%   Detailed explanation goes here
P0 = (4*10^(-6)).*exp(-(0.134+9./EP).*LC);

if LC < 1
sigmaP = ((((1.503*10^(-5))*LC^(-1.425))+P0).*sigmai);
elseif (LC >= 1)&&(LC < 5)
sigmaP = ((((1.58*10^(-5))*LC^(-2.56))+P0).*sigmai);
else
sigmaP = ((P0).*sigmai);
end

end
```

```
function [ fitresult , gof] = createFit(SEUtempx, SEUtempy)
%CREATEFIT(SEUTEMPX,SEUTEMPY)
%  Create a fit.
%
%  Data for 'Ion Cross Section SEU' fit:
%      X Input : SEUtempx
%      Y Output: SEUtempy
%  Output:
%       fitresult  : a fit object representing the fit.
%       gof : structure with goodness-of fit info.
%
%  See also FIT, CFIT, SFIT.

%  Auto-generated by MATLAB on 03-May-2016 14:48:45


%% Fit: 'Ion Cross Section SEU'.
[xData, yData] = prepareCurveData( SEUtempx, SEUtempy );

```

```
% Set up fittype and options.
ft = fittype( 'a*(1-real(exp(-((x-b)/22)^.5)))', 'independent', 'x', 'dependent', 'y' );
opts = fitoptions( 'Method', 'NonlinearLeastSquares' );
opts.Display = 'Off';
opts.Robust = 'Bisquare';
opts.StartPoint = [0.876711128995048 0.604160393243033];

% Fit model to data.
[ fitresult , gof] = fit( xData, yData, ft, opts );

% Plot fit with data.
figure( 'Name', 'Ion Cross Section SEU' );
plot( fitresult , xData, yData, 'predobs', 0.9 );
% Label axes
xlabel 'LET MeVcm^2/mg'
ylabel '\sigma_i SEU'
grid on
```

```
function [ sum ] = etaF_ions( LET_thresh, Ion_Flux )
%UNTITLED3 Summary of this function goes here
%   Detailed explanation goes here

Filter = eta(Ion_Flux(:,1),LET_thresh);
temp = zeros(length(Ion_Flux(:,1)),29);
for j = [2:29]
    temp(:,j) = Ion_Flux(:,j).*Filter(:,j);
end
sum = 0;
for j = [2:29]
    sum = sum+trapz(Ion_Flux(:,1),temp(:,j));
end
end
```

```
function [ sum ] = etaP( threshold, P_Flux )
%UNTITLED4 Summary of this function goes here
%   Detailed explanation goes here
P_LET =
    [0.040000000000000,0.534000000000000;0.100000000000000,0.505000000000000;0.200000000000

Filter = zeros(length(P_Flux(:,1)),2);
Filter(:,1) = P_Flux(:,1);
[b,i,j] = unique(P_LET(:,1));
Filter(:,2) = interp1(b,P_LET(i,2),P_Flux(:,1),'pchip') > threshold;
sum = 0;
for i = [2:length(P_Flux)]
    sum = sum+(((P_Flux(i,2).*Filter(i,2) + P_Flux(i-1,2).*Filter(i-1,2))/2)*(
        P_Flux(i,1)-P_Flux(i-1,1)));
end

end
```

```

figure1 = figure;
axes1 = axes('Parent',figure1);
hold(axes1,'on');
temp = HerculesR.*MicronR.*CANTRXR.*DSPR.*Codec.*GyroR.*AccelR.*MagR
    .*Reg18R.*Reg33R;
plot([0:10*24*365],temp,'DisplayName','Total')
plot([0:10*24*365],HerculesR,'DisplayName','TMS570')
plot([0:10*24*365],DSPR,'DisplayName','TMS320')
plot([0:10*24*365],MicronR,'DisplayName','e.MMC')
plot([0:10*24*365],Codec,'DisplayName','TLV320 Codec')
plot([0:10*24*365],CANTRXR,'DisplayName','CAN TRX')
plot([0:10*24*365],GyroR,'DisplayName','Gyroscope')
plot([0:10*24*365],AccelR,'DisplayName','Accelerometer')
plot([0:10*24*365],MagR,'DisplayName','Magnetometer')
```

```
15 plot([0:10*24*365],Reg18R,'DisplayName','1.8V Regulator')
16 plot([0:10*24*365],Reg33R,'DisplayName','3.3V Regulator')
17
18
19 xlabel('Time (hrs)');
20 ylabel(' Reliability ');
21 legend1 = legend(axes1,'show');
22 set(legend1 ,...
23     'Position',[0.763690477627374 0.626587306128608 0.121428569991674
           0.165476185934884]);
24
25 annotation(figure1,'textbox' ,...
26     [0.651785714285714 0.546619048825332 0.232142857142857
           0.0642857130794301],...
27     'String',{sprintf('R(2 years) = %0.3f',temp(2*24*365))},...
28     'FitBoxToText','on');
29 line([17520  17520],[0  1])
30
31 ht = text(15500,0.5,'2 years');
32 set(ht,'Rotation',90)
33
34 ax = axes('position',[.65  .175  .25  .25], 'XLim',[17520-(24*30) 17520+(24*30)],'
       YLim',[1-1.2*(1-temp(2*24*365)) 1]);
35 hold(ax,'on');
36 box on
37
38 plot([0:10*24*365],temp,'DisplayName','Total')
39 plot([0:10*24*365],HerculesR,'DisplayName','TMS570')
40 plot([0:10*24*365],DSPR,'DisplayName','TMS320')
41 plot([0:10*24*365],MicronR,'DisplayName','e.MMC')
42 plot([0:10*24*365],Codec,'DisplayName','TLV320 Codec')
43 plot([0:10*24*365],CANTRXR,'DisplayName','CAN TRX')
44 plot([0:10*24*365],GyroR,'DisplayName','Gyroscope')
45 plot([0:10*24*365],AccelR,'DisplayName','Accelerometer')
46 plot([0:10*24*365],MagR,'DisplayName','Magnetometer')
```

```
function K = KTDF( D,B )
%UNTITLED Summary of this function goes here
%   Detailed explanation goes here
K = B*((-log(0.05))^(1/B))/(D);

end
```

```
function [ rad ] = MeVToRad( mev )
%UNTITLED10 Summary of this function goes here
%   Detailed explanation goes here

rad = mev / (6.2415*10^7);

end
```

```
function [ MeV ] = radToMeV( rad )
%UNTITLED9 Summary of this function goes here
%   Detailed explanation goes here

MeV = rad * 6.2415*10^7;

end
```

```
function [ output ] = PiA( AlphaS, AlphaC )
%UNTITLED Summary of this function goes here
%   Detailed explanation goes here

output = 0.06*(abs(AlphaS-AlphaC))^1.68;
end
```

```
function [ output ] = PiN( Ni )
%UNTITLED2 Summary of this function goes here
%   Detailed explanation goes here

```

```
5  if Ni > 8760
6      output = 1.7*Ni^(0.6);
7  else
8      output = Ni^(0.76);
9  end
10
11
12 end
```

```
1  function [ output ] = PiT( A, B, tc, thermalResistance, Power )
2  %UNTITLED3 Summary of this function goes here
3  % low voltage BiCMOS A,B 3480,328
4  % high voltage BiCMOS A,B 4640,328
5  % Numerical AsGa A,B 3480,373
6  % MMIC AsGa A,B 4640,373
7
8  tj = tc + Power*thermalResistance;
9
10 output = exp((A/B)*((1/(273+tj))));
11
12
13 end
```

```
1  function [ output_args ] = PlotReliability(time, LambdaTM, LambdaSEE,
       LambdaTID, beta )
2  %UNTITLED12 Summary of this function goes here
3  %   Detailed explanation goes here
4
5
6  figure1 = figure;
7  axes1 = axes('Parent',figure1);
8  hold(axes1,'on');
9  plot(time, calculate_reliability (time,LambdaSEE,1),'DisplayName','SEE','
       LineWidth',2,'LineStyle',':')
10 plot(time, calculate_reliability (time,LambdaTID,beta),'DisplayName','TID','
```

```
    LineWidth',1,'LineStyle','--')
plot(time, calculate_reliability (time,LambdaTM,1),'DisplayName','TM','
    LineWidth',2,'LineStyle','-.')
temp = calculate_reliability (time,LambdaTM,1).*calculate_reliability(time,
    LambdaTID,beta).*calculate_reliability(time,LambdaSEE,1);
plot(time,temp,'DisplayName','Total','LineWidth',1)
xlabel('Time (hrs)');
ylabel(' Reliability ');
legend1 = legend(axes1,'show');
set(legend1 ,...
    'Position',[0.763690477627374 0.626587306128608 0.121428569991674
        0.165476185934884]);

annotation(figure1,'textbox' ,...
    [0.651785714285714 0.546619048825332 0.232142857142857
        0.0642857130794301],...
    'String',{sprintf('R(2 years) = %0.3f',temp(2*24*365))},...
    'FitBoxToText','on');
line([17520 17520],[0 1])

ht = text(15500,0.5,'2 years');
set(ht,'Rotation',90)

ax = axes('position',[.65 .175 .25 .25], 'XLim',[17520-(24*30) 17520+(24*30)],'
    YLim',[1-1.2*(1-temp(2*24*365)) 1]);
hold(ax,'on');
box on
plot(time, calculate_reliability (time,LambdaSEE,1),'DisplayName','SEE','
    LineWidth',2,'LineStyle',':')
plot(time, calculate_reliability (time,LambdaTID,beta),'DisplayName','TID','
    LineWidth',1,'LineStyle','--')
plot(time, calculate_reliability (time,LambdaTM,1),'DisplayName','TM','
    LineWidth',2,'LineStyle','-.')
plot(time,temp,'DisplayName','Total','LineWidth',1)

```

```
output_args = temp;
end
```

```
function lambda = PCBlambda(Tamb,layers,Nt,S,Np,PiL,ni,DeltaT)
%UNTITLED Summary of this function goes here
%   Detailed explanation goes here

lambda = 5e-3*(exp(1740*(1/303 - 1/(273+Tamb))))*(0.7*layers^(0.5))*((Nt
    *(1+Nt/S)^0.5)+Np*(1+0.1*(S^0.5)/3)*PiL)*(1+3e-3*(PiN(ni)*DeltaT))*1e
    -9;
end
```

D.0.2 Information related scripts and functions

```
function [ output ] =  calculate_reliability ( time, lambda, beta)
%UNTITLED5 Summary of this function goes here
%   Detailed explanation goes here
output = exp(-((lambda.*time)./beta).^beta);

end
```

```
function unc_err = calculate_rs_uncorrected(hazardRate, SampleTime, memsize,
    symbolsize, blocksize, corr_capability)

pd = makedist('poisson','lambda',blocksize*symbolsize*(1-exp(-hazardRate*
    SampleTime)));
pd2 = makedist('poisson','lambda',floor(((memsize*8)/(blocksize*symbolsize)))
    *(1-cdf(pd,corr_capability)));

%iterate over  all  the blocks and find symbol errors

unc_err=8;
temp = rand(1,1,'single') < (1-cdf(pd2,unc_err-1));
while ~temp
```

```
    unc_err = unc_err - 1;
    temp = rand(1,1,'single') < (1-cdf(pd2,unc_err-1));
end
```

```
function createfigurecontour1(xdata1, ydata1, zdata1)
%CREATEFIGURE(XDATA1, YDATA1, ZDATA1)
%  XDATA1: contour x
%  YDATA1: contour y
%  ZDATA1: contour z

%  Auto-generated by MATLAB on 16-Apr-2016 16:18:00

% Create figure
figure1 = figure;
colormap('jet');

% Create axes
axes1 = axes('Parent',figure1);
hold(axes1,'on');

% Create contour
[c1,h1] = contour(xdata1,ydata1,zdata1,'LineWidth',1,...
    'LevelList',[0.05  0.1  0.2  0.4  0.6  0.7  0.75  0.8  0.85  0.9  0.935  0.95  0.96  0.975
        0.98  0.985  0.99  0.995  0.9995]);
clabel(c1,h1);

% Create xlabel
xlabel('Time (hrs)');

% Create ylabel
ylabel('ECC block size');

% Uncomment the following line to preserve the X-limits of the axes
% xlim(axes1,[0 4]);
box(axes1,'on');
```

```
% Set the remaining axes properties
set(axes1,'XGrid','on','YGrid','on');
```

```
function out = nchoosek2( n,j)
%UNTITLED2 Summary of this function goes here
%   Detailed explanation goes here
out = exp( gammaln(n+1)-gammaln(j+1)-gammaln(n-j+1) );

end
```

```
histogram=zeros(1,100);
for i = 1:100
    spmd
        done = false;
        while ~done
            temp = Simulation2((SERUIRate+SEUPRate)*2,(1.28*10^8)
                /32,5,136,3); %over 16MB
            done = true;
        end

    end
    histogram(i) = min([cell2mat(temp(1)),cell2mat(temp(2)),cell2mat(temp(3)),
        cell2mat(temp(4))]);
end
```

```
figure,plot(time,graph(1,:),'DisplayName','1 symbol correction')
hold on
plot(time,graph(2,:),'DisplayName','2 symbol correction')
plot(time,graph(3,:),'DisplayName','3 symbol correction')
plot(time,graph(4,:),'DisplayName','4 symbol correction')
plot(time,graph(5,:),'DisplayName','5 symbol correction')
plot(time,graph(6,:),'DisplayName','6 symbol correction')
plot(time,graph(7,:),'DisplayName','7 symbol correction')
```

```
function [ output] = Simulation( time, hazardRate, MemorySizeBytes, ts, n,
    correction )
```

```
%UNTITLED6 Summary of this function goes here
%   Detailed explanation goes here
tic
b = size(time);
Mem = repmat(uint8(0),b(2)+1,MemorySizeBytes);
error  = zeros(1,8);
t2=0;
terror  = 0;
for  t  = time %for the requested time simulate bit  errors
    %scrub
    if (mod(t,ts) == 0)
      for  c  = 0:(floor (MemorySizeBytes/n)-1)
          count = 0;
        for  d = 1:n
          if  Mem(t,d+c*n) > 0
              count = count+1;
          end
        end
        if  count > correction
          %more than t errors occured, declare  failure  and break somehow
          %output = t;
          %return;
          for  d = 1:n
                Mem(t,d+c*n) = 50;
           end
        else
           %clear correctable  errors
           for  d = 1:n
                Mem(t,d+c*n) = 0;
           end
        end
      end
    end

    %add errors
```

```
37      for i = [1:MemorySizeBytes] %for each symbol (Byte) determine if errors
            occured
38          error = uint8(rand(8,1)<(hazardRate));
39          Mem(t+1,i) = bitor(Mem(t,i),(error(1)*2^0 + error(2)*2^1 + error(3)*2^2
                + error(4)*2^3 + error(5)*2^4 + error(6)*2^5 + error(7)*2^6 + error
                (8)*2^7));
40      end
41  end %time steps
42  output = double(Mem);
43  toc
44  end
```

```
1   function [ output] = Simulation2( hazardRate, MemorySizeBytes, ts, n, correction
        )
2   %UNTITLED6 Summary of this function goes here
3   %   Detailed explanation goes here
4   %tic
5   Mem = repmat(uint8(0),ts+1,MemorySizeBytes);
6   error = zeros(1,8);
7   t2=0;
8   terror = 0;
9   t = 0;
10  output = 0;
11  while 1 %for the requested time simulate bit errors
12      %scrub
13      if (mod(t,ts) == 0)
14        for c = 0:(floor(MemorySizeBytes/n)-1)
15            count = 0;
16          for d = 1:n
17              if Mem(mod(t,ts+1)+1,d+c*n) > 0
18                  count = count+1;
19              end
20          end
21          if count > correction
22              %more than t errors occured, declare failure and break somehow
```

```
23              output = t;
24              disp( sprintf ('t  = %d hrs',output))
25              return
26          else
27              %clear correctable  errors
28              for  d = 1:n
29                  Mem(mod(t,ts+1)+1,d+c*n) = 0;
30              end
31          end
32        end
33      end
34
35
36      %add errors
37      for  i  = [1:MemorySizeBytes] %for each symbol (Byte) determine if errors
            occured
38          error  = uint8(rand(8,1)<(hazardRate));
39          Mem(mod(t,ts+1)+2,i) = bitor(Mem(mod(t,ts+1)+1,i),(error(1)*2^0 +
                error(2)*2^1 + error(3)*2^2 + error(4)*2^3 + error(5)*2^4 + error(6)
                *2^5 + error(7)*2^6 + error(8)*2^7));
40      end
41      t  = t+1;
42  end %time steps
43  toc
44  end
```

Bibliography

[1] "Canadian satellite design challenge management society inc., home, canadian satellite design challenge." Available: http://csdcms.ca/. Accessed: 2015-12-15.

[2] M. Swartwout, "Cubesat database." https://sites.google.com/a/slu.edu/swartwout/home/cubesat-database, 2015-12-17. Accessed: 2015-12-17.

[3] M. J. Viens, "Outgassing data for selecting spacecraft materials online." Available: http://outgassing.nasa.gov/, 2014-12-5. Accessed: 2014-12-10.

[4] "Atmosphere properties." Available: http://www.braeunig.us/space/atmos.htm. Accessed: 2014-11-24.

[5] A. C. Tribble, *The Space Environment, Implications for Spacecraft Deign, Revised and expanded edition.* Princeton New Jersey, Princeton University Press, 2003.

[6] G. L. Cook, "Satellite drag coefficients," *Planet. Space Sci.*, vol. 13, pp. 929–946, 1965.

[7] B. J. J. and H. L. B. Roth, "An analytical formula and important parameters for low-energy ion sputtering," *J. Appl Phys.*, vol. 51, p. 2681, 2008.

[8] J. ALLEN, "Understanding single event effects for space applications." Available: http://sourcetech411.com/2013/06/understanding-single-event-effects-for-space-applications/, 7 June 2013. Accessed: 2014-09-24.

[9] C. E. Vaughan, W. W. Green, "Space station program natural environment definition for design," tech. rep., NASA, 1994.

[10] L. R. and S. R., "Characteristics of an anomalous orbital debris population inferred from theoretical modeling," *J. Spacecraft*, vol. 36, no. 5, pp. 726–735, 1999.

[11] *IEC TR 62380, Reliability data handbook Universal model for reliability prediction of electronics components, PCBs and equipment*, 2004.

[12] K. P. V. P. N.M Khamidullina, N.V. Kuznetsov, "predictions of integrated circuit serviceability in space radiation fields," *Radiation Measurements*, vol. 30, pp. 633–638, 1999.

[13] "Ecss: European cooperation for space standardization, energetic particle radiation." http://www.spenvis.oma.be, 2013-10-04. Accessed: 2015-11-12.

[14] "The b n l tandem van de graaff accelerator tvdg let calculator." http://tvdg10.phy.bnl.gov/LETCalc.html, 2004-07-12. Accessed: 2015-11-23.

[15] "Stopping-power and range tables for electrons, protons, and helium ions." http://www.nist.gov/pml/data/star/, 2009-10-07. Accessed: 2015-11-23.

[16] G. Brucker, "Exposure-dose-rate-dependence for a cmos/sos memory," *IEEE Transactions on Nuclear Science*, vol. NS-28, No. 6, pp. 4056–4059, 1981.

[17] J. Barak, "Simple calculations of proton seu cross sections from heavy ion cross sections," *IEEE Transactions on Nuclear Science*, vol. 53, No. 6, pp. 3336–3342, 2006.

[18] P. D. T. O'Connor and A. Kleyner, *Practical Reliability Engineering*. West Sussex, United Kingdom, Wiley,, 5th ed ed., 2012.

[19] S. B. Wicker, *Error Control Systems for Digital Communication and Storage*. PRENTICE HALL, Upper Saddle River, New Jersey 07458, 1st ed., 2012.

[20] Siemens, "Nx space systems thermal." http://www.plm.automation.siemens.com/zh_tw/Images/10654_tcm943-54518.pdf, 2015.

[21] C. Technologies, "Thermal desktop." http://www.crtech.com/sites/default/files/product-files/ThermalDesktop.pdf, 2015.

[22] J. Curran, *Design and optimization of the ECOSat satellite requirements and integration: a trade study analysis of vibrational, thermal, and integration constraints*. PhD thesis, University of Victoria, 2015.

[23] L. Reeves, "The canadian satellite design challenge design interface and environment testing requirements." Available: http://csdcms.ca/images/Documents/CSDC_DIETR_3a_RELEASED_2014-10.pdf, October 2014. Accessed: 2014-06-10.

[24] C. Mauney, "Thermal considerations for surface mount layouts," tech. rep., Texas Instruments. Accessed: 2015-08-15.

[25] "Tms570ls3137 16- and 32-bit risc flash microcontroller," tech. rep., Texas Instruments, 2015.

[26] S. M. Guertin, "Radiation test results for common cubesat microcontrollers and microprocessors," *Radiation Effects Data Workshop (REDW), 2015 IEEE*, pp. 1 – 9, 2015.

[27] A. SAMARAS, "Tid influence on the see sensitivity of active eee," tech. rep., ESA, 2015.

[28] S.Paice, "Tms320c25 radiation testing," tech. rep., ESA, 1990.

[29] "Embedded emmc v4.41 2gb 4gb 8gb 16gb 32gb 64gb 25c to 85c 153b169b," tech. rep., Micron, 2015.

[30] A. B. S. H. K. M. B. Tim Oldham Mark Friendlich "Heavy ion see test report for the micron 4gbit nand flash memory for mms," tech. rep., NASA, 2009.

[31] H. K. Tim Oldham, Jonathan Pellish, "Heavy ion see test report for the micron 8gbit nand flash memory," tech. rep., NASA, 2011.

[32] M. F. Tim Oldham, Ted Wilcox, "Heavy ion see test report for the micron 16gbit nand flash memory," tech. rep., NASA, 2011.

[33] "Ltc2875: 60v fault protected 3.3v or 5v 25kv esd high speed can transceiver," tech. rep., Linear Technologies, 2015.

[34] "Package thermal resistance table," tech. rep., Linear Technologies, 2015.

[35] F. B. J. G. S. S. W. F. J.-F. P. Florence Malou David Dangla "Compendium oftid and sel test results for various candidate spacecraft electronics," *IEEE Radiation and Its Effects on Components and Systems 2011*, pp. 1 – 8, 2011.

[36] P. Kazakoff, "Ecosat-ii communications system - design study january 2015," tech. rep., UVIC ECOSat, 2015.

[37] "Tms320c5535, 'c5534, 'c5533, 'c5532 fixed-point digital signal processors," tech. rep., Texas Instruments, 2015.

[38] F. F. M. Huhtinen, "Computational method to estimate single event upset rates in an accelerator environment," tech. rep., CERN, 1999.

[39] "Mems motion sensor: 3-axis digital output gyroscope," tech. rep., STMicroelectronics, 2012.

[40] H. R. Shea, "Reliability of mems (microsystems) for space applications," *Proceedings of the 11th European Space Mechanisms and Tribology Symposium, ESMATS*, pp. 17–24, 2005.

[41] "Tps735 500-ma, low quiescent current, ultra-low noise, high psrr, low-dropout linear regulator," tech. rep., Texas Instruments, 2015.

[42] "Radiation design test data for advanced cmos product," tech. rep., Texas Instruments, 2012.

[43] V. Ramachandran, B. Narasimham, D. M. Fleetwood, R. D. Schrimpf, W. T. Holman, A. F. Witulski, R. L. Pease, G. W. Dunham, J. E. Seiler, and D. G. Platteter, "Modeling total-dose effects for a low-dropout voltage regulator," *IEEE Transactions on Nuclear Science*, vol. 53, pp. 3223–3231, Dec 2006.

[44] S. B. Wicker, *Error Control Systems for Digital Communication and Storage*. Pearson Prentice Hall, Englewood Cliffs, NJ, 1995.

[45] D. Schipani, M. Elia, and J. Rosenthal, "On the decoding complexity of cyclic codes up to the bch bound," *CoRR*, vol. abs/1102.2939, 2011.